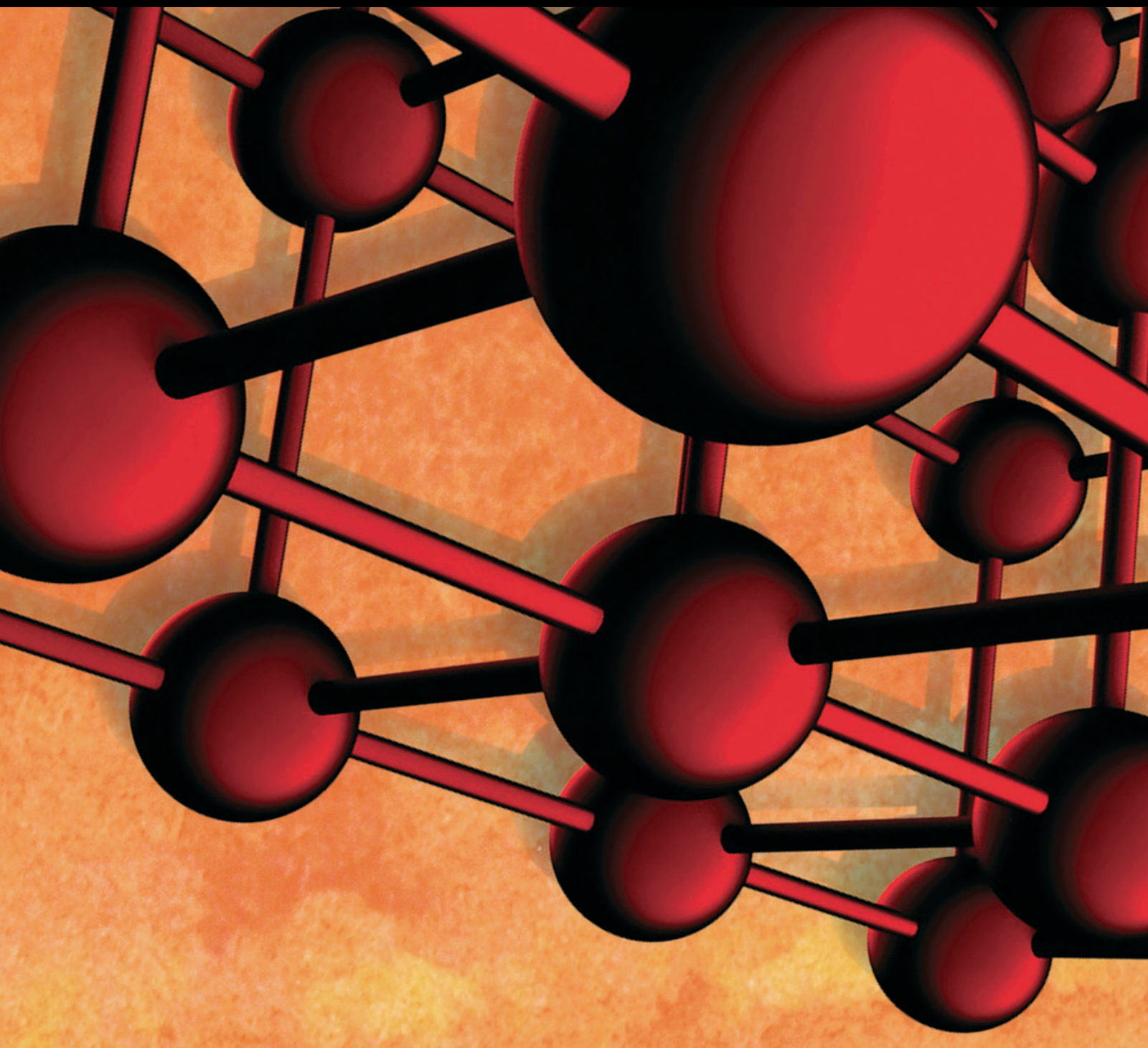


Advances in Materials Science and Engineering

Thermal Spray Technology

Lead Guest Editor: Shuo Yin

Guest Editors: Xinkun Suo, Hanlin Liao, Wenya Li, and Jan Cizek






Thermal Spray Technology

Advances in Materials Science and Engineering

Thermal Spray Technology

Lead Guest Editor: Shuo Yin

Guest Editors: Xinkun Suo, Hanlin Liao, Wenya Li, and Jan Cizek



Copyright © 2019 Hindawi. All rights reserved.

This is a special issue published in “Advances in Materials Science and Engineering.” All articles are open access articles distributed under the Creative Commons Attribution License, which permits unrestricted use, distribution, and reproduction in any medium, provided the original work is properly cited.

Editorial Board

- Antonio Abate, Germany
Michael Aizenshtein, Israel
Hamed Akhavan, Portugal
Jarir Aktaa, Germany
Amelia Almeida, Portugal
Rajan Ambat, Denmark
K. G. Anthymidis, Greece
Santiago Aparicio, Spain
Raul Arenal, Spain
Alicia E. Ares, Argentina
Farhad Aslani, Australia
Apostolos Avgeropoulos, Greece
Renal Backov, France
Markus Bambach, Germany
Amit Bandyopadhyay, USA
Massimiliano Barletta, Italy
Stefano Bellucci, Italy
Avi Bendavid, Australia
Brahim Benmokrane, Canada
Jamal Berakdar, Germany
Jean-Michel Bergheau, France
G. Bernard-Granger, France
Giovanni Berselli, Italy
Patrice Berthod, France
Michele Bianchi, Italy
Hugo C. Biscaia, Portugal
Antonio Boccaccio, Italy
Susmita Bose, USA
H.-G. Brokmeier, Germany
Steve Bull, UK
Gianlorenzo Bussetti, Italy
Jose M. Cabrera, Spain
Antonio Caggiano, Germany
Veronica Calado, Brazil
Marco Cannas, Italy
Paolo Andrea Carraro, Italy
Victor M. Castaño, Mexico
Michelina Catauro, Italy
Robert Černý, Czech Republic
Jose Cesar de Sa, Portugal
Daolun Chen, Canada
Wensu Chen, Australia
Francisco Chinesta, France
Er-Yuan Chuang, Taiwan
Gianluca Cicala, Italy
Francesco Colangelo, Italy
Marco Consales, Italy
José A. Correia, Portugal
María Criado, Spain
Gabriel Cuello, France
Lucas da Silva, Portugal
Narendra B. Dahotre, USA
João P. Davim, Portugal
Angela De Bonis, Italy
Abílio De Jesus, Portugal
Luca De Stefano, Italy
Francesco Delogu, Italy
Luigi Di Benedetto, Italy
Aldo Di Carlo, Italy
Maria Laura Di Lorenzo, Italy
Marisa Di Sabatino, Norway
Luigi Di Sarno, Italy
Ana María Díez-Pascual, Spain
Guru P. Dinda, USA
Nadka Tzankova Dintcheva, Italy
Hongbiao Dong, China
Mingdong Dong, Denmark
Frederic Dumur, France
Stanislaw Dymek, Poland
Kaveh Edalati, Japan
Philip Eisenlohr, USA
Claude Estournès, France
Lúís Evangelista, Norway
Michele Fedel, Italy
F. J. Fernández Fernández, Spain
Isabel J. Ferrer, Spain
Paolo Ferro, Italy
Dora Foti, Italy
Massimo Fresta, Italy
Pasquale Gallo, Japan
Germà Garcia-Belmonte, Spain
Santiago Garcia-Granda, Spain
Carlos Garcia-Mateo, Spain
Georgios I. Giannopoulos, Greece
Ivan Giorgio, Italy
Antonio Gloria, Italy
Vincenzo Guarino, Italy
Daniel Guay, Canada
Gianluca Gubbiotti, Italy
Jenő Gubicza, Hungary
Xuchun Gui, China
Benoit Guiffard, France
Ivan Gutierrez-Urrutia, Japan
Hiroki Habazaki, Japan
Simo-Pekka Hannula, Finland
Akbar Heidarzadeh, Iran
David Holec, Austria
Satoshi Horikoshi, Japan
David Houivet, France
Rui Huang, USA
Yi Huang, UK
Michele Iafisco, Italy
Erdir Ibrahim, UK
Saliha Ilican, Turkey
Md Mainul Islam, Australia
Ilia Ivanov, USA
kenji Kaneko, Japan
Fuat Kara, Turkey
Katsuyuki Kida, Japan
Akihiko Kimura, Japan
Soshu Kirihara, Japan
Paweł Kłosowski, Poland
Jan Koci, Czech Republic
Fantao Kong, China
Ling B. Kong, Singapore
Lingxue Kong, Australia
Pramod Koshy, Australia
Hongchao Kou, China
Alexander Kromka, Czech Republic
Andrea Lamberti, Italy
Luciano Lamberti, Italy
Fulvio Lavecchia, Italy
Marino Lavorgna, Italy
Laurent Lebrun, France
Joon-Hyung Lee, Republic of Korea
Pavel Lejcek, Czech Republic
Cristina Leonelli, Italy
Ying Li, USA
Yuanshi Li, Canada
Yuning Li, Canada
Guang-xing Liang, China
Barbara Liguori, Italy




Jun Liu, China
Meilin Liu, Georgia
Shaomin Liu, Australia
Yunqi Liu, China
Zhiping Luo, USA
Fernando Lusquiños, Spain
Peter Majewski, Australia
Georgios Maliaris, Greece
Muhamamd A. Malik, UK
Dimitrios E. Manolakos, Greece
Necmettin Maraşlı, Turkey
Enzo Martinelli, Italy
Alessandro Martucci, Italy
Yoshitake Masuda, Japan
Bobby Kannan Mathan, Australia
Roshan Mayadunne, Australia
Mamoun Medraj, Canada
Shazim A. Memon, Kazakhstan
Philippe Miele, France
A. E. Miroshnichenko, Australia
Hossein Moayedi, Iran
Sakar Mohan, India
Jose M. Monzo, Spain
Michele Muccini, Italy
Alfonso Muñoz, Spain
Roger Narayan, USA
Rufino M. Navarro, Spain
Miguel Navarro-Cia, UK
Ali Nazari, Australia
Behzad Nematollahi, Australia
Luigi Nicolais, Italy
Peter Niemz, Switzerland
Hiroshi Noguchi, Japan
Chérif Nouar, France
Olanrewaju Ojo, Canada
Dariusz Oleszak, Poland
Laurent Orgéas, France
Togay Ozbakkaloglu, Australia
Nezih Pala, USA
Marián Palcut, Slovakia
Davide Palumbo, Italy
Gianfranco Palumbo, Italy
A. Maria Paradowska, Australia

Zbyšek Pavlík, Czech Republic
Matthew Peel, UK
Alessandro Pegoretti, Italy
Gianluca Percoco, Italy
Claudio Pettinari, Italy
Giorgio Pia, Italy
Silvia M. Pietralunga, Italy
Daniela Pilone, Italy
Teresa M. Piqué, Argentina
Candido Fabrizio Pirri, Italy
Marinos Pitsikalis, Greece
Alain Portavoce, France
Simon C. Potter, Canada
Ulrich Prah, Germany
Viviana F. Rahhal, Argentina
Carlos R. Rambo, Brazil
Shahed Rasekh, Portugal
Manijeh Razeghi, USA
Paulo Reis, Portugal
Yuri Ribakov, Israel
Aniello Riccio, Italy
Anna Richelli, Italy
Antonio Riveiro, Spain
Marco Rossi, Italy
Sylvie Rossignol, France
Pascal Roussel, France
Fernando Rubio-Marcos, Spain
Francesco Ruffino, Italy
Mark H. Rummeli, China
Pietro Russo, Italy
Antti Salminen, Finland
F.H. Samuel, Canada
MariaGabriella Santonicola, Italy
Hélder A. Santos, Finland
Carlo Santulli, Italy
Fabrizio Sarasini, Italy
Michael J. Schütze, Germany
Raffaele Sepe, Italy
Kenichi Shimizu, USA
Fridon Shubitidze, USA
Mercedes Solla, Spain
Donato Sorgente, Italy
Charles C. Sorrell, Australia


Andres Sotelo, Spain
Costas M. Soukoulis, USA
Damien Soulat, France
Adolfo Speghini, Italy
Antonino Squillace, Italy
Manfred Stamm, Germany
Koichi Sugimoto, Japan
Baozhong Sun, China
Sam-Shajing Sun, USA
Youhong Tang, Australia
Kohji Tashiro, Japan
Miguel Angel Torres, Spain
Laszlo Toth, France
Achim Trampert, Germany
Tomasz Trzepieciński, Poland
Matjaz Valant, Slovenia
Luca Valentini, Italy
Ashkan Vaziri, USA
Lijing Wang, Australia
Rui Wang, China
Zhongchang Wang, Portugal
Lu Wei, China
Jörg M. K. Wiezorek, USA
Jiang Wu, UK
Guoqiang Xie, China
Dongmin Yang, UK
Zhonghua Yao, China
Hemmige S. Yathirajan, India
Yee-wen Yen, Taiwan
Wenbin Yi, China
Ling Yin, Australia
Tetsu Yonezawa, Japan
Hiroshi Yoshihara, Japan
Belal F. Yousif, Australia
L. Zajić-kova, Czech Republic
Michele Zappalorto, Italy
Gang Zhang, Singapore
Jinghuai Zhang, China
Li Zhang, China
Mikhail Zheludkevich, Germany
Wei Zhou, China
You Zhou, Japan
Hongtao Zhu, Australia

Contents

Thermal Spray Technology

Shuo Yin , Jan Cizek, Xinkun Suo , Wenya Li , and Hanlin Liao
Editorial (2 pages), Article ID 8654764, Volume 2019 (2019)





Oxidation Resistance and Modification Reaction Mechanism of Al Coating Sprayed on Pure Ti Substrate

Qianqian Jia, Deyuan Li, Sheng Guan, Zhuang Zhang, Nannan Zhang , and Wenzhen Zhao
Research Article (9 pages), Article ID 1403521, Volume 2018 (2019)




Automatic Robot Trajectory for Thermal-Sprayed Complex Surfaces

Dandan Fang, You Zheng , Botao Zhang, Xiangbo Li, Pengfei Ju, Hua Li , and Cunnian Zeng
Research Article (11 pages), Article ID 8697056, Volume 2018 (2019)



Ni-Ti Shape Memory Alloy Coatings for Structural Applications: Optimization of HVOF Spraying Parameters

Carmen De Crescenzo , Despina Karatza, Dino Musmarra , Simeone Chianese ,
Theocharis Baxevanis, Panagiota T. Dalla, Dimitrios A. Exarchos, Konstantinos G. Dassios ,
and Theodore E. Matikas
Research Article (10 pages), Article ID 7867302, Volume 2018 (2019)

Cold-Sprayed Metal Coatings with Nanostructure

Shuo Yin , Chaoyue Chen, Xinkun Suo , and Rocco Lupoi 
Review Article (19 pages), Article ID 2804576, Volume 2018 (2019)

Cold-Sprayed Aluminum-Silica Composite Coatings Enhance Antiwear/Anticorrosion Performances of AZ31 Magnesium Alloy

Lijia Fang, Yuting Xu, Li Gao, Xinkun Suo , Jianguo Gong, and Hua Li 
Research Article (8 pages), Article ID 3215340, Volume 2018 (2019)


Deposition of Coating to Protect Waste Water Reservoir in Acidic Solution by Arc Thermal Spray Process

Han-Seung Lee, Jin-ho Park, Jitendra Kumar Singh , and Mohamed A. Ismail
Research Article (13 pages), Article ID 4050175, Volume 2018 (2019)

Predictive Analysis for the Thermal Diffusion of the Plasma-Assisted Machining of Superalloy Inconel-718 Based on Exponential Smoothing

Chen Shao-Hsien , and Kun-Tan Tsai
Research Article (9 pages), Article ID 9532394, Volume 2018 (2019)

Microstructure and Wear Resistance of TIG Remelted NiCrBSi Thick Coatings

Guo-lu Li, Ya-long Li, Tian-shun Dong , Hai-dou Wang, Xiao-dong Zheng, and Xiu-kai Zhou
Research Article (10 pages), Article ID 8979678, Volume 2018 (2019)

The Influence of Anode Inner Contour on Atmospheric DC Plasma Spraying Process

Kui Wen, Min Liu, Kesong Zhou, Xuezhong Liu, Renzhong Huang, Jie Mao, Kun Yang, Xiaofeng Zhang, Chunming Deng, and Changguang Deng
Research Article (12 pages), Article ID 2084363, Volume 2017 (2019)

Thermal Effect on Structural Interaction between Energy Pile and Its Host Soil

Qingwen Li, Lu Chen, and Lan Qiao
Research Article (9 pages), Article ID 7121785, Volume 2017 (2019)

Editorial

Thermal Spray Technology

Shuo Yin ¹, **Jan Cizek**,² **Xinkun Suo** ³, **Wenya Li** ⁴, and **Hanlin Liao**⁵

¹Trinity College Dublin, The University of Dublin, Department of Mechanical and Manufacturing Engineering, Parsons Building, Dublin 2, Ireland

²Institute of Plasma Physics, The Czech Academy of Sciences, Za Slovankou 1782/3, 182 00 Prague, Czech Republic

³Key Laboratory of Marine Materials and Related Technologies, Zhejiang Key Laboratory of Marine Materials and Protective Technologies, Ningbo Institute of Materials Technology and Engineering, Zhejiang, China

⁴State Key Laboratory of Solidification Processing, Shaanxi Key Laboratory of Friction Welding Technologies, School of Materials Science and Engineering, Northwestern Polytechnical University, Xi'an 710072, China

⁵LERMPS, ICB UMR 6303, CNRS, University of Bourgogne Franche-Comté, UTBM, F-90010 Belfort, France

Correspondence should be addressed to Shuo Yin; yins@tcd.ie

Received 19 November 2018; Accepted 4 December 2018; Published 9 January 2019

Copyright © 2019 Shuo Yin et al. This is an open access article distributed under the Creative Commons Attribution License, which permits unrestricted use, distribution, and reproduction in any medium, provided the original work is properly cited.

Thermal spray is a surface modification technique where solid, semimolten, or molten feedstock powders from metals to ceramics are propelled towards and deposited onto the target surface to form the coating. So far, a variety of thermal spray processes (e.g., HVOF spray, plasma spray, flame spray, wire arc spray, and cold spray) have been developed and widely applied in a broad range of industries including aerospace, automatic, energy, medical, and marine industries. The thermal sprayed coatings provide effective protection against high temperature, corrosion, erosion, oxidation, wear, chemicals, bacteria, and so on. Particularly, certain thermal spray processes can be utilized as an additive manufacturing technique to fabricate standing-free parts or restore damaged components. Given the aforementioned advantages and great potentials, investigations regarding thermal spray processes are always a focal subject and attracting great attentions from both scientific and industrial communities.

This special issue holds 1 review and 9 original research articles. Various thermal spray technologies including cold spray, HVOF spray, arc spray, and plasma spray were used to produce coatings for wear resistance, oxidation resistance, chemical resistance, thermal resistance, and structural applications.

Q. Jia and coworkers reported improved oxidation-resistance properties of arc-sprayed Al coating onto the Ti substrate through modification reaction. Their study focused

on the effect of heating temperature and heating time on the Ti-Al diffusion and the consequent Ti-Al intermetallic phase formation. The experimental result demonstrated that thick intermetallic phases including TiAl, TiAl₂, and TiAl₃ were formed after heating in different conditions. Due to the formation of the intermetallic layers after modification treatment, the Ti substrate with the arc-sprayed Al coatings on the surface had better oxidation-resistance properties in a high-temperature environment than the pure Ti substrate without coating protection.

S. Yin and coworkers contributed a review on nanostructured metal coatings produced with cold spray. They first provided a comprehensive literature review on the nanocrystallization phenomenon occurring in cold-sprayed coatings. Then, the focus was switched to the microstructure and properties of cold-sprayed nanocrystalline metal coatings. They also summarized the current existing studies concerning 1D, 2D, and 3D nanoparticle-reinforced metal matrix composite coatings and their properties. Based on the review, future perspectives of the cold spray technology in producing metal coatings with the nanostructure were proposed at the end of their paper.

D. Fang and coworkers contributed a research paper on the application of robotics and automation in thermal spray processes. They proposed a new method to automatically generate nozzle trajectories for producing uniform coatings on complex curved surfaces. Experimental validation

positively proved the capability and advances of this novel method.

C. De Crescenzo and coworkers proposed a revolutionary technology based on shape memory alloy (SMA) coatings deposited on-site to large-scale metallic structural elements. Investigations were carried out by depositing commercial NiTiInol Ni50.8Ti (at.%) powder onto AISI 316L stainless steel substrates using the HVOF thermal spray technology. The main concern of this paper was studying the effect of main processing parameters including spray distance, fuel-to-oxygen feed rate ratio, and coating thickness on the quality and properties of the coating in terms of hardness, adhesion, roughness, and microstructure. The results confirmed that using optimal spray parameters could significantly improve the properties of HVOF Ni-Ti coatings. The HVOF spraying technique could produce oxide-free SMA coatings without changing the chemical composition of the coating material as compared to the original powder feedstock.

L. Fang and coworkers contributed a research article on cold-sprayed Al + SiO₂ metal matrix composite coatings for protecting the underlying AZ31 Mg alloy substrate. They mainly studied the role of SiO₂ reinforcement in the coating property improvement. The experimental result revealed that adding SiO₂ particles in the metallic Al coatings could significantly improve the coating properties including microhardness, adhesion strength, wear resistance, and corrosion resistance. They also found that the content of SiO₂ particles in the coatings had no significant effects on the coating properties. This work proved that the cold-sprayed Al + SiO₂ metal matrix composite coatings could facilitate the structural applications of Mg alloys.

H.-S. Lee and coworkers studied the corrosion-resistance properties of arc-sprayed AISI 304L stainless steel and Ti coatings in pH 4 solution. They reported that the Ti coating exhibited a uniform, less porous, and adherent coating morphology compared to the AISI 304L coating. The potentiodynamic study showed that the Ti coating reduced the corrosion rate by more than six times compared to the AISI 304L coating after 312 h of exposure to sulfuric acid (H₂SO₄) contaminated water solution due to the uniform and globular morphology of the passive film formed on the Ti coating.

G.-I. Li and coworkers reported a new method to remelt thick plasma-sprayed self-fluxing NiCrBSi coatings with the tungsten inert gas (TIG) arc technology and to improve the properties of the NiCrBSi coatings. They found that TIG-remelting treatment significantly eliminated the micro-defects in the coatings and improved their density. The main phases in the as-sprayed coating changed from γ -Ni, Cr₇C₃, and Cr₂B before remelting treatment to γ -Ni, Cr₂₃C₆, CrB, Ni₃B, and Fe₃C after. The remelted coatings had improved surface roughness, hardness, and wear-resistance properties. The result clearly suggested that the TIG-remelting technique is promising as a post-treatment method to improve the coating properties.

K. Wen and coworkers conducted a research to investigate the thermal and flow dynamics in a plasma torch using the numerical simulation method. The flow regime of a

plasma jet determines the acceleration and heating behaviors of powder particles and hence influences the quality of a plasma-sprayed coating. In this study, based on a well-designed transient CFD model, the authors studied a number of key parameters involved in a plasma torch including arc voltage, net power, thermal efficiency, and in-flight particle velocity based on a standard cylindrical plasma nozzle and a cone-shaped plasma nozzle. The modelling result showed that the geometry of a plasma torch significantly affected the thermal and flow regime of a plasma jet, therefore influencing the final coating quality.

In summary, this special issue provides a detailed account of the present status of the thermal spray technology and highlights the recent developments which cover the novel and important aspects of these technologies and their applications.

Conflicts of Interest

The editors declare that there are no conflicts of interest regarding the publication of this editorial.

Acknowledgments

The editors would like to thank all authors who submitted their research to this special issue, as well as all reviewers for their valuable contribution.

*Shuo Yin
Jan Cizek
Xinkun Suo
Wenya Li
Hanlin Liao*

Research Article

Oxidation Resistance and Modification Reaction Mechanism of Al Coating Sprayed on Pure Ti Substrate

Qianqian Jia,^{1,2} Deyuan Li,¹ Sheng Guan,³ Zhuang Zhang,¹ Nannan Zhang ,¹ and Wenzhen Zhao⁴

¹Department of Material Science and Engineering, Shenyang University of Technology, Shenyang 110870, China

²Guidao Jiaotong Polytechnic Institute, Shenyang 110023, China

³Dalian Huarui Heavy Industrial Special Spare Parts Co., Ltd., Dalian 116052, China

⁴School of Mechanical Engineer, Shenyang University of Technology, Shenyang 110870, China

Correspondence should be addressed to Nannan Zhang; zhangnn@sut.edu.cn

Received 27 July 2018; Revised 5 September 2018; Accepted 12 September 2018; Published 15 October 2018

Academic Editor: Shuo Yin

Copyright © 2018 Qianqian Jia et al. This is an open access article distributed under the Creative Commons Attribution License, which permits unrestricted use, distribution, and reproduction in any medium, provided the original work is properly cited.

An Al coating was deposited on the surface of pure Ti substrate by arc spray technology. In order to enable the modification reaction between the Al coating and Ti substrate, the specimen was heated to a temperature above the melting point of Al. Oxidation testing of the uncoated Ti and coated specimen was conducted at 1073 K under an air atmosphere. The microstructure, chemical composition, and phase determination of the coatings and interfaces, before and after modification treatment, were done using SEM, EDS, and XRD methods. The relationships between the modification results and time and temperature were discussed. The results showed that, after heating at 973 K for 5 hours, there was still sufficient Al on the surface of the specimen. Only intermetallic TiAl₃ was formed in the diffusion region. After heating at 1073 K for 5 hours, all the Al elements diffused into the Ti substrate. Intermetallics TiAl₂ and Ti₃Al were also formed in the diffusion front of Al, in addition to TiAl₃. After heating at 1173 K for 5 hours, a new intermetallic TiAl phase was formed at the interface of TiAl₂ and Ti₃Al. As the modification reaction time was prolonged at 1173 K, the formation of intermetallics TiAl₂, TiAl, and Ti₃Al were all increased. Among them, the formation amount of TiAl₂ > Ti₃Al > TiAl. The specimen after modification treatment had better high temperature oxidation resistance than the pure Ti substrate without coating.

1. Introduction

Titanium and titanium alloys are widely used in the fields of aerospace, chemical production, and the like, due to their high specific strength, low density, and the superior corrosion resistance [1–5]. However, when the temperature is higher than 873 K, the life of the materials is seriously affected due to several factors [4]. These include a decrease in the strength and decay of other mechanical properties, such as plasticity. After adding a coating that has excellent oxidation resistance to the surface of Ti alloys, the oxidation resistance was significantly improved while it maintained outstanding performance [6].

Al always has excellent oxidation resistance since a dense, stable Al₂O₃ film can be formed on the surface of

metal materials [7]. Ti-Al intermetallics are often used as the materials for heat-resistant coatings on titanium and titanium alloys due to the capability of forming Al-rich oxide scales of TiAl [8]. At present, different methods have been used by many researchers to fabricate Ti-Al intermetallic coatings on alloys directly or by modification treatment, such as mechanical alloying [9], laser cladding [10], tungsten inert gas welding surfacing [11], laser surface alloying [12], high-vacuum arc ion plating [8], and high-energy ball milling that combines heat treatment [13], and a solid phase diffusion reaction [14]. However, the fabrication of an Al coating on the surface of pure Ti substrate by arc spray technology, and then heating the specimen to a temperature above the melting point of Al in order to form a TiAl intermetallic, has seldom been reported [15].

In this paper, an Al coating was fabricated on the surface of a pure Ti substrate by arc spray technology. In order to enable the reaction between the Al coating and Ti substrate, the specimen was heated at different temperatures (above the melting point of Al) and times, and the impact of the modification temperature and time was determined. Oxidation testing of the specimen after modification treatment and a pure Ti control was conducted at 1073 K. The effect of the coating on the oxidation resistance, and its protection mechanism, were investigated. The results may provide some theoretical basis for the production of Ti-Al intermetallic coating by the method of modification reaction between coating and substrate at higher temperature.

2. Experimental Procedure

The substrate material used in this study was industrial pure Ti. All of the substrate specimens were formed into a 30 mm long, 30 mm wide, and 10 mm thick shape. Prior to spraying the coatings, ethanol and acetone were used to remove oil on the surfaces of substrates, and then the substrate surfaces were grit blasted with granular corundum to obtain a roughened surface. All of the surfaces of the specimens were sprayed with 0.5 mm thick Al coatings by arc spray technology, and then the specimens in different ceramic boats were treated by heating as follows under an air atmosphere in the resistance furnace: 973 K/5 h, 1073 K/5 h, 1173 K/5 h, 1173 K/10 h, and 1173 K/20 h (better results might be obtained if the heat treatment of the specimens were performed under vacuum or protection gas atmosphere. But in consideration of the practical application, the large titanium plate would be difficult to be performed heat treatment under vacuum or protection gas atmosphere). The spraying material was industrial Al welding wire (2 mm in diameter) which had a purity of greater than 99.8%. The arc spray equipment was type XDP-5, which was homemade by Shenyang University of Technology. The parameters for the arc spray process are listed in Table 1.

The microstructures of the coatings before and after modification treatment were characterized by a scanning electron microscope (SEM; S-3400 and S-4800, Hitachi, Japan). The distribution of chemical elements at the coating-interface-substrate regions was characterized by EDS. The intermetallic compounds formed in the diffusion reaction process were characterized by X-ray diffraction (XRD; Shimadzu, 7000, Kyoto, Japan) with Cu-K α radiation ($\lambda = 0.1541$ nm) at 40 KV 30 mA. Since the thickness of most Ti-Al intermetallic layers which were formed during the modification reaction was too thin, it was difficult to polish to reveal the surfaces of different layers. So in this experiment, not all the layers were identified with XRD, the chemical composition of most diffusion reaction regions was characterized by energy-dispersive spectrometer (EDS) ($V_{a/c} = 20.0$ KV), which was equipped with SEM.

The Al₂O₃ film on the specimen was removed by the waterproof abrasive paper (500#) after modification

TABLE 1: Arc-sprayed parameters.

Materials	Voltage (V)	Current (A)	Atomization compressed air supply pressure (MPa)	Distance (mm)
Al	31	180	0.6	150

treatment. It was then put in a ceramic boat, which was dried to constant weight. Oxidation resistance of the specimen after treatment was performed at 1073 K for 100 hours under an air atmosphere in the furnace. Every 10 hours, the specimen was removed from the furnace, and then it was cooled to room temperature in the atmosphere; the heating rate of the furnace was 293 K/min, and the air cooling rate was about 298 K/min. The comparative experiments for the pure Ti control were performed under similar conditions. The mass gain of the specimen was weighed during every period on an electronic balance, which was accurate to 0.1 mg. The oxidation kinetics curves of the specimen and the pure Ti were then obtained.

3. Results and Discussion

Figure 1 shows the microstructure of the interface that was not heated. As shown in Figure 1, the dark gray area is the Al coating, which was about 500 μ m thick, and the region under the Al coating is the Ti substrate. There were some black pores in the coating. This occurred because after the Al particles in a molten state were sprayed on the surface of the substrate, the surface temperature of the particles decreased rapidly and lead to the large temperature difference between the surface and inside of the particles. As a result, Al particles were present as spheres and pores appeared. The porosity of the thermal spraying coating was about 3%–5%. In addition, the bonding between the Al coating and Ti substrate was mechanical. It was not very compact, and there were also some pores at the interface between the Al coating and the substrate.

Figure 2 shows the cross-sectional BSD image of the Al coating after testing for 5 hours at 973 K (Figure 2(a)) and the distributions of Al (Figure 2(b)) and Ti (Figure 2(c)). As shown in Figure 2, after heating at 973 K for 5 hours, there was still surplus Al on the surface of the specimen, and some of the Al diffused into the Ti substrate.

As shown in Figure 3, after heating at 973 K for 5 hours, a 0.5 mm thick light gray diffusion region was formed between the Al coating and the Ti substrate. The pores between the Al coating and the Ti substrate, which are shown in Figure 1, disappeared as the modification reaction proceeded. Figure 3(b) is the expanded view of region I in Figure 3(a), and it can be seen from Figures 3(a) and 3(b) that a new phase with a continuous distribution was formed in the diffusion region. The chemical composition (at.%) at points A, B, C, and D, as marked in Figure 3(b), is listed in Table 2.

It can be determined that the phases of points A, B, C, D, and E were intermetallic TiAl₃ upon comparing their chemical compositions with the theoretical ratio ranges of intermetallic TiAl₃. The white-gray region which was

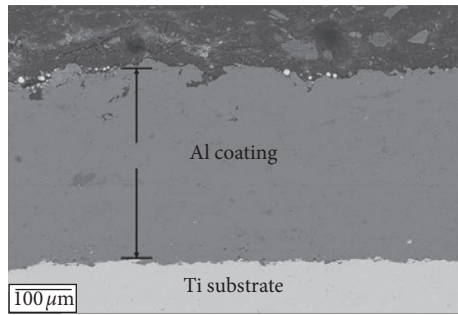


FIGURE 1: Cross-sectional BSD image of Al coating without heating.

represented by F point was Ti substrate. Since Al in the diffusion zone close to the substrate-diffusion zone interface is not homogenous, that part was represented by A, C, and D points which looks like darker.

After heating at 973 K for 5 hours, Al coating (400–500 μm) was still on the surface of the specimen. A 500 μm thick surface layer was then removed in order to expose the diffusion region completely. The XRD results are shown in Figure 4. This data indicate that the diffusion region between the Al coating and the Ti substrate consisted of the TiAl_3 phase. This is the intermetallic structure that formed during the modification reaction between Al and Ti. Since XRD can detect phases that are typically above 2–5%, some Al might be also present on the surface of the specimen.

Figure 5 shows the cross-sectional BSD image of the Al coating after testing for 5 hours at 1073 K (Figure 5(a)) and the distributions of Al (Figure 5(b)) and Ti (Figure 5(c)). As shown in Figure 5, after heating at 1073 K for 5 hours, the Al coating disappeared and all of the Al elements diffused into the Ti substrate.

As shown in Figure 6, after the modification reaction at 1073 K for 5 hours, all of the Al diffused into the Ti substrate and a 0.9 mm thick diffusion region was formed. Compared with the thickness of the diffusion region which was formed at 973 K, the thickness increased at 1073 K. As can be seen in Figure 6, a region with different shades appeared in the diffusion region near the Ti substrate. This showed that different kinds of intermetallic compounds were formed in the diffusion front of Al. Figures 6(c) and 6(d) show the EDS results of points A, B, C, and D marked in Figure 6(b). The chemical compositions (at.%) are listed in Table 3.

After combining the data in Figures 6(c) and 6(d), along with the data in Table 3, and then comparing the chemical composition of points A, B, and C with the theoretical ratio ranges of intermetallic TiAl_3 , TiAl_2 , and Ti_3Al , it can be determined that the phases of A, B, and C were intermetallics TiAl_3 , TiAl_2 , and Ti_3Al , respectively. The 0.9 mm thick diffusion region mainly consisted of TiAl_3 phase, which was formed during the modification reaction between Al and Ti. The TiAl_2 and Ti_3Al phases were formed in the diffusion front of Al, which consumed Al and Ti gradually. The region D was Ti substrate accorded to the chemical composition.

As shown in Figures 7(a) and 7(b), after the modification reaction at 1173 K for 5 hours, the thickness of the diffusion region was about 1.1 mm, which increased compared to 1073 K. Also, the region of different shades that appeared in the diffusion front of Al, and the thickness of regions B and D, all increased compared to 1073 K. Figures 7(c) and 7(d) show the EDS results for points A, B, C, D, and E marked in Figure 7(b). The chemical compositions (at.%) are listed in Table 4.

After combining data in Figures 7(c) and 7(d), along with the data in Table 4, it can be determined that the phases of A, B, C, D, and E were intermetallics TiAl_3 , TiAl_2 , TiAl , Ti_3Al , and Ti substrate, respectively. The diffusion region still mainly consisted of TiAl_3 phase after the modification reaction at 1173 K for 5 hours. The TiAl_2 , TiAl , and Ti_3Al phases were formed in sequence in the diffusion front of Al, which advanced to the Ti substrate. Compared with the modification reaction products which were formed at 1073 K, a new TiAl phase was formed at the interface between TiAl_2 layer and Ti_3Al layer.

From the results above, it is clear that the thickness of the diffusion layer increased with modification reaction temperature, namely, the higher the temperature, the easier the diffusion from Al to the Ti substrate for the same reaction time. Furthermore, Ti changed from α to β during heating up above 1155 K, and Al is a relatively fast diffuser in β -Ti [16].

At test temperature in this paper, Ti in the substrate also diffused into Al coating. In theory, the higher the temperature, the easier the diffusion from Ti to the Al coating as well. Since Ti is a high-melting-point metal, EDS (Figure 2) showed that it was not found that there were a large number of Ti in residual Al coating.

There was still sufficient Al on the surface of the specimen after heating at 973 K for 5 hours. The obvious layer phenomenon (the interface between Ti substrate and the TiAl_3 phase) did not appear in the diffusion front of Al. The diffusion region only consisted of intermetallic TiAl_3 , according to the XRD result. In other words, only $3\text{Al} + \text{Ti} \rightarrow \text{TiAl}_3$ reaction occurred in the diffusion region when there were still sufficient Al elements on the surface of the specimen.

The Al coating disappeared and all the Al elements diffused into the Ti substrate when the modification reaction temperature was raised to 1073 K. The diffusion region still mainly consisted of TiAl_3 phase, but the layered distribution region appeared in the diffusion front of Al. The TiAl_2 and Ti_3Al phases formed in sequence in the diffusion front of Al, with decreasing Al content and increasing Ti content. In other words, the other Ti-Al intermetallic compounds were formed as the reaction proceeded between the TiAl_3 phase and Ti substrate, when there was not any Al on the surface of the specimen.

When the reaction temperature was raised to 1173 K, a new TiAl phase was formed besides the intermetallics TiAl_2 and Ti_3Al , which were layered in the diffusion front of Al. According to the result of Sujata et al. [17], $\Delta G_f \text{TiAl}_2 < \Delta G_f \text{TiAl}_3 < \Delta G_f \text{Ti}_3\text{Al} < \Delta G_f \text{TiAl} < 0$ when the temperature range is about 900–1400 K. Intermetallic TiAl was more difficult to be formed than TiAl_2 and Ti_3Al from the

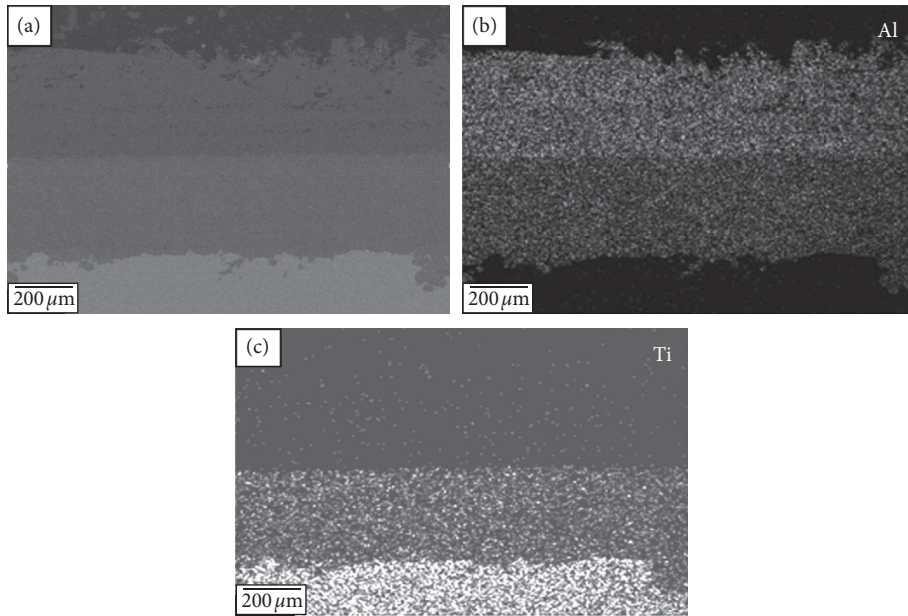


FIGURE 2: (a) Cross-sectional BSD image of Al coating after testing for 5 hours at 973 K and the distributions of (b) Al and (c) Ti.

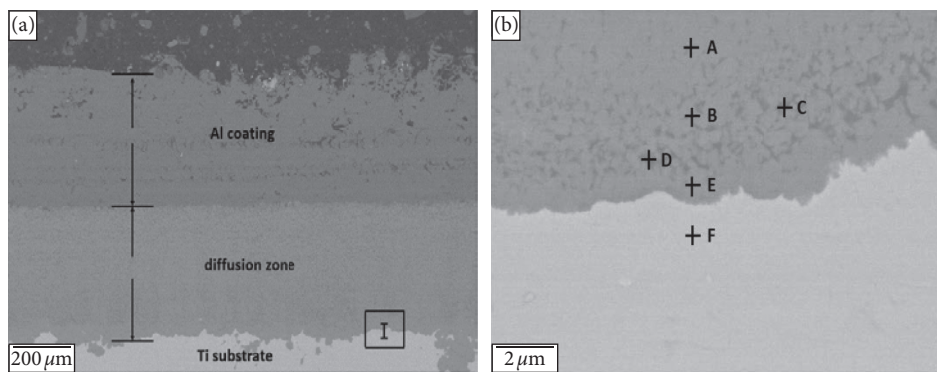


FIGURE 3: (a) Cross-sectional BSD image of Al coating after testing for 5 hours at 973 K, and (b) the expanded view of region I in Figure 3(a).

TABLE 2: The chemical composition (at.%) of different points, as marked in Figure 3(b).

Points	Al	Ti
A	77.61	22.39
B	75.28	24.72
C	78.62	21.38
D	77.79	22.21
E	74.43	25.57
F	0	100

thermodynamics, which explains why the TiAl phase formed during the modification reaction at 1173 K, but not at 1073 K.

In addition, the thickness of TiAl₂ and Ti₃Al both increased at 1173 K compared with at 1073 K. This showed that the increase in the temperature could contribute to further reaction between TiAl₃ phase and Ti substrate.

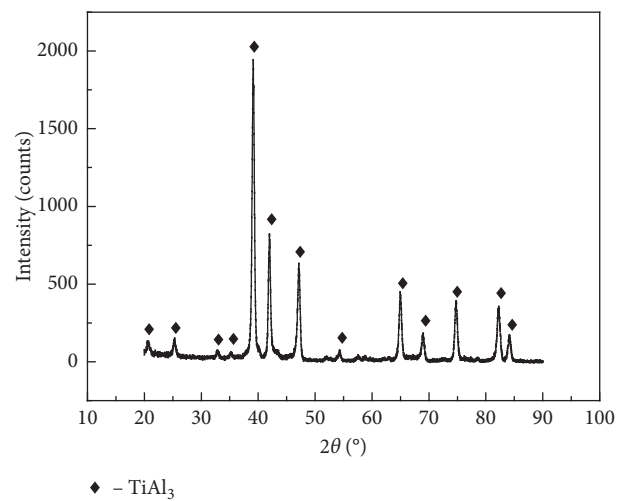


FIGURE 4: XRD spectrum after removal of 500 μm thick surface layer.

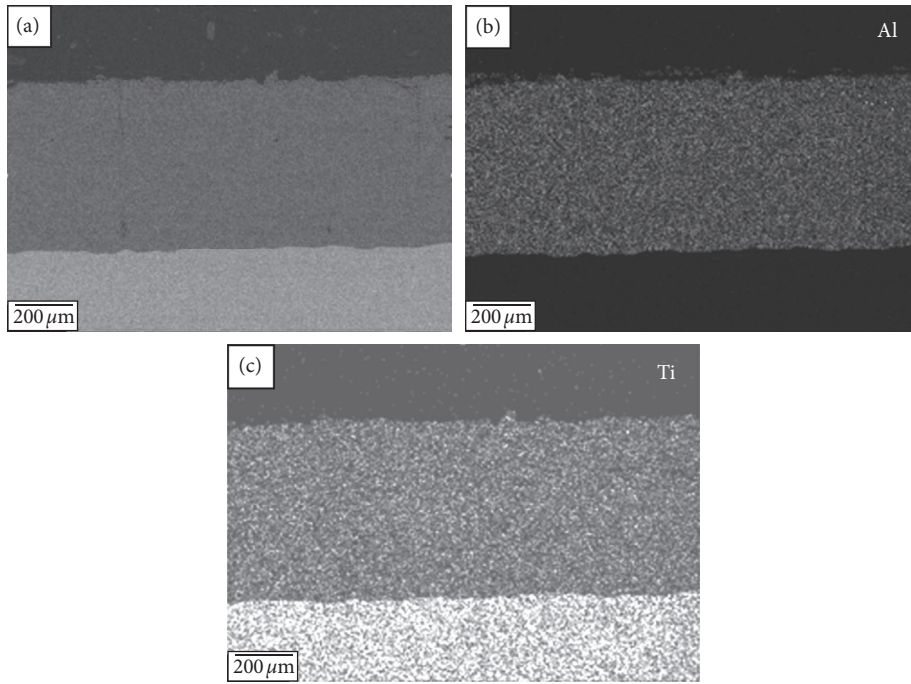


FIGURE 5: (a) Cross-sectional BSD image of Al coating after testing for 5 hours at 1073 K and the distribution of (b) Al and (c) Ti.

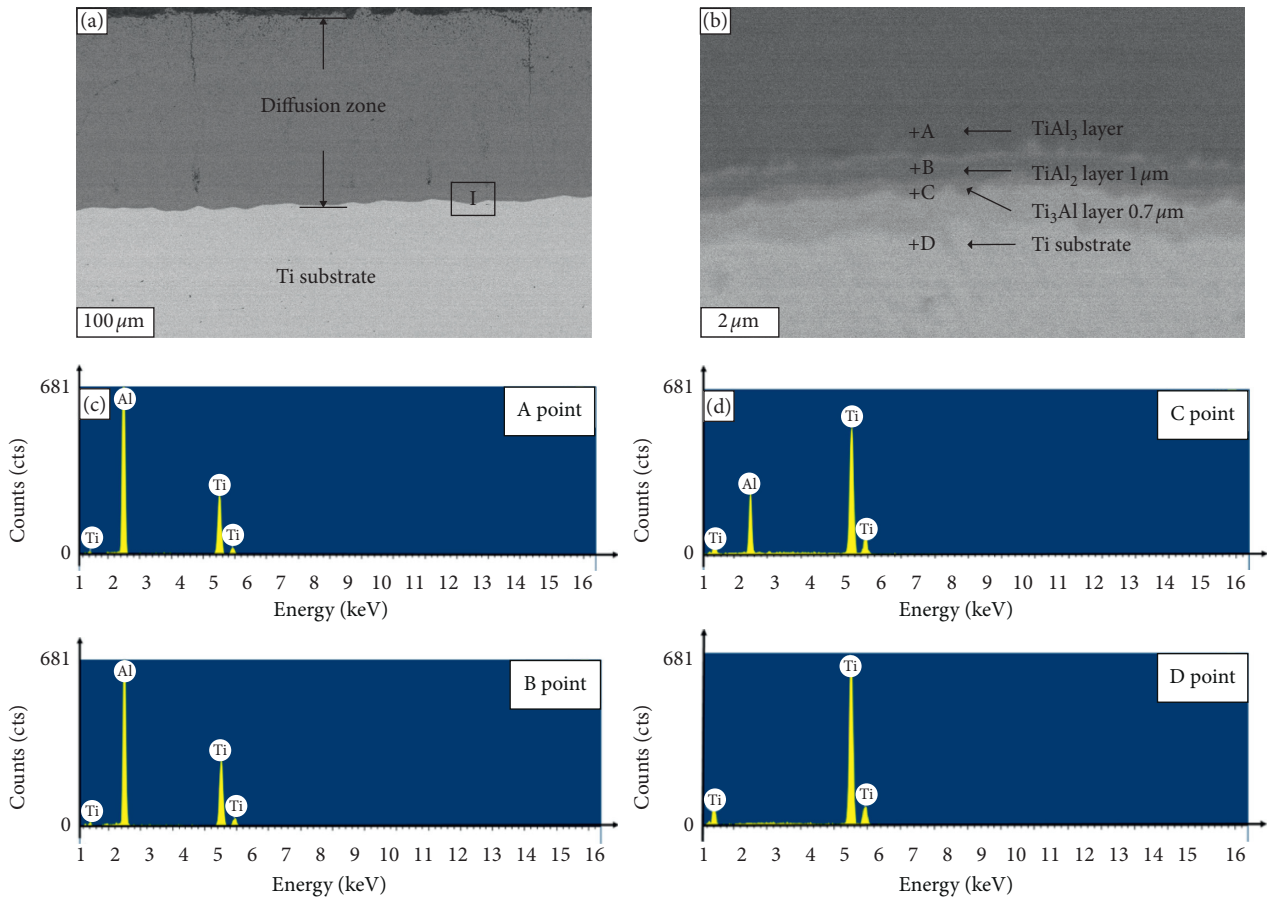


FIGURE 6: (a) Cross-sectional BSD image of Al coating after testing for 5 hours at 1073 K, (b) the expanded view of region I in Figure 6(a), (c) EDS results of points A and B in Figure 6(b), and (d) EDS results of points C and D marked in Figure 6(b).

TABLE 3: The chemical composition (at.%) in different points, as marked in Figure 6(b).

Points	Al	Ti
A	73.77	26.23
B	67.49	32.51
C	29.27	70.73
D	0	100

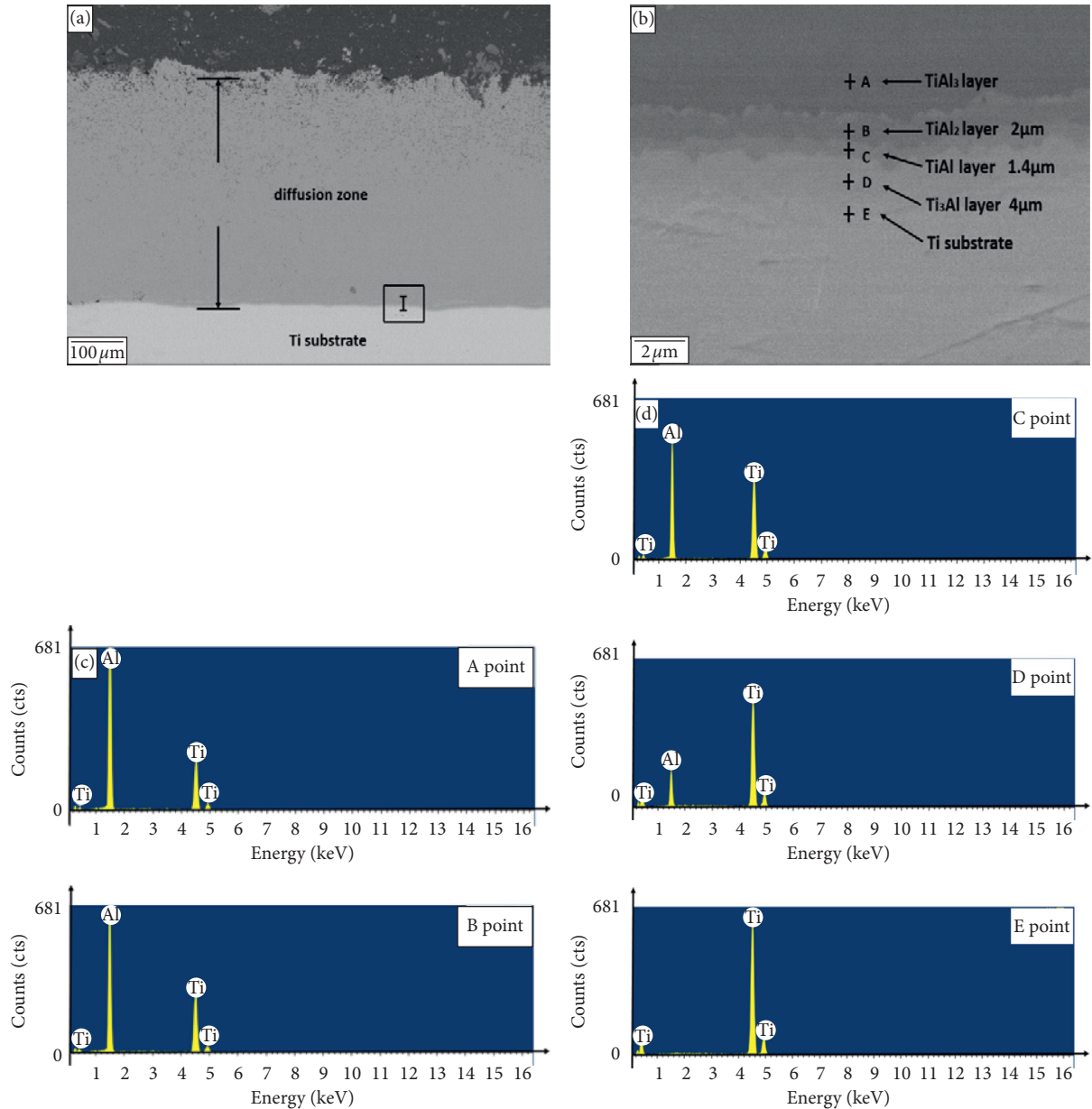


FIGURE 7: (a) Cross-sectional BSD image of Al coating after testing for 5 hours at 1173 K, (b) the expanded view of region I in Figure 7(a), (c) EDS results of points A and B marked in Figure 7(b), and (d) EDS results of points C, D, and E marked in Figure 7(b).

As shown in Figure 8(a), the microstructure of the diffusion region after modification treatment at 1173 K for 10 hours was basically identical to it after 5 hours. Figure 8(b) shows that the thickness of B, C, and D layers in the diffusion region near the Ti substrate was thicker than that under the reaction condition of 1173 K/5 hr. The largest increase in the

thickness was layer B, and the smallest one was layer C. The chemical compositions (at.%) of points A, B, C, D, and E as marked in Figure 8(b) are listed in Table 5.

As seen from the data in Table 5, the products which were formed after modification treatment at 1173 K for 10 hours, and their distributions, were not significantly

TABLE 4: The chemical composition (at.%) in different points, as marked in Figure 7(b).

Points	Al	Ti
A	74.08	25.92
B	65.12	34.88
C	52.22	47.78
D	22.08	77.92
E	0	100

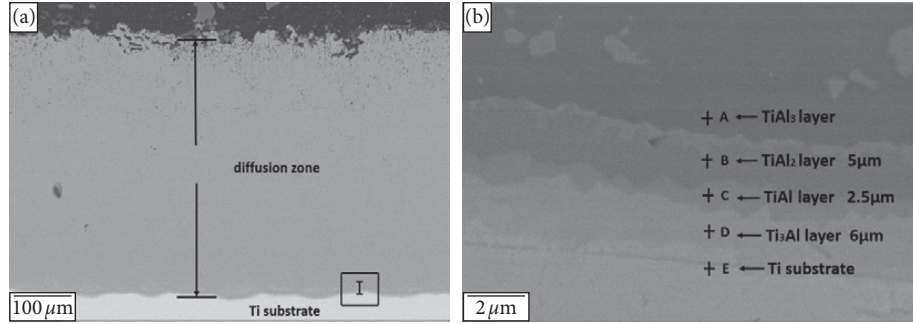


FIGURE 8: (a) Cross-sectional BSD image of Al coating after testing for 10 hours at 1173 K and (b) the expanded view of region I in Figure 8(a).

TABLE 5: The chemical composition (at.%) in different points, as marked in Figure 8(b).

Points	Al	Ti
A	74.08	25.92
B	65.37	34.63
C	48.06	51.94
D	26.42	73.58
E	0	100

changed compared with that under the reaction condition of 1173 K for 5 h. The diffusion region still mainly consisted of TiAl_3 phase and intermetallics TiAl_2 , TiAl , and Ti_3Al formed in sequence in the diffusion front of Al.

As shown in Figure 9(a), the layered structure was more obvious in the diffusion front of Al after modification treatment at 1173 K for 20 hours. In addition, it can be seen in Figure 9(a) that the thickness of B and D layers increased compared with that under the reaction condition of 1173 K for 10 hours. The C layer had less change in the thickness. The chemical compositions (at.%) of points A, B, C, D, and E as marked in Figure 9(b) are listed in Table 6.

As can be seen from the data in Table 6, the products which were formed after the modification treatment of the specimen at 1173 K for 20 hours, and their distributions, were all the same with that under the reaction condition of 1173 K for 5 hours and 1173 K for 10 hours.

As shown in Figure 9(c), the layered structure in the diffusion front of Al was comprised of different kinds of Ti-Al intermetallic. It could be revealed that the element ratio of titanium to aluminum in TiAl_3 and TiAl_2 was a fixed value, but for TiAl and Ti_3Al , it was within a certain range.

The products formed after the modification treatment of the specimens at 1173 K for 10 and 20 hours, and their distributions, were the same as that under the reaction condition of 1173 K for 5 hours. The diffusion region mainly consisted of intermetallic TiAl_3 , and intermetallics TiAl_2 , TiAl , and Ti_3Al were formed in sequence in the diffusion front of Al, with decreasing Al content and increasing Ti content.

As can be seen from the data in Table 7, the thickness of TiAl_2 , TiAl , and Ti_3Al layers were all increased as the reaction time was prolonged. This was because a concentration gradient of Ti was still present between TiAl_3 phase and Ti substrate. The Ti element in Ti substrate continuously diffused into TiAl_3 layer and reacted with it under the concentration gradient driving forces, and then intermetallics TiAl_2 , TiAl , and Ti_3Al were formed. It is also apparent from Table 7 that the increased thickness of TiAl_2 layer > the increased thickness of Ti_3Al layer > the increased thickness of TiAl layer. This was because, as mentioned above, $\Delta G_f \text{TiAl}_2 < \Delta G_f \text{TiAl}_3 < \Delta G_f \text{Ti}_3\text{Al} < \Delta G_f \text{TiAl} < 0$ when the temperature range is about 900–1400 K. Therefore, the formation amount of TiAl_2 phase > the formation amount of Ti_3Al phase > the formation amount of TiAl phase. The growth of TiAl_2 phase and TiAl phase was in a competitive relationship, and the growth speed of TiAl_2 was 1.4 times the growth speed of TiAl [18]. This also made that the increase in the thickness of TiAl_2 layer larger than that of TiAl layer as the reaction proceeded.

In order to test the high temperature oxidation resistance of Ti-Al intermetallics which were formed during the modification reaction, 100 μm thick Al_2O_3 surface layer that occurred after the modification reaction at 1173 K for 20 hours was removed by waterproof abrasive paper to expose the TiAl_3 layer completely. Then, oxidation resistance of the Al/Ti specimen after treatment and the pure Ti without

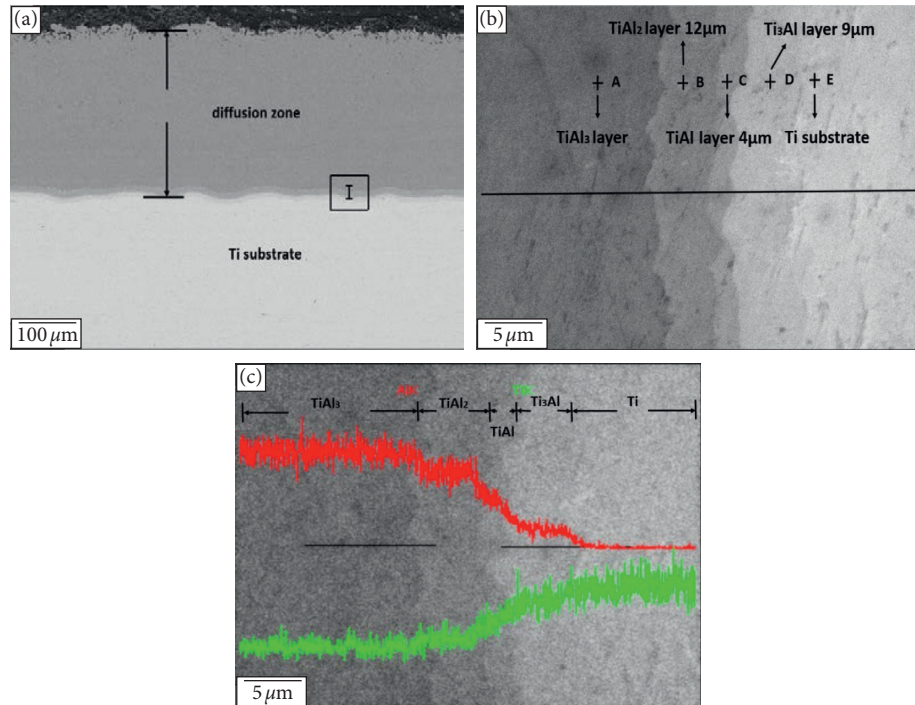


FIGURE 9: (a) Cross-sectional BSD image of Al coating after testing for 20 hours at 1173 K, (b) the expanded view of region I in Figure 9(a), and (c) concentration profiles of Al, Ti elements in Figure 9(b).

TABLE 6: The chemical composition (at.%) in different points, as marked in Figure 9(b).

Points	Al	Ti
A	74.74	25.26
B	65.65	34.35
C	50.44	49.56
D	22.04	77.96
E	0	100

TABLE 7: Thickness (μm) of different Ti-Al Intermetallics layers with 1173 K/5 h, 1173 K/10 h, and 1173 K/20 h.

Ti-Al intermetallics	1173 K/5 h	1173 K/10 h	1173 K/20 h
TiAl ₂	2	5	12
TiAl	1.4	2.5	4
Ti ₃ Al	4	6	9

coating were performed at 1073 K for 100 hours under air atmosphere.

It could be seen from the oxidizing dynamic curves in Figure 10 that the curve for the pure Ti without coating is nearly straight. This was in a high-temperature environment, so it was easy for Ti to be oxidized by molecular oxygen to produce TiO₂, which was easy to break. The TiO₂, which had a rutile structure, peeled off from the surface of the pure Ti specimen and the exposed Ti substrate to be oxidized again.

The oxygen weight gain of the Al/Ti specimen (after modification treatment and removal of the Al₂O₃ film) in the later stage of the oxidation exhibited a reduction as compared to the beginning of the oxidation. This was because intermetallics TiAl₃, TiAl₂, and others, which were rich in Al,

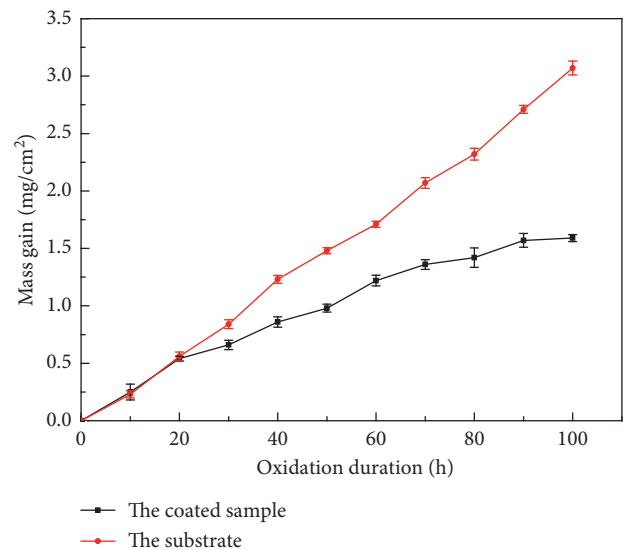


FIGURE 10: Oxidation kinetics curves of Ti alloy with and without coating at 1073 K for 100 h (10 cycles).

formed in the process of modification reaction between the Al coating and Ti substrate. The Al₂O₃ was formed by the reaction between Al-rich TiAl₃ phase and the oxygen in air at the beginning of the oxidation. The surface of the specimen was covered with Al₂O₃ film, which increased constantly. Furthermore, the oxidation of the specimen was sufficiently suppressed. But a little amount of the Al₂O₃ film peeled off from the surface of the specimen with the increase in the high temperature oxidation time, and the exposed TiAl₃

phase would be oxidized again. The weight of the specimen also increased during the later stage of the oxidation but with smaller increasing amount.

The total weight gain of noncoated Ti and coated Al/Ti specimen was 3.1 mg and 1.6 mg, respectively, after oxidation for 100 hours as it is shown in Figure 10. The total weight gain of noncoated Ti was almost twice than the coated Al/Ti specimens.

The Al/Ti specimens after modification treatment had a better high temperature oxidation resistance than the pure Ti without protection coating.

4. Conclusions

- (1) After heating at 973 K for 5 hours, there was still sufficient Al on the surface of the specimen, and only intermetallic TiAl_3 formed in the diffusion region.
- (2) After heating at 1073 K for 5 hours, all of the Al diffused into the Ti substrate, and intermetallics TiAl_2 and Ti_3Al also formed in the diffusion front of Al, in addition to TiAl_3 .
- (3) After heating at 1173 K for 5 hours, a new intermetallic TiAl phase was formed at the interface of TiAl_2 and Ti_3Al , in addition to the intermetallics TiAl_2 and Ti_3Al in the zone of the diffusion reaction.
- (4) As the modification reaction time was prolonged at 1173 K, the formation of intermetallics TiAl_2 , TiAl , and Ti_3Al all increased, and among them, the formation amount of TiAl_2 phase > the formation amount of Ti_3Al phase > the formation amount of TiAl phase.
- (5) The Al/Ti specimens after modification treatment had better high temperature oxidation resistance than the pure Ti without protection coating.

Data Availability

The data used to support the findings of this study are available from the corresponding author upon request.

Conflicts of Interest

The authors declare that there are no conflicts of interest regarding the publication of this paper.

Acknowledgments

This work was financially supported by the Natural Science Foundation of Liaoning Province (No. 201602553) Chinese National Natural Science Foundation (No. 51301112).

References

- [1] H. Riedl, C. M. Koller, F. Munnik et al., "Influence of oxygen impurities on growth morphology, structure and mechanical properties of Ti-Al-N thin films," *Thin Solid Films*, vol. 603, pp. 39–49, 2016.
- [2] H. Z. Cui, L. Ma, L. L. Cao, F. L. Teng, and N. Cui, "Effect of NiAl content on phases and microstructures of TiC-TiB2-NiAl composites fabricated by reaction synthesis," *Transactions of Nonferrous Metals Society of China*, vol. 24, no. 2, pp. 346–353, 2014.
- [3] H. Sina, K. B. Surreddi, and S. Iyengar, "Phase evolution during the reactive sintering of ternary Al-Ni-Ti powder compacts," *Journal of Alloys and Compounds*, vol. 661, pp. 294–305, 2016.
- [4] M. L. Vera, Á. Colaccio, M. R. Rosenberger, C. E. Schvezov, and A. E. Ares, "Influence of the electrolyte concentration on the smooth TiO_2 anodic coatings on Ti-6Al-4V," *Coatings*, vol. 7, no. 3, p. 39, 2017.
- [5] C. O'Sullivan, P. O'Hare, G. Byrne, L. O'Neill, K. B. Ryan, and A. M. Crean, "A modified surface on titanium deposited by a blasting process," *Coatings*, vol. 1, no. 1, pp. 53–71, 2011.
- [6] Q. Jia, D. Li, S. Li, Z. Zhang, and N. Zhang, "High-temperature oxidation resistance of NiAl intermetallic formed in situ by thermal spraying," *Coatings*, vol. 8, no. 8, p. 292, 2018.
- [7] Y. M. Xiong, S. L. Zhu, and F. H. Wang, "The oxidation behavior of TiAlNb intermetallics with coatings at 800°C," *Surface and Coatings Technology*, vol. 197, no. 2-3, pp. 322–326, 2005.
- [8] M. M. Zhang, M. L. Shen, L. Xin, X. Y. Ding, S. L. Zhu, and F. H. Wang, "High vacuum arc ion plating TiAl coatings for protecting titanium alloy against oxidation at medium high temperatures," *Corrosion Science*, vol. 112, pp. 36–43, 2016.
- [9] C. Cheng, X. M. Feng, and Y. F. Shen, "Oxidation behavior of a high Si content Al-Si composite coating fabricated on Ti-6Al-4V substrate by mechanical alloying method," *Journal of Alloys and Compounds*, vol. 701, pp. 27–36, 2017.
- [10] I. N. Maliutina, H. Mohand, J. Sijobert, P. Bertrand, D. V. Lazurenko, and I. A. Bataev, "Structure and oxidation behavior of γ -TiAl coating produced by laser cladding on titanium alloy," *Surface and Coatings Technology*, vol. 319, pp. 136–144, 2017.
- [11] M. Tavoosi and S. Arjmand, "In situ formation of Al/ Al_3Ti composite coating on pure Ti surface by TIG surfacing process," *Surfaces and Interfaces*, vol. 8, pp. 1–7, 2017.
- [12] J. J. Dai, F. Y. Zhang, A. M. Wang, H. J. Yu, and C. Z. Chen, "Microstructure and properties of Ti-Al coating and Ti-Al-Si system coatings on Ti-6Al-4V fabricated by laser surface alloying," *Surface and Coatings Technology*, vol. 309, pp. 805–813, 2017.
- [13] J. Q. Wang, L. Y. Kong, T. F. Li, and T. Y. Xiong, "A novel $\text{TiAl}_3/\text{Al}_2\text{O}_3$ composite coating on γ -TiAl alloy and evaluating the oxidation performance," *Applied Surface Science*, vol. 361, pp. 90–94, 2016.
- [14] Y. Sun, Z. P. Wan, L. X. Hu, B. H. Wu, and T. Q. Deng, "Characterization on solid phase diffusion reaction behavior and diffusion reaction kinetic of Ti/Al," *Rare Metal Materials and Engineering*, vol. 46, no. 8, pp. 2080–2086, 2017.
- [15] J. Q. Wang, L. Y. Kong, J. Wu, T. F. Li, and T. Y. Xiong, "Microstructure evolution and oxidation resistance of silicon-aluminizing coating on γ -TiAl alloy," *Applied Surface Science*, vol. 356, pp. 827–836, 2015.
- [16] Y. Mishin and C. Herzig, "Diffusion in the Ti-Al system," *Acta Materialia*, vol. 48, no. 3, pp. 589–623, 2000.
- [17] M. Sujata, S. Bhargava, and S. Sangal, "On the formation of TiAl_3 during reaction between solid Ti and liquid Al," *Journal of Materials Science Letters*, vol. 16, no. 13, pp. 1175–1178, 1997.
- [18] R. Martin, S. L. Kampe, J. S. Marte, and T. P. Pete, "Microstructure/processing relationships in reaction-synthesized titanium aluminide intermetallic matrix composites," *Metallurgical and Materials Transactions A*, vol. 33, no. 8, pp. 2747–2753, 2002.

Research Article

Automatic Robot Trajectory for Thermal-Sprayed Complex Surfaces

Dandan Fang,^{1,2} You Zheng ,^{2,3} Botao Zhang,⁴ Xiangbo Li,⁵ Pengfei Ju,⁶ Hua Li ,⁴ and Cunnian Zeng²

¹Aux Group, Ningbo 315201, China

²Wuhan University of Technology, Wuhan 430000, China

³SELF Electronics Co., Ningbo 315201, China

⁴Key Laboratory of Marine Materials and Related Technologies, Key Laboratory of Marine Materials and Protective Technologies of Zhejiang Province, Ningbo Institute of Materials Technology and Engineering, Chinese Academy of Sciences, Ningbo 315201, China

⁵State Key Laboratory for Marine Corrosion and Protection, Luoyang Ship Material Research Institute (LSMRI), Qingdao 266101, China

⁶Shanghai Aerospace Equipment Manufacture, Shanghai 200245, China

Correspondence should be addressed to You Zheng; zhengyou@nbut.edu.cn and Hua Li; lihua@nimte.ac.cn

Received 15 January 2018; Revised 27 March 2018; Accepted 22 April 2018; Published 8 July 2018

Academic Editor: Shuo Yin

Copyright © 2018 Dandan Fang et al. This is an open access article distributed under the Creative Commons Attribution License, which permits unrestricted use, distribution, and reproduction in any medium, provided the original work is properly cited.

Automatic trajectory generation for thermal spray application is highly desirable for today's automotive manufacturing. Automatic robot trajectory for free-form surfaces to satisfy the coating uniform is still highly challenging due to the complex geometry of free-form surfaces. The purpose of this study is to present and implement a method for automatic generation of robot trajectory according to the given spray parameters on polygon profile and complex curved free-form surfaces, such as torch speed, spray distance, spray angle, and so on. This software development foundation is an Add-In programme of RobotStudio, which is off-line programming and simulation software of ABB Company. The experimental results show that the robot trajectory can be generated rapidly, accurately, and automatically on the complex geometries by this method.

1. Introduction

Robot manipulators are programmable mechanical systems designed to execute many tasks in industry. The advanced robot system has been widely used in thermal spray application in recent years [1–3]. When a robot is used, trajectory generation represents an important part of the work, because the uniformity of spray thickness can significantly influence the quality of coating, and the robot trajectory has a great effect on the uniformity of coating [4–6].

Robot trajectory tells the robot how to move around. It is composed of a series of curves which are defined by the spray parameters in thermal spray operations, and there are several targets which are represented by orientation and Cartesian position on each curve. The generation of robot trajectory on plane surface in thermal spraying is traditionally made by

such methods as point-by-point or teaching-playback. This method is tedious and time-consuming. The demand for coating on curved surface has increased over the last few years. It requires hundreds of points in the trajectory and different orientation for each point, so it is very difficult to create such a trajectory by manual point-by-point programming method [7–9]. With the development of the robotics, the robot manufacturers provide software for off-line programming, such as RobotStudio, which is a simulation and off-line programming software of ABB Company [10]. A virtual workshop can be elaborated, and the robot program can be prepared and simulated with RobotStudio.

The complete robot trajectory can be generated manually point by point, which is a very laborious process and not precise in RobotStudio. Furthermore, the functions of RobotStudio are too narrow to process some complex

workpieces for thermal spray applications since the fact that spraying trajectory is composed of many lines or curves with certain offset. Consequently, it is necessary to develop a software tool to generate robot trajectory for free-form surfaces according to the given spray parameters.

Most previous researchers typically focused on the mesh method for automated trajectory generation since such method is capable of generating trajectories on all types of complex workpieces [8, 11]. In the mesh method, the mesh of the CAD model is generated at first, then the trajectory from the mesh points and normal vectors to the surface are found out according to graphics theories. Unfortunately, the off-line programming software does not provide any application programming interface (API) for the mesh method. Most of the off-line programming software such as RobotStudio uses the bounding box method to represent 3D models since the bounding box method is efficient in real-time collision detection algorithms. In other words, developers need to develop various functions and programs of the off-line programming software independently. For example, developers must transfer the coordinates of points to the robot system by geometrical transformations. Although some mathematical software such as MATLAB could help realize the functions, too much heavy labor is still involved in software developing and porting.

To blend into the off-line programming software, the cutting method was proposed and applied to generate robot trajectories in thermal spraying. With this method, every point of curves can be obtained by some special APIs to realize object Boolean operations, and the trajectories data also can be calculated and simulated in the off-line programming software directly. It means that the entire development process with the orthogonal cutting method can be simpler and faster than the process with the method of mesh generation. Thermal Spray Toolkit (TST) is one such application, which was developed based on the RobotStudio software for thermal spraying to provide solutions to generate automatic trajectories on various workpieces according to the right spray parameters and trajectory parameters. Some details of TST for the simple workpiece were introduced in [12]. In this paper, we try to answer the question how to generate robot trajectory for complex surfaces automatically.

2. Development Environment

2.1. RobotStudio Software. Off-line programming is the best way to generate robot trajectory on complex geometry. ABB's simulation and off-line programming software, RobotStudio, allow robot programming to be done on a PC in the office without shutting down production. It also enables robot programs to be prepared in advance, which increases overall productivity. RobotStudio provides the tools to increase the profitability of a robot system by performing tasks such as training, programming, and optimization without disturbing production. This provides numerous benefits including risk reduction, quicker start-up, shorter changeover, and increased productivity [10].

RobotStudio is built on the ABB Virtual Controller, an exact copy of the real software that runs the robots in

production. It thus allows very realistic simulations to be performed, using real robot programs and configuration files identical to those used on the shop floor. RobotStudio allows creating Add-In programs that enable users to customize and extend its functionality. Thermal Spray Toolkit is an Add-In program to extend RobotStudio's functions.

Currently, there are two different methods for Add-In development. One is creating an Add-In in Visual Studio Tool for Applications (VSTA), and the other is creating an Add-In based on RobotStudio API in Visual Studio.

2.2. RobotStudio API. An Application Programming Interface (API) is an interface implemented by a software program, which enables it to interact with other software. It is similar to the interaction of user interface which facilitates communication between humans and computers. An API is implemented by applications, libraries, and operating systems to determine their vocabularies and calling conventions and used to access their services. It may include specifications for routines, data structures, object classes, and protocols used to create communications between the consumer and the implementer of the API.

RobotStudio API shows the RobotStudio Object Model and explains the methods, properties, and events for each object. In the development of Thermal Spray Toolkit, the RobotStudio API is used.

2.3. Create an Add-In with VSTA. Add-Ins are programs that add optional commands and features to RobotStudio. Before using an Add-In, RobotStudio must be installed on the computer and then loaded in the memory. Loading an Add-In program makes the feature available in RobotStudio and adds any associated commands to the appropriate menus.

Visual Studio Tool for Applications (VSTA) is included in RobotStudio and can allow create Add-Ins in a simple way, but there are some limitations when using VSTA to create the Add-Ins which are caused by Microsoft Proxy Generator. These things will not work:

- (i) A method that has an array type as parameter.
- (ii) A method or property that references the System. Drawing or System. Windows. Forms namespaces.
- (iii) A method or property that references the type.
- (iv) An event that is declared static.

Since Add-Ins created with Visual Studio do not use the proxy, these limitations do not apply.

2.4. Create an Add-In in Visual Studio. To be able to use the entire RobotStudio API without limitations, Visual Studio can be used to create an Add-In. All the codes and interface can be developed in Visual Studio (C# or VB.NET), and RobotStudio can load the Add-In program automatically when it is opened. Thermal Spray Toolkit was developed in environment C#, which is more powerful than VB.NET. The specific steps for creating an Add-In in Visual Studio are listed in Appendix.

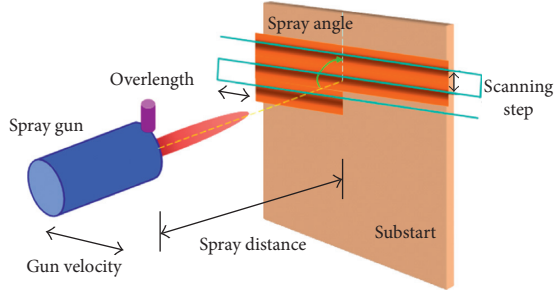


FIGURE 1: The kinematic parameters of cold spray process.

3. Autogeneration of Trajectory

3.1. 3D Model. Computer-aided design (CAD) is a well-known computer-based tool that assists engineers, architects, and other design professionals in their design activities. Model-based object representations are known from computer graphics and CAD. RobotStudio is based on a 3D model. The model of workpiece can be imported to RobotStudio, and trajectory can be generated directly based on the CAD model in RobotStudio [13]. But RobotStudio meets the challenges in thermal spray application. The function of RobotStudio is not powerful enough to deal with the Boolean operation of a 3D model, especially when confronted with the complex surface. It is difficult to get a series of curves on the complex surface according to the spray parameters, such as the robot velocity, the spray distance, the spray angle, the step between each pass, and the over-length. The development of Thermal Spray Toolkit must be based on the API of RobotStudio. As a result, Thermal Spray Toolkit has a great flexibility to deal with complex surfaces.

3.2. Parameters of Cold Spray Process. The kinematic parameters of the cold spray process are demonstrated in Figure 1. Spray distance is the distance from the nozzle exit of spray gun to the substrate surface; scanning step is the distance between two neighbor scanning passes; spray angle is the angle between the centerline of the spray gun and the substrate surface; gun velocity is the relative velocity between spray gun and substrate [14–16].

3.3. The Methodology of Generation of Trajectory. As mentioned above, the methodology of generation of trajectory proposed in this paper is based on the cutting method. Known by the characteristics of thermal spray, the uniform scanning step could keep a stable TCP velocity so that the uniformity of coating can usually be guaranteed. That is, when designing with cutting method, the uniformity of the distance of two neighbor scanning passes should be considered.

With a polygonal substrate, the key of algorithm is to create a plane orthogonal with the polygon profile to equally divide the substrate. In this algorithm, to create an initial plane Π , a point on the polygon should be selected at first. Using the theory of differential geometry [17], the equation of the polygon is described as

$$\begin{aligned} x &= x(t), \\ y &= y(t), \\ z &= z(t), \quad \alpha \leq t \leq \beta, \end{aligned} \quad (1)$$

$P_0(x(t_0), y(t_0), z(t_0)) \in L$ is the selected point.

Based on the differential geometry [17], the tangent vector $\vec{\tau}$ at this point should be

$$\vec{\tau} = \{x'(t_0), y'(t_0), z'(t_0)\}. \quad (2)$$

And the unit normal vector of the polygon can be generated easily by the vector product of two noncollinear vectors on the polygon.

In the RobotStudio, the scroll bar tools can indicate all the points around the surface for selection, the API function `Edge.GetTangent(·)` is able to get the tangent vector on point P_0 and the API function `Faces.GetNormalToSurface(·)` can get the unit normal vector of a polygon.

Particularly, when one edge of the polygon is a straight line, the direction vector on the line is just right to be the tangent vector of the point on the line. Simply connect the two end-points of that line, and the tangent vector can be generated.

When the tangent vector on the point of that curve and the unit normal vector is available, the normal vector of initial orthogonal plane Π is supposed to be

$$\vec{\beta} = \vec{\tau} \times \vec{n} = \{a, b, c\}. \quad (3)$$

Thus, the initial orthogonal plane equation involving $P_0(x(t_0), y(t_0), z(t_0)) \in L$ on the curve should be

$$a(x(t) - x(t_0)) + b(y(t) - y(t_0)) + c(z(t) - z(t_0)) = 0. \quad (4)$$

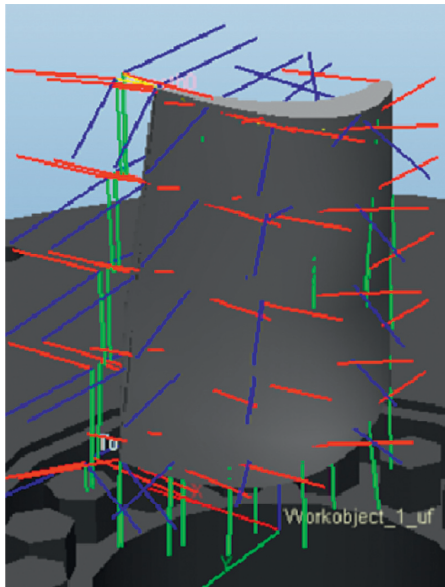
After that, just move the plane up or down with equal distance, and the trajectory with equal scanning step can be generated.

For plane surface, the robot trajectory is simple because the unit normal vector on every point of the surface is the same. But for curved surface, there are many targets on each curve for keeping the same spray distance. Some curved surfaces are very complex and unsymmetrical. For example, as shown in Figure 2, the product is a propeller blade, and its spraying area consists of small surfaces which have different curvatures (the blue lines represent the normal direction of small surfaces, and the red lines represent the tangent direction of small surfaces).

The unit normal vectors on surface vary with the surface curvature, which brings a great challenge to cutting methods. To keep the uniformity of scanning step as much as possible, first of all, select two borders on the substrate, and get some equidistant points on these two borders. Then choose a curve with the largest curvature from the surface on the directions of the two edges, and divide it equally to get some equidistant points. The cutting plane can be created by the three corresponding points on these three lines. Since on a smooth surface, the longest curve is usually the curve with the largest curvature. So, the curves on the same direction of the longest curve can be divided as equally as possible if the longest curve is divided. Also, it is difficult to choose



(a)



(b)

FIGURE 2: Complex curved surface model.

the curve with the largest curvature. In previous research, the manual selection method was widely used. However, this method is not convenient or accurate enough. Based on the contour line theory in GIS, a method to choose a curve with the largest curvature automatically with the help of the density of contour lines is presented in this paper. According to the contour line theory, the denser the contour, the steeper the slope in the area, and the thinner the contour, the smaller the gradient of the terrain. As shown in Figure 3, from C1 height to C9 height, the contour density along the direction of L1 is higher than that along the direction of L2 and L3, and the path along the direction of L1 is also the shortest. In other words, the denser the contour along a certain direction, the shorter the path along this direction.

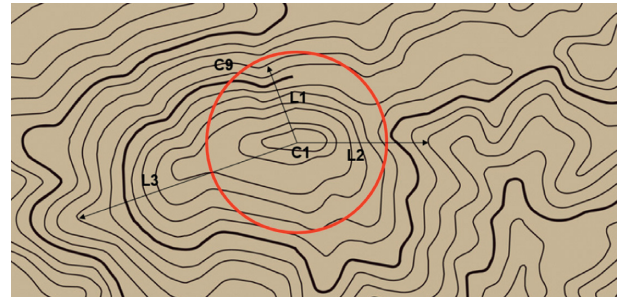


FIGURE 3: The contour line map.

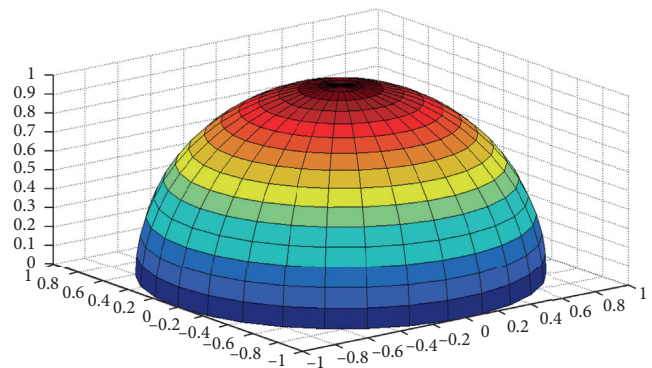


FIGURE 4: A hemisphere model with a radius of 1 m.

In the following section, the density analysis method is replaced with the path analysis method to find the line with the greatest curvature.

Consequently, starting from the contour line on the top, the path to the edge with the denser is the projection of the curve with the largest curvature. For instance, there is a hemisphere model with a radius of 1 m in Figure 4. And a plane which is parallel to the substrate is used to cut the sphere in every 0.1 m interval, so 11 contour lines can be generated. The distribution of contour lines is as shown in Figure 5.

The result of calculation shows that the length of the shortest path starting from the contour line a is $d_{\min} = n1 + n2 + \dots + n11$ along with the radius direction of the sphere. It is because the shortest path between two contour lines is along the direction of radius. As shown in Figure 5, starting from point b , the length of $n2$ on the radius direction is shorter than any other path (e.g., path $m2$). Using the shortest path and the unit normal vector of plane at the bottom, a new plane or surface can be created. The intersection line of the plane or the surface is the curve with the largest curvature. As shown in Figure 6, the curve n is the largest curvature selected on the hemisphere in Figure 4.

By cutting planes (polygon cases) or objects (surface cases), a series of lines could be generated. Then, find out the endpoints of each line, and calculate the three-dimensional coordinate (x, y, z) and quaternion-vector $(q1, q2, q3, q4)$ of these endpoints in the world coordinate system by some functions. The quaternion-vector $(q1, q2, q3, q4)$ is used to represent the orientation of endpoint in the three-dimensional space.

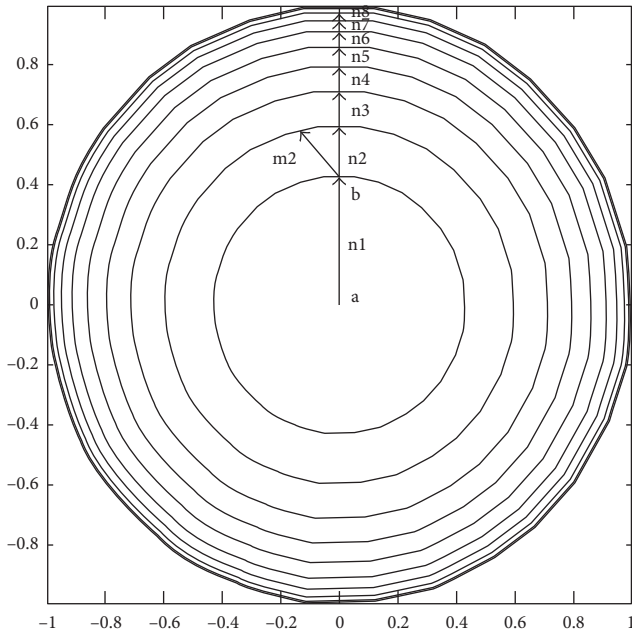


FIGURE 5: The contour lines of the hemisphere model.

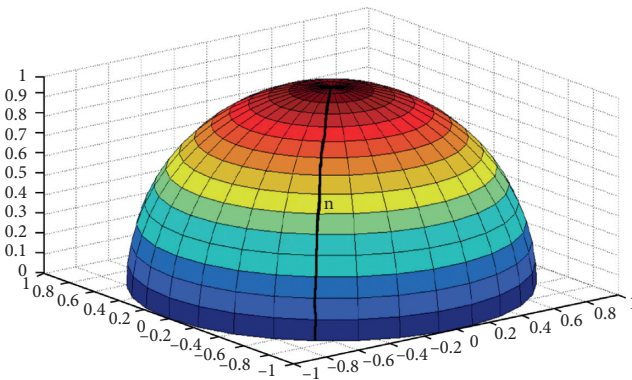


FIGURE 6: The largest curvature n selected on the hemisphere.

Finally, the spray parameter over-length is defined. Theoretically, the over-length is equal to the distance during which the robot accelerates from a halt to a necessary spray speed. In such a way, the scanning speed on the workpiece could be constant and the overheating on the edge could be avoided. Furthermore, it means obviously a great amount of power savings. Thus, the best solution is to keep a constant over-length of each point on the edge of the workpiece. Since different types of robots have different kinematic parameters, the over-length depends on a specific robot type. It is very difficult to find the exact position of these over-lengths on real workpiece in the work cell, even in off-line programming under RobotStudio.

For clarity of description of the algorithm above, two examples using an arbitrary polygon and a curved surface to generate trajectory are used for illustration, respectively.

3.4. Automatic Generation on a Polygon Profile. The method used for automatic generation on a curved-edge polygon

profile is as follows, and the sketch map is shown in Figure 7:

- (1) Click on the surface of CAD model workpiece in the graphics window.
- (2) Pull the scroll bar which indicates all the points around the surface, the direction of tangent of this point is the direction of trajectory, and then choose the trajectory starting from left or right.
- (3) Create a large plane involving two points to intersect the spraying surface and ensure the large plane and the spraying surface are orthogonal. Create the first intersection line.
- (4) According to the value of step, move down the large plane and create a series of lines.
- (5) Create targets on both the ends of series of lines according to the interlength. Calculate the robot velocity and orientation for each target.
- (6) Add all the targets to trajectory in order.

This function is not only suitable to round and ellipse, but also suitable to many irregular curved-edge polygon surfaces. With the straight-edge polygon profile, the straight edge is selected instead of the point on the edge. In this way, autogeneration of trajectory could be simpler. The method used for automatic generation on a straight-edge polygon profile is as follows, and the sketch map is shown in Figure 8:

- (1) Click on the surface of the CAD model workpiece in the graphics window, all the edges of the surface will be displayed in the list.
- (2) Select one edge as the direction of trajectory and choose the trajectory starting from left or right.
- (3) Create a large plane on the edge to intersect the spraying surface, and ensure that the large plane and the spraying surface are orthogonal. Create the first intersection line.
- (4) According to the value of step, move down the large plane. Create a series of lines.
- (5) Create targets on both the ends of series of lines according to the interlength. Calculate the robot velocity and orientation for each target.
- (6) Add all the targets to trajectory in order.

3.5. AutoGeneration for Curved Surface. The following presents the method of autogeneration for a curved surface, and the sketch map is shown in Figure 9.

- (1) Create two edges of the complex 3D coating surface.
- (2) The two edges are divided into equal parts according to the spray parameters.
- (3) Find the line with the greatest curvature of the complex 3D coating surface on the directions of the two edges, and divide this line equally to get some equidistant points. Create a large plane through the corresponding points on the edges and the line with

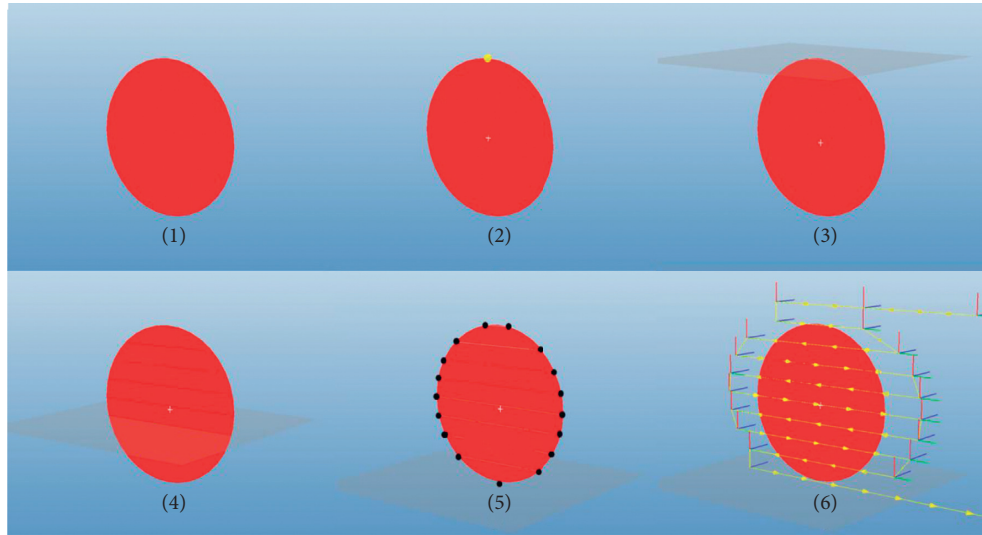


FIGURE 7: Autogeneration on a curved-edge polygon profile.

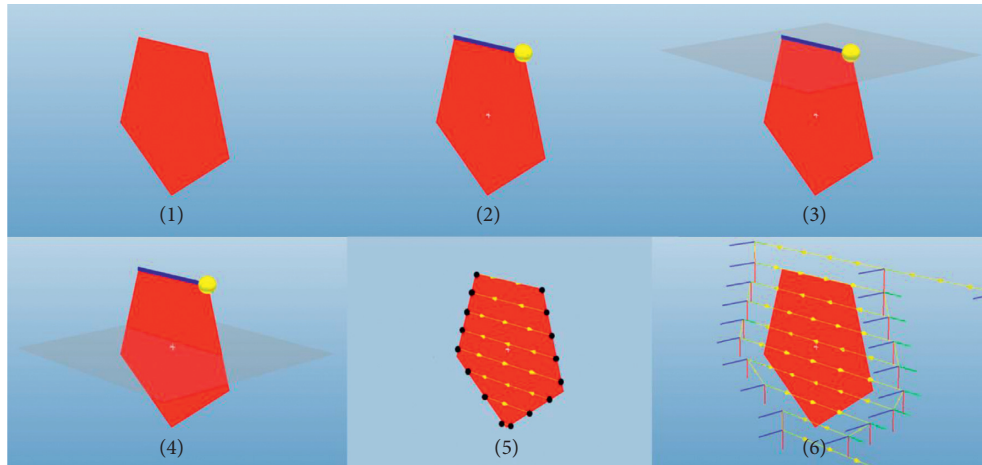


FIGURE 8: Autogeneration on a straight-edge polygon profile.

the greatest curvature to intersect this 3D model. Create the first closed intersection curve. This step is suitable for a smooth curved surface. For an irregular curved surface, manual adjustment is necessary to ensure that these closed intersection curves are equidistant.

- (4) Offset the large plane to the next corresponding points on the edges and the line with the greatest curvature to create a series of closed intersection curves.
- (5) Choose the part of closed intersection curves which are located on the spraying area.
- (6) Create targets on the series of selected curves according to the interlength. Calculate the robot velocity and orientation for each target. Add all the targets to trajectory in order.

3.6. Calculation of Velocity. Robot velocity plays a significant role in coating quality. A robot usually has a continual

motion and robot velocity is planned as constant as possible to obtain a uniform thickness if the step is constant. But with the methodology used in thermal spray toolkit, the step is varied, so the robot velocity should change with the step. In theory, the robot velocity is inversely proportional to the step: $v_2/v_1 = d_1/d_2$. Figure 10 shows the meaning of character v_1 , v_2 , d_1 and d_2 . The robot velocities are calculated in the Add-In program and assigned to corresponding targets in order to keep the uniformity.

4. Program Implementation and Experimentations

To validate the methodology and visualize the trajectories, an Add-In programme with interface has been developed in the C# environment, and it can be loaded automatically when opening the RobotStudio. The function of the program has been tested using a different 2D model and 3D model. Furthermore, the real experiment has been implemented to evaluate the effect of autogeneration of trajectory.

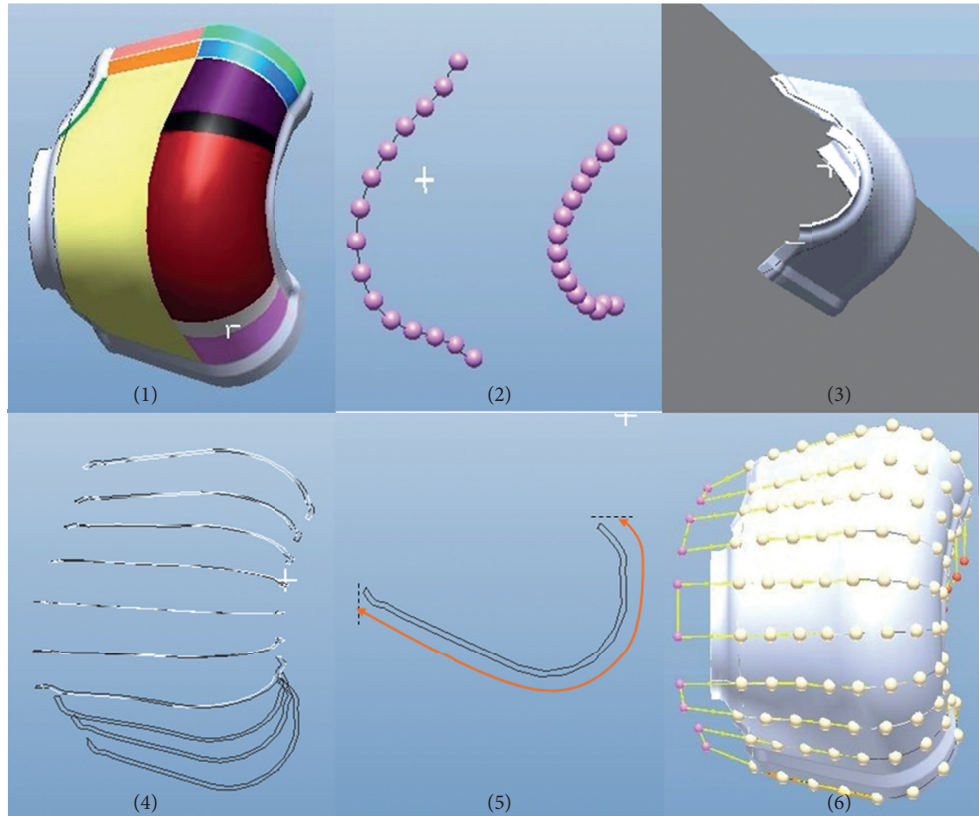


FIGURE 9: Autogeneration for complex curved surface.

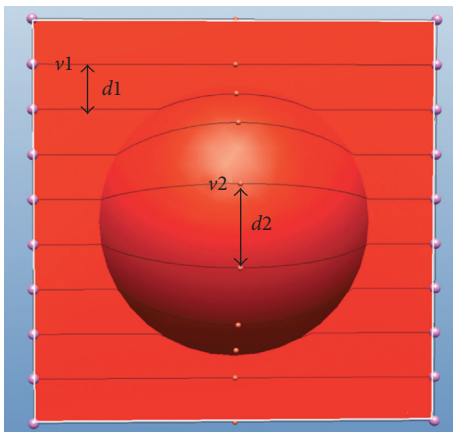


FIGURE 10: Meaning of character v_1 , v_2 , d_1 , and d_2 .

4.1. Implementation on a Straight-Edge Polygon Profile. The following figures provide some typical examples to illustrate the function of autogeneration of trajectory on a polygon profile. According to the thermal spray characteristics, it can be clearly seen that the first line and the last line of trajectory are located outside the workpiece in order to ensure the uniformity of coating. Figure 11 shows the autogenerated trajectory on a type of regular polygons, and Figure 12 shows the autogenerated trajectory on a type of irregular polygons.

4.2. Implementation on a Curved-Edge Polygon Profile. As seen from Figure 13, the autogenerated trajectory on different kinds of curved-edge polygons can be realized by TST. The beginning part and the end part of the trajectory are prolonged to a certain distance as the start and end of torch, respectively.

4.3. Implementation of on Free-Form Surfaces. Figure 14 shows the program implementation of autogeneration of trajectory on free-form surfaces. As shown in the figure, the function can process various complex 3D workpieces, even propeller blades.

4.4. Experiments and Analysis. It is well known that the scanning speed is the most important parameter for the coating homogeneity during the deposition. So, the experiment is implemented to analyse the TCP velocity according to the selected robot trajectory. As a professional robot off-line programming platform, RobotStudio is able to supply the kinematics data in simulations, which are highly close with the data generated in actual motions of robots. The simulation process of RobotStudio enables users to obtain the real-time value of TCP position, speed, and the rotation angle of robot axis and to implement the collision detection between robot, torch, and workpiece. A virtual experimental environment which is completely consistent with the real experimental environment is

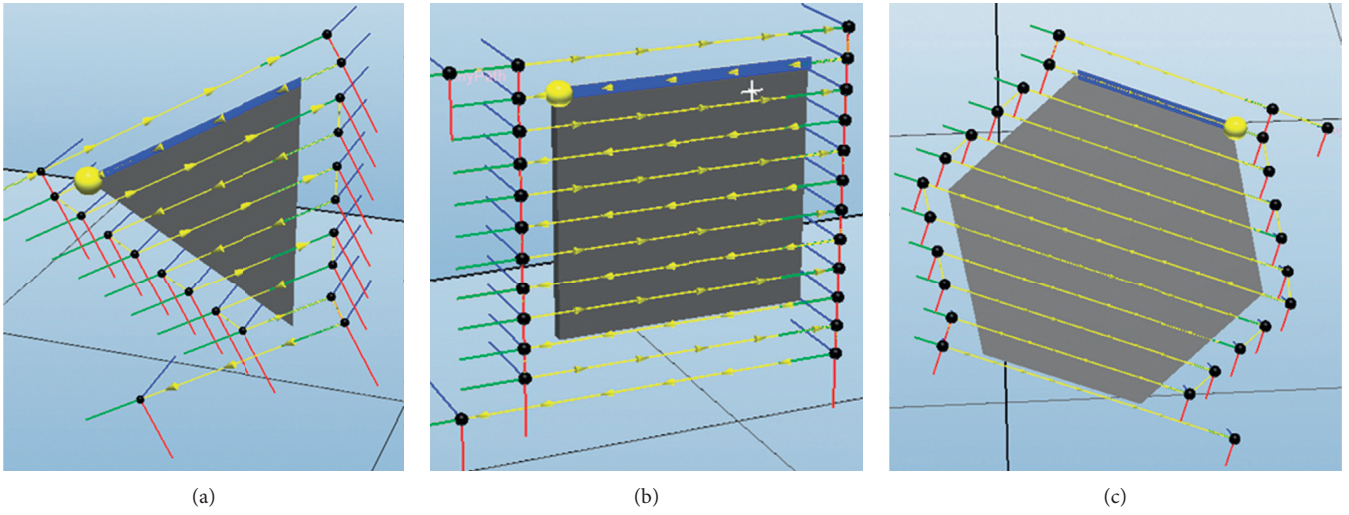


FIGURE 11: Autogenerated trajectory on a type of regular straight-edge polygons.

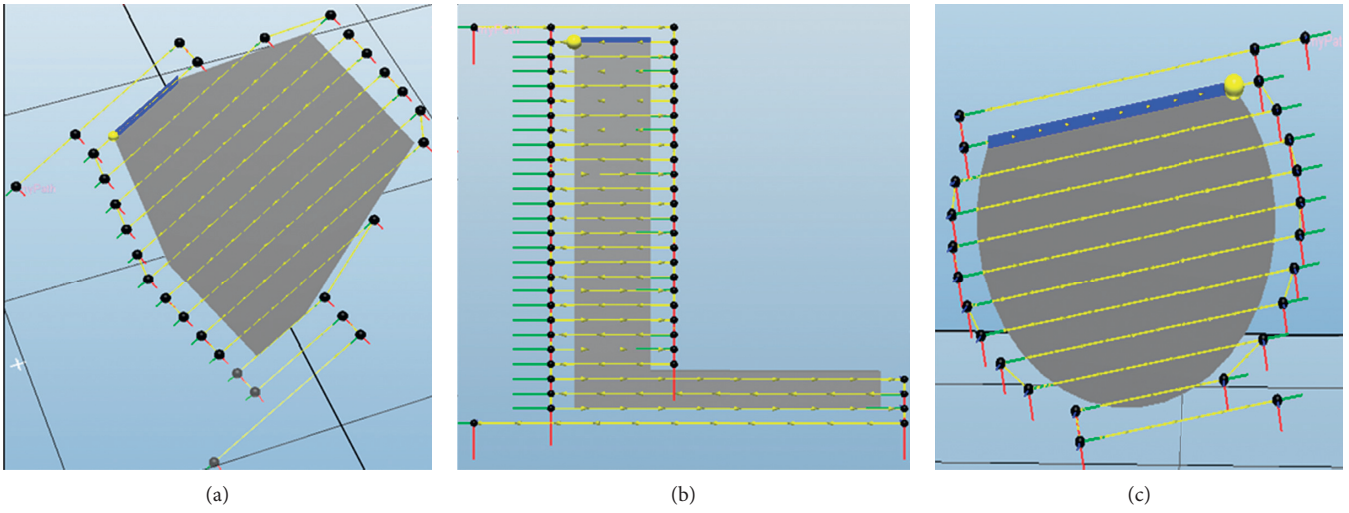


FIGURE 12: Autogenerated trajectory on a type of irregular straight-edge polygons.

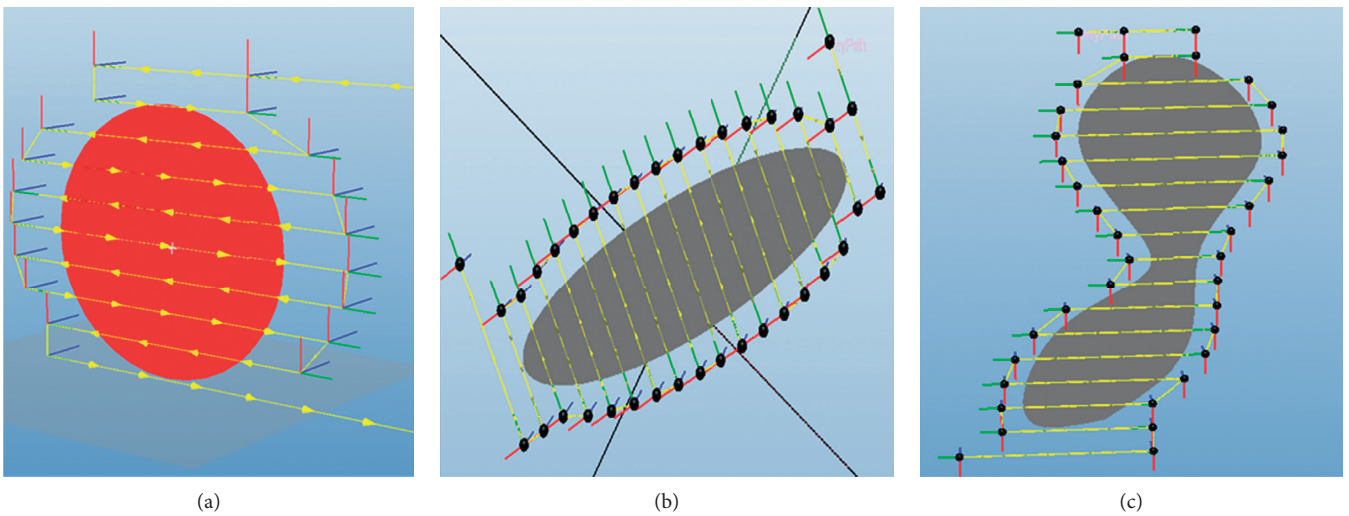


FIGURE 13: Autogenerated trajectory on a type of curved-edge polygons.

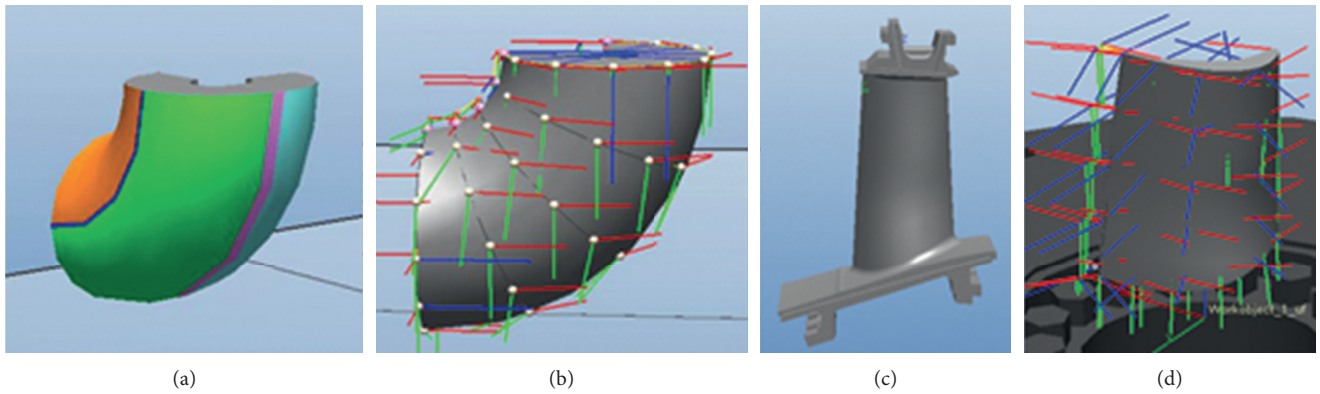


FIGURE 14: Autogeneration of trajectory on free-form surfaces.

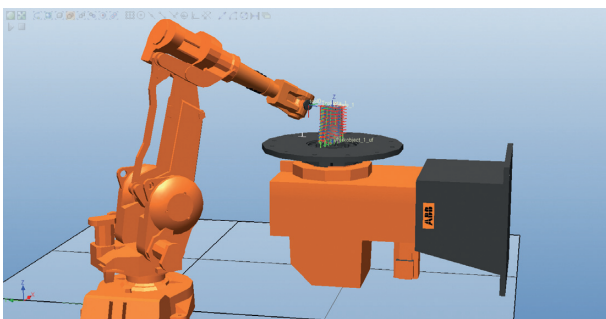
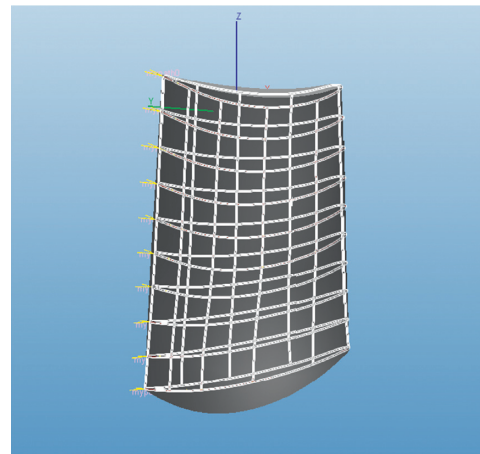


FIGURE 15: The virtual experimental environment.



(a)

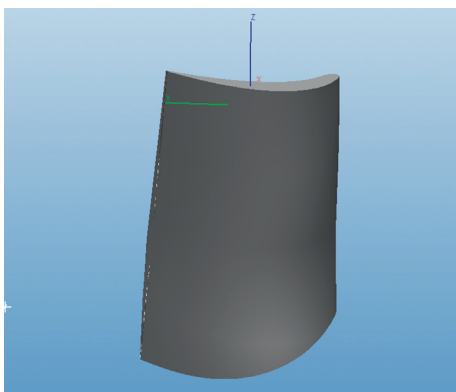
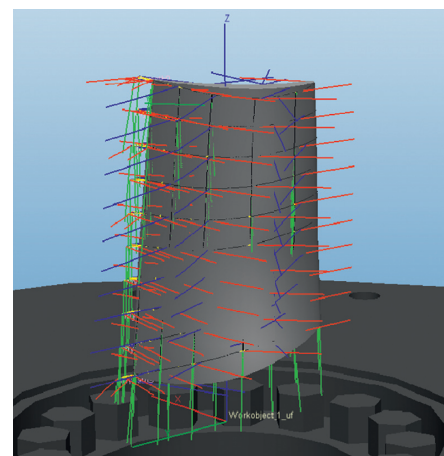


FIGURE 16: The shape of the substrate surface.



(b)

FIGURE 17: A series of curves (a) and several targets (b) in the robot trajectories.

created as shown in Figure 15, which simulated the spray process to get the record of TCP velocity. The shape of the substrate surface is described in Figure 16. A series of curves and several targets in the robot trajectories generated by TST are shown in Figures 17(a) and 17(b), respectively.

AF4-MB type torch is guided by a robot of IRB4400. The scanning step is 0.022 m and the over-length is 0.03 m. During the simulation process, the real-time TCP velocity and position are recorded on each trajectory point. The simulated TCP velocity and the calculated TCP velocity for robot trajectory are shown in Figure 18, respectively.

When passing through the complex curved surface, each pass has 5 samples, and the starting point is on the left of the model. As mentioned in the calculation of velocity section, the TCP velocity on first pass is the reference velocity which equals to 300 mm/s in this experiment. Theoretically, the

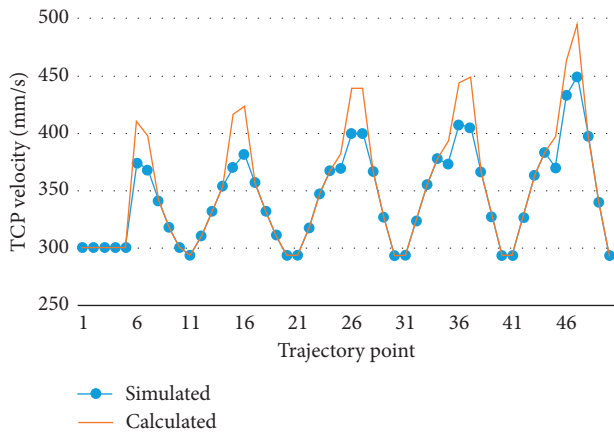


FIGURE 18: The simulated TCP velocity and the calculated TCP velocity for robot trajectory.

robot velocity is inversely proportional to the scanning step. Since the left border of the model is wider than the right border of the model, the TCP velocity of the pass from right to left should be increasing. In the same way, the TCP velocity of the pass from left to right should be decreasing. The simulated TCP velocity (blue line) in Figure 18 is basically close to the calculated TCP velocity (red line), which is inversely proportional to the scanning step. It means that the method for autogeneration trajectory works well for thermal spray application. The simulated TCP velocity decreased by about 10% less than the calculated TCP velocity that corresponds to the passage of torch at the rounded area of the workpiece where the rotation is the most difficult.

5. Conclusion

Autogeneration trajectory is needed to operate the spray process on a free-form surface, but no off-line programming system has yet been developed to meet this need. In this paper, Thermal Spray Toolkit was developed based on RobotStudio, it is flexible and robust enough to deal with any complex 2D and 3D model, and the robotic trajectory can be generated automatically according to the spray parameters with high efficiency.

Appendix

- (1) Create a new project with Class Library as your template.
- (2) To use the RobotStudio API, you need to reference the ABB.Robotics.*.dll assemblies. These are as follows:

ABB.Robotics.Math—Vector and matrix math.
 ABB.Robotics.RobotStudio—General and top-level (e.g., nonstation specific) classes.
 ABB.Robotics.RobotStudio.Environment—For manipulating the GUI, for example, adding menus, buttons and so on.
 ABB.Robotics.RobotStudio.Stations—For manipulating stations and their contents.

ABB.Robotics.RobotStudio.Stations.Forms—GUI controls used by RobotStudio.

You can add a new reference to your project by right click on References in the Solution Explorer and choose Add Reference....

Go to the Browse tab and browse to your RobotStudio installation directory. This is where you will find the dll.

- (3) Add the following lines to the top of your code:

```
CopyC#
using ABB.Robotics.Math;
using ABB.Robotics.RobotStudio;
using ABB.Robotics.RobotStudio.Environment;
using ABB.Robotics.RobotStudio.Stations;
using ABB.Robotics.RobotStudio.Stations.Forms;
```

- (4) Add the following code to the class:

```
CopyC#
public static void AddinMain()
{
    //This is where you write your code.
}
The AddinMain()-method is the entry point for your Add-In.
```

- (5) Go to the properties of your project (right click on your project in the Solution Explorer and select Properties) and select the Build Events. Add the following line to the Post-built event command line:

```
XCopy/y "$(TargetPath)" "C:\Program Files\ABB Industrial IT\Robotics IT\RobotStudio 5.12\Bin\Addins\"
```

Assuming that this is the directory for your RobotStudio installation.

This will copy your Add-In dll-file to the RobotStudio Add-In directory when building your Add-In.

- (6) You could also add the path to RobotStudio.exe to Start external program under Debug in Properties, so RobotStudio will start every time you want to debug your Add-In.
- (7) Write your code (or copy and paste one of the examples into AddinMain()).
- (8) Select Start Debugging from Debug menu (or press F5). This will start RobotStudio and autoload your Add-In. Since your Add-In will load and execute directly when RobotStudio starts (even though there is not active station) it will probably throw an exception. It might be a good idea to add a menu button to start your code. Have a look at the Add Menus and Buttons Example for how to create menus and buttons.
- (9) If you go to the Add-Ins menu you can find your Add-In under the General folder. If you right click on your Add-In you can select whether or not it should autoload, and you can load it if it is not already loaded.

RobotStudio Add-Ins can be created in VB.NET or C#.

Data Availability

The data used to support the findings of this study are not available from the corresponding author upon request due to the commercial interests in the research.

Conflicts of Interest

The authors declare that there are no conflicts of interest regarding the publication of this article.

Acknowledgments




This work was supported by the National Natural Science Foundation of China (31500772, 21705158, 51401127, and 51771122), Key Research and Development Program of Zhejiang Province (2015C01036 and 2107C01003), Zhejiang Provincial Natural Science Foundation of China (LQ14F010001, LY15F010006, LY16F10014, LQ15F020004, and LY18F020025), Key Scientific and Technological Projects of Ningbo (2014B92001), Postdoctoral Science Foundation of Zhejiang Province (BSH02020), Ningbo Natural Science Foundation (2017A610109 and 2015A610132), Research Fund of State Key Laboratory for Marine Corrosion and Protection of Luoyang Ship Material Research Institute (LSMRI) under the Contract no. KF160409, International Scientific and Technological Cooperation Project of Ningbo, and Science and Technology Commission of Shanghai Municipality (Grant nos. 16QB1401100 and 15QB1401500).

References

- [1] R. Gadow and M. Floristán, "Manufacturing engineering in thermal spraying by advanced robot systems and process kinematics," in *Future Development of Thermal Spray Coatings*, pp. 259–280, Elsevier, New York, NY, USA, 2015.
- [2] N. Espallargas, *Future Development of Thermal Spray Coatings: Types, Designs, Manufacture and Applications*, Elsevier, New York, NY, USA, 2015.
- [3] S. Deng and C. Chen, "Generation of robot trajectory for thermal spray," in *Robot Kinematics and Motion Planning*, Nova Science Publishers, Hauppauge, NY, USA, 2015.
- [4] M. Floristán, J. A. Montesinos, J. A. García-Marín, A. Killinger, and R. Gadow, *Robot Trajectory Planning for High Quality Thermal Spray Coating Processes on Complex Shaped Components*, ASM International, Geauga County, OH, USA, 2012.
- [5] D. Fang, S. Deng, H. Liao, and C. Coddet, "The effect of robot kinematics on the coating thickness uniformity," *Journal of Thermal Spray Technology*, vol. 19, no. 4, pp. 796–804, 2010.
- [6] R. Gadow, A. Candel, and M. Floristán, "Optimized robot trajectory generation for thermal spraying operations and high quality coatings on free-form surfaces," *Surface and Coatings Technology*, vol. 205, no. 4, pp. 1074–1079, 2010.
- [7] B. Zhou, X. Zhang, Z. Meng, and X. Dai, "Off-line programming system of industrial robot for spraying manufacturing optimization," in *Proceedings of the 33th Chinese Control Conference*, pp. 8495–8500, Nanjing, China, July 2014.
- [8] A. Candel and R. Gadow, "Trajectory generation and coupled numerical simulation for thermal spraying applications on complex geometries," *Journal of Thermal Spray Technology*, vol. 18, no. 5-6, pp. 981–987, 2009.
- [9] D. Hegels, T. Wiederkehr, and H. Müller, "Simulation based iterative post-optimization of paths of robot guided thermal spraying," *Robotics and Computer-Integrated Manufacturing*, vol. 35, pp. 1–15, 2015.
- [10] ABB Robotics, *RobotStudio™ Users Guide*, ABB Robotic Products, Zürich, Switzerland, 2015.
- [11] P. N. Atkar, A. Greenfield, D. C. Conner, H. Choset, and A. A. Rizzi, "Uniform coverage of automotive surface patches," *International Journal of Robotics Research*, vol. 24, no. 11, pp. 883–898, 2005.
- [12] S. Deng, H. Liao, and C. Coddet, "Robotic trajectory auto-generation in thermal spraying," in *Proceedings of the Thermal Spray Connects: Explore Its Surfacing Potential*, Basel, Switzerland, May 2005.
- [13] R. Holubek, D. R. Delgado Sobrino, P. Košťál, and R. Ružarovský, "Offline programming of an ABB robot using imported CAD models in the RobotStudio software environment," *Applied Mechanics and Materials*, vol. 693, pp. 62–67, 2014.
- [14] K. Wen, M. Liu, K. Zhou et al., "The influence of anode inner contour on atmospheric DC plasma spraying process," *Advances in Materials Science and Engineering*, vol. 2017, Article ID 2084363, 12 pages, 2017.
- [15] P. Ctibor, M. Kašparová, J. Bellin, E. Le Guen, and F. Zahálka, "Plasma spraying and characterization of tungsten carbide-cobalt coatings by the water-stabilized system WSP," *Advances in Materials Science and Engineering*, vol. 2009, Article ID 254848, 11 pages, 2009.
- [16] L. Pawlowski, *The Science and Engineering of Thermal Spray Coatings*, John Wiley & Sons, Hoboken, NY, USA, 2nd edition, 2008.
- [17] V. Y. Rovenski, *Differential Geometry of Curves and Surfaces*, Prentice-Hall Inc., Upper Saddle River, NY, USA, 2004.

Research Article

Ni-Ti Shape Memory Alloy Coatings for Structural Applications: Optimization of HVOF Spraying Parameters

Carmen De Crescenzo ¹, Despina Karatza,¹ Dino Musmarra ¹, Simeone Chianese ¹,
Theocharis Baxevanis,² Panagiota T. Dalla,³ Dimitrios A. Exarchos,³
Konstantinos G. Dassios ³, and Theodore E. Matikas³

¹Department of Engineering, University of Campania Luigi Vanvitelli, 81031 Aversa, Italy

²Department of Mechanical Engineering, University of Houston, Houston, TX 77204, USA

³Department of Materials Science and Engineering, University of Ioannina, Ioannina 45110, Greece

Correspondence should be addressed to Dino Musmarra; dino.musmarra@unicampania.it

Received 9 February 2018; Revised 21 April 2018; Accepted 6 May 2018; Published 28 June 2018

Academic Editor: Shuo Yin

Copyright © 2018 Carmen De Crescenzo et al. This is an open access article distributed under the Creative Commons Attribution License, which permits unrestricted use, distribution, and reproduction in any medium, provided the original work is properly cited.

This work aims at contributing to the development of a revolutionary technology based on shape memory alloy (SMA) coatings deposited on-site to large-scale metallic structural elements, which operate in extreme environmental conditions, such as steel bridges and buildings. The proposed technology will contribute to improve the integrity of metallic civil structures, to alter and control their mechanical properties by external stimuli, to contribute to the stiffness and rigidity of an elastic metallic structure, to safely withstand the expected loading conditions, and to provide corrosion protection. To prove the feasibility of the concept, investigations were carried out by depositing commercial NiTiNol Ni50.8Ti (at.%) powder, onto stainless steel substrates by using high-velocity oxygen-fuel thermal spray technology. While the NiTiNol has been known since decades, this intermetallic alloy, as well as no other alloy, was ever used as the SMA-coating material. Due to the influence of dynamics of spraying and the impact energy of the powder particles on the properties of thermally sprayed coatings, the effects of the main spray parameters, namely, spray distance, fuel-to-oxygen feed rate ratio, and coating thickness, on the quality and properties of the coating, in terms of hardness, adhesion, roughness, and microstructure, were investigated.

1. Introduction

Ni-Ti shape memory alloys are extremely interesting materials both for their ability of showing the shape memory effect (SME) and for their elevated strength and ductility [1].

An attractive Ni-Ti-based SMA is NiTiNol, a nearly equiatomic intermetallics of nickel and titanium. NiTiNol shape memory properties were first discovered by Buehler and Wiley at the Naval Ordnance Laboratory, Maryland, United States [2] (the name NiTiNol is derived from the chemical symbol “NiTi” followed by “NOL,” the acronym for Naval Ordnance Laboratory).

In common with other SMAs, NiTiNol shows two important mechanical features: shape memory effect and pseudoelasticity. The former is related to fatigue and fracture resistances of an

alloy and consists in its ability to return to its initial shape upon heating to the austenite phase (high-temperature phase having B2 cubic structure) after having been deformed in the martensite phase (low-temperature monoclinic phase) [3–5]; the latter is due to the stress-induced martensitic transformation upon loading and the subsequent strain recovery upon unloading at temperatures above the austenite temperature A_f [1, 6]. NiTiNol’s ability to undergo a thermal- or stress-induced martensitic phase transformation and its recoverable strains that are much greater than those in traditional alloys, specifically between 8% and 10% [3, 7], make it the most popular shape memory alloy [3].

NiTiNol offers additional advantage for the targeted application since there is a good understanding of its thermo-mechanical response and the crystallography, as well as of the

effects of changes of the transformation temperatures and the heat treatment with variations in composition.

Among the several technologies for depositing metallic coatings on metallic substrates, thermal spray high-velocity oxygen-fuel (HVOF) is one of the most versatile [8] and efficient technologies, with many multiscale features [9, 10], capacity to produce homogeneous [11] and very dense coatings [12–17] with porosity levels typically in the range 0.1–2% [13], low oxide content [11, 12], high hardness [13, 18], excellent bond strength frequently exceeding 69 MPa [11, 13, 19], and low decarburization [13, 20]. Also, the low gas temperature of particles avoids superheating during flight and preserves the nanocrystalline structure of the starting powders of the coating [21].

The HVOF thermal spray system utilizes high-pressure combustion (6–10 bars for the HVOF spray system of third generation [13]) of oxygen and gaseous fuels, such as hydrogen, propane, and propylene, or liquid fuels, such as kerosene. Combustion produces a flow of hot gas at supersonic or hypersonic velocity of approximately 2000 m/s [19, 22–24]. The flame achieves supersonic velocities in the process of expansion at the exit of the convergent-divergent nozzle with a diameter size from 8 to 9 mm [13, 22] and temperatures in the range of 2500–3200°C, depending on the type of the fuel, the fuel-to-oxygen ratio, and the combustion pressure [13, 25, 26].

Powders, with typical particle sizes of 10–63 μm [13], are axially or radially introduced into the stream of gases at the exit of the nozzle [19, 26, 27], molten or semimolten in a temperature range of 900–1800°C [28], and, passing through the gun barrel nozzle, propelled with the produced gas at a supersonic velocity [29] of 300–800 m/s toward the surface of the substrate [13, 19, 26] at typical mass flow rates in the range of 2.3–14 kg/h [25].

Molten or semimolten droplets or particles cool rapidly upon impact at a range of approximately 10^5 K/s, causing splat quenching and resulting in very fine submicrometric crystals [30].

The HVOF thermal spray technology has primarily been used for wear-resistant coatings; however, because HVOF produces very dense coatings, it can be used for very good corrosion-resistant coatings providing longer lifetimes than the uncoated substrate [13, 19].

As reported in other studies, the properties of HVOF coatings are dependent on spraying and coating process parameters, such as spray distance, oxygen-fuel ratio, and powder feed rate [31, 32], and on chemical and physical states of particles, such as velocity, temperature, melting degree, and oxide content [31, 32]. Spray distance acts on velocity and temperature of the in-flight particles and influences porosity, hardness of the coating [31], and oxide content of the sprayed powders [23]; powder feed rate and melting degree of powders affect the coating hardness and corrosion resistance, respectively [30, 32]; the fuel-to-oxygen mixing ratio influences the flame temperature and velocity [33] and particle velocity [21] and affects oxide content and density of coating [23]. On the basis of these findings, to obtain the best properties of the coating, it is necessary to define the optimal spraying and coating parameters.

Currently, NiTi alloys are often deposited as thin films. The deposition of NiTi thin films on steel substrates has been following two main directions: the former is the direct deposition on top of a supporting structure, such as a bulk micromachined silicon cantilever [34]; the second is their use as stand-alone thin films to become microactuators [34, 35]. NiTi thin films are also used in the field of microelectromechanical systems (MEMS) for several reasons, such as their high actuation force and displacement at low frequencies [34–38], simplification of the design, and friction-free and nonvibrating movement [37]. Due to the versatility and flexibility of NiTi thin films and their multiple degrees of freedom and compact structure, they are used in the aerospace industry, automotive applications, and the biomedical field for microgrippers and implant stents because of its excellent biocompatibility [35, 37, 39].

The development of SMA thin films on metallic substrates is very challenging for three reasons: (a) it is related to the need for controlling the SMA thin-film composition; (b) it is associated to the large mismatch of thermal expansion coefficients between the substrate and thin film [40]; and (c) it is linked to the development of future applications of thin films [41]. For these reasons, very limited work exists in the literature about the deposition of potential SMA materials on substrates, and the most of them are developed for microactuating devices.

This study presents a new class of SMA-based HVOF-prone coatings for elastic metallic structures, such as civil constructions, which would contribute to their stiffness and rigidity, withstand the expected loading conditions, improve their integrity before or during their in-service life, and offer corrosion protection. Herein, the effects of thermal spraying parameters, namely, spray distance, distance between the exit of the nozzle of the HVOF gun and substrate, fuel-to-oxygen feed rate ratio, and coating thickness on the mechanical and microstructural properties of NiTiInol coatings on metallic substrates are evaluated by investigating hardness, adhesion, surface roughness, and microstructure of the specimens. The optimal values of the spraying parameters are established for thermal spraying application of NiTiInol powders by means of HVOF technology.

It is worth highlighting that, while there is limited work on using NiTiInol as a coating material [42], the development of such coating with the shape memory effect is a pioneering objective, which was followed before the experimental work described in the present manuscript; as a consequence, the selection of a proper technology for a powdered SMA deposition technology in large scale is another innovative purpose of the present investigation.

2. Materials and Methods

A commercial prealloyed NiTiInol, Ni50.8Ti (at.%), powder S/BB superelastic, supplied by Memry Corporation (Connecticut, USA) was used as a starting material. As per manufacturer specifications, the powder particles occupied a particle size range of 15 to 40 μm . To demonstrate the feasibility of the concept, rectangular, common stainless steel coupons, AISI-type 316, with dimensions $100 \times 25 \times 1.5 \text{ mm}^3$, were employed

TABLE 1: Spraying parameters employed in the HVOF spraying process.

Spraying parameter	Spray distance (mm)	Kerosene/oxygen feed rate ratio (l/h-l/min)	Coating thickness (mm)	Specimen
Spray distance	300	20–800	0.30	A
	350	20–800	0.30	B
	400	20–800	0.30	C
Kerosene/oxygen feed rate ratio	300	20–800	0.30	A
	300	22–860	0.30	D
	300	25–900	0.30	E
Coating thickness	300	20–800	0.15	F
	300	20–800	0.30	A
	300	20–800	0.60	G

as substrates for coating deposition. A GTV HVOF-K2 system (GTV Verschleiss-Schutz GmbH, Germany) using kerosene as the liquid fuel and argon as the powder carrier gas was employed for the deposition of SMA coatings; the processes took place at the establishment of Thermal Spray Service Ltd (Italy).

To improve the adhesion of the coating, before thermal spraying, the substrates were grit-blasted with an alumina grit using an ACB shot peening machine (ACB Sabbiatrici S.R.L., Italy) up to an average Ra roughness value of $3\ \mu\text{m}$ and cleaned using compressed air. All specimens were mounted on a horizontally rotating turntable and cooled during and after spraying with compressed air jets. A robotic manipulator was programmed to operate the torch spraying NiTiInol powder at predefined distances from the substrates.

A parameter variation study was carried out in order to investigate the effect of spray distance (in the range 300–400 mm), fuel-to-oxygen feed rate ratio (in the range 20 l/h–800 l/min–25 l/h–900 l/min), and coating thickness (in the range 0.15–0.60 mm) on the characteristics of the coating. The powder feed rate and argon flow rate were kept constant at 70 g/min and 8 l/min for all depositions, respectively.

Seven sets of spray parameters were considered and are summarized in Table 1.

A Galileo Ergotest COMP 25 (LTF, Italy) hardness tester was used to measure superficial Rockwell Hardness 15 N as per the requirements in ASTM E18 [43]. This test is performed to define the NiTiInol coating's ability to resist a permanent indentation or deformation when in contact with a diamond cone indenter under a load of 15 kgf [44].

The adhesion of coating was tested by tensile adhesion tests as per the recommendations in the dedicated standard test method for adhesion strength of thermal spray coatings, ASTM C633 [45]. The tests were performed on a M30K universal tensile testing machine equipped with a 50 kN load cell (JJ Lloyd, UK). Therein, tensile loads were applied on the faces of thermally sprayed cylindrical specimens adhered to the sandblasted faces of identically shaped uncoated specimens. A steel specimen of diameter of 0.9 inches (about 23 mm) and length of 38.1 mm was used as given in [45]. The specimen faces were adhered together with one-part high-density epoxy adhesive, 3M Scotch-Weld 2214, of an ultimate tensile stress of approximately 70 MPa. Coating thickness of 0.015 inches (0.38 mm) is recommended for high porosity coatings in

order to avoid possible penetration of the resin into the voids of the sprayed porous coating; if the coating porosity is less than 2%, the thickness of 0.015 inches required by the ASTM Standard is not necessary [45, 46]. Hence, 0.25 mm thick coatings were tested.

A Polytec TMS-1200 white light interference microscope with resolution 3.65 nm (Polytec GmbH, Germany) was used for rapid, noncontact, two- and three-dimensional microtopography of the materials' surface. All samples were examined at a $2.24 \times 1.67\ \text{mm}^2$ field of view. In terms of surface profilometry, the following parameters were investigated:

- (i) Sq (μm), which represents the quadratic average roughness value, "RMS" roughness within the definition area. It is equivalent to the standard deviation for surface amplitude.
- (ii) Sa (μm), which represents the arithmetic average roughness value, the average surface roughness. It expresses, as an absolute value, the difference in height of each point compared to the arithmetical mean of the surface.
- (iii) Ssk (-), which represents the skewness of height distribution: Ssk > 0 means that the height distribution is skewed below the mean plane.
- (iv) Sz (μm), which represents the maximum height of surface texture, the height between highest profile peak and lowest profile value within the defined area.
- (v) Spk (μm), which represents the reduced peak height, roughness height of profile peaks. It indicates the mean height of peaks above the core surface.

The microstructure of coating/substrate cross sections was examined by optical microscopy (OM) while the morphology of the coatings' surfaces was assessed by scanning electron microscopy (SEM). Optical microscopy provides valuable feedback on microstructural aspects such as voids, unmelted particles, lamellae obtained from particles that have been modified chemically at spraying by reduction or oxidation, and solid inclusions at the interface between the coating and substrate [46]. This investigation was performed using Nikon Eclipse L150 optical microscope (Nikon Instruments Europe BV, Netherlands).

Scanning electron microscopy allows observing the individual lamella after a "splash" onto the substrate's surface, surfaces of as-sprayed coatings, fine-grained microstructure, fine or recrystallized structure, and porosities [46]. SEM

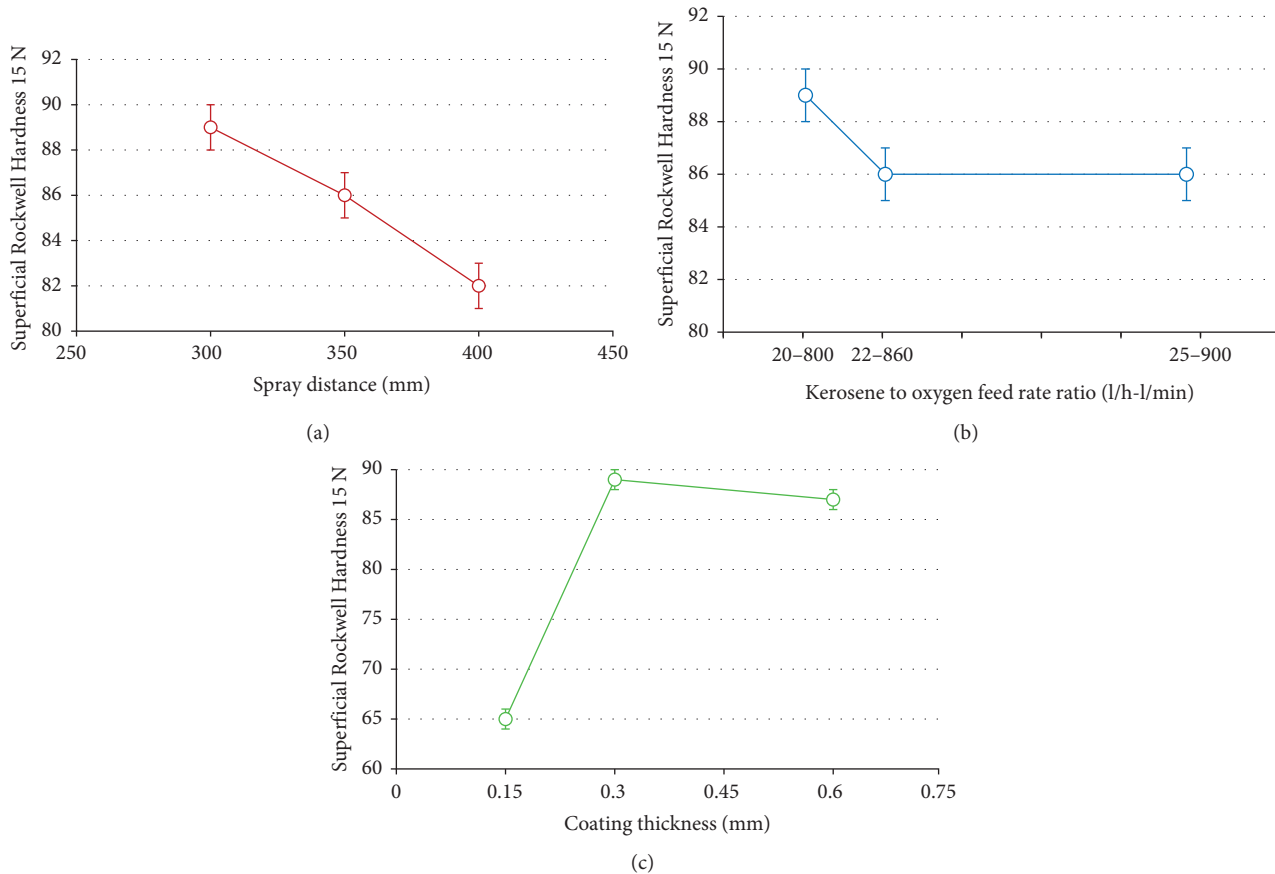


FIGURE 1: Effect of (a) spray distance, (b) kerosene to oxygen feed rate ratio, and (c) coating thickness on coating hardness.

investigations were carried out using JEOL JSM-5600 scanning electron microscope (JEOL USA, Inc., USA).

The chemical composition of the NiTiInol coating was assessed using X-ray fluorescence (XRF). The XRF measurements were performed using a micro-XRF M1-Mistral X-ray fluorescence spectrometer (Bruker, Germany) with 700 μm diameter circular beam spot.

In addition, energy dispersive spectroscopy (EDS) was used to investigate if oxidation occurred in the coating material during the deposition process by the HVOF spraying technique. The measurements were performed using an Oxford Instruments EDS system (Oxford Instruments, Oxfordshire, UK).

A TA Instruments Q series differential scanning calorimeter (DSC) (TA Instruments, New Castle, Delaware) was used to precisely determine the transformation temperatures. The temperature range of the instrument is -180°C to 600°C while inert atmosphere was not used and cooling was performed using liquid nitrogen. The heating and cooling rates of the tests were fixed to $10^{\circ}\text{C}/\text{min}$.

3. Results

3.1. Hardness of the Coating. After grinding the specimens for equal surface roughness, the coating hardness was evaluated. The superficial Rockwell Hardness 15 N as a function of spray distance, kerosene to oxygen feed rate ratio, and coating thickness are plotted in Figure 1. The hardness increases from a value of 60, measured for the

uncoated specimen, to a minimum value of 65 with a coating thickness of 0.15 mm. Results demonstrate that Rockwell Hardness 15 N decreases monotonically by spray distance, decreases up to a plateau value with kerosene to oxygen feed rate ratio up to 22 l/h-860 l/min, whereas with coating thickness, a fluctuating behavior consisting of an initial increase up to 0.3 mm thick coating followed by a decrease thereon is noted. The maximum hardness value of 89 is attained for a spray distance of 300 mm and a kerosene to oxygen feed rate ratio of 20 l/h-800 l/min, where the coating thickness is 0.3 mm.

3.2. Quality of Adhesion to Substrate. In this work, the effects of spray distance and kerosene to oxygen feed rate ratio on the coating adhesion strength were studied, and the results are reported in Figure 2. It is therein observed that adhesion strength decreases with spray distance while a fluctuating behavior consisting of an initial decrease followed by increase is noted with kerosene to oxygen feed rate ratio. The maximum tensile adhesion strength corresponds to sample "E" having been thermally sprayed from a distance of 300 mm with the highest combustion energy stemming from a kerosene to oxygen feed rate ratio equal to 25 l/h-900 l/min.

3.3. Surface Profilometry. The arithmetic average roughness (S_a) is the most widely used because it is a simple parameter to obtain, and it is an effective method for monitoring

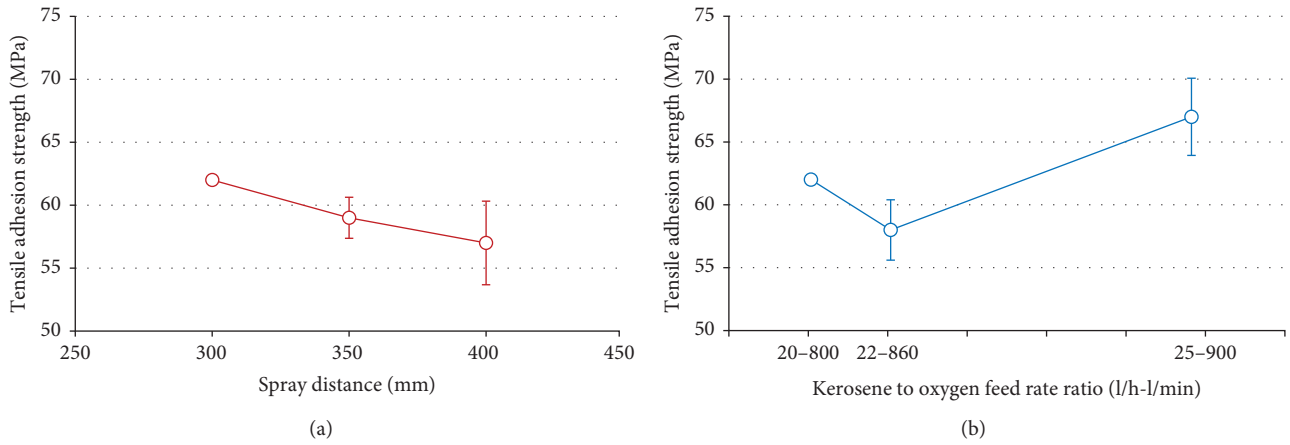


FIGURE 2: Effect of (a) spray distance and (b) kerosene to oxygen feed rate ratio on coating tensile adhesion strength.

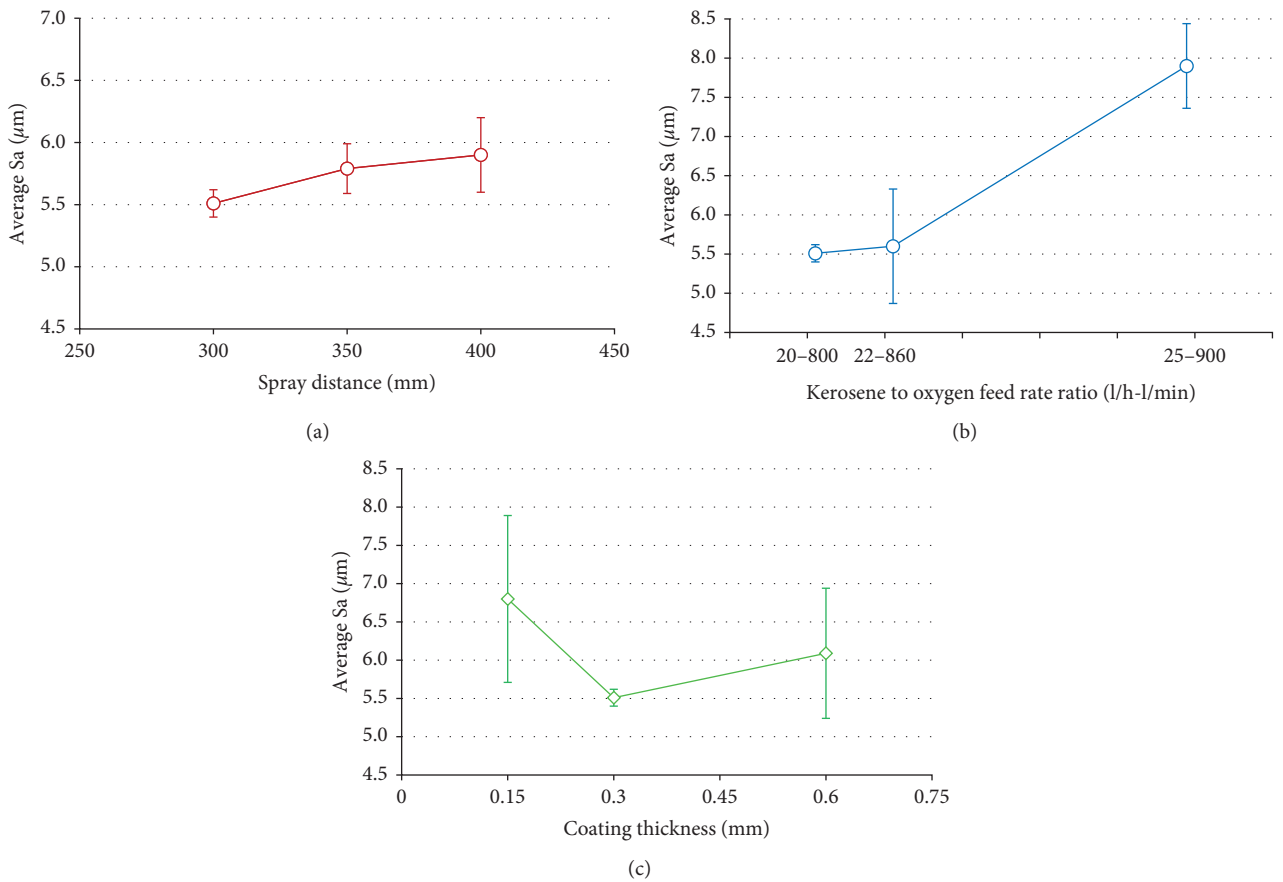


FIGURE 3: Effect of (a) spray distance, (b) kerosene to oxygen feed rate ratio, and (c) coating thickness on Sa roughness parameter.

surface texture and ensuring consistency in measurement of multiple surfaces [47].

Figure 3 depicts the variation of average Sa with spray distance, kerosene to oxygen feed rate ratio, and coating thickness.

As it can be observed in Figure 3, Sa parameter increases with spray distance and kerosene to oxygen feed rate ratio, but shows the lowest value for a coating thickness of 0.3 mm.

Specimen A shows the minimum value of roughness in terms of Sa.

The average values of the other roughness parameters investigated are reported in Table 2. Therein, it is observed that the coating of thickness of 0.30 mm on sample A, sprayed at a distance of 300 mm at a kerosene to oxygen feed rate ratio of 20 l/h-800 l/min, exhibits the optimal profilometry fingerprint with minimum values for all parameters, across all specimens.

Figure 4 illustrates the typical appearance of the morphology of NiTiInol coatings' surface in two- and

TABLE 2: Surface profilometry results.

Specimen	Average Sq (μm)	Average Ssk	Average Sz (μm)	Average Spk (μm)
A	6.99 ± 0.19	0.31 ± 0.13	92.28 ± 17.37	8.00 ± 0.62
B	7.38 ± 0.05	0.52 ± 0.22	96.44 ± 15.7	9.14 ± 1.46
C	7.67 ± 0.49	0.37 ± 0.05	115.78 ± 10.42	10.09 ± 1.23
D	7.21 ± 1.01	0.53 ± 0.06	93.72 ± 34.68	9.41 ± 1.38
E	10.60 ± 1.19	1.10 ± 0.64	102.12 ± 8.68	17.59 ± 4.86
F	11.31 ± 3.74	0.56 ± 0.21	145.13 ± 53.98	19.00 ± 8.74
G	7.86 ± 1.14	1.32 ± 1.47	104.16 ± 43.08	9.40 ± 2.17

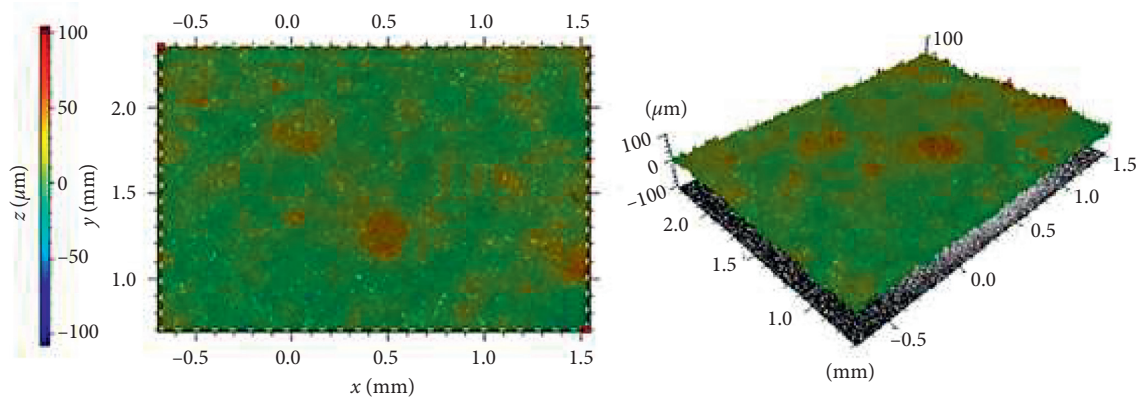


FIGURE 4: Two- and three-dimensional view of the NiTiInol coating's surface observed with the light profilometer.

three-dimensional displays. Coating morphology is dependent on the different conditions of spraying process.

3.4. Microstructure. Scanning electron microscopy (SEM) and optical microscopy (OM) reveal good homogeneity and uniformity. All coatings present the lamellas and porous and unmelted particles that are all inherent to the HVOF thermal spraying. A better adherence is found in the coatings sprayed with the highest kerosene to oxygen ratio and lower spray distance, specimens A and E, respectively. In contrast, the highest combustion energy level may produce higher amounts of oxides attributable to the high feed rate of oxygen (E). A lower porosity is revealed in the coatings sprayed with a lower spray distance (A, D, and E) because of the shorter exposure time in flight and the high particle velocities that yield higher impact energies (Figures 5 and 6).

3.5. Chemical Composition and Shape Memory Effect. To assess the chemical composition of the coating material, two types of samples were used: (a) Ni-Ti-coated samples sprayed by HVOF using Ni-rich Ni50.8Ti (at.%) powder and (b) bulk SMA samples on known composition Ni50.8Ti (at.%).

Figure 7 shows the XRF results from these two types of samples that were compared for assessing the coating chemical composition. The figure clearly shows that the chemical composition of the NiTiInol coating sprayed using the HVOF technique is almost identical with that of the bulk sample of known Ni50.8Ti (at.%) composition.

Figure 8(a) shows the EDS spectrum of the NiTiInol coating, and Figure 8(b) depicts the corresponding EDS-layered image that gives complete picture of chemical

composition of the coating. The compositional distribution of the coating was found to be Ni50.8 (at.%) and Ti49.2 (at.%), confirming the findings of XRF. Moreover, no presence of oxygen or carbon was observed, indicating the absence of oxides or carbides in the Ni-Ti coating. This is proof that the NiTiInol coating deposited on the substrate was not oxidized or burned-out during HVOF spraying.

The ability of the NiTiInol SMA coating to maintain its intrinsic properties during the spraying process was assessed using differential scanning calorimetry (DSC). Ni-Ti SMAs exhibit the shape memory effect based on the thermoelastic martensitic transformation occurring during cooling and the reverse transformation occurring during heating. Hence, the DSC analysis allows assessment of the obtained shape memory effect.

The DSC curve for the NiTiInol Ni50.8Ti (at.%) SMA coating is presented in Figure 9, which exhibits peaks clearly revealing transformation temperatures of $M_s = 54.2^\circ\text{C}$, $M_f = 45.3^\circ\text{C}$, $A_s = 67.5^\circ\text{C}$, and $A_f = 86.6^\circ\text{C}$.

XRD measurements showed the presence of two phases in this NiTiInol material, martensitic (B19') and austenitic (B2). As the cooling progresses and temperature decreases from above 100°C down to -90°C , the intensity of B2 diffraction peak decreases, and peaks related to B19' martensite appear. On heating, the diffraction peaks corresponding to B19' start disappearing while the B2 phase peak reappears.

4. Discussion

The results of this study demonstrate that spray distance, kerosene to oxygen feed rate ratio, and coating thickness affect the characteristics and properties of HVOF-prone

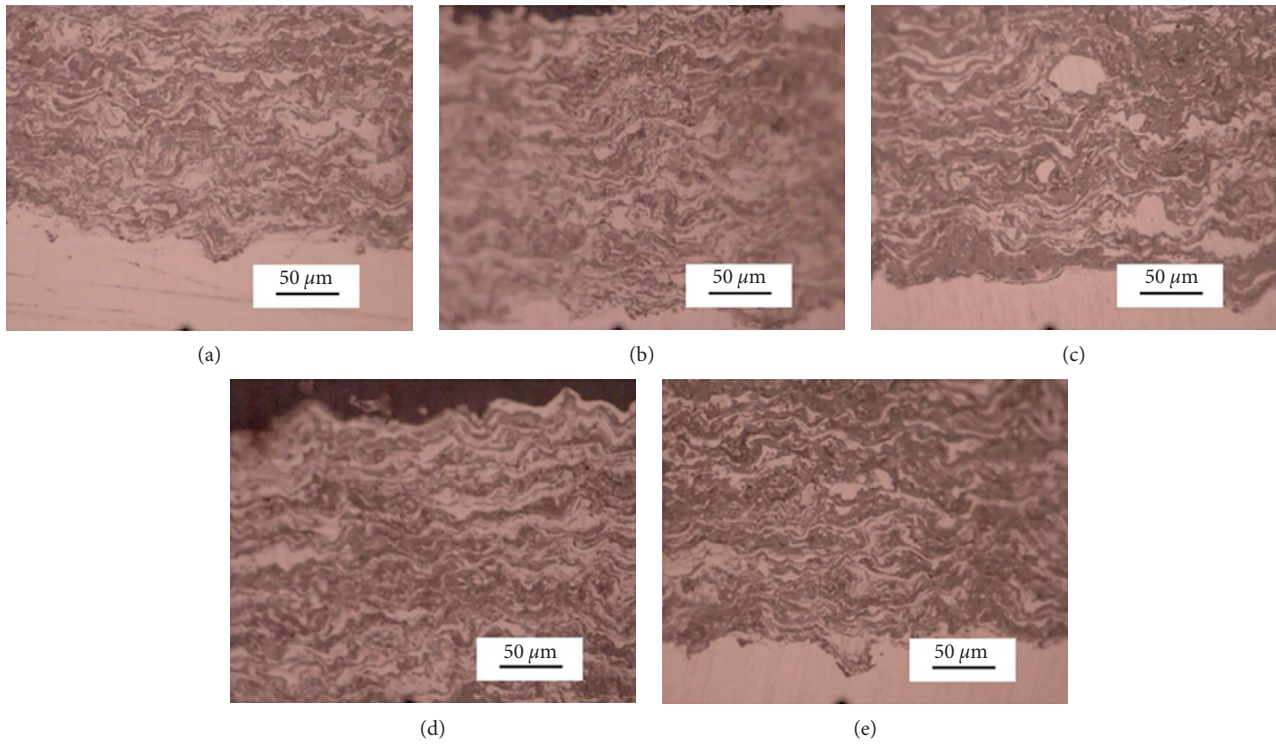


FIGURE 5: OM images of NiTiInol coatings' cross section of samples A (a), B (b), C (c), D (d), and E (e).

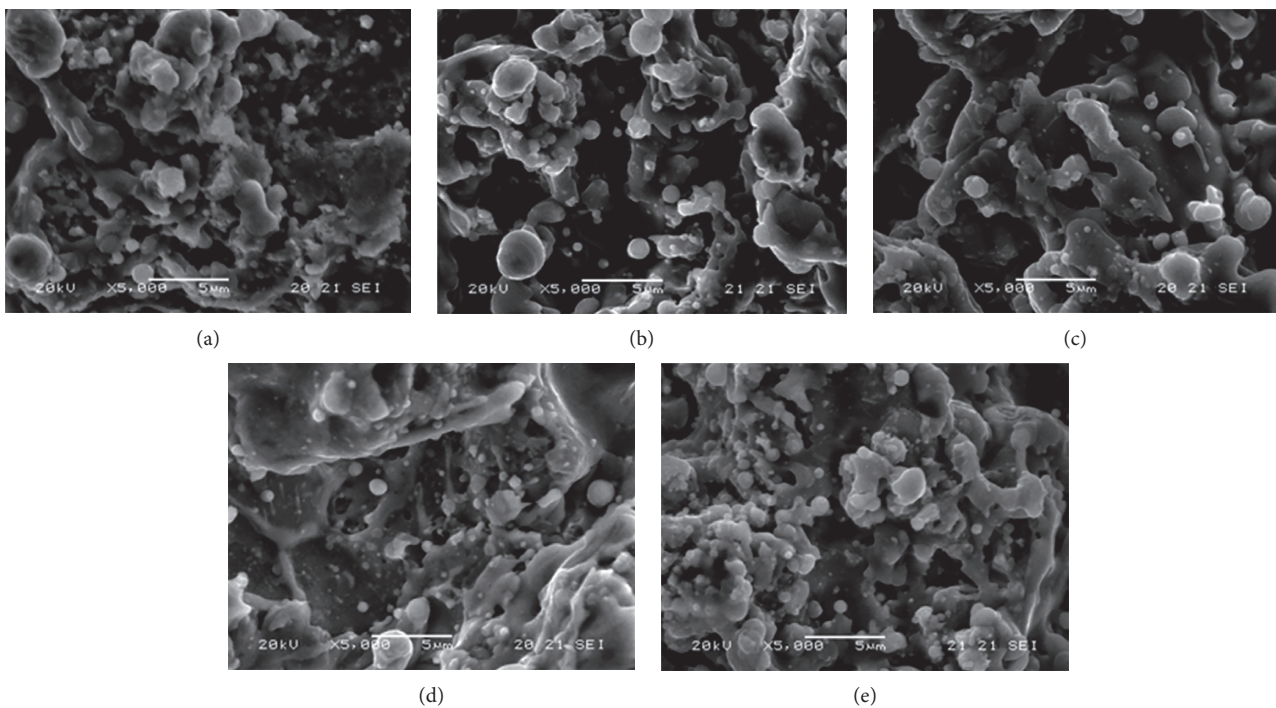


FIGURE 6: SEM micrographs of NiTiInol coatings' surface of samples A (a), B (b), C (c), D (d), and E (e).

NiTiInol coatings. Spray distance in particular influences both particle temperature and velocity, with higher distances found associated with increased temperatures and decreased velocities [31, 48]. Herein, the maximum values of superficial Rockwell Hardness 15 N and adhesion are achieved at

a spray distance of 300 mm, which is the lowest among distances investigated. The coatings' surface roughness is influenced by temperature and velocity of the particles [49]. At spray distance of 300 mm, surface profilometry shows lowest roughness parameters, and OM and SEM investigations

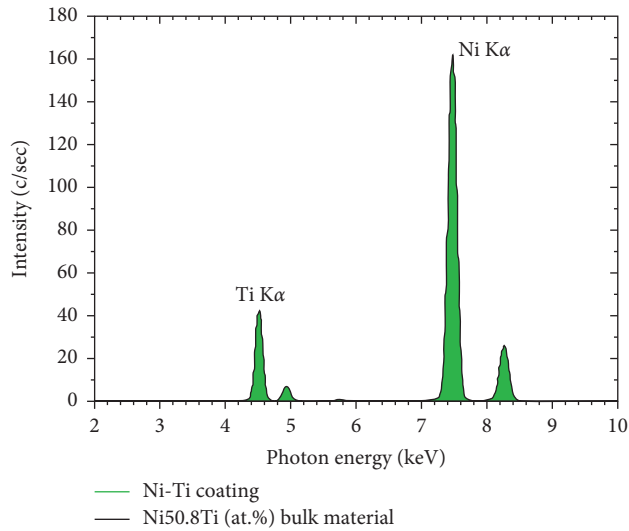
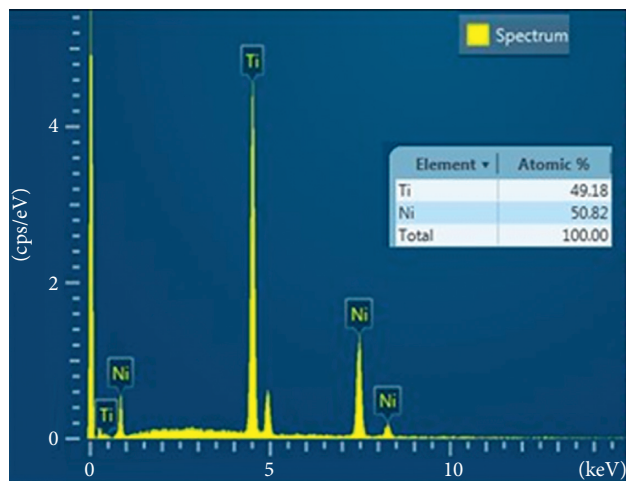
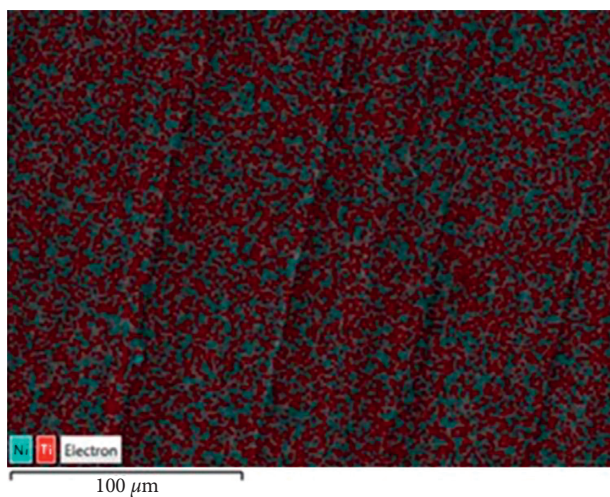


FIGURE 7: Ni and Ti K X-ray transitions from the NiTiInol coating versus the bulk Ni-rich Ni50.8Ti (at.%) sample.



(a)



(b)

FIGURE 8: EDS results of the NiTiInol coating sprayed with the HVOF technique: (a) EDS spectrum and (b) EDS-layered image.

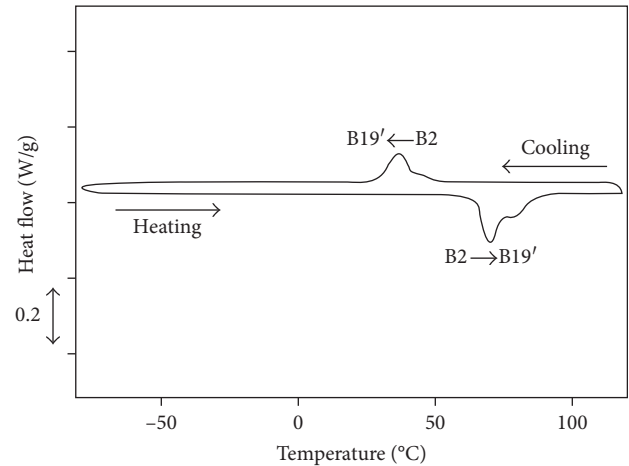


FIGURE 9: DSC curve for the NiTiInol Ni50.8Ti (at.%) coating revealing its shape memory effect.

demonstrate the greatest density and lowest porosity. This behavior can be explained with the higher velocity and the higher energy of the particles that impact the substrates leading to lower porosity and higher density coatings.

The fuel to oxygen ratio influences both particle temperature and velocity: the increasing of fuel to oxygen ratio provides either a decrease in particle velocity or an increase in particle temperature [50]. Maximum hardness is obtained at kerosene to oxygen feed rate ratio of 20 l/h-800 l/min, but the highest adhesion value is observed in the coating sprayed at intermediate kerosene to oxygen feed rate ratio. The higher the kerosene to oxygen feed rate ratio, the less smooth the coatings, and OM and SEM images reveal a molten surface between substrate and coating due to the greater heat released from combustion.

XRF analysis clearly showed that the chemical composition of the NiTiInol coating sprayed using the HVOF technique remained of Ni50.8Ti (at.%) composition, as the composition of the original powder used. EDS characterization also confirmed the findings of XRF. In addition, EDS showed the absence of oxides or carbides in the Ni-Ti coating, indicating that the NiTiInol coating was not oxidized or burned-out during the HVOF spraying process.

Finally, the ability of the NiTiInol SMA coating to maintain its intrinsic properties during the spraying process was demonstrated using DSC, which revealed the coating transformation temperatures and proved the existence of shape memory effect.

5. Conclusions

SMA NiTiInol powder was sprayed on stainless steel AISI 316 specimens by using an industrial-scale HVOF thermal spray. The effect of spray distance, kerosene to oxygen feed rate ratio, and coating thickness on coating properties, in terms of hardness, adhesion, surface roughness, and microstructure was experimentally investigated in order to define the best set of parameters for coating application.

Best hardness was found for minimal spray distance, minimal kerosene to oxygen feed rate ratio, and for 0.3 mm

coating thickness. Coating adhesion to substrate decreased with increasing spray distance, but the highest adhesion value was observed for the coating sprayed at an intermediate kerosene to oxygen feed rate ratio. Surface profilometry revealed smoothest surfaces in the coating sprayed at shortest distance and lowest kerosene to oxygen feed rate ratio with a thickness of 0.30 mm. OM and SEM images showed greatest density in the coatings sprayed at a short distance and greater adhesion for greater kerosene to oxygen feed rate ratios.

Coating adhesion and microstructure characterization results pointed out the effectiveness of the HVOF technology for the powdered SMA-coating deposition since good adhesion conditions and good quality of the coating were achieved.

Furthermore, the optimal HVOF spraying parameter, resulting in the highest value of Rockwell Hardness 15 N (89), a great adhesion (62 MPa), lowest porosity and greatest density, and the smoothest coating surface was found for the specimen A, with a spray distance of 300 mm, a kerosene to oxygen feed rate ratio of 20 l/h-800 l/min, and a coating thickness of 0.30 mm.

Finally, it was demonstrated that the HVOF spraying technique did not alter the chemical composition of coating material in relation to the original powder and produced oxidation-free SMA coatings.

Data Availability

The data used to support the findings of this study are available from the corresponding author upon request.

Conflicts of Interest

The authors declare that they have no conflicts of interest.

Acknowledgments

This work has been financially supported under “Horizon 2020-The Framework Programme for Research and Innovation (2014–2020): Future and Emerging Technologies (FET Open),” project title “An Innovative Method for Improving the Structural Integrity using SMA Revolutionary Technology (InnoSMART)” (Grant agreement no. 664892). The authors would like to thank Dr. Dimitrios Anagnostopoulos and Assistant Professor Alexandros Karantzalis from the Department of Materials Science and Engineering, University of Ioannina, for assistance with the XRF and EDS measurements, respectively.

References

- [1] K. Otsuka and X. Ren, “Physical metallurgy of Ti-Ni-based shape memory alloys,” *Progress in Materials Science*, vol. 50, no. 5, pp. 511–678, 2005.
- [2] W. Buehler and R. Wiley, *US Patent 3,174,851*, Nickel-Base Alloys, USA, 1965.
- [3] S. Robertson, A. R. Pelton, and R. O. Ritchie, “Mechanical fatigue and fracture of nitinol,” *International Materials Reviews*, vol. 57, no. 1, pp. 1–37, 2012.
- [4] L. Janke, C. Czaderski, M. Motavalli, and J. Ruth, “Applications of shape memory alloys in civil engineering structures-overview, limits and new ideas,” *Materials and Structures*, vol. 38, no. 5, pp. 578–592, 2005.
- [5] P. Novák, L. Mejlíková, A. Michalcová, J. Čapek, P. Beran, and D. Vojtěch, “Effect of SHS conditions on microstructure of NiTi shape memory alloy,” *Intermetallics*, vol. 42, pp. 85–91, 2013.
- [6] P. Kumar and L. Dimitris, *Shape Memory Alloys: Modelling and Engineering Applications*, Springer Science Business Media, Berlin, Germany, 2008.
- [7] N. B. Morgan, “Medical shape memory alloy applications—the market and its products,” *Materials Science and Engineering*, vol. 378, no. 1-2, pp. 16–23, 2004.
- [8] V. Shibe and V. Chawla, “Combating wear of ASTM A36 steel by surface modification using thermally sprayed cermet coatings,” *Advances in Materials Science and Engineering*, vol. 2016, Article ID 3894145, 10 pages, 2016.
- [9] P. D. Christofides, N. El-Farra, M. Li, and P. Mhaskar, “Model-based control of particulate processes,” *Chemical Engineering Science*, vol. 63, no. 5, pp. 1156–1172, 2008.
- [10] M. Li and P. D. Christofides, “Modeling and control of high-velocity oxygen-fuel (HVOF) thermal spray: a tutorial review,” *Journal of Thermal Spray Technology*, vol. 18, no. 5-6, pp. 753–768, 2009.
- [11] H. Ruiz-Luna, D. Lozano-Mandujano, J. M. Alvarado-Orozco et al., “Effect of HVOF processing parameters on the properties of NiCoCrAlY coatings by design of experiments,” *Journal of Thermal Spray Technology*, vol. 23, no. 6, pp. 950–961, 2014.
- [12] T. C. Totemeier, R. N. Wright, and W. D. Swank, “FeAl and Mo-Si-B intermetallic coatings prepared by thermal spraying,” *Intermetallics*, vol. 12, no. 12, pp. 1335–1344, 2004.
- [13] T. S. Sidhu, S. Prakash, and R. D. Agrawal, “Studies on the properties of high-velocity oxy-fuel thermal spray coatings for higher temperature applications,” *Materials Science*, vol. 41, no. 6, pp. 805–823, 2005.
- [14] T. Sahraoui, S. Guessasma, M. Ali Jeridane, and M. Hadji, “HVOF sprayed WC-Co coatings: microstructure, mechanical properties and friction moment prediction,” *Materials and Design*, vol. 31, no. 3, pp. 1431–1437, 2010.
- [15] S. Hong, Y. Wu, B. Wang, Y. Zheng, W. Gao, and G. Li, “High-velocity oxygen-fuel spray parameter optimization of nanostructured WC-10Co-4Cr coatings and sliding wear behavior of the optimized coating,” *Materials and Design*, vol. 55, pp. 286–291, 2014.
- [16] M. Xie, Y. Lin, P. Ke et al., “Influence of process parameters on high velocity oxy-fuel sprayed Cr₃C₂-25% NiCr coatings,” *Coatings*, vol. 7, no. 7, p. 98, 2017.
- [17] E. Bakan, G. Mauer, Y. J. Sohn, D. Koch, and R. Vaßen, “Application of high-velocity oxygen-fuel (HVOF) spraying to the fabrication of Yb-silicate environmental barrier coatings,” *Coatings*, vol. 7, no. 4, p. 55, 2017.
- [18] Y. Liu, G. Gou, X. Wang, Q. Jia, H. Chen, and M. Tu, “Effects of rare earth elements on the microstructure and mechanical properties of HVOF-sprayed WC-Co coatings,” *Journal of Thermal Spray Technology*, vol. 23, no. 7, pp. 1225–1231, 2014.
- [19] J. D. Majumdar, “Thermal and cold spraying technology in manufacturing,” in *Handbook of Manufacturing Engineering and Technology*, pp. 2805–2850, Springer, Berlin, Germany, 2015.
- [20] T. Sahraoui, N. E. Fenineche, G. Montavon, and C. Coddet, “Structure and wear behaviour of HVOF sprayed Cr₃C₂-NiCr and WC-Co coatings,” *Materials and Design*, vol. 24, no. 5, pp. 309–313, 2003.
- [21] M. Li and P. D. Christofides, “Modeling and analysis of HVOF thermal spray process accounting for powder size distribution,” *Chemical Engineering Science*, vol. 58, no. 3–6, pp. 849–857, 2003.
- [22] D. Cheng, Q. Xu, E. J. Lavernia, and G. Trapaga, “The effect of particle size and morphology on the in-flight behavior of

- particles during high velocity oxy fuel thermal spraying,” *Metallurgical and Materials Transactions B*, vol. 32, no. 3, pp. 525–535, 2001.
- [23] J. Saaedi, T. W. Coyle, H. Arabi, S. Mirdamadi, and J. Mostaghimi, “Effects of HVOF process parameters on the properties of Ni-Cr coatings,” *Journal of Thermal Spray Technology*, vol. 19, no. 3, pp. 521–530, 2010.
- [24] X. Wang, Q. Song, and Z. Yu, “Numerical investigation of combustion and flow dynamics in a high velocity oxygen-fuel thermal spray gun,” *Journal of Thermal Spray Technology*, vol. 25, no. 3, pp. 441–450, 2016.
- [25] S. Amin and H. Panchal, “A review on thermal spray coating processes,” *International Journal of Current Trends in Engineering and Research*, vol. 2, no. 1, pp. 556–563, 2016.
- [26] L. Pawlowski, “Thermal spraying techniques,” in *The Science and Engineering of Thermal Spray Coatings*, pp. 67–113, Wiley, Hoboken, NJ, USA, 2008.
- [27] P. Fauchais, J. V. Heberlein, and M. I. Boulos, “Industrial applications of thermal spraying technology,” in *Thermal Spray Fundamentals*, pp. 1401–1545, Springer, Boston, MA, USA, 2014.
- [28] G. S. Settles and S. R. Bekofske, “HVOF thermal spray velocity, temperature, and stainless coating properties,” in *Proceedings of the Sixteenth Symposium on Energy Engineering Sciences*, Argonne, IL, USA, May 1998.
- [29] M. Löbel, T. Lindner, T. Mehner, and T. Lampke, “Microstructure and wear resistance of AlCoCrFeNiTi high-entropy alloy coatings produced by HVOF,” *Coatings*, vol. 7, no. 9, p. 144, 2017.
- [30] B. Saeedi and A. S. Rouhaghdam, “The study of high temperature oxidation behavior of different microstructures of HVOF thermally sprayed coatings,” *Journal of Advanced Materials and Processing*, vol. 2, no. 2, pp. 3–12, 2014.
- [31] O. Maranhão, D. Rodrigues, M. Boccalini, and A. Sinatora, “Influence of parameters of the HVOF thermal spray process on the properties of multicomponent white cast iron coatings,” *Surface and Coatings Technology*, vol. 202, no. 15, pp. 3494–3500, 2008.
- [32] Y. Wang, S. L. Jiang, Y. G. Zheng et al., “Effect of processing parameters on the microstructures and corrosion behaviour of high-velocity oxy-fuel (HVOF) sprayed Fe-based amorphous metallic coatings,” *Materials and Corrosion*, vol. 64, no. 9, pp. 801–810, 2013.
- [33] M. Bozorgtabar, M. Salehi, M. Rahimpour, and M. Jafarpour, “Influence of high velocity oxy-fuel parameters on properties of nanostructured TiO₂ coatings,” *Bulletin of Materials Science*, vol. 33, no. 6, pp. 671–675, 2010.
- [34] P. Krulevitch, A. P. Lee, P. B. Ramsey, J. C. Trevino, J. Hamilton, and M. A. Northrup, “Thin film shape memory alloy microactuators,” *Journal of Microelectromechanical Systems*, vol. 5, no. 4, pp. 270–282, 1996.
- [35] J. Mohd Jani, M. Leary, A. Subic, and M. A. Gibson, “A review of shape memory alloy research, applications and opportunities,” *Materials and Design*, vol. 56, pp. 1078–1113, 2014.
- [36] B. Winzek, S. Schmitz, H. Rumpf et al., “Recent developments in shape memory thin film technology,” *Materials Science and Engineering A*, vol. 378, no. 1-2, pp. 40–46, 2004.
- [37] Y. Fu, H. Du, W. Huang, S. Zhang, and M. Hu, “TiNi-based thin films in MEMS applications: a review,” *Sensors and Actuators A: Physical*, vol. 112, no. 2-3, pp. 395–408, 2004.
- [38] S. Miyazaki and A. Ishida, “Martensitic transformation and shape memory behavior in sputter-deposited TiNi-base thin films,” *Materials Science and Engineering: A*, vol. 273–275, pp. 106–133, 1999.
- [39] K. Li, X. Huang, Z. S. Zhao, Y. Li, and Y. Q. Fu, “Electrochemical and corrosion behaviors of sputtered TiNi shape memory films,” *Smart Materials and Structures*, vol. 25, no. 3, p. 35039, 2016.
- [40] X. Wu, T. Pence, and D. Grummon, “Model tracking of stress and temperature induced martensitic transformations for assessing superelasticity and shape memory actuation,” *MRS Proceedings*, vol. 459, 1996.
- [41] H. Kahn, W. L. Benard, M. A. Huff, and A. H. Heuer, “Titanium-nickel shape memory thin film actuators for micromachined valves,” in *Proceedings of International Solid State Sensors and Actuators Conference (Transducers’97)*, pp. 227–232, Chicago, IL, USA, June 1997.
- [42] J. M. Guilemany, N. Cinca, S. Dosta, and A. V. Benedetti, “Corrosion behaviour of thermal sprayed nitinol coatings,” *Corrosion Science*, vol. 51, no. 1, pp. 171–180, 2009.
- [43] ASTM E18–16, *Standard Test Methods for Rockwell Hardness of Metallic Materials*, American Society for Testing and Materials, West Conshohocken, PA, USA, 2016.
- [44] E. L. Tobolski and A. Fee, “Macroindentation hardness testing,” in *ASM Handbook: Mechanical Testing and Evaluation*, pp. 428–469, ASM International, Geauga County, OH, USA, 2000.
- [45] ASTM C633–13, *Standard Test Method for Adhesion or Cohesion Strength of Thermal Spray Coatings*, American Society for Testing and Materials, West Conshohocken, PA, USA, 2017.
- [46] L. Pawlowski, “Methods of coatings’ characterization,” in *The Science and Engineering of Thermal Spray Coatings*, pp. 291–370, John Wiley & Sons, Ltd., 2nd edition, 2008.
- [47] G. Schuetz, *Modern Machine Shop*, 2002, <http://www.mmsonline.com/columns/surface-texture-from-ra-to-rz>.
- [48] V. V. Sobolev and J. M. Guilemany, “Investigation of coating porosity formation during high velocity oxy-fuel (HVOF) spraying,” *Materials Letters*, vol. 18, no. 5-6, pp. 304–308, 1994.
- [49] Š. Houdková, M. Kašparová, and J. Schubert, “The spraying parameters optimization of the HVOF satellite 6 coating,” in *Proceedings of the Metal 2012*, Brno, Czech Republic, 2012.
- [50] J. A. Hearley, J. A. Little, and A. J. Sturgeon, “The effect of spray parameters on the properties of high velocity oxy-fuel NiAl intermetallic coatings,” *Surface and Coatings Technology*, vol. 123, no. 2-3, pp. 210–218, 2000.

Review Article

Cold-Sprayed Metal Coatings with Nanostructure

Shuo Yin ¹, Chaoyue Chen,² Xinkun Suo ³, and Rocco Lupoi ¹

¹Department of Mechanical and Manufacturing Engineering, Trinity College Dublin, The University of Dublin, Parsons Building, Dublin 2, Ireland

²ICB UMR 6303, CNRS, Univ. Bourgogne Franche-Comté, UTBM, 90010 Belfort, France

³Key Laboratory of Marine Materials and Related Technologies, Ningbo Institute of Materials Technology and Engineering, Chinese Academy of Sciences, Ningbo 315201, China

Correspondence should be addressed to Shuo Yin; yins@tcd.ie; Xinkun Suo; suoxinkun@nimte.ac.cn and Rocco Lupoi; lupoir@tcd.ie

Received 4 November 2017; Revised 15 January 2018; Accepted 20 March 2018; Published 20 May 2018

Academic Editor: Federica Bondioli

Copyright © 2018 Shuo Yin et al. This is an open access article distributed under the Creative Commons Attribution License, which permits unrestricted use, distribution, and reproduction in any medium, provided the original work is properly cited.

Cold spray is a solid-state coating deposition technology developed in the 1980s. In comparison with conventional thermal spray processes, cold spray can retain the original properties of feedstock, prevent the adverse influence on the underlying substrate materials, and produce very thick coatings. Coatings with nanostructure offer the potential for significant improvements in physical and mechanical properties as compared with conventional non-nanostructured coatings. Cold spray has also demonstrated great capability to produce coatings with nanostructure. This paper is aimed at providing a comprehensive overview of cold-sprayed metal coatings with nanostructure. A brief introduction of the cold spray technology is provided first. The nanocrystallization phenomenon in the conventional cold-sprayed metal coatings is then addressed. Thereafter, focus is switched to the microstructure and properties of the cold-sprayed nanocrystalline metal coatings, and the cold-sprayed nanomaterial-reinforced metal matrix composite (MMC) coatings. At the end, summary and future perspectives of the cold spray technology in producing metal coatings with nanostructure are concluded.

1. Introduction

Cold spray as an emerging coating technique has been developed for decades since its discovery in the 1980s [1]. In this process, powders are accelerated by the supersonic driving gas passing through a convergent-divergent nozzle and impacting onto a substrate at a very high velocity as schematized in Figure 1. Intensive plastic deformation induced by the high-velocity impact occurs in a cold sprayed particle, substrate (or already deposited coating), or both, enabling a low-oxidized cold-sprayed coating to be formed. Metals, metal matrix composites (MMCs), and even pure ceramics are able to deposit onto similar or dissimilar substrates with cold spray [2–4]. Unlike in conventional thermal spray, the feedstock used for cold spray remains solid state during the deposition process without any melting because of the relatively low temperature of the driving gas. Therefore, the inevitable defects emerging in the thermal-sprayed coating, for example, oxidation, thermal

residual stress, and phase transformation, can be considerably avoided in the cold-sprayed coating [5]. Besides, the coating growth is almost unlimited for most metals and MMCs, which allows cold spray to act as an additive manufacturing technique for fabricating bulk materials [6, 7].

As a low-temperature deposition technology, cold spray is primarily applied for producing metal-based coatings. In general, particle velocity prior to the impact is an important factor for cold spray because the successful deposition of cold-sprayed particles relies only on the kinetic energy rather than the combined effect of both kinetic and thermal energies available in conventional thermal spraying. It has been widely accepted that there exists a unique critical velocity for a given condition (e.g., specific particle size, temperature, and material properties), above which successful bonding can be achieved [8–10]. Therefore, the feedstock powders for cold spray must have a proper size range (normally between 10 and 100 μm) to achieve a high particle impact velocity [11, 12]. Nanoparticles, due to their low weights, are difficult

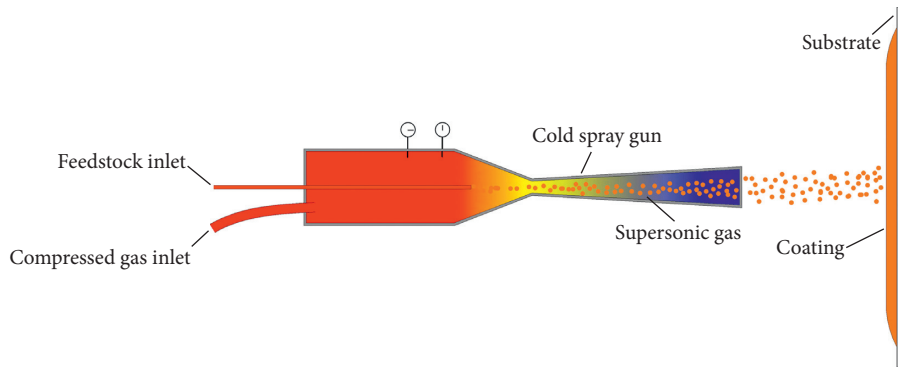


FIGURE 1: Schematic of the cold spray process.

to deposit on the substrate via cold spray. They are easy to be picked up by the driving gas and thereby suffer from dramatic deceleration when passing through the compressed bow-shock in front of the substrate [13]. Consequently, the impact velocity of nanoparticles is very low so that coating is hard to form on the substrate.

It is known that nanostructured materials generally have improved properties as compared with conventional materials [14]. Therefore, it is of importance for cold spray to gain the capability to produce coatings with nanostructure. Fortunately, although nanoparticles cannot be deposited directly by cold spray, cold-sprayed metal coatings can still exhibit nanostructure. Firstly, nanocrystallization in the form of grain refinement always occurs at the interparticle and coating-substrate interfacial regions during the deposition process due to the dynamic recrystallization, which can result in nanostructured grains within the cold-sprayed coating [10, 15–21]. Secondly, the starting feedstock for cold spray can be nanocrystalline powders [14, 22–31]; in this case, the coating retains the nanostructure of the starting powders. Thirdly, using nanomaterials to reinforce MMC coatings can also make the coating to present nanostructure [32–50]. Up till now, a large number of studies have been done to study the cold sprayed coatings with nanostructure. However, a systematic review of these studies still lacks. Therefore, this paper aims to provide an overview of the metal coatings with nanostructure produced by cold spray, particularly focusing on the coating microstructure and properties. The nanocrystallization phenomenon in the cold-sprayed metal coatings is addressed first. Thereafter, the microstructure and properties of the cold-sprayed nanocrystalline metal coatings are discussed. Then, focus is switched to review the cold-sprayed nanomaterial-reinforced MMC coatings. According to the dimensions of the reinforcements, the MMC coatings were classified as 1D material-reinforced, 2D material-reinforced, and 3D material-reinforced MMC coatings. The final part of this paper is a summary and further perspective of the cold spray technology in the fabrication of metal coatings with nanostructure.

2. Nanocrystallization in Cold-Sprayed Metal Coating

2.1. Nanocrystallization Phenomenon. During cold spray process, metal particles experience intensive plastic deformation

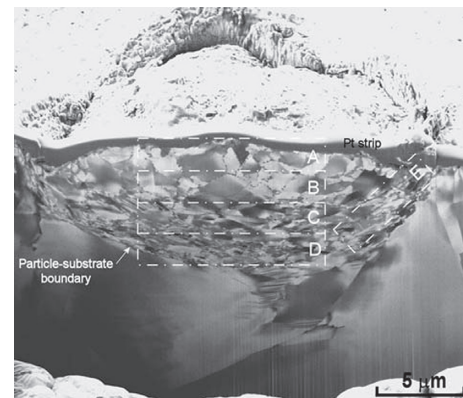


FIGURE 2: FIB-SEM imaging of the cross section of a Cu particle depositing onto a Cu substrate [17].



FIGURE 3: Euler angle EBSD patterns of the cross section of an Al 6061 particle in the cold-sprayed coating [18].

at the interparticle and coating-substrate interfacial regions due to the high-velocity impact. At highly deformed jetting areas, adiabatic shear instability takes place, which results in a significant temperature rise [51]. These rapid physical and

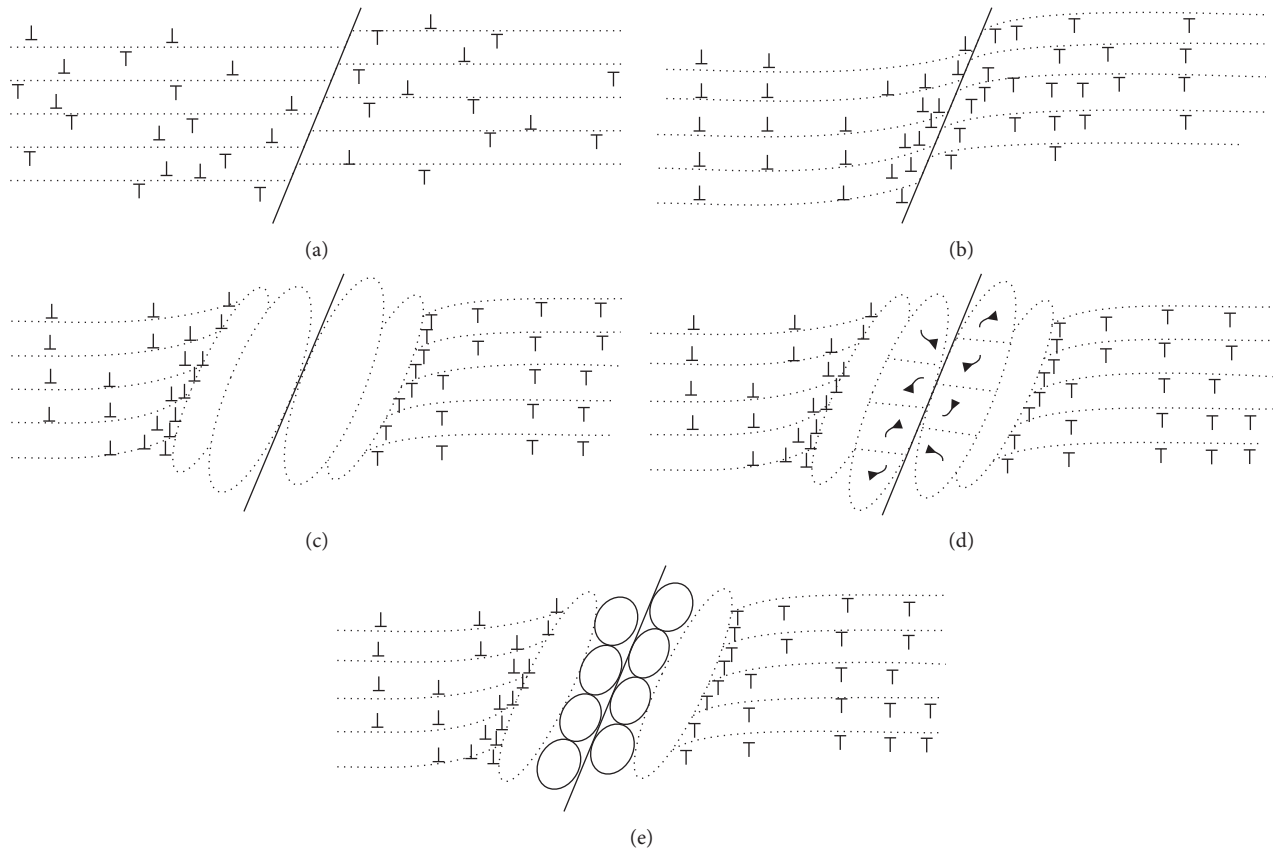


FIGURE 4: Schematic of the subgrains and ultrafine grain formation mechanism [20].

chemical changes work together, leading to the nanocrystallization of metal particles in the form of grain refinement [10, 15, 16]. Figure 2 shows the FIB-SEM imaging of the cross section of a Cu particle depositing onto a Cu substrate [17]. Clearly, particle grain structures showed an obvious change from the particle top surface towards the bottom, and such change was much dependent on the plastic deformation level. Based on the deformation level and grain size, the particle can be divided into three areas. The grains in the “A and B” areas had a large size because the top and inner parts of the particle did not experience too much plastic deformation. At the “C and D” areas, material underwent extensive high-strain/strain-rate plastic deformation; grains were highly deformed and elongated to subgrains. Particularly, at the peripheral “E” area where localized adiabatic shear instability took place, grains were significantly refined to ultrafine grains. Figure 3 shows the EBSD imaging of the cross section of an Al 6061 particle in the cold-sprayed coating, providing a clearer view of different regions [18]. Note that the cross section was perpendicular to the particle impact direction. As can be seen, in the center of the particle, grain size was much larger as compared with the surrounding area. Adjacent to the central zone, elongated subgrains can be clearly observed. At the far surrounding region, ultrafine grains marked by black dotted circle can be noticed. This microstructure is quite similar to the Cu particle grain structure as shown in Figure 2, which demonstrates the universality of the nanocrystallization of the cold-sprayed metal particles after deposition.

2.2. Nanocrystallization Formation Mechanism. In order to explain the substantial reason behind the nanocrystallization phenomenon, Figure 4 shows the schematic of the subgrains and equiaxed ultrafine grain formation mechanism [20]. At the beginning, the large grain of the original particle contains uniformly distributed low-density dislocations (Figure 4(a)). When the particle starts to plastically deform upon impact, dislocation multiplication takes place and the dislocation density begins to increase at highly deformed zone (Figure 4(b)). As the deformation continues, the accumulated dislocations produce a number of dislocation cells, forming the elongated subgrains (Figure 4(c)). The TEM imaging in Figure 5 shows some elongated subgrains in a cold-sprayed Al 7075 particle after deposition [52]. Following the formation of subgrains, adiabatic shear instability happens at extreme deformation areas, resulting in a rapid temperature rise to a value higher than recrystallization temperature. Plastic deformation and heating then work together to induce the dynamic recrystallization at these areas [15, 17, 18, 53, 54]. Basically, dynamic recrystallization is controlled by two mechanisms: rotational and migrational types [16, 19, 20]. In terms of the cold-sprayed particles, rotation has been found to be the dominant mechanism for the occurrence of dynamics recrystallization [20, 55]. Under the rotational dynamic recrystallization, elongated subgrains are further divided into equiaxed subgrains due to the increased dislocation density (Figure 4(d)). These equiaxed subgrains are rotated by additional shear forces to form the

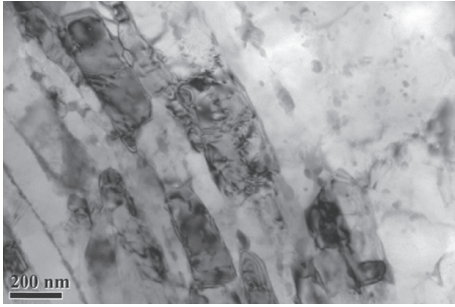


FIGURE 5: TEM imaging of elongated subgrains in a cold-sprayed Al 7075 particle [52].

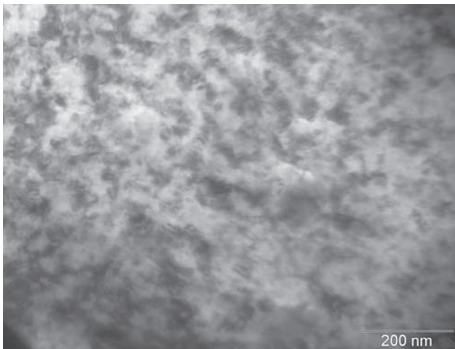


FIGURE 6: TEM imaging of cold-sprayed nanocrystalline Al 2018 coating [23].

ultrafine grains (Figure 4(e)) [16, 20]. Due to the increased dislocations and grain boundaries, the nanohardness and strength at these refined areas are higher as compared to at the other areas [14, 21].

3. Nanocrystalline Metal Coatings via Cold Spray

Nanocrystalline metals are polycrystalline metals with a crystallite size of a few nanometers (normally smaller than 100 nm). They generally exhibit increased strength and hardness, improved toughness, reduced elastic modulus and ductility, enhanced diffusivity, higher specific heat, enhanced thermal expansion coefficient, and superior soft magnetic properties in comparison with conventional polycrystalline metals [56]. Cold spray, due to its low working temperature, has been found to be a robust tool to produce nanocrystalline metal coatings because nanocrystalline structure can be well retained in the coating after deposition. As an evidence, Figure 6 shows a TEM imaging of nanocrystalline Al 2018 coating produced via cold spray, where nanocrystalline grains can be clearly observed in the coating [23].

Preparation of nanocrystalline powders is one of the most important steps in the coating fabrication process. Mechanical ball milling is regarded as a simple, effective, and efficient method to produce nanocrystalline powders with a grain size as small as 20 nm or below [57]. It is a process where mixed powders are placed in a chamber and subjected to high-energy collision of balls to induce

mechanical alloying. So far, various nanocrystalline powders have been produced through mechanical ball milling for cold spray [14, 22–31]. Table 1 summarizes the nanocrystalline powders produced for cold spray and their milling conditions.

Due to the increase of grain boundaries, the nanocrystalline powder hardness was normally much higher than the conventional counterpart, which makes the nanocrystalline coating to be harder but more porous as compared to the conventional coating [23, 29, 30]. For the same reason, the work hardening effect in the nanocrystalline coatings was not as prominent as in the conventional coatings [23, 25]. Figure 7 shows a comparison of cross-sectional microstructure between conventional and nanocrystalline Al coatings produced under the same working parameters [23]. It is seen that nanocrystalline coating had higher porosity than conventional coating due to the lack of sufficient plastic deformation. However, the coating hardness showed an opposite trend; nanocrystalline coating had a hardness of 4.41 GPa which was higher than the hardness of conventional coating (3.75 GPa).

In terms of the mechanical properties, cold-sprayed nanocrystalline coatings have shown better wear-resistance performance than conventional coatings as a result of higher hardness [29]. However, due to the simultaneous higher porosity, fatigue strength was found to not improve significantly [30]. So far, the property investigation of cold-sprayed nanocrystalline coatings is still very limited; for example, investigations on coating cohesion strength are still lacking. Considering the unique advantages of hard nanocrystalline coatings, more mechanical property tests such as coating tensile stress and elongation are encouraged in the future work.

4. 1D Material-Reinforced MMC Coatings via Cold Spray

Carbon nanotube (CNT) is an allotrope of carbon with a cylindrical nanostructure. The diameter of CNT can be as small as 1 nm but the length can be up to several centimeters; thus, CNT is also recognized as 1D nanomaterial. As a member of carbon family, CNT has extraordinary thermal conductivity, electrical, and mechanical properties. These novel properties make CNT potentially valuable and useful in a wide variety of applications in nanotechnology, electronics, optics, thermal engineering, and other fields of material science [58]. Due to the 1D nanostructure, CNT cannot exist in the form of bulk state. Thereby, it is widely employed as reinforcements for improving the properties of pure metals. Currently, CNT-reinforced MMCs are mainly produced by powder metallurgy [59, 60] and thermal spray technologies [61, 62]. These processes generally require high temperature to melt the binder phase, resulting in damage and phase transformation of CNT during fabrication [63, 64]. Cold spray, due to its low working temperature, has been applied to produce CNT-reinforced MMC coatings in recent years.

A number of investigations have proved that dense and thick CNT-reinforced MMC coatings can be fabricated via cold spray [41–44]. Among all these works, mechanical ball

TABLE 1: Nanocrystalline powders for cold spray and the milling conditions [14, 22–31].

Materials	Milling time (h)	Speed (rpm)	Ball diameter (mm)	BPR	Control agent
Al alloy 2009	10	200	6.4	20:1	Liquid nitrogen
Al alloy 2618	8	180	6.4	32:1	Liquid nitrogen
Al alloy 5083	8	180	6.4	32:1	Liquid nitrogen
Al alloy 7075	N/A	180	11.6	32:1	Stearic acid
Al-Mg alloy	8	180	6.4	32:1	Liquid nitrogen
Ni	15	180	6.4	30:1	Liquid nitrogen
Ni-Ti alloy	48, 1/2 h rest per h	400	20	13:4	Alcohol
Ni-20Cr alloy	20, 1/3 h rest per h	300	N/A	10:2	Toluene
Cu	12	200	6.4	30:1	Liquid nitrogen

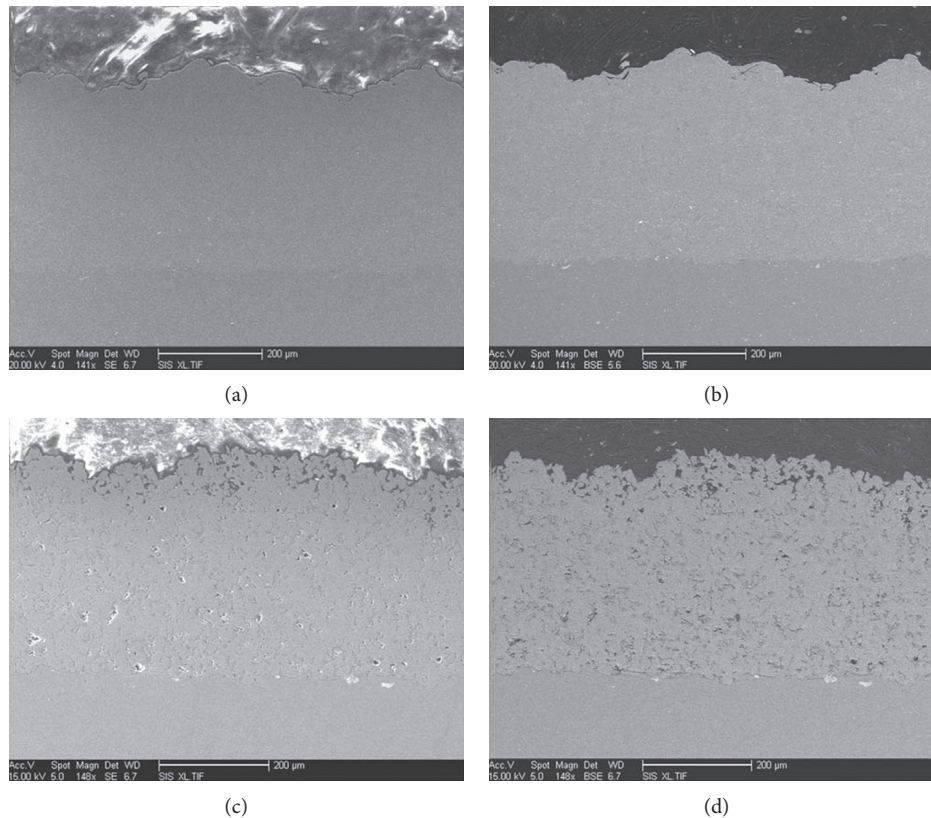


FIGURE 7: Comparison of the microstructure between cold-sprayed conventional and nanocrystalline Al coatings produced under same working parameters: (a) secondary electron imaging of conventional coating, (b) backscattered electron imaging of conventional coating, (c) secondary electron imaging of nanocrystalline coating, and (d) backscattered electron imaging of nanocrystalline coating [23].

milling as a robust technology was prevalently used to prepare CNT-reinforced MMC powders. Figure 8 shows the cross-sectional view and EDX mapping of a ball-milled CNT-Cu MMC powder. As can be seen, CNT was successfully incorporated into the MMC powder and exhibited a homogenous distribution [41]. Following the preparation of the MMC powders, various CNT-reinforced MMC coatings were fabricated as listed in Table 2 [41–44, 65–68]. As an example, Figure 9 shows the TEM imaging of a cold-sprayed CNT-Cu MMC produced by low-pressure cold spray [65]. Clearly, CNT was successfully involved in the cold-sprayed Cu-based MMC coatings.

Although mechanical ball milling is promising for producing CNT-reinforced MMC powders, it also brings negative aspects. CNT reinforcements suffered from damage

during the milling process due to the plastic deformation of the binder phase [65]. In addition, the high-velocity impact happening during the coating deposition process also led to the fracture of CNT [44, 65]. Figure 10 shows the TEM imaging of damaged CNT in the cold-sprayed CNT-Cu coatings [44]. Two different damaging features can be noticed, which are impact-induced and shear-induced damages, respectively. The impact-induced damage was present in the form of a systematic fracture of the concentric tubes which progresses inward until the innermost tube has broken, while the shear-induced damage was featured uneven or asymmetric with respect to the tube axis [44]. Currently, prevention of damage of CNT during ball milling process is still a challenging work, which may be a research focus in the future work.

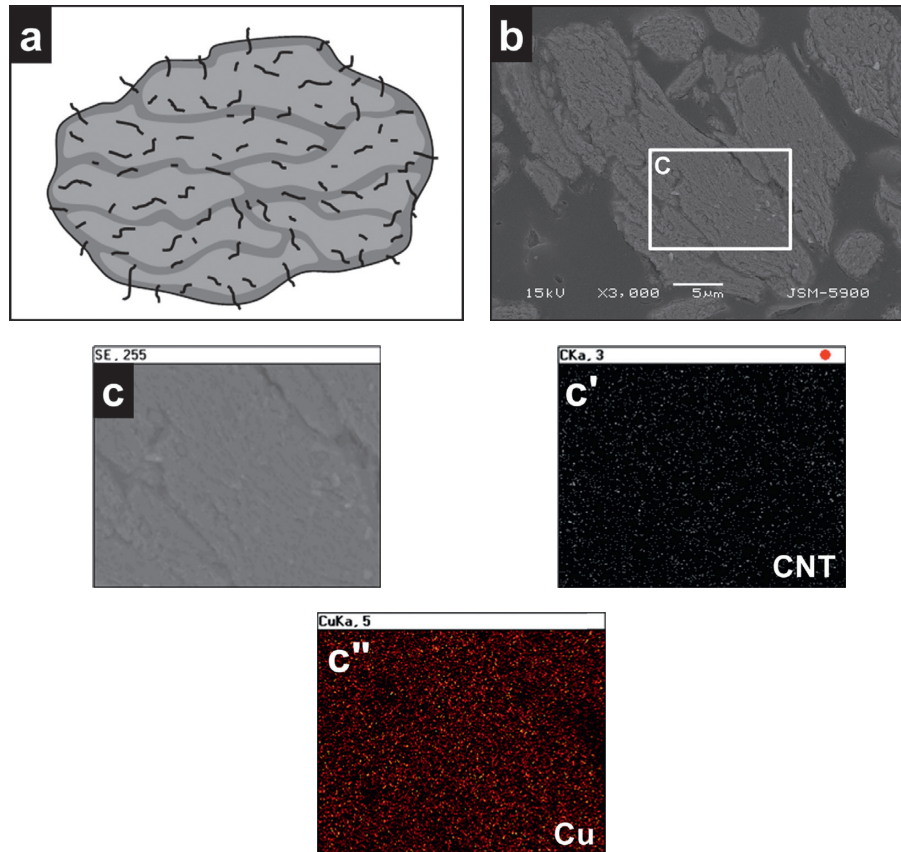


FIGURE 8: Cross-sectional view and EDX mapping of a ball-milled CNT-Cu MMC powder [41].

TABLE 2: CNT-reinforced MMC coatings produced by cold spray and their thermal properties [41–44, 65–68].

Composites	Contents of CNT	Thermal properties	References
CNT-Al	0.5–1.0% by weight	N/A	[44]
CNT-Cu	3% by volume	Higher thermal diffusivity	[65]
CNT-Cu	5–15% by volume	Better heat transfer performance	[41, 66]
CNT-Cu-SiC	4–4.5% by volume	Better heat transfer performance	[43, 67, 68]
CNT-Cu-AlN	4–4.5% by volume	Better heat transfer performance	[42, 67, 68]
CNT-Cu-BN	4% by volume	Better heat transfer performance	[67, 68]

In addition to mechanical ball milling, spray drying technology has also been used to disperse CNT within agglomerated metal powders. Spray drying is a process that produces powders from a liquid solution by rapid drying with hot gases. With this method, CNT was mainly embedded on the surface of agglomerated metal powders but hard to be homogeneously incorporated inside the individual powder. Figure 11 shows the schematic of the coating fabrication procedure using spray drying MMC powders. As can be seen, a consequence of using spray drying powders is the inhomogeneous distribution of CNT in the cold-sprayed coatings as shown in Figure 12 [44].

As for the properties of cold-sprayed CNT-reinforced MMC coatings, it has been revealed that mechanical properties improved with additional CNT reinforcements. In the CNT-Al MMC coatings, local hardness was found to be higher at CNT-rich zone due to the higher stiffness of CNT [44]. Similar results were also concluded in the CNT-Cu MMC

coatings. CNT reinforcements were also found to lead to the improvement of thermal properties in terms of both heat transfer performance and thermal diffusivity [65, 66]. Table 2 lists the existing CNT-reinforced MMC coatings produced by cold spray and their improved thermal properties [41–44, 65–68]. The existing works clearly demonstrate that cold spray is a promising technology to produce CNT-reinforced MMC coatings.

5. 2D Material-Reinforced MMC Coatings via Cold Spray

5.1. Graphene-Reinforced MMC Coatings. Graphene, as the single layer of sp^2 bonded carbon atoms, has extraordinary mechanical, thermal, and electrical properties, attracting great attentions from both scientific and industrial communities. It is normally applied as reinforcements of MMCs to improve the matrix material properties. The

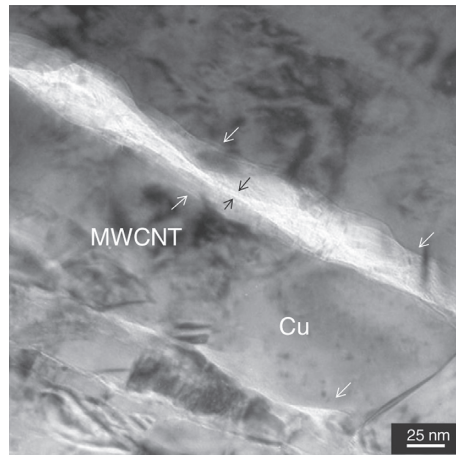


FIGURE 9: TEM imaging of a cold-sprayed CNT-Cu MMC coating produced by low-pressure cold spray [65].

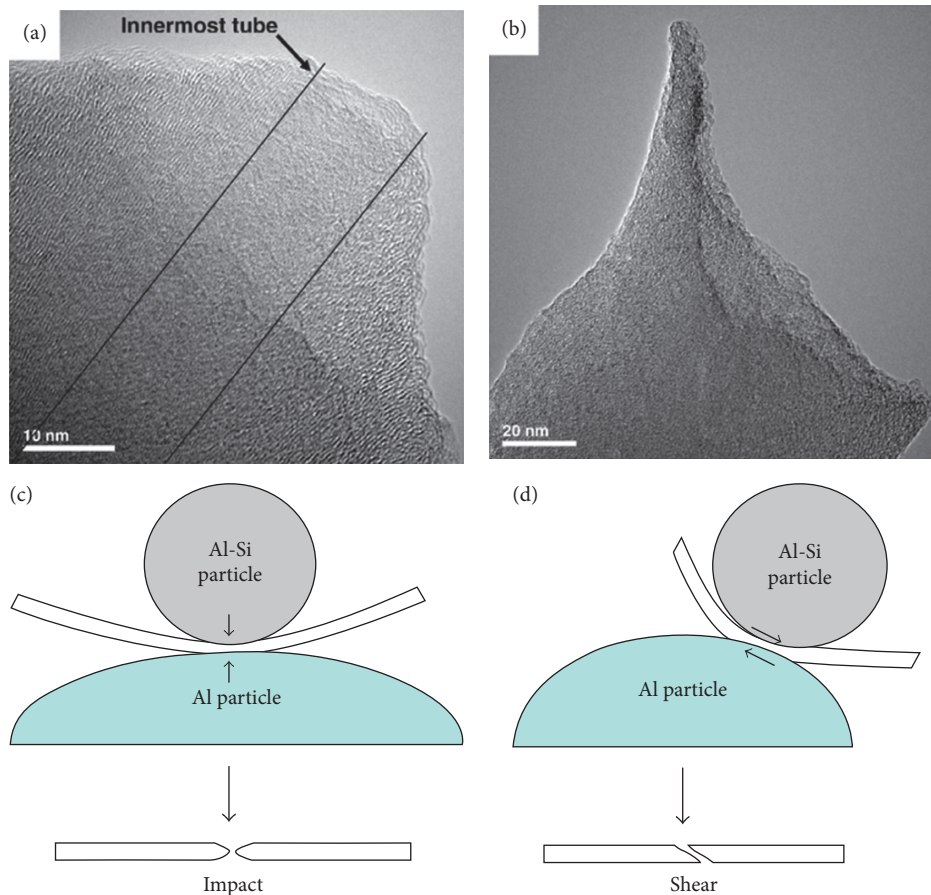


FIGURE 10: TEM imaging of damaged CNT in the cold-sprayed CNT-Cu coatings and their damaging mechanism: (a, c) impact-induced damage and (b, d) shear-induced damage [44].

graphene-reinforced MMCs have exhibited superior properties over the pure metals [69]. Currently, the most common ways for fabricating graphene-reinforced MMCs are a number of powder metallurgy techniques, for example, spark plasma sintering, laser sintering, and hot pressing [70–75]. The existing studies showed great capability of graphene-reinforced

MMCs to improve the material properties, for example, strength [70–72], Young's modulus [72, 76], hardness [72, 76], wear resistance [72–74], and electrical conductivity [75].

Graphene-reinforced MMCs were successfully produced via cold spray in very recent years [32, 33]. As a key step, preparation of MMC powders is of great importance to the

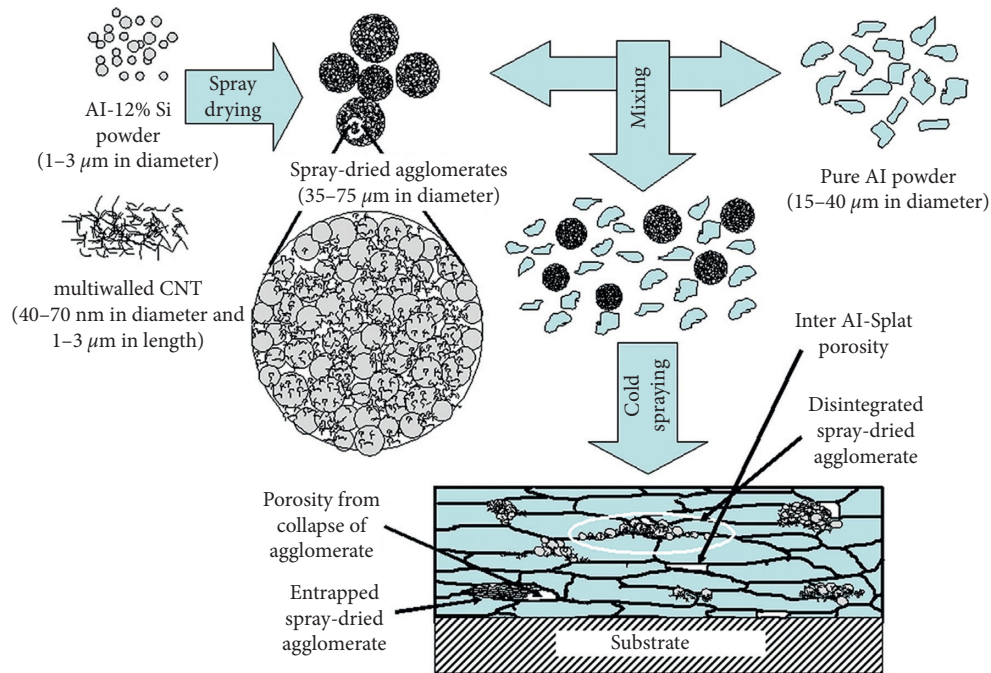


FIGURE 11: Schematic of the coating fabrication procedure using spray drying MMC powders [44].

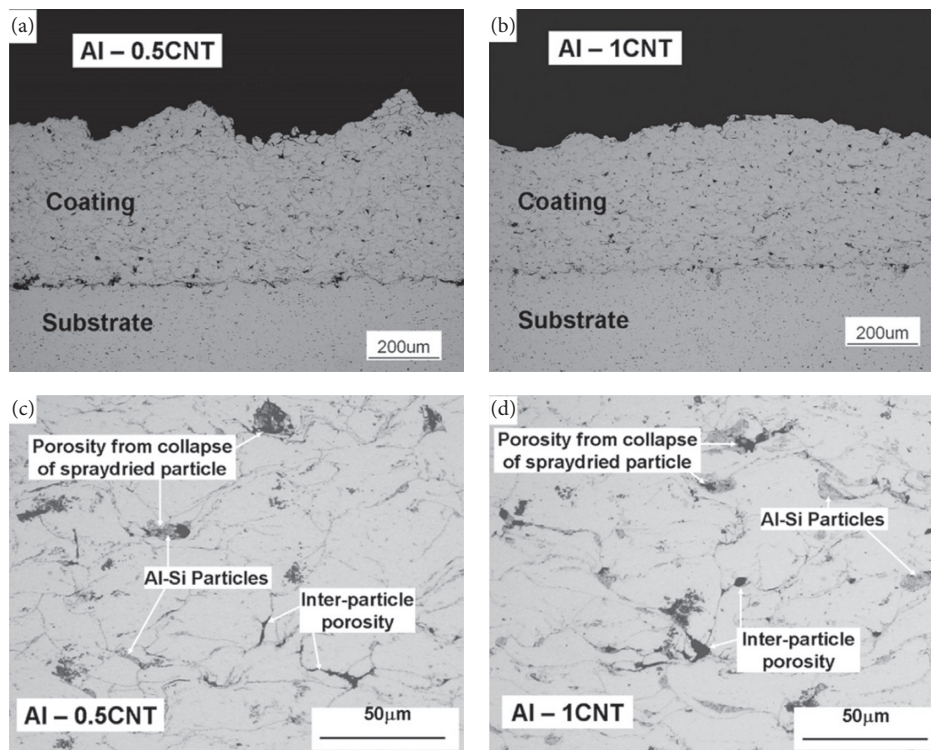


FIGURE 12: SEM imaging of the cross section of cold-sprayed CNT-Al MMC coatings with different CNT contents: (a) CNT content of 0.5%, (b) CNT content of 1%, and (c, d) high-magnification view [44].

coating deposition process and final coating quality. So far, two manufacturing methods have been used for MMC powder fabrication. In Yin et al.'s work, mechanical ball milling was applied to incorporate graphene nanosheets into spherical Cu particles [32]. Because the energy for ball

milling is not high in that work, graphene nanosheets were mainly embedded on the Cu particle surface rather than homogeneously distributed inside the Cu particle. Alternatively, in the work of Dardona et al., the graphene-reinforced MMC powders were synthesized through electroless plating

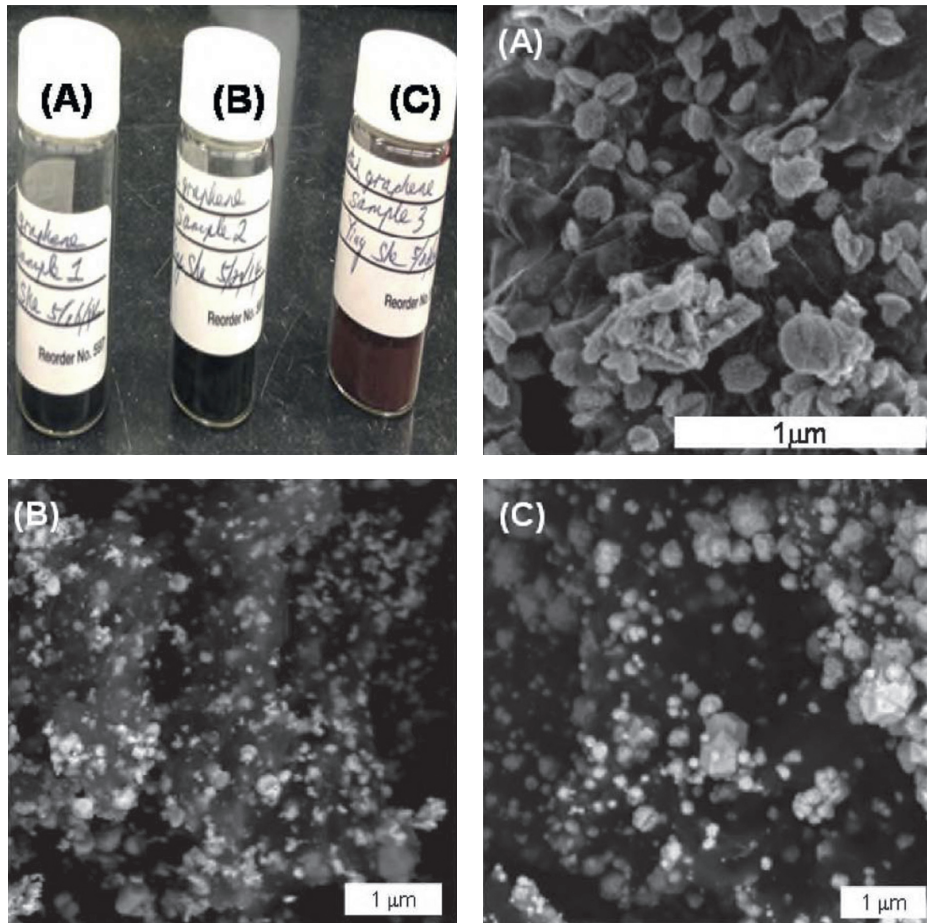


FIGURE 13: Morphology of the graphene-Cu MMC powders produced through electroless plating under different plating time. Digital photo of all samples, (A) plating for 1.5 h, (B) plating for 3 h, and (C) plating for 4.5 h [33].

of Cu film on the surface of graphene nanosheets [33]. Electroless plating is a method that deposits metals onto a solid piece by chemical approach. The piece to be plated is immersed in a reducing agent where metal ions can be changed to metal when catalyzed by certain materials to form a deposit. Figure 13 shows the morphology of the graphene-reinforced Cu MMC powders produced through electroless plating under different plating time. Powders produced in this way basically have a graphene core and an outside Cu film. Longer plating time would result in more Cu phase on the graphene surface as can be seen from Figure 13.

As for the coating microstructure, ball-milled MMC powders resulted in dense and thick coating with uniformly distributed graphene nanosheets as shown Figure 14. However, the electroless-plated MMC powders seemed to produce a low-quality coating with insufficient cohesion strength and inhomogeneous distribution of graphene nanosheets in the coating, as shown in Figure 15 [32]. This may be due to the low fraction of the Cu phase in the MMC powders, which significantly limits the effective metallic bonding between interparticles [33]. In terms of the coating properties, currently, only the wear resistance and electrical conductivity have been tested. In Yin et al.'s work, the

graphene-reinforced MMC coatings exhibited excellent wear-resistance performance, better than those produced by spark plasma sintering [32]. In the work of Dardona et al., the coating demonstrated worse electrical conductivity than bulk Cu, which was probably due to the low Cu thickness on the graphene powder surface, poor interparticle bonding, and inhomogeneous distribution of graphene nanosheets in the coating [33].

5.2. WS_2 -Reinforced MMC Coatings. Monolayer tungsten disulfide (WS_2) has great potential in the optical sector due to its direct band gap and high photoluminescence intensity [34]. It also possesses excellent solid lubrication properties due to the 2D layered structure and easy interlayer sliding. In addition, the special structure of WS_2 allows it to be usable in high temperature, high pressure, high vacuum, high load, and with radiation and corrosive media environments [35, 36]. Moreover, because WS_2 has an excellent adsorption capacity on the metal surface, it can be used as reinforcements in MMCs to improve the lubrication performance [77]. The WS_2 -Al MMCs made by sparking plasma sintering have shown better wear-resistance performance than graphene-Al MMCs under ball-on-disk wear tests, which clearly demonstrates the superiority of WS_2 than other lubricants [36].

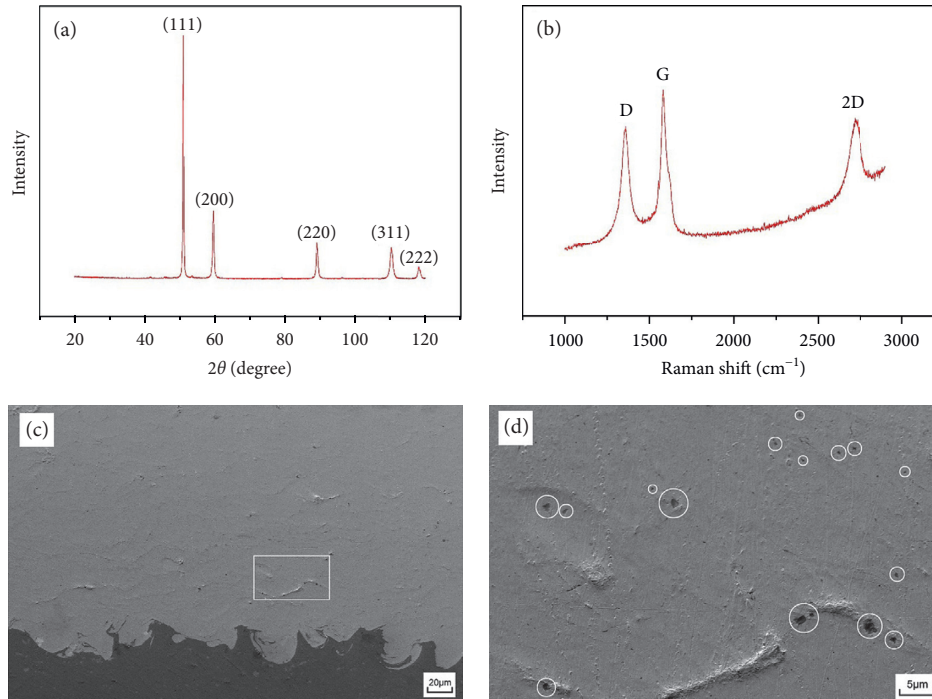


FIGURE 14: Characterization of graphene-Cu MMC coating produced using ball-milled powders: (a) XRD spectrum, (b) Raman spectrum, (c) coating cross-sectional view, and (d) a magnified view [32].

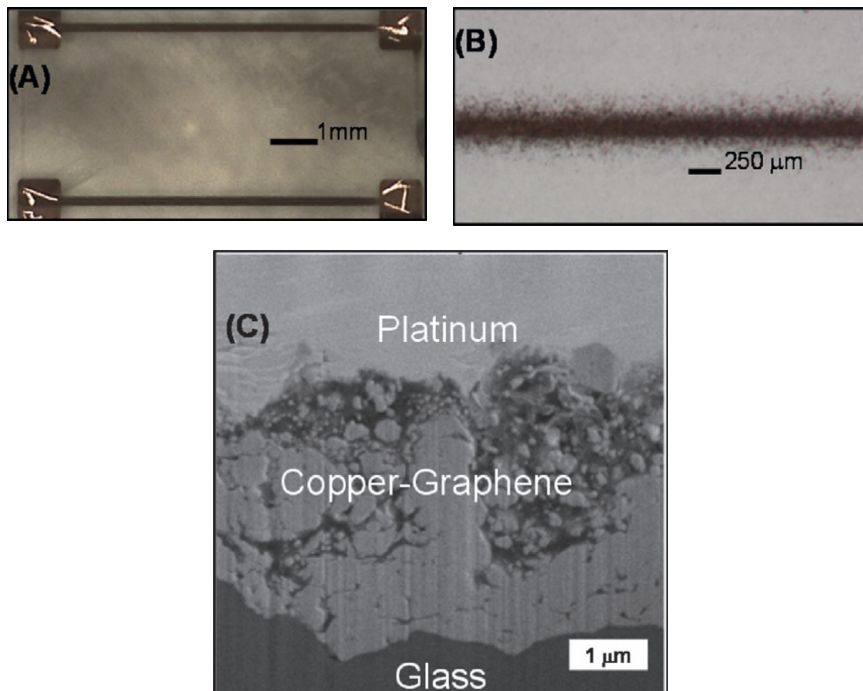


FIGURE 15: Characterization of graphene-Cu MMC coating produced using electroless-plated powders: (A) optical view of two tracks, (B) single-line track, and (C) coating cross-sectional view [33].

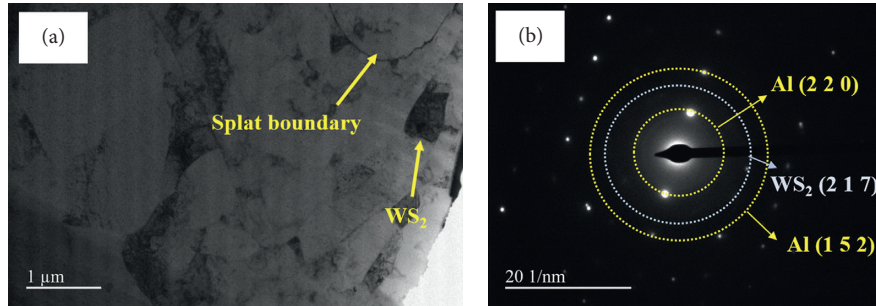


FIGURE 16: TEM imaging of WS_2 -Al MMC coating: (a) bright field imaging with multiple splats, subgrains, and (b) SAED pattern [78].

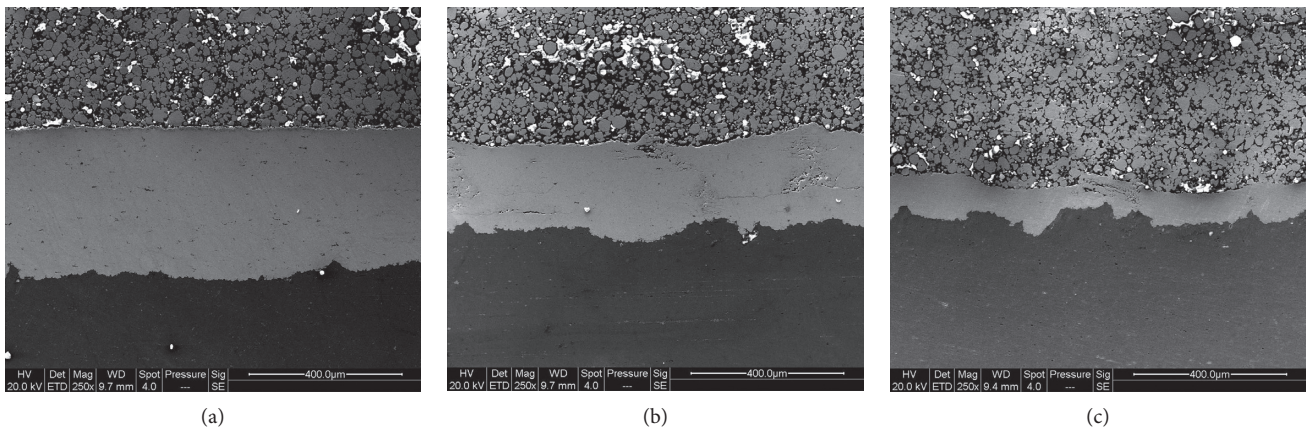


FIGURE 17: SEM imaging of the cross section of cold-sprayed hBN-Ni MMC coatings produced using (a) unaltered powders, (b) ball-milled powders for 1 h, and (c) ball-milled powders for 2 h [39].

WS_2 -Al MMC coatings were produced via cold spray for wear resistance in a recent work [78]. Ball milling technology was used to produce the MMC powders. After low-energy ball milling, Al particles still remained spherical shape, and WS_2 was mostly attached on the surface of the Al particles. The surface morphology of the WS_2 -Al MMC powders is quite similar with the graphene-Cu powders used in Yin et al.'s study [32]. The coatings were then produced using nitrogen under the pressure of 3.8 MPa and temperature of 400°C. Figure 16 shows the TEM imaging of the coating cross section. As can be seen, WS_2 was successfully deposited with Al onto the carbon steel substrate and uniformly distributed within the coating, which demonstrates the feasibility of cold spray to produce WS_2 -reinforced MMC coatings. The wear test revealed that the WS_2 -reinforced MMC coating had an outstanding wear-resistance performance due to the presence of 2D layered WS_2 which aids in shearing of WS_2 layers and uniform tribofilm formation comprised of WS_2 and WO_3 .

5.3. hBN-Reinforced MMC Coatings. Hexagonal boron nitride (hBN) nanosheets are 2D crystalline form of hBN, which have a thickness of one to few atomic layers. It is similar in geometry to graphene but having completely different chemical, thermal, and electronic properties. Cold spray has been successfully used for producing hBN-reinforced MMC coatings, mainly hBN-Ni coatings [37–40].

Electroless plating was used to encapsulate hBN powders and to produce hBN-reinforced MMC powders. During the encapsulation process, the MMC particles tended to agglomerate and form large clusters. Therefore, as a comparison, following the electroless plating, ball milling was employed to de-agglomerate the clustered feedstock powders [38]. Both low- and high-energy ball milling methods were employed: low energy can eliminate voids inside the clusters and leads to higher density and uniform particle size; high energy resulted in breakup of agglomerations and destroyed the Ni encapsulant. Figure 17 shows the SEM imaging of the cross section of cold-sprayed hBN-Ni MMC coatings using various powders. As can be seen, the unaltered hBN-Ni MMC powders resulted in the thickest and densest coatings due to the significant plastic deformation as compared with ball-milled powders which experienced work hardening during the powder preparation process [39]. The tribological study demonstrates that the cold-sprayed hBN-Ni MMC coatings had a very promising wear-resistance performance. They can reduce the friction coefficient by almost 50% and significantly increase the wear resistance as compared with pure Ni [40].

6. 3D Nanoparticle-Reinforced MMC Coatings via Cold Spray

6.1. WC-Reinforced MMC Coatings. Tungsten carbide (WC) has very high hardness and stiffness, which has been widely

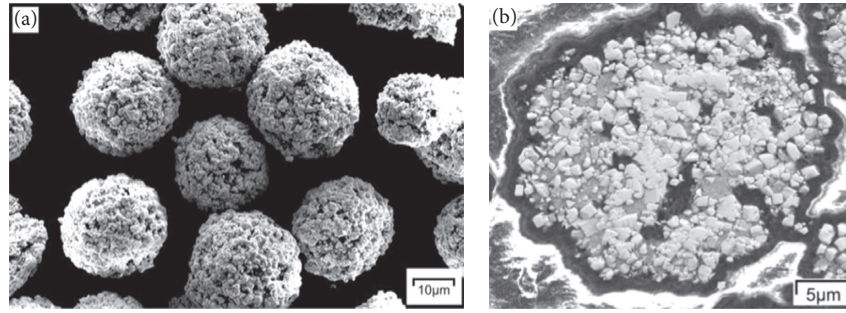


FIGURE 18: Morphology of WC-Co powder: (a) surface morphology and (b) cross-sectional view [84].

TABLE 3: Review of working parameters used for producing cold-sprayed WC-Co coatings [84].

Feedstock	Gas	Pressure (MPa)	Temperature (°C)	Preheating (°C)	Hardness (Hv)
WC-12Co	He	3.0	600	500	2053
	He	2.0	600	No	1812 ± 121
	He	2.0	650	No	N/A
	He	2.0	600	No	1600–2000
	He	2.0	650	No	1800
	N ₂	2.5–3.5	800	Yes	1419 ± 93
	N ₂	4.5	700	250	984
WC-15Co	N ₂	2.4	750 ± 30	Yes	1525 ± 143
	He	1.7	550	No	462 ± 92
	N ₂	4.5	800	250	1480
WC-17Co	He	3.5	600	200	918
	He	1.2–1.7	600	No	1312 ± 39, 1094 ± 51
	N ₂	2.5–3.5	800	Yes	1223 ± 59
WC-25Co	N ₂	2.4	750 ± 30	Yes	1316 ± 80, 1625 ± 115
	N ₂	4.0	800	No	845 ± 55, 981 ± 58
WC-10Co	N/A	2.2	650	No	893 ± 75

used in industrial machinery, cutting tools, and abrasives. It is normally present in the form of nanosized powder, sintered or agglomerated in soft Co to generate WC-Co MMCs. WC-Co protecting coating is one of the most important products of WC-Co MMCs, commonly used for preventing the underlying base materials from serious wear in aggressive environments [79]. The WC-Co coating fabrication mostly relies on high-temperature thermal spray processes to melt the Co matrix phase in the agglomerated WC-Co powder feedstock for achieving superior cohesion [79–83]. Figure 18 shows the typical morphology of WC-Co powders used for coating fabrications [84]. However, high deposition temperature frequently results in decarburization, phase transformation, and oxidation of hard WC reinforcements or soft Co matrix phase, significantly deteriorating the coating mechanical properties and wear-resistance performance [80–83, 85, 86]. Cold spray can effectively prevent the coating defects in relation to high-temperature processes and thereby has been found to be promising for fabricating WC-Co wear-resistance coatings.

Investigations have revealed that WC-Co particles were difficult to deposit with cold spray due to the lack of the sufficient binder phase to induce the particle plastic deformation. Thereby, the working parameters for fabricating

WC-Co coatings must be extremely high so that WC-Co particles can obtain sufficient kinetic energy to promote the metallic bonding between Co matrix phases during the particle deposition. Table 3 lists the working parameters ever used for producing cold-sprayed WC-Co coatings [87]. As can be seen, cold-sprayed WC-Co coatings were mostly achieved by using compressed high-temperature helium as propulsive gas or using nitrogen as propulsive gas combined with powder preheating treatment. Although the manufacturing cost is relatively high, cold-sprayed WC-Co coatings have shown several incomparable advantages. It has been proved that cold spray can produce fully dense WC-Co coatings as shown in Figure 19 [87]. The cold-sprayed coatings experienced no decarburization and phase transformation during the fabrication process due to the low working temperature [88–91]. This is a unique advantage that other thermal spray processes cannot achieve. In addition, it is also demonstrated that the Vickers hardness of cold-sprayed WC-Co coatings mostly fell into the range between 800 and 2000 Hv as listed in Table 3 [84]. The hardness is much higher than most metals, and comparable to or even higher than thermal-sprayed coatings. In terms of tribological performance, cold-sprayed WC-Co coatings showed lower wear

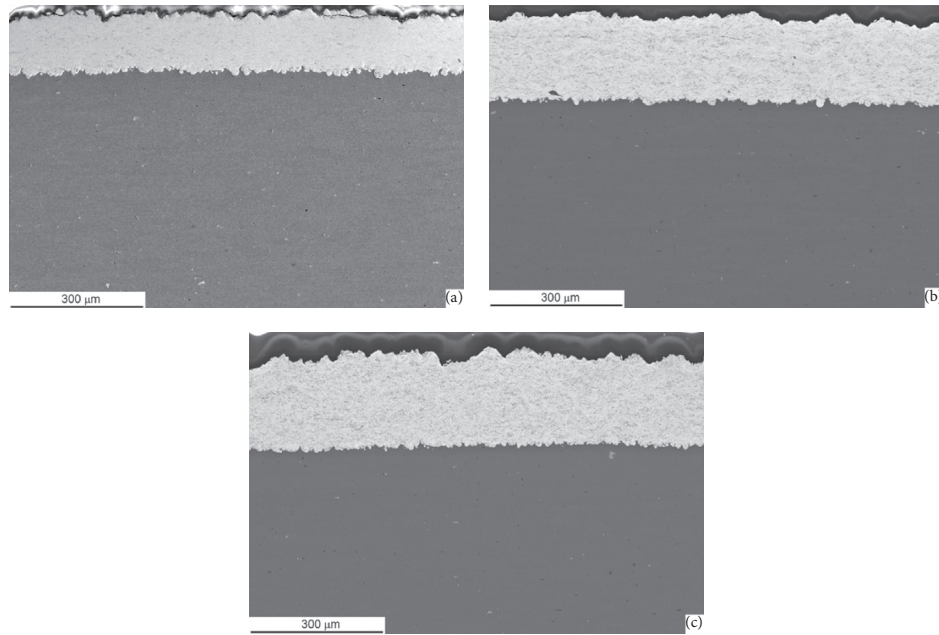


FIGURE 19: SEM imaging of the cross section of WC-Co coatings: (a)WC-12Co, (b)WC-17Co, and (c)WC-25Co coatings deposited onto the Al 7075-T6 substrate [87].

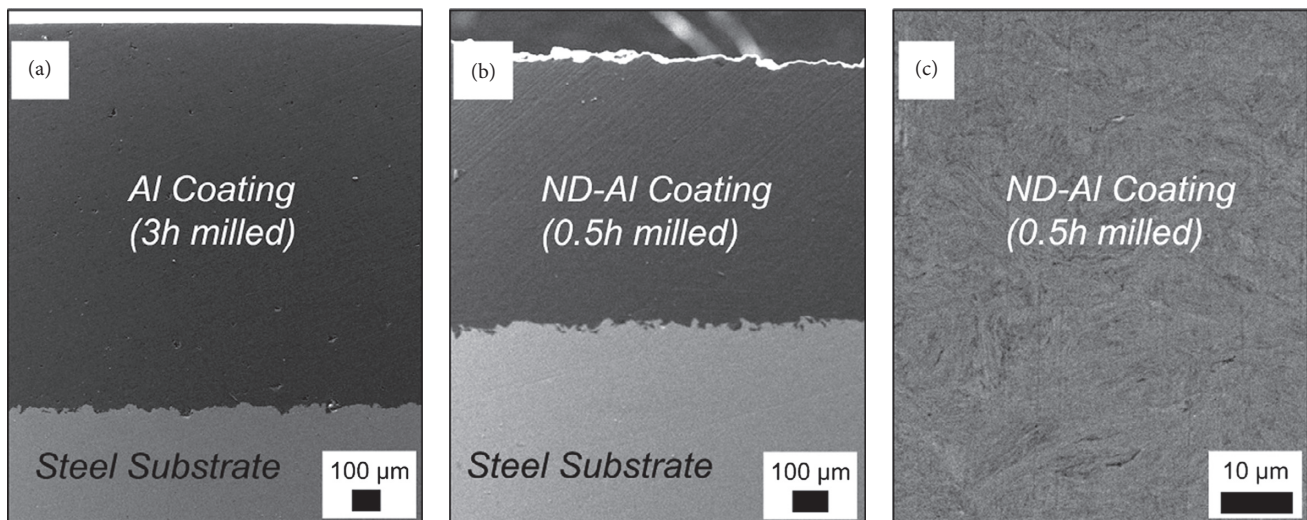


FIGURE 20: SEM imaging of the cross section of cold-sprayed nanodiamond-Al MMC coatings: (a) pure Al coating, (b) nanodiamond-Al MMC coating, and (c) magnified view.

rate than high-velocity oxy-fuel-sprayed coatings under both ball-on-disk sliding and dry abrasion tests, exhibiting superior wear-resistance performance [90, 92–94].

6.2. Diamond-Reinforced MMC Coatings. Diamond is known to possess extremely high hardness, allowing it to be used as an excellent wear-resistance material. However, for the same reason, it is difficult to be machined, which in turn limits its direct applications. Diamond-reinforced MMCs are novel materials in which the metallic phase acts as a binder, while the diamond phase helps to improve the

material properties. Currently, the common ways to fabricate bulk diamond-reinforced MMCs or MMC coatings are powder metallurgy [95–99], pressure infiltration techniques [100–104], and thermal spray techniques [105–109]. These methods mostly require extremely high processing temperatures to melt the metal binder, thereby significantly increasing the risk of the metal phase transformation and diamond graphitization [97]. Cold spray would greatly avoid the risk of high-temperature-induced diamond phase graphitization and simultaneously retain high diamond contents [110, 111].

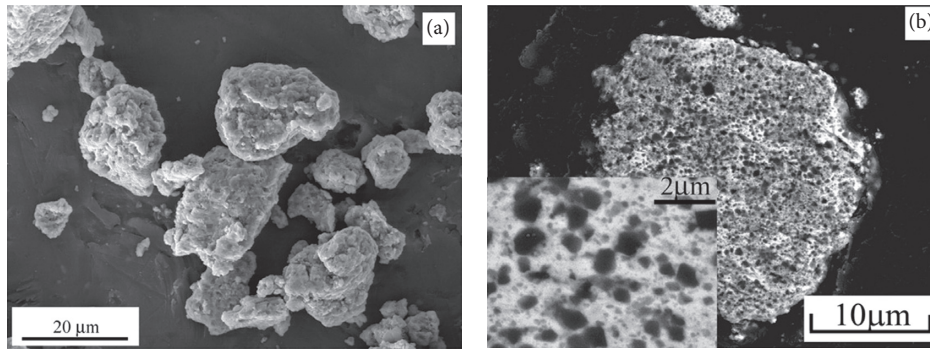


FIGURE 21: SEM imaging of the cBN-NiCrAl MMC powder after ball milling for 40 h: (a) morphology and (b) cross section. The bright regions and dark dots in (b) correspond to NiCrAl alloy and cBN particles.

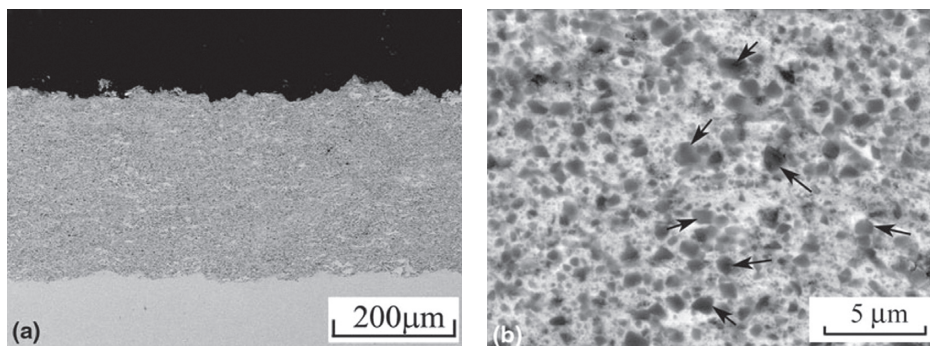


FIGURE 22: SEM imaging of cold sprayed cBN-NiCrAl MMC coatings with 40 vol.% cBN [49]. The bright regions and dark dots in (b) correspond to NiCrAl alloy and cBN particles.

Nanodiamond-reinforced MMC coatings have been successfully fabricated via cold spray [45, 46]. Analogous to most MMC powders, ball milling technology was used to produce the nanodiamond-reinforced MMC powders. In order to maximize the performance of the MMC powders, the effect of ball milling parameters and nanodiamond content on the powder properties were studied. The results revealed that powder properties including particle size distribution, hardness, and uniformity of reinforcements can be well controlled through modifying the nanodiamond content, milling time, and BPR ratio [45]. Figure 20 shows the SEM imaging of cold-sprayed nanodiamond-Al MMC coatings. The MMC coatings exhibited thick and dense features with homogeneously dispersed nanodiamond reinforcements. In addition, coatings showed significant strengthening as compared with the pure Al coating. The reason for the mechanical performance strengthening was attributed to the dispersion strengthening, grain refinement, and strain hardening [46]. So far, property testing on the nanodiamond-reinforced MMC coatings was still very limited. As diamond also possesses high hardness and thermal and electrical conductivity, such coating may also possess high wear-resistance performance and thermal performance. Therefore, further investigations are encouraged in the future work.

6.3. cBN-Reinforced MMC Coatings. Cubic boron nitride (cBN), having similar crystal structure with diamond, is the second-known hardest material after diamond. It is synthesized from hBN under conditions similar to those used to produce synthetic diamond from graphite. It has been increasingly used as cutting and drilling tools in substitution for diamond-based tools owing to its superior thermal stability and chemical inertness. It is suitable especially for processing hard ferrous materials to which diamond is not applicable since diamond reacts with these materials at high temperature [112].

Cold spray has been used to fabricate cBN-NiCrAl MMC coatings [47–50]. As the most prevailing technology for MMC powder production, ball milling was also used to produce the cBN-reinforced MMC powders. Figure 21 shows the SEM imaging of the cBN-NiCrAl MMC powders after ball milling for 40 h. As can be seen, the MMC powders exhibited a near spherical shape; the cBN particles were uniformly distributed in the NiCrAl alloy matrix [47]. Figure 22 shows a SEM imaging of cold-sprayed cBN-NiCrAl MMC coatings with 40 vol.% of cBN particles [49]. Experimental results clearly showed that the as-sprayed coating had a rather dense microstructure with uniformly dispersed nano-cBN particles. In addition, no phase transformation and grain growth of the NiCrAl matrix

occurred during the spraying process. The hardness of the 20 vol.% and 40 vol.% cBN-NiCrAl coatings were 1063 and 1175 Hv, respectively [47–49].

In addition, annealing treatment was found to significantly affect the microstructure of the cBN-reinforced NiCrAl MMC coatings. The nanostructure in the MMC coatings could be retained when the annealing temperature was below 825°C. However, a significant growth of dispersion reinforcements due to the occurrence of reaction between cBN particles and the NiCrAl matrix was observed at an annealing temperature higher than 825°C. This phenomenon led to a reduction of hardness as the annealing temperature increased. Furthermore, the tribological performance of the cold sprayed cBN-NiCrAl MMC coatings was also investigated. The as-sprayed coatings exhibited excellent wear-resistance performance. Coatings with 20 vol.% nano-cBN resulted in a wear resistance which is comparable to the HVOF-sprayed WC-12Co. Low-temperature heat treatment (750°C for 5 h) would further improve the wear-resistance performance due to the promoted interparticle bonding strength [48].

7. Summary and Perspectives

Cold spray is a solid-state coating deposition technology which can retain the original properties of feedstock in the final coating and prevent the adverse influence caused by high working temperature. As a low-temperature process, cold spray has been showing great potential in producing high-performance metal coatings with nanostructure. This paper provides an overview of cold-sprayed metal coatings with nanostructure. Basically, cold-sprayed coatings with nanostructure can be produced in the following three ways. Firstly, nanocrystallization in the form of grain refinement always occurs at the interparticle and coating-substrate interfacial regions during the deposition process due to the dynamic recrystallization, which can result in nanostructured grains within the cold-sprayed coating. This theory has been well understood so far. Secondly, the starting feedstock for cold spray is nanocrystalline powders; then the coating can retain the nanostructure of the starting powders. In this aspect, cold-sprayed nanocrystalline coatings are very promising as cold spray can completely retain the nanostructure of the starting powders in the coating. In the future, the relevant work should be continued, and special attention can be paid on the coating densification and coating property exploration. Thirdly, cold-sprayed nanomaterial-reinforced MMC coatings also exhibit nanostructure. In this field, although ball milling has been accepted as the most commonly used method for producing nanomaterial-reinforced MMC powders, the effect of milling parameters on the powder property is still now well clarified. Also, new technologies for producing more uniform MMC powders are needed. Therefore, preparation of nanomaterial-reinforced MMC powders will be a research focus in the future work. Moreover, investigation on the properties of cold-sprayed nanomaterial-reinforced MMC coatings will be another highlight as currently such property tests are still very limited.

Conflicts of Interest

The authors declare that they have no conflicts of interest.

References

- [1] A. Papyrin, "Cold spray technology," *Advanced Materials and Processing*, vol. 159, pp. 49–51, 2001.
- [2] P. C. King, S. H. Zahiri, and M. Jahedi, "Focused ion beam micro-dissection of cold-sprayed particles," *Acta Materialia*, vol. 56, no. 19, pp. 5617–5626, 2008.
- [3] N. M. Melendez, V. V. Narulkar, G. A. Fisher, and A. G. McDonald, "Effect of reinforcing particles on the wear rate of low-pressure cold-sprayed WC-based MMC coatings," *Wear*, vol. 306, no. 1-2, pp. 185–195, 2013.
- [4] S. Dosta, M. Couto, and J. M. Guilemany, "Cold spray deposition of a WC-25Co cermet onto Al7075-T6 and carbon steel substrates," *Acta Materialia*, vol. 61, no. 2, pp. 643–652, 2013.
- [5] M. Grujicic, C. L. C. Zhao, W. S. W. DeRosset, and D. Helfritsch, "Adiabatic shear instability based mechanism for particles/substrate bonding in the cold-gas dynamic-spray process," *Materials and Design*, vol. 25, no. 8, pp. 681–688, 2004.
- [6] H. J. Choi, M. Lee, and J. Y. Lee, "Application of a cold spray technique to the fabrication of a copper canister for the geological disposal of CANDU spent fuels," *Nuclear Engineering and Design*, vol. 240, no. 10, pp. 2714–2720, 2010.
- [7] V. K. Champagne, "The repair of magnesium rotorcraft components by cold spray," *Journal of Failure Analysis and Prevention*, vol. 8, no. 2, pp. 164–175, 2008.
- [8] S. Yin, X. Wang, X. Suo et al., "Deposition behavior of thermally softened copper particles in cold spraying," *Acta Materialia*, vol. 61, no. 14, pp. 5105–5118, 2013.
- [9] T. Klassen, H. Assadi, H. Kreye, and F. Gartner, "Cold spraying—a materials perspective," *Acta Materialia*, vol. 116, pp. 382–407, 2016.
- [10] M. R. Rokni, S. R. Nutt, C. A. Widener, V. K. Champagne, and R. H. Hrabec, "Review of relationship between particle deformation, coating microstructure, and properties in high-pressure cold spray," *Journal of Thermal Spray Technology*, vol. 26, no. 6, pp. 1–48, 2017.
- [11] S. Yin, M. Meyer, W. Li et al., "Gas flow, particle acceleration, and heat transfer in cold spray: a review in cold spray: a review," *Journal of Thermal Spray Technology*, vol. 25, no. 5, pp. 1–23, 2016.
- [12] S. Yin, X. F. Wang, W. Y. Li, and H. E. Jie, "Effect of substrate hardness on the deformation behavior of subsequently incident particles in cold spraying," *Applied Surface Science*, vol. 257, no. 17, pp. 7560–7565, 2011.
- [13] T. C. Jen, L. Li, W. Cui, Q. Chen, and X. Zhang, "Numerical investigations on cold gas dynamic spray process with nano- and microsize particles," *International Journal of Heat and Mass Transfer*, vol. 48, no. 21-22, pp. 4384–4396, 2005.
- [14] J. Liu, H. Cui, X. Zhou, X. Wu, and J. Zhang, "Nano-crystalline copper coatings produced by cold spraying," *Metals and Materials International*, vol. 18, no. 1, pp. 121–128, 2012.
- [15] K. Kim, M. Watanabe, J. Kawakita, and S. Kuroda, "Grain refinement in a single titanium powder particle impacted at high velocity," *Scripta Materialia*, vol. 59, no. 7, pp. 768–771, 2008.

- [16] C. Lee and J. Kim, "Microstructure of kinetic spray coatings: a review," *Journal of Thermal Spray Technology*, vol. 24, no. 4, pp. 592–610, 2015.
- [17] P. C. King, S. H. Zahiri, and M. Jahedi, "Microstructural refinement within a cold-sprayed copper particle," *Metallurgical and Materials Transactions A*, vol. 40, no. 9, pp. 2115–2123, 2009.
- [18] M. R. Rokni, C. A. Widener, and V. R. Champagne, "Microstructural evolution of 6061 aluminum gas-atomized powder and high-pressure cold-sprayed deposition," *Journal of Thermal Spray Technology*, vol. 23, no. 3, pp. 514–524, 2014.
- [19] X.-T. Luo, C.-X. Li, F.-L. Shang, G.-J. Yang, Y.-Y. Wang, and C.-J. Li, "High velocity impact induced microstructure evolution during deposition of cold spray coatings: a review," *Surface and Coatings Technology*, vol. 254, pp. 11–20, 2014.
- [20] Y. Zou, W. Qin, E. Irissou, J. G. Legoux, S. Yue, and J. A. Szpunar, "Dynamic recrystallization in the particle/particle interfacial region of cold-sprayed nickel coating: electron backscatter diffraction characterization," *Scripta Materialia*, vol. 61, no. 9, pp. 899–902, 2009.
- [21] Y. Zou, D. Goldbaum, J. A. Szpunar, and S. Yue, "Microstructure and nanohardness of cold-sprayed coatings: electron backscattered diffraction and nanoindentation studies," *Scripta Materialia*, vol. 62, no. 6, pp. 395–398, 2010.
- [22] L. Ajdelsztajn, B. Jodoin, G. E. Kim, and J. M. Schoenung, "Cold spray deposition of nanocrystalline aluminum alloys," *Metallurgical and Materials Transactions A*, vol. 36, no. 3, pp. 657–666, 2005.
- [23] L. Ajdelsztajn, A. Zúñiga, B. Jodoin, and E. J. Lavernia, "Cold-spray processing of a nanocrystalline Al-Cu-Mg-Fe-Ni alloy with Sc," *Journal of Thermal Spray Technology*, vol. 15, no. 2, pp. 184–190, 2006.
- [24] L. Ajdelsztajn, B. Jodoin, and J. M. Schoenung, "Synthesis and mechanical properties of nanocrystalline Ni coatings produced by cold gas dynamic spraying," *Surface and Coatings Technology*, vol. 201, no. 3–4, pp. 1166–1172, 2006.
- [25] P. Richer, B. Jodoin, L. Ajdelsztajn, and E. J. Lavernia, "Substrate roughness and thickness effects on cold spray nanocrystalline Al-Mg coatings," *Journal of Thermal Spray Technology*, vol. 15, no. 2, pp. 246–254, 2006.
- [26] P. Sudharshan Phani, V. Vishnukanthan, and G. Sundararajan, "Effect of heat treatment on properties of cold sprayed nanocrystalline copper alumina coatings," *Acta Materialia*, vol. 55, no. 14, pp. 4741–4751, 2007.
- [27] Y. Y. Zhang, X. K. Wu, H. Cui, and J. S. Zhang, "Cold-spray processing of a high density nanocrystalline aluminum alloy 2009 coating using a mixture of as-atomized and as-cryomilled powders," *Journal of Thermal Spray Technology*, vol. 20, no. 5, pp. 1125–1132, 2011.
- [28] S. Tria, O. Elkedim, R. Hamzaoui et al., "Deposition and characterization of cold sprayed nanocrystalline NiTi," *Powder Technology*, vol. 210, no. 2, pp. 181–188, 2011.
- [29] J. Liu, X. Zhou, X. Zheng, H. Cui, and J. Zhang, "Tribological behavior of cold-sprayed nanocrystalline and conventional copper coatings," *Applied Surface Science*, vol. 258, no. 19, pp. 7490–7496, 2012.
- [30] R. Ghelichi, S. Bagherifard, D. Mac Donald et al., "Fatigue strength of Al alloy cold sprayed with nanocrystalline powders," *International Journal of Fatigue*, vol. 65, pp. 51–57, 2014.
- [31] M. Kumar, H. Singh, N. Singh et al., "Development of nanocrystalline cold sprayed Ni-20Cr coatings for high temperature oxidation resistance," *Surface and Coatings Technology*, vol. 266, pp. 122–133, 2015.
- [32] S. Yin, Z. Zhang, E. J. Ekoi et al., "Novel cold spray for fabricating graphene-reinforced metal matrix composites," *Materials Letters*, vol. 196, pp. 172–175, 2017.
- [33] S. Dardona, J. Hoey, Y. She, and W. R. Schmidt, "Direct write of copper-graphene composite using micro-cold spray," *AIP Advances*, vol. 6, no. 8, p. 085013, 2016.
- [34] K. M. McCreary, A. T. Hanbicki, G. G. Jernigan, J. C. Culbertson, and B. T. Jonker, "Synthesis of large-area WS₂ monolayers with exceptional photoluminescence," *Scientific Reports*, vol. 6, no. 1, p. 19159, 2016.
- [35] X. Zhang, H. Xu, J. Wang et al., "Synthesis of ultrathin WS₂ nanosheets and their tribological properties as lubricant additives," *Nanoscale Research Letters*, vol. 11, no. 1, p. 442, 2016.
- [36] S. Rengifo, *A Comparison between Graphene and WS₂ as Solid Lubricant Additives to Aluminum for Automobile Applications*, M.S. thesis, Florida International University, Miami, FL, USA, 2015.
- [37] I. Smid, A. E. Segall, P. Walia, G. Aggarwal, T. J. Eden, and J. K. Potter, "Cold-sprayed Ni-hBN self-lubricating coatings," *Tribology Transactions*, vol. 55, no. 5, pp. 599–605, 2012.
- [38] M. Neshastehriz, I. Smid, and A. E. Segall, "In-situ agglomeration and de-agglomeration by milling of nano-engineered lubricant particulate composites for cold spray deposition," *Journal of Thermal Spray Technology*, vol. 23, no. 7, pp. 1191–1198, 2014.
- [39] M. Neshastehriz, *Influence of Pre-Process Work Hardening of Nickel Encapsulated Hexagonal Boron Nitride Powders on Cold Spray Coatings*, The Pennsylvania State University, State College, PA, USA, 2014.
- [40] L. M. Stark, *Engineered Self-Lubricating Coatings Utilizing Cold Spray Technology*, The Pennsylvania State University, State College, PA, USA, 2010.
- [41] E. J. T. Pialago and C. W. Park, "Cold spray deposition characteristics of mechanically alloyed Cu-CNT composite powders," *Applied Surface Science*, vol. 308, pp. 63–74, 2014.
- [42] E. J. T. Pialago, O. K. Kwon, M. S. Kim, and C. W. Park, "Ternary Cu-CNT-AlN composite coatings consolidated by cold spray deposition of mechanically alloyed powders," *Journal of Alloys and Compounds*, vol. 650, pp. 199–209, 2015.
- [43] E. J. T. Pialago, O. K. Kwon, and C. W. Park, "Cold spray deposition of mechanically alloyed ternary Cu-CNT-SiC composite powders," *Ceramics International*, vol. 41, no. 5, pp. 6764–6775, 2015.
- [44] S. R. Bakshi, V. Singh, K. Balani, D. G. McCartney, S. Seal, and A. Agarwal, "Carbon nanotube reinforced aluminum composite coating via cold spraying," *Surface and Coatings Technology*, vol. 202, no. 21, pp. 5162–5169, 2008.
- [45] D. J. Woo, B. Sneed, F. Peerally et al., "Synthesis of nanodiamond-reinforced aluminum metal composite powders and coatings using high-energy ball milling and cold spray," *Carbon*, vol. 63, pp. 404–415, 2013.
- [46] D. J. Woo, F. C. Heer, L. N. Brewer, J. P. Hooper, and S. Osswald, "Synthesis of nanodiamond-reinforced aluminum metal matrix composites using cold-spray deposition," *Carbon*, vol. 86, pp. 15–25, 2015.
- [47] X. T. Luo, G. J. Yang, and C. J. Li, "Multiple strengthening mechanisms of cold-sprayed cBNp/NiCrAl composite coating," *Surface and Coatings Technology*, vol. 205, no. 20, pp. 4808–4813, 2011.
- [48] X. T. Luo, E. J. Yang, F. L. Shang, G. J. Yang, C. X. Li, and C. J. Li, "Microstructure, mechanical properties, and two-body

- abrasive wear behavior of cold-sprayed 2 vol.% cubic BN-NiCrAl nanocomposite coating,” *Journal of Thermal Spray Technology*, vol. 23, no. 7, pp. 1181–1190, 2014.
- [49] X. T. Luo and C. J. Li, “Thermal stability of microstructure and hardness of cold-sprayed cBN/NiCrAl nanocomposite coating,” *Journal of Thermal Spray Technology*, vol. 21, no. 3-4, pp. 578–585, 2012.
- [50] X. T. Luo, G. J. Yang, C. J. Li, and K. Kondoh, “High strain rate induced localized amorphization in cubic BN/NiCrAl nanocomposite through high velocity impact,” *Scripta Materialia*, vol. 65, no. 7, pp. 581–584, 2011.
- [51] H. Assadi, F. Gärtner, T. Stoltenhoff, and H. Kreye, “Bonding mechanism in cold gas spraying,” *Acta Materialia*, vol. 51, no. 15, pp. 4379–4394, 2003.
- [52] M. R. Rokni, C. A. Widener, and G. A. Crawford, “Microstructural evolution of 7075 Al gas atomized powder and high-pressure cold sprayed deposition,” *Surface and Coatings Technology*, vol. 251, pp. 254–263, 2014.
- [53] K. Kim, M. Watanabe, and S. Kuroda, “Thermal softening effect on the deposition efficiency and microstructure of warm sprayed metallic powder,” *Scripta Materialia*, vol. 60, no. 8, pp. 710–713, 2009.
- [54] K. Kang, H. Park, G. Bae, and C. Lee, “Microstructure and texture of Al coating during kinetic spraying and heat treatment,” *Journal of Materials Science*, vol. 47, no. 9, pp. 4053–4061, 2012.
- [55] Q. Wang, N. Birbilis, and M. X. Zhang, “Interfacial structure between particles in an aluminum deposit produced by cold spray,” *Materials Letters*, vol. 65, no. 11, pp. 1576–1578, 2011.
- [56] M. A. Meyers, A. Mishra, and D. J. Benson, “Mechanical properties of nanocrystalline materials,” *Progress in Materials Science*, vol. 51, no. 4, pp. 427–556, 2006.
- [57] A. I. Gusev and A. A. Rempel, *Nanocrystalline Materials*, Cambridge International Science Publishing, Great Abington, Cambridge, UK, 2004.
- [58] X. Wang, Q. Li, J. Xie et al., “Fabrication of ultralong and electrically uniform single-walled carbon nanotubes on clean substrates,” *Nano Letters*, vol. 9, no. 9, pp. 3137–3141, 2009.
- [59] J. L. Song, W. G. Chen, L. L. Dong, J. J. Wang, and N. Deng, “An electroless plating and planetary ball milling process for mechanical properties enhancement of bulk CNTs/Cu composites,” *Journal of Alloys and Compounds*, vol. 720, pp. 54–62, 2017.
- [60] B. Cheng, R. Bao, J. Yi et al., “Interface optimization of CNT/Cu composite by forming TiC nanoprecipitation and low interface energy structure via spark plasma sintering,” *Journal of Alloys and Compounds*, vol. 722, pp. 852–858, 2017.
- [61] D. Kaewsai, A. Watcharapasorn, P. Singjai, S. Wirojanupatump, P. Niranatlumpong, and S. Jiansirisomboon, “Thermal sprayed stainless steel/carbon nanotube composite coatings,” *Surface and Coatings Technology*, vol. 205, no. 7, pp. 2104–2112, 2010.
- [62] S. Moonngam, P. Tunjina, D. Deesom, and C. Banjongprasert, “Fe-Cr/CNTs nanocomposite feedstock powders produced by chemical vapor deposition for thermal spray coatings,” *Surface and Coatings Technology*, vol. 306, pp. 323–327, 2016.
- [63] W. A. Curtin and B. W. Sheldon, “CNT-reinforced ceramics and metals,” *Materials Today*, vol. 7, no. 11, pp. 44–49, 2004.
- [64] A. Dorri Moghadam, E. Omrani, P. L. Menezes, and P. K. Rohatgi, “Mechanical and tribological properties of self-lubricating metal matrix nanocomposites reinforced by carbon nanotubes (CNTs) and graphene—a review,” *Composites Part B: Engineering*, vol. 77, pp. 402–420, 2015.
- [65] S. Cho, K. Takagi, H. Kwon et al., “Multi-walled carbon nanotube-reinforced copper nanocomposite coating fabricated by low-pressure cold spray process,” *Surface and Coatings Technology*, vol. 206, no. 16, pp. 3488–3494, 2012.
- [66] E. J. T. Pialago, O. K. Kwon, and C. W. Park, “Nucleate boiling heat transfer of R134a on cold sprayed CNT-Cu composite coatings,” *Applied Thermal Engineering*, vol. 56, no. 1-2, pp. 112–119, 2013.
- [67] E. J. T. Pialago, O. K. Kwon, J. S. Jin, and C. W. Park, “Nucleate pool boiling of R134a on cold sprayed Cu-CNT-SiC and Cu-CNT-AlN composite coatings,” *Applied Thermal Engineering*, vol. 103, pp. 684–694, 2016.
- [68] E. J. Pialago, X. R. Zheng, K. A. Ada, et al., “A study on the effects of ceramic content of CNT/metal composite surface coatings fabricated by cold spray for boiling heat transfer enhancement,” in *Proceedings of the ASME 2012 3rd Micro/Nanoscale Heat & Mass Transfer International Conference*, Atlanta, GA, USA, 2012.
- [69] D. Lin, C. Richard Liu, and G. J. Cheng, “Single-layer graphene oxide reinforced metal matrix composites by laser sintering: microstructure and mechanical property enhancement,” *Acta Materialia*, vol. 80, pp. 183–193, 2014.
- [70] L. Y. Chen, H. Konishi, A. Fehrenbacher et al., “Novel nanoprocessing route for bulk graphene nanoplatelets reinforced metal matrix nanocomposites,” *Scripta Materialia*, vol. 67, no. 1, pp. 29–32, 2012.
- [71] F. Chen, J. Ying, Y. Wang, S. Du, Z. Liu, and Q. Huang, “Effects of graphene content on the microstructure and properties of copper matrix composites,” *Carbon*, vol. 96, pp. 836–842, 2016.
- [72] W. Zhai, X. Shi, M. Wang et al., “Grain refinement: a mechanism for graphene nanoplatelets to reduce friction and wear of Ni3Al matrix self-lubricating composites,” *Wear*, vol. 310, no. 1-2, pp. 33–40, 2014.
- [73] Z. Xu, X. Shi, W. Zhai, J. Yao, S. Song, and Q. Zhang, “Preparation and tribological properties of TiAl matrix composites reinforced by multilayer graphene,” *Carbon*, vol. 67, pp. 168–177, 2014.
- [74] Y. Fan, L. Kang, W. Zhou, W. Jiang, L. Wang, and A. Kawasaki, “Control of doping by matrix in few-layer graphene/metal oxide composites with highly enhanced electrical conductivity,” *Carbon*, vol. 81, pp. 83–90, 2015.
- [75] X. Huang, X. Qi, F. Boey, and H. Zhang, “Graphene-based composites,” *Chemical Society Reviews*, vol. 41, no. 2, pp. 666–686, 2012.
- [76] J. Dutkiewicz, P. Ozga, W. Maziarz et al., “Microstructure and properties of bulk copper matrix composites strengthened with various kinds of graphene nanoplatelets,” *Materials Science and Engineering: A*, vol. 628, pp. 124–134, 2015.
- [77] S. Xu, X. Gao, M. Hu et al., “Dependence of atomic oxygen resistance and the tribological properties on microstructures of WS₂ films,” *Applied Surface Science*, vol. 298, pp. 36–43, 2014.
- [78] A. Loganathan, S. Rengifo, A. F. Hernandez et al., “Effect of 2D WS₂ addition on cold-sprayed aluminum coating,” *Journal of Thermal Spray Technology*, vol. 26, no. 7, pp. 1585–1597, 2017.
- [79] A. Rahbar-kelishami, A. Abdollah-zadeh, M. M. Hadavi, A. Banerji, A. Alpas, and A. P. Gerlich, “Effects of friction stir processing on wear properties of WC-12%Co sprayed on 52100 steel,” *Materials and Design*, vol. 86, pp. 98–104, 2015.
- [80] C. J. Li and G. J. Yang, “Relationships between feedstock structure, particle parameter, coating deposition, microstructure and properties for thermally sprayed conventional

- and nanostructured WC-Co,” *International Journal of Refractory Metals and Hard Materials*, vol. 39, pp. 2–17, 2013.
- [81] S. Al-Mutairi, M. S. J. Hashmi, B. S. Yilbas, and J. Stokes, “Microstructural characterization of HVOF/plasma thermal spray of micro/nano WC-12%Co powders,” *Surface and Coatings Technology*, vol. 264, pp. 175–186, 2015.
- [82] H. L. D. V. Lovelock, “Powder/processing/structure relationships in WC-Co thermal spray coatings: a review of the published literature,” *Journal of Thermal Spray Technology*, vol. 7, no. 3, pp. 357–373, 1998.
- [83] J. He and J. M. Schoenung, “A review on nanostructured WC-Co coatings,” *Surface and Coatings Technology*, vol. 157, no. 1, pp. 72–79, 2002.
- [84] S. Yin, E. J. Ekoi, T. L. Lupton, D. P. Dowling, and R. Lupoi, “Cold spraying of WC-Co-Ni coatings using porous WC-17Co powders: formation mechanism, microstructure characterization and tribological performance,” *Materials and Design*, vol. 126, pp. 305–313, 2017.
- [85] K. Kumari, K. Anand, M. Bellacci, and M. Giannozzi, “Effect of microstructure on abrasive wear behavior of thermally sprayed WC-10Co-4Cr coatings,” *Wear*, vol. 268, no. 11–12, pp. 1309–1319, 2010.
- [86] A. A. Burkov and S. A. Pyachin, “Formation of WC-Co coating by a novel technique of electrospark granules deposition,” *Materials and Design*, vol. 80, pp. 109–115, 2015.
- [87] S. Dosta, G. Bolelli, A. Candeli, L. Lusvarghi, I. G. Cano, and J. M. Guilemany, “Plastic deformation phenomena during cold spray impact of WC-Co particles onto metal substrates,” *Acta Materialia*, vol. 124, pp. 173–181, 2017.
- [88] H.-J. Kim, C.-H. Lee, and S.-Y. Hwang, “Fabrication of WC-Co coatings by cold spray deposition,” *Surface and Coatings Technology*, vol. 191, no. 2–3, pp. 335–340, 2005.
- [89] H.-J. Kim, C.-H. Lee, and S.-Y. Hwang, “Superhard nano WC-12%Co coating by cold spray deposition,” *Materials Science and Engineering: A*, vol. 391, no. 1–2, pp. 243–248, 2005.
- [90] M. Couto, S. Dosta, and J. M. Guilemany, “Comparison of the mechanical and electrochemical properties of WC-17 and 12Co coatings onto Al7075-T6 obtained by high velocity oxy-fuel and cold gas spraying,” *Surface and Coatings Technology*, vol. 268, pp. 180–189, 2014.
- [91] A. S. M. Ang, C. C. Berndt, and P. Cheang, “Deposition effects of WC particle size on cold sprayed WC-Co coatings,” *Surface and Coatings Technology*, vol. 205, no. 10, pp. 3260–3267, 2011.
- [92] M. Couto, S. Dosta, J. Fernández, and J. M. Guilemany, “Comparison of the mechanical and electrochemical properties of WC-25Co coatings obtained by high velocity oxy-fuel and cold gas spraying,” *Journal of Thermal Spray Technology*, vol. 23, no. 8, pp. 1251–1258, 2014.
- [93] H.-T. Wang, X. Chen, X.-B. Bai, G.-C. Ji, Z.-X. Dong, and D.-L. Yi, “Microstructure and properties of cold sprayed multimodal WC-17Co deposits,” *International Journal of Refractory Metals and Hard Materials*, vol. 45, pp. 196–203, 2014.
- [94] G.-J. Yang, P.-H. Gao, C.-X. Li, and C.-J. Li, “Mechanical property and wear performance dependence on processing condition for cold-sprayed WC-(nanoWC-Co),” *Applied Surface Science*, vol. 332, pp. 80–88, 2015.
- [95] Q. L. Che, J. J. Zhang, X. K. Chen et al., “Spark plasma sintering of titanium-coated diamond and copper-titanium powder to enhance thermal conductivity of diamond/copper composites,” *Materials Science in Semiconductor Processing*, vol. 33, pp. 67–75, 2015.
- [96] A. M. Abyzov, M. J. Kruszewski, Ł. Ciupiński, M. Mazurkiewicz, A. Michalski, and K. J. Kurzydłowski, “Diamond-tungsten based coating-copper composites with high thermal conductivity produced by pulse plasma sintering,” *Materials & Design*, vol. 76, pp. 97–109, 2015.
- [97] W. Z. Shao, V. V. Ivanov, L. Zhen, Y. S. Cui, and Y. Wang, “A study on graphitization of diamond in copper-diamond composite materials,” *Materials Letters*, vol. 58, no. 1–2, pp. 146–149, 2004.
- [98] K. Chu, Z. Liu, C. Jia et al., “Thermal conductivity of SPS consolidated Cu/diamond composites with Cr-coated diamond particles,” *Journal of Alloys and Compounds*, vol. 490, no. 1–2, pp. 453–458, 2010.
- [99] T. Schubert, Ł. Ciupiński, W. Zieliński, A. Michalski, T. Weißgärber, and B. Kieback, “Interfacial characterization of Cu/diamond composites prepared by powder metallurgy for heat sink applications,” *Scripta Materialia*, vol. 58, no. 4, pp. 263–266, 2008.
- [100] A. M. Abyzov, S. V. Kidalov, and F. M. Shakhov, “High thermal conductivity composite of diamond particles with tungsten coating in a copper matrix for heat sink application,” *Applied Thermal Engineering*, vol. 48, pp. 72–80, 2012.
- [101] H. Feng, J. K. Yu, and W. Tan, “Microstructure and thermal properties of diamond/aluminum composites with TiC coating on diamond particles,” *Materials Chemistry and Physics*, vol. 124, no. 1, pp. 851–855, 2010.
- [102] Q. Kang, X. He, S. Ren et al., “Preparation of copper-diamond composites with chromium carbide coatings on diamond particles for heat sink applications,” *Applied Thermal Engineering*, vol. 60, no. 1–2, pp. 423–429, 2013.
- [103] J. Li, H. Zhang, Y. Zhang, Z. Che, and X. Wang, “Microstructure and thermal conductivity of Cu/diamond composites with Ti-coated diamond particles produced by gas pressure infiltration,” *Journal of Alloys and Compounds*, vol. 647, pp. 941–946, 2015.
- [104] Y. Dong, R. Zhang, X. He, Z. Ye, and X. Qu, “Fabrication and infiltration kinetics analysis of Ti-coated diamond/copper composites with near-net-shape by pressureless infiltration,” *Materials Science and Engineering: B*, vol. 177, no. 17, pp. 1524–1530, 2012.
- [105] K. Venkateswarlu, A. K. Ray, M. K. Gunjan, D. P. Mondal, and L. C. Pathak, “Tribological wear behavior of diamond reinforced composite coating,” *Materials Science and Engineering: A*, vol. 418, no. 1–2, pp. 357–363, 2006.
- [106] A. F. Richardson, A. Neville, and J. I. B. Wilson, “Developing diamond MMCs to improve durability in aggressive abrasive conditions,” *Wear*, vol. 255, no. 1–6, pp. 593–605, 2003.
- [107] K. Venkateswarlu, V. Rajinikanth, T. Naveen, D. P. Sinha, Atiquzzaman, and A. K. Ray, “Abrasive wear behavior of thermally sprayed diamond reinforced composite coating deposited with both oxy-acetylene and HVOF techniques,” *Wear*, vol. 266, no. 9–10, pp. 995–1002, 2009.
- [108] L. Yang, B. Li, J. Yao, and Z. Li, “Effects of diamond size on the deposition characteristic and tribological behavior of diamond/Ni60 composite coating prepared by supersonic laser deposition,” *Diamond and Related Materials*, vol. 58, pp. 139–148, 2015.
- [109] J. Yao, L. Yang, B. Li, and Z. Li, “Beneficial effects of laser irradiation on the deposition process of diamond/Ni60 composite coating with cold spray,” *Applied Surface Science*, vol. 330, pp. 300–308, 2015.
- [110] S. Yin, Y. Xie, J. Cizek et al., “Advanced diamond-reinforced metal matrix composites via cold spray: properties and

- deposition mechanism,” *Composites Part B: Engineering*, vol. 113, pp. 44–54, 2017.
- [111] Y. Xie, S. Yin, C. Chen, M. Planche, H. Liao, and R. Lupoi, “New insights into the coating/substrate interfacial bonding mechanism in cold spray,” *Scripta Materialia*, vol. 125, pp. 1–4, 2016.
- [112] W. J. Zhang, Y. M. Chong, I. Bello, and S. T. Lee, “Nucleation, growth and characterization of cubic boron nitride (cBN) films,” *Journal of Physics D: Applied Physics*, vol. 40, no. 20, pp. 6159–6174, 2007.

Research Article

Cold-Sprayed Aluminum-Silica Composite Coatings Enhance Antiwear/Anticorrosion Performances of AZ31 Magnesium Alloy

Lijia Fang,^{1,2} Yuting Xu,² Li Gao,¹ Xinkun Suo ,² Jianguo Gong,¹ and Hua Li ²

¹Qinghai Provincial Key Laboratory of New Light Alloys, School of Mechanical Engineering, Qinghai University, Xining 810016, China

²Key Laboratory of Marine Materials and Related Technologies, Zhejiang Key Laboratory of Marine Materials and Protective Technologies, Ningbo Institute of Materials Technology and Engineering, Chinese Academy of Sciences, Ningbo 315201, China

Correspondence should be addressed to Xinkun Suo; suoxinkun@nimte.ac.cn

Received 10 September 2017; Accepted 19 November 2017; Published 6 May 2018

Academic Editor: Aniello Riccio

Copyright © 2018 Lijia Fang et al. This is an open access article distributed under the Creative Commons Attribution License, which permits unrestricted use, distribution, and reproduction in any medium, provided the original work is properly cited.

Extensive efforts devoted in recent years to booming structural applications of lightweight magnesium alloys are usually undermined by their insufficient surface properties. Surface modification is therefore necessarily required in most cases for enhanced surface integrity of the alloys. Here, we report construction of aluminum-silica protective layers by cold spray on AZ31 magnesium alloys, and the effect of the silica additives on microstructure and mechanical properties of the coatings was examined. The ceramic particles were dispersed evenly in the coatings, and increased silica content gives rise to enhanced adhesion, antiwear performances, and microhardness of the coatings. The even distribution of silica in the coatings altered the wear regimes from adhesive to abrasive wear. The cold spray fabrication of the aluminum-silica protective coatings would facilitate structural applications of the magnesium alloys.

1. Introduction

Magnesium alloys are promising lightweight materials with extensive applications in automotive, aerospace, and electronics industries. However, challenges persist due to their relatively poor corrosion and wear resistance, which has been one of the major hurdles affecting development of the alloys [1]. One of the most effective solutions to prevent the corrosion is to coat an anticorrosion layer on magnesium alloys. Many surface techniques, such as thermal spraying, chemical vapor deposition, sol-gel, plating, anodizing oxidation, and microarc oxidation, have therefore been attempted to improve the anticorrosion performances of magnesium alloys [2–7], in which it was reported that a thin layer is effective in preventing penetration of corrosive substances. In many cases, corrosion is accompanied by wear for magnesium alloy components; it is therefore essential that the protective layers must simultaneously possess anticorrosion/antiwear performances.

Addition of ceramic materials to alloy-based coating can effectively improve its wear resistance, corrosion resistance, or

temperature oxidation resistance [8, 9]. Lee et al. [10, 11], Shkodkin et al. [12], and Irissou et al. [8] reported that incorporating ceramic particles into metallic coatings not only improved the quality of the coatings by reducing their porosity but also increased their bonding strength. Porosity reduction of the coatings contributes to further enhanced corrosion resistance [8]. A variety of ceramics such as Al_2O_3 [10, 13], SiC [14–17], and TiN [18, 19] have been investigated as the secondary phase in metallic matrix ceramic composites.

As one of the recently developed surface coating techniques, cold spraying differs from the conventional thermal spray methods. During cold spray processing, micron-sized particles are accelerated by an inert gas stream to a high velocity, and the feedstock remains in the solid state throughout the entire processing. This in turn solves the problems associated with high processing temperature, such as chemical reaction, phase transition, oxidation, or unfavorable structural changes. Apart from the advantages of spraying temperature-sensitive materials, cold spray provides the coatings with very dense microstructure [20], giving rise to better mechanical properties and corrosion resistance. For the temperature-sensitive

magnesium alloy substrates, cold spray might be an appropriate technique for fabricating protective coatings. It has been clear that addition of hard ceramic particles into cold-sprayed coatings remarkably improves their hardness and wear resistance [12, 21]. In this study, Al-SiO₂ composite coatings were deposited by cold spray on the AZ31 magnesium alloy. The effect of SiO₂ content on the microstructure, mechanical properties, and anticorrosion properties of the coatings was examined and elucidated.

2. Materials and Methods

2.1. Deposition of Coatings. Spherical commercial pure aluminum powder (Beijing General Research Institute of Mining and Metallurgy, China) with a mean size of 25 μm and angular SiO₂ powder (Beijing General Research Institute of Mining and Metallurgy, China) with a mean size of 16 μm were used in this study. As reported in [22], the ceramic particle can only deposit to form a coating unless it impacts on a metallic surface, and that impacting onto a ceramic surface cannot form a coating. Therefore, the ceramic content in the coating is less than that in the designed original powder. Depending on the nature and the particle size of the ceramic phase, the corresponding relation of the ceramic content in the original powder and in the composite coating is different. For the new addition phase SiO₂, this corresponding relation is unclear. Therefore, SiO₂ particles with different contents from 10 vol.% to 40 vol.% were added into the powder by mechanical blending. The composite coatings with different SiO₂ content were fabricated by cold spraying (CGT KINETIKS 4000, Germany). Nitrogen was used as acceleration gas and carrier gas at the temperature of 350°C and the pressure of 3 MPa. The spraying distance was 30 mm, and the traverse speed of the gun was 200 mm/s. The pure Al coating and composite coatings with 10 vol.%, 20 vol.%, and 40 vol.% SiO₂ particles were named as coating 0, coating 10, coating 20, and coating 40, respectively. AZ31 magnesium alloy (AZ31) plates with a dimension of 20 mm \times 20 mm \times 3 mm were used as substrates. Prior to spraying, the substrates were surface grit blasted using 60-mesh black fused alumina sands and subsequently degreased by sonication cleaning in acetone.

2.2. Characterization of the Coatings. Phase composition of the powder and the coatings were characterized by X-ray diffraction (XRD, D8 Advance, Bruker AXS, Germany) at a scanning rate of 0.02°/s over a 2θ range of 10°–90° using Cu K α radiation operated at 35 mA and 40 kV. Topography and cross-sectional morphology of the coatings were examined by using field emission scanning electron microscope (FESEM, Hitachi S-550N, Japan). Element analyses were carried out by using energy dispersive X-ray spectra (EDX) equipped with FESEM. The porosity of the coating was measured by image analysis, and at least ten images per coating were taken. The microhardness of the coating was measured using a Vickers hardness tester with 100 g load with dwelling time of 10 s. Five points per sample were acquired randomly to obtain reliable data. Bonding strength of the coating was tested following the ASTM standard C633-01.

The tribological properties of the coatings were evaluated using a reciprocating-type ball-on-disc tribometer (JLTB-02, J&L Tech Co. Ltd., Korea). The tests were performed under a load of 3 N for 30 min at 18.6°C with a relative humidity of 70%. Steel balls (1Cr15) with a diameter of 6 mm were used as the counterparts. The coatings and balls were ultrasonically cleaned in acetone prior to the tests, and a new ball or a new position of the ball was used for each friction test. The friction coefficients and sliding time were automatically recorded during the tests. For each sample, the measurement was repeated three times. Electrochemical impedance spectroscopy (EIS) measurements were performed using a Solartron ModuLab system (2100A, UK). The tests were conducted in 3.5 wt.% NaCl solution at room temperature. AC signal of 10 mV and the frequency ranging from 100 kHz to 0.01 Hz were employed. Before the electrochemical measurement, the coating samples were immersed in an aerobic chamber containing 3.5 wt.% NaCl solution for 30 min. Each measurement was repeated three times.

3. Results and Discussion

Figure 1 shows the topographical morphology and cross section of the cold-sprayed coatings produced in this study. As can be seen from Figures 1(a) and 1(b), the pure Al coating and Al + SiO₂ coatings exhibited significantly different surface morphologies. For coating 0 (Figure 1(a)), particles on the top of the coating remained smooth features with only few very small carterers that were induced by debonding Al particles as indicated by white arrows. However, for the composite coating as shown in Figures 1(b)–1(d), the top surface of the coatings was much rougher. Many angular carterers can be observed as indicated by white arrows, which were due to the rebound of SiO₂ during the coating formation process. For better understanding the deposition features of the coatings, the cross-sectional views of the coatings are provided in Figures 1(e) and 1(f). Clearly, composite coating was much denser than pure Al coating as the rebound SiO₂ particles can tamp on the already deposited coating. For quantitative analysis, the porosity and SiO₂ content of different coatings are listed in Table 1. The composite coatings demonstrated much denser structure than the pure Al coating. In addition, from Table 1, it is also found that the SiO₂ content in the coating was lower than that in the original feedstock. Such difference became even larger as the SiO₂ content in the feedstock increased. This fact suggests that a large amount of SiO₂ particles will rebound during the deposition process.

Figure 2 shows the typical XRD spectra of the coatings and the EDS mapping of the composite coating named as coating 40. As can be seen from the XRD spectra, all coatings experienced no oxidation during the deposition process, which clearly indicates the advances of cold spray in producing oxide-free coatings. In addition, as the SiO₂ content reduced significantly during the deposition process, no SiO₂ peaks were detected in the composite coatings. However, from the EDS mapping as shown in Figures 2(b)–2(d), the Si phase was clearly seen in the coating, which indicates the existence of SiO₂ in the coating. Also, the SiO₂ phase was found to be uniformly distributed in the coating.

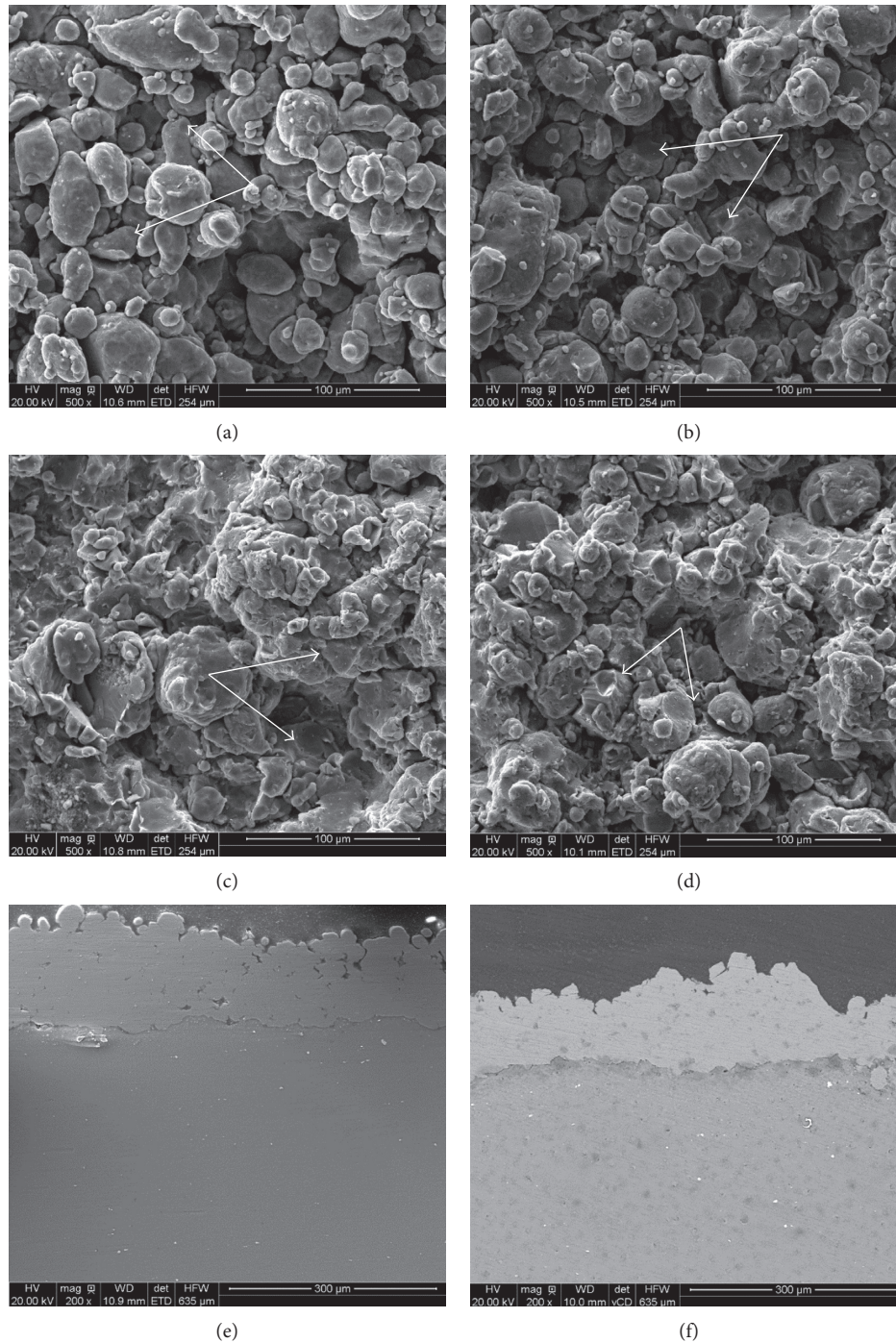


FIGURE 1: The surface morphologies of the as-sprayed coating 0 (a), coating 10 (b), coating 20 (c), and coating 40 (d) and the cross-sectional morphologies of coating 0 (e) and the composite coating 40 (f).

TABLE 1: Porosity and SiO_2 content of the coatings.

Sample	Coating porosity (%)	SiO_2 content (%)
Coating 0	5.11 ± 1.39	0
Coating 10	1.23 ± 0.45	8.98 ± 0.97
Coating 20	1.33 ± 0.70	11.46 ± 1.85
Coating 40	0.77 ± 0.19	15.75 ± 1.37

As for the coating properties, Figure 3 shows the microhardness and adhesion strength of different coatings. It is clearly seen from Figure 3(a) that coating microhardness increased gradually as the SiO_2 content increased. The reason for this phenomenon is the increased hard-phase reinforcement. On the one hand, SiO_2 itself is much harder than Al matrix; higher SiO_2 content certainly led to higher hardness. On the other hand, increased reinforcement helped to compact the coating and resulted in more work-hardening

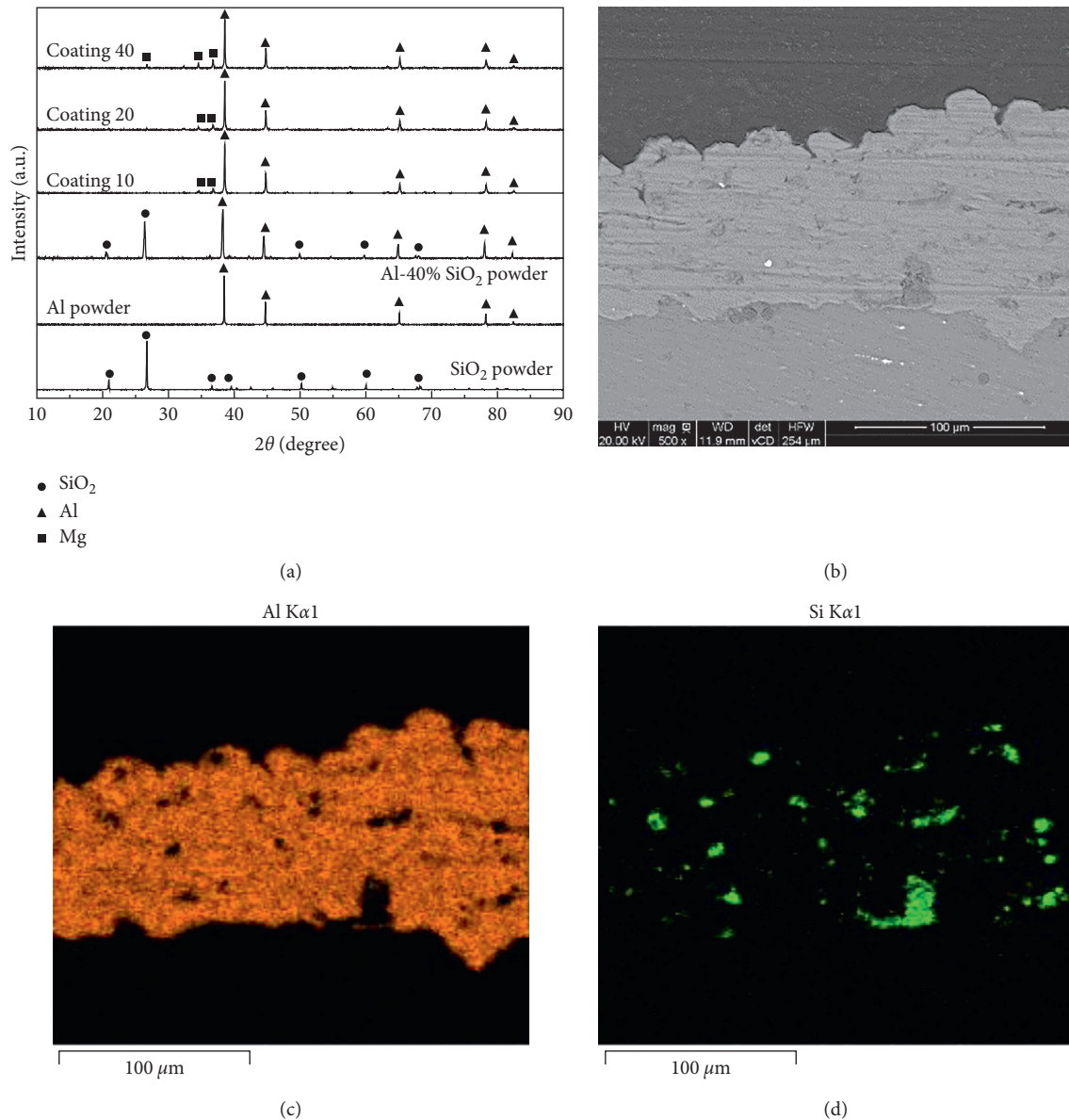


FIGURE 2: XRD spectra of the powders and the coatings (a) and the typical EDS mapping analysis of the composite coating named as coating 40 (b–d).

effect. Moreover, in Figure 3(b), the adhesion strength of the coating was also found to increase with increasing SiO₂ content. This may also be attributed to the compacting effect of the hard SiO₂ phase. Increased SiO₂ content resulted in the reduction of pores and defects, hence increasing the adhesion strength. Another possible explanation contributing to the increase of the adhesion strength could be the anchor effect of the ceramic particles [23]. However, the interface between the coatings and the substrates did not present significant difference as a function of the ceramic content in the coatings in this investigation. Therefore, the increase of the adhesion strength of the coatings is mainly attributed to the compacting effect of the ceramic particles. The surface roughness of the substrate also influences the adhesion strength of the coating [24, 25], which would be investigated in the next study.

The tribological behavior of the coating was also investigated. Figure 4 shows the friction coefficient and wear weight loss of different coatings. It is seen that the friction coefficients of the cold-sprayed coatings were higher as compared with those of the substrate (Figure 4(a)), which may be due to the interior defects and ceramic particles [26–28]. However, it seems that the pure coating and composite coatings had no significant difference in friction coefficient. Furthermore, the weight loss of different coatings as shown in Figure 4(b) indicates that the composite coatings had less weight loss than the pure Al coating, which clearly demonstrates the wear resistance capability of the Al + SiO₂ composite coatings. For better understanding the wear mechanism, the morphology of the wear surface of the coatings is shown in Figure 5. In Figure 5(a) and 5(b), the

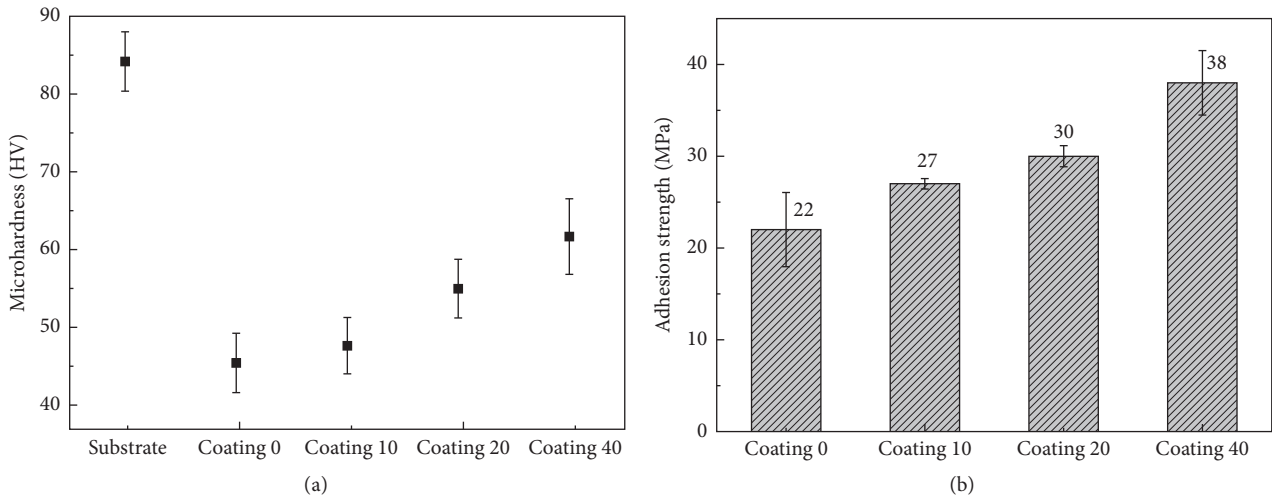


FIGURE 3: Microhardness (a) and adhesion strength (b) of the coatings.

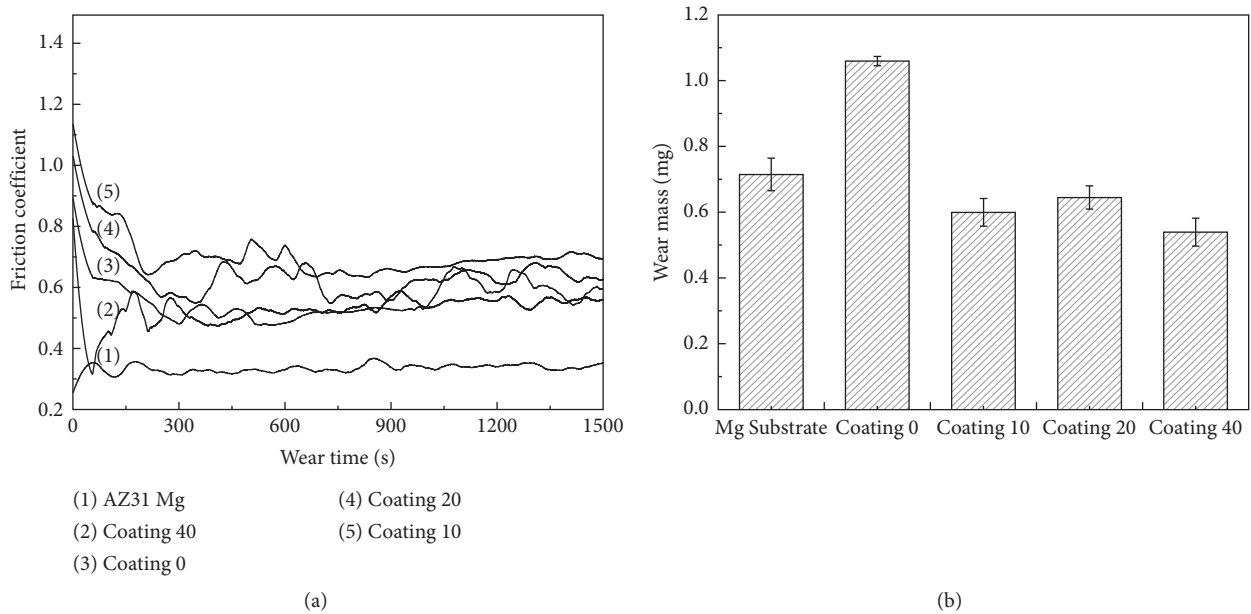


FIGURE 4: Friction coefficient (a) and wear mass (b) of the substrate and the coatings.

severe delamination of the substrate material and pure Al coating was observed, indicating the serious wear. However, for the Al + SiO₂ composite coatings, plough and extrusion characterization were found on the wear surface without obvious material delamination phenomenon. This explains why the weight loss of the composite coatings was smaller than that of the pure Al coating and substrate.

The corrosion behavior of the composite coating was also evaluated by potentiodynamic polarization technique. Figure 6 shows the polarization curves, corrosion potential, and corrosion current density of the different coatings. As can be seen, the current density of the composite coating is much lower than that of the Mg alloy substrate. The corrosion potential of the composite coating shifts toward positive. Both results suggest that Al + SiO₂ composite coating had better corrosion

resistance. Moreover, it is also found that the corrosion current density of the composite coating presents a decreasing trend as the ceramic content of the coating increases. The corrosion potential also shifts to positive with the increase of the ceramic content in the composite coating. The increase of the corrosion resistance of the composite coating with a higher ceramic content could be attributed to the decrease of the coating porosity. As shown in Table 1, the porosity of the coating decreases as the ceramic content in the composite coating increases.

4. Conclusions

For preventing Mg alloy from serious corrosion, Al and Al + SiO₂ composite coatings were fabricated on the AZ31

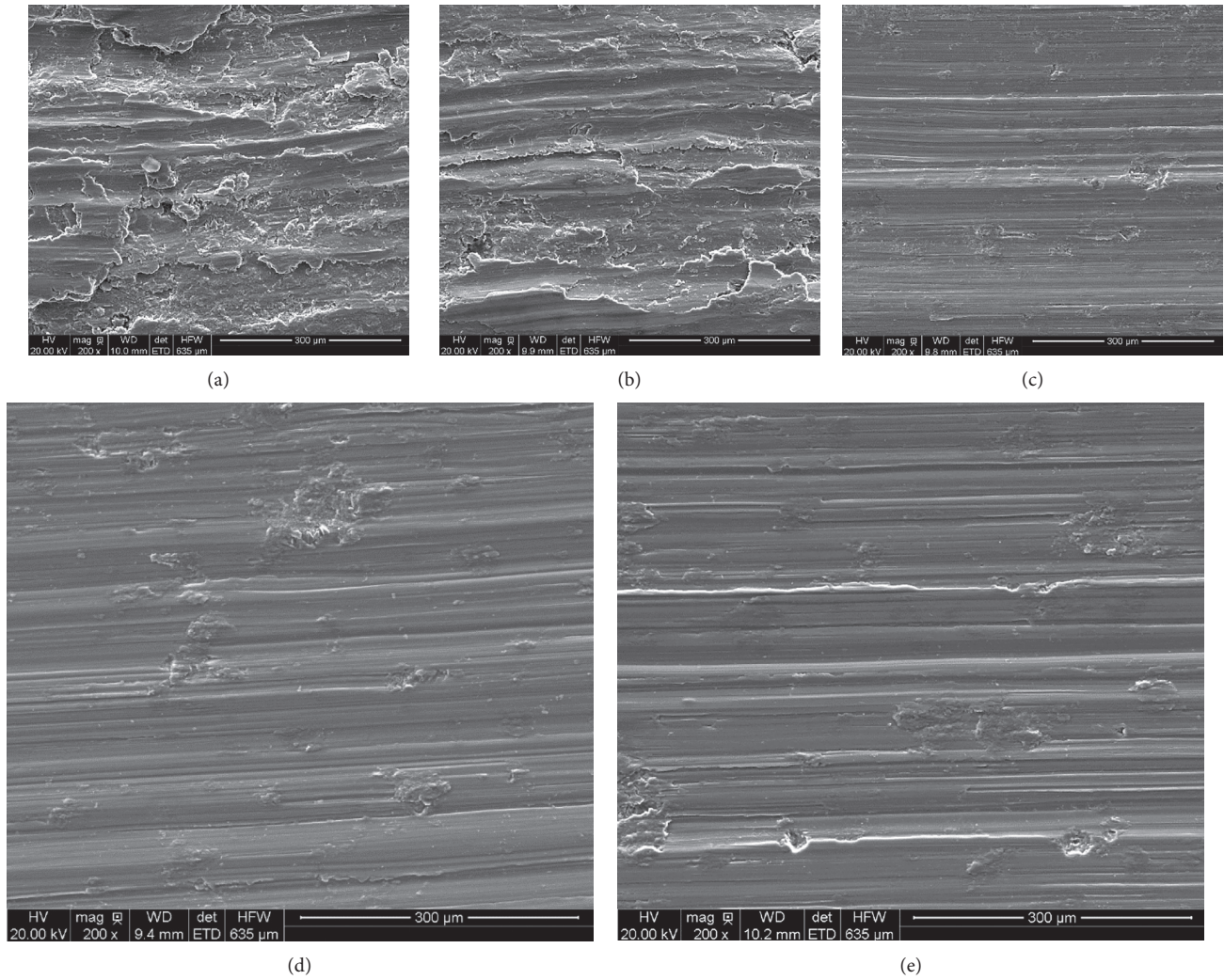
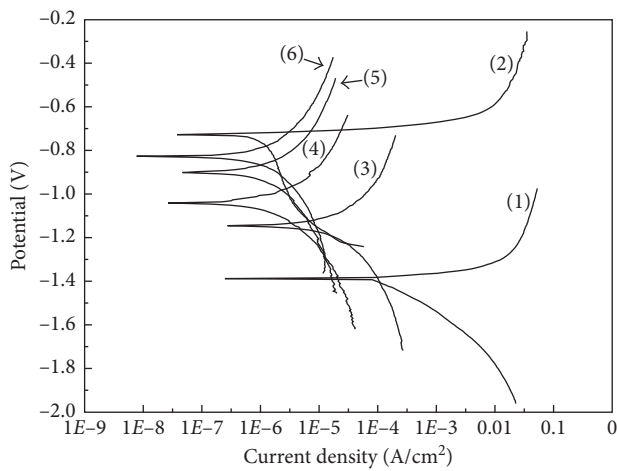


FIGURE 5: The typical wear track of the AZ31 magnesium alloy substrate (a), coating 0 (b), coating 10 (c), coating 20 (d), and coating 40 (e).



- (1) AZ31
- (2) Bulk Al
- (3) Coating 0
- (4) Coating 10
- (5) Coating 20
- (6) Coating 40

Samples	Corrosion potential (E_{corr}) (V/SCE)	Corrosion current density (I_{corr}) (A/cm^2)
AZ31 substrate	-1.387	8.796×10^{-5}
Bulk pure Al	-0.7276	7.335×10^{-7}
Coating 0	-1.146	5.79×10^{-6}
Coating 10	-1.04	6.66×10^{-7}
Coating 20	-0.9	6.04×10^{-7}
Coating 40	-0.826	4.87×10^{-7}

(a)

(b)

FIGURE 6: Potentiodynamic polarization curves and electrochemical characteristics of the substrates and the coatings.

magnesium alloy substrate by cold spraying. The results suggest that the Al-SiO₂ composite coatings had higher performances than the pure Al coating. The composite coatings showed higher density, microhardness, bonding strength, wear resistance, and corrosion resistance. The content of SiO₂ particles in the coatings had no significant effects on the coating properties. Moreover, SiO₂ was found to significantly reduce in the coatings as compared with that in the feedstock due to the rebounding during the deposition. With the addition of SiO₂ particles, the wear mechanism transfers from adhesive wear to abrasive wear.

Conflicts of Interest

The authors declare that they have no conflicts of interest.

Acknowledgments

This study was supported by the Natural Science Foundation of China (21705158), Fundamental Research Project of Qinghai Province (2016ZJ757), Project of Scientific Innovation Team of Ningbo (2015B11050), National Key Research and Development Program of Zhejiang Province (2015C01036), International Scientific and Technological Cooperation Project of Ningbo (2016D10012), and 3315 Program of Ningbo.

References

- [1] C. Christoglou, N. Voudouris, G. N. Angelopoulos, M. Pant, and W. Dahl, "Deposition of aluminium on magnesium by a CVD process," *Surface and Coatings Technology*, vol. 184, no. 2-3, pp. 149–155, 2004.
- [2] C. S. Lin and W. J. Li, "Corrosion resistance of cerium-conversion coated AZ31 magnesium alloys in cerium nitrate solutions," *Materials Transactions*, vol. 47, no. 4, pp. 1020–1025, 2006.
- [3] Z. Shao, Z. Cai, and J. Shi, "Preparation and performance of electroless nickel on AZ91D magnesium alloy," *Materials and Manufacturing Processes*, vol. 31, no. 9, pp. 1238–1245, 2015.
- [4] R. F. Zhang and S. F. Zhang, "Formation of micro-arc oxidation coatings on AZ91HP magnesium alloys," *Corrosion Science*, vol. 51, no. 12, pp. 2820–2825, 2009.
- [5] X. Zhong, Q. Li, B. Chen, J. Wang, J. Hu, and W. Hu, "Effect of sintering temperature on corrosion properties of sol-gel based Al₂O₃ coatings on pre-treated AZ91D magnesium alloy," *Corrosion Science*, vol. 51, no. 12, pp. 2950–2958, 2009.
- [6] H. Altun and S. Sen, "The effect of DC magnetron sputtering AlN coatings on the corrosion behaviour of magnesium alloys," *Surface and Coatings Technology*, vol. 197, no. 2-3, pp. 193–200, 2005.
- [7] M. Carboneras, M. D. López, P. Rodrigo et al., "Corrosion behaviour of thermally sprayed Al and Al/SiCp composite coatings on ZE41 magnesium alloy in chloride medium," *Corrosion Science*, vol. 52, no. 3, pp. 761–768, 2010.
- [8] E. Irissou, J. G. Legoux, B. Arsenaault, and C. Moreau, "Investigation of Al-Al₂O₃ cold spray coating formation and properties," *Journal of Thermal Spray Technology*, vol. 16, no. 5-6, pp. 661–668, 2007.
- [9] Y. Tao, T. Xiong, C. Sun, H. Jin, H. Du, and T. Li, "Effect of α -Al₂O₃ on the properties of cold sprayed Al/ α -Al₂O₃ composite coatings on AZ91D magnesium alloy," *Applied Surface Science*, vol. 256, no. 1, pp. 261–266, 2009.
- [10] H. Y. Lee, S. H. Jung, S. Y. Lee, Y. H. You, and K. H. Ko, "Correlation between Al₂O₃ particles and interface of Al-Al₂O₃ coatings by cold spray," *Applied Surface Science*, vol. 252, no. 5, pp. 1891–1898, 2005.
- [11] H. Y. Lee, Y. H. Yu, Y. C. Lee, Y. P. Hong, and K. H. Ko, "Cold spray of SiC and Al₂O₃ with soft metal incorporation: a technical contribution," *Journal of Thermal Spray Technology*, vol. 13, no. 2, pp. 184–189, 2004.
- [12] A. Shkodkin, A. Kashirin, O. Klyuev, and T. Buzdygar, "Metal particle deposition stimulation by surface abrasive treatment in gas dynamic spraying," *Journal of Thermal Spray Technology*, vol. 15, no. 3, pp. 382–386, 2006.
- [13] Q. Wang, K. Spencer, N. Birbilis, and M. X. Zhang, "The influence of ceramic particles on bond strength of cold spray composite coatings on AZ91 alloy substrate," *Surface and Coatings Technology*, vol. 205, no. 1, pp. 50–56, 2010.
- [14] E. Sansoucy, P. Marcoux, L. Ajdelsztajn, and B. Jodoin, "Properties of SiC-reinforced aluminum alloy coatings produced by the cold gas dynamic spraying process," *Surface and Coatings Technology*, vol. 202, no. 16, pp. 3988–3996, 2008.
- [15] G. Eesley, A. Elmoursi, and N. Patel, "Thermal properties of kinetic spray Al-SiC metal-matrix composite," *Journal of Materials Research*, vol. 18, no. 4, pp. 855–860, 2003.
- [16] M. Yu, X. K. Suo, W. Y. Li, Y. Y. Wang, and H. L. Liao, "Microstructure, mechanical property and wear performance of cold sprayed Al5056/SiCp composite coatings: effect of reinforcement content," *Applied Surface Science*, vol. 289, pp. 188–196, 2014.
- [17] H. Lee and K. Ko, "Effect of SiC particle size on cold sprayed Al-SiC composite coatings," *Surface Engineering*, vol. 25, no. 8, pp. 606–611, 2013.
- [18] W. Y. Li, G. Zhang, H. L. Liao, and C. Coddet, "Characterizations of cold sprayed TiN particle reinforced Al2319 composite coating," *Journal of Materials Processing Technology*, vol. 202, no. 1–3, pp. 508–513, 2008.
- [19] W. Y. Li, G. Zhang, C. Zhang, O. Elkedim, H. Liao, and C. Coddet, "Effect of ball milling of feedstock powder on microstructure and properties of TiN particle-reinforced Al alloy-based composites fabricated by cold spraying," *Journal of Thermal Spray Technology*, vol. 17, no. 3, pp. 316–322, 2008.
- [20] T. H. Van Steenkiste, J. R. Smith, and R. E. Teets, "Aluminum coatings via kinetic spray with relatively large powder particles," *Surface and Coatings Technology*, vol. 154, pp. 237–252, 2002.
- [21] E. Irissou, J. G. Legoux, A. N. Ryabinin, B. Jodoin, and C. Moreau, "Review on cold spray process and technology: part I-intellectual property," *Journal of Thermal Spray Technology*, vol. 17, no. 4, pp. 495–516, 2008.
- [22] S. Yin, Y. C. Xie, J. Cizek et al., "Advanced diamond-reinforced metal matrix composites via cold spray: properties and deposition mechanism," *Composites Part B-Engineering*, vol. 113, pp. 44–54, 2017.
- [23] M. Yu, W. Y. Li, X. K. Suo, and H. L. Liao, "Effects of gas temperature and ceramic particle content on microstructure and microhardness of cold sprayed SiCp/Al 5056 composite coatings," *Surface and Coatings Technology*, vol. 220, pp. 102–106, 2013.
- [24] W. Sun, A. W. Y. Tan, I. Marinescu, E. J. Liu, and ASME, *Effects of Surface Roughness on Bonding Behavior of Cold Spray Ti6AL4V Coatings*, American Society of Mechanical Engineers, New York, NY, USA, 2017.
- [25] S. Kumar, G. Bae, and C. Lee, "Influence of substrate roughness on bonding mechanism in cold spray," *Surface and Coatings Technology*, vol. 304, pp. 592–605, 2016.

- [26] Y. S. Zoo, J. W. An, D. P. Lim, and D. S. Lim, "Effect of carbon nanotube addition on tribological behavior of UHMWPE," *Tribology Letters*, vol. 16, no. 4, pp. 305–309, 2004.
- [27] R. G. Kelly, J. R. Scully, D. W. Shoesmith, and R. G. Buchheit, "Electrochemical techniques in corrosion science and engineering," *Chemphyschem*, vol. 4, pp. 296–298, 2003.
- [28] S. T. Aruna, V. Ezhil Selvi, V. K. William Grips, and K. S. Rajam, "Corrosion- and wear-resistant properties of Ni-Al₂O₃ composite coatings containing various forms of alumina," *Journal of Applied Electrochemistry*, vol. 41, no. 4, pp. 461–468, 2011.

Research Article

Deposition of Coating to Protect Waste Water Reservoir in Acidic Solution by Arc Thermal Spray Process

Han-Seung Lee,¹ Jin-ho Park,¹ Jitendra Kumar Singh ¹ and Mohamed A. Ismail²

¹Department of Architectural Engineering, Hanyang University, 1271 Sa 3-dong, Sangrok-gu, Ansan 15588, Republic of Korea

²Department of Civil and Construction Engineering, Faculty of Engineering and Science, Curtin University Malaysia, CDT 250, 98009 Miri, Sarawak, Malaysia

Correspondence should be addressed to Jitendra Kumar Singh; jk200386@hanyang.ac.kr

Received 30 January 2018; Accepted 29 March 2018; Published 23 April 2018

Academic Editor: Jan Cizek

Copyright © 2018 Han-Seung Lee et al. This is an open access article distributed under the Creative Commons Attribution License, which permits unrestricted use, distribution, and reproduction in any medium, provided the original work is properly cited.

The corrosion characteristics of 304 stainless steel (SS) and titanium (Ti) coatings deposited by the arc thermal spray process in pH 4 solution were assessed. The Ti-sprayed coating exhibits uniform, less porous, and adherent coating morphology compared to the SS-sprayed coating. The electrochemical study, that is, electrochemical impedance spectroscopy (EIS), revealed that as exposure periods to solution were increased, the polarization resistance (R_p) decreased and the charge transfer resistance (R_{ct}) increased owing to corrosion of the metallic surface and simultaneously at the same time the deposition of oxide films/corrosion on the SS-sprayed surface, while Ti coating transformed unstable oxides into the stable phase. Potentiodynamic studies confirmed that both sprayed coatings exhibited passive tendency attributed due to the deposition of corrosion products on SS samples, whereas the Ti-sprayed sample formed passive oxide films. The Ti coating reduced the corrosion rate by more than six times compared to the SS coating after 312 h of exposure to sulfuric acid- (H_2SO_4 -) contaminated water solution, that is, pH 4. Scanning electron microscope (SEM) results confirmed the uniform and globular morphology of the passive film on the Ti coating resulting in reduced corrosion. On the other hand, the corrosion products formed on SS-sprayed coating exhibit micropores with a net-like microstructure. X-ray diffraction (XRD) revealed the presence of the composite oxide film on Ti-sprayed samples and lepidocrocite (γ -FeOOH) on the SS-coated surface. The transformation of TiO and Ti_3O into TiO_2 (rutile and anatase) and Ti_3O_5 after 312 h of exposure to H_2SO_4 acid reveals the improved corrosion resistance properties of Ti-sprayed coating.

1. Introduction

Concrete is a material that can withstand and sustain exposure to an aggressive environment over long periods and resist deterioration. Therefore, concrete is a reliable and durable construction material with versatile applications in waste water reservoirs, buildings, bridges, towers, roads, and so on. However, it is also a porous material, which means that aggressive ions such as Cl^- , CO_3^- , and SO_4^- can slowly or steadily penetrate and move toward the embedded steel rebar, thus causing corrosion that leads to premature concrete failure [1–3].

The major factor in concrete deterioration is acidic impurities in its surrounding [4]. Different external coatings have been applied to protect concrete and the embedded steel rebar. Swamy and Tanikawa used acrylic rubber as an

external coating material for concrete in accelerated wet-dry and saline environments [5]. They found that this coating withstood saline and ozone exposures but suffered extensive cracking when exposed to ultraviolet radiation. Therefore, polymeric coating is not suitable for concrete coating because of vast differences in the thermal contraction and expansion coefficients between the concrete and polymer.

The presence of sulfur-reducing bacteria in waste water makes it acidic [6, 7]. The minimum pH, that is, 4.5, of waste water can be obtained [8] depending on the source and environment where it is produced.

The acidity of waste water influences the deterioration of the concrete and steel rebar. Therefore, to protect these from corrosion, SS grouting and anchoring have been widely used [6, 7]. SS plates are used in waste water reservoirs to protect the concrete and embedded steel rebar. But cost factors are

affecting the use of such steel plates on the outer surface of concrete. Nonetheless, SS plates and other protective methods or surface treatments are frequently used to protect the concrete and waste water reservoirs owing to their high resistance to corrosion [9]. Also, the nanostructured and PVD coatings were used in high-speed drilling and cutting instruments to enhance the mechanical properties of tools [10, 11].

A method to deposit coatings onto the concrete surface is an important factor in the deposition of high melting point corrosion-resistant metals. One view is that the coating process should be considered for deposition on account of its feasibility and applicability. High corrosion-resistant materials such as SS, nickel (Ni), tungsten (W), molybdenum (Mo), chromium (Cr), and Ti need a specific deposition process. The arc thermal spray process is suitable and feasible for depositing these metals onto any substrate [12–17].

The arc thermal spray process is an easy process for the deposition of coatings onto concrete and steel substrates. This process involves arc spraying with twin metal wires on oppositely charged tips that use atomized hot air to deposit the coating onto the substrate [12]. During the coating process, melted metal droplets are deposited and form a thick layer on the substrate. During coating deposition, pores/defects are formed, which is an inherent property of the arc thermal spray process [13–15]. Pore formation depends on the metal to be used and spraying parameters of the process.

Our recently published paper showed that the 316L SS coating applied on the concrete substrate, and then sealed with alkyl epoxide, effectively protected the surface from corrosion in pH 4, 5, and 6 solutions. The most destructive was the pH 4 solution because of its higher acidity compared with the other solutions [16]. In the pH 5 solution, the tested coatings exhibited the highest corrosion resistance because of the presence of undissociated water molecules that formed a protective passive film on the coating surface. This experiment was carried out for instantaneous exposure; there is currently no study on prolonged exposure.

The pH 4 solution is an aggressive environment, and the surface is expected to deteriorate dramatically. This pH solution increases the risk of corrosion due to its more acidic nature. If a coating can withstand this pH, then it can extend the protection of a waste water reservoir against corrosion.

The present investigation aims to protect the concrete of a waste water reservoir from deterioration, spalling, and thawing during prolonged exposure to an acidic environment using surface treatment with 304 SS and Ti metallic coatings by an arc thermal spray process. This communication is an advancement of our earlier published work [16]. The acidic condition was simulated by mixing 0.1 M- H_2SO_4 (pH = 1) in distilled water to reduce the pH of distilled water from 6.5 to 4.0 at 25°C. Assessments of the corrosion resistance of these coatings were carried out using different electrochemical techniques.

2. Experimental Section

2.1. Process of Coating. The 304 SS and Ti coatings were applied to grit-blasted mild steel containing carbon (C) = 0.24,

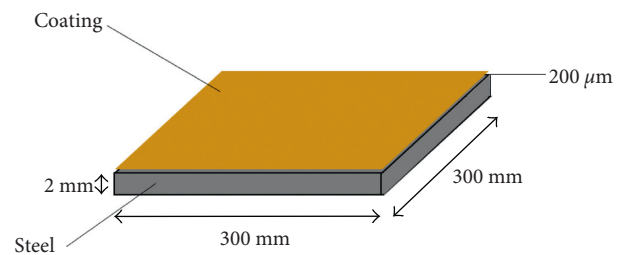


FIGURE 1: Sketch of coating applied on the steel substrate.

silicon (Si) = 0.26, manganese (Mn) = 0.95, phosphorus (P) = 0.016, sulfur (S) = 0.008, copper (Cu) = 0.02, chromium (Cr) = 0.04, nickel (Ni) = 0.03, and iron (Fe) = balance (wt.%) and to concrete substrates by an arc thermal spray process. The coating deposited onto the steel substrate was used to study its electrochemical and physical characteristics as shown in Figure 1, while the coating deposited onto the concrete surface was used for bond adhesion measurement.

Concrete is a low-conducting material that cannot be used for electrochemical studies. Hence, it was not considered for electrochemical studies. A 1.6 mm diameter wire of 304 SS and commercially pure Ti was used for metal spraying in the arc thermal spraying process to deposit the coatings onto the substrates.

Prior to the deposition of coatings, the steel substrate was pickled with 10% v/v HCl, thoroughly washed with distilled water, dried, and finally grit-blasted with 0.7 and 0.8 mm steel balls using a pressure machine at 0.7 MPa. Coating thickness was measured using a nondestructive Elcometer 456 dry film thickness gauge at different locations on the steel and concrete substrate; the thickness was approximately 200 μm ($\pm 5 \mu\text{m}$).

The coatings were applied to the substrate by the arc thermal spray gun (LD/U3 electric arc wire spray gun, Oerlikon MetcoTM, Switzerland) process using 304 SS and Ti wires with a circular slit of hot and compressed air [17–20]. The melted metal particles diffused onto the substrate and cooled at room temperature, resulting in the formation of pores/defects on the coating.

The spraying of metallic coating on the target substrate was carried out by keeping the sample 20 cm away from the spray gun at an air pressure of 6 bar. The spraying voltage and current were maintained at approximately 30 V and 200 mA, respectively [15, 21–23].

After applying the coating on the concrete substrate, coating adhesion was measured according to the KS F4716 test method [24]. In this process, a 300 mm \times 300 mm section of the coated substrate was taken for the adhesion test (Figure 1).

2.2. Electrochemical Experiments. Electrochemical experiments were carried out on the deposited coatings and 304 SS plate. For the sake of comparison with deposited coating, we have chosen to characterize the 304 SS plate.

To perform the electrochemical experiments, a solution was prepared in double distilled water by adding a few drops of 0.1 M- H_2SO_4 to reduce the pH to 4 at 25°C. These

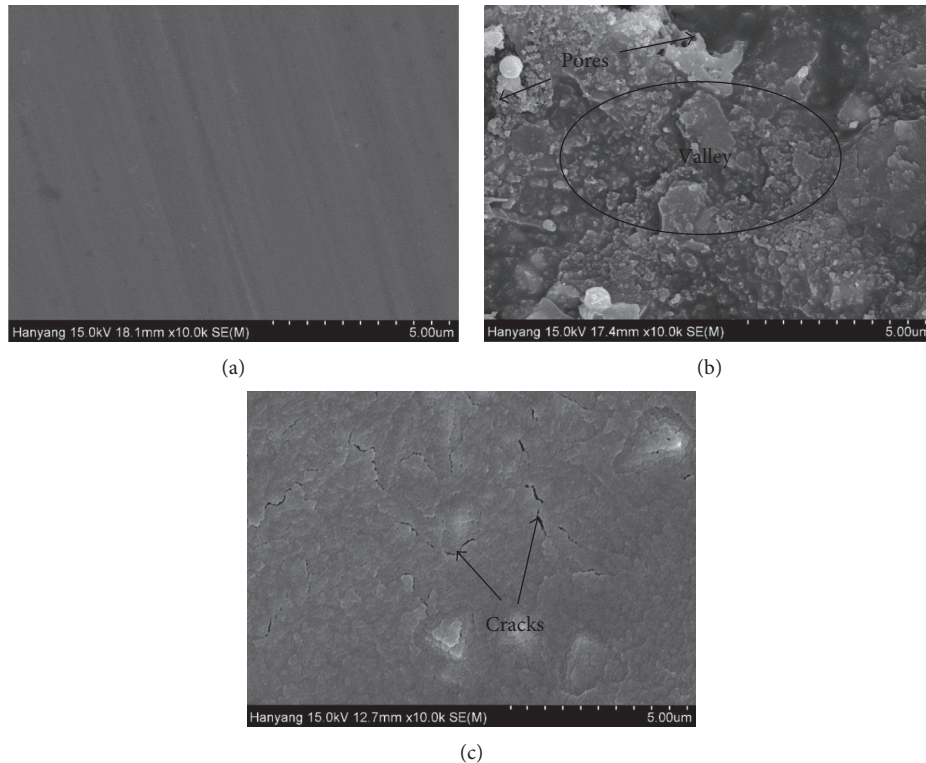


FIGURE 2: FE-SEM images of the (a) SS plate, (b) SS-sprayed surface, and (c) Ti-sprayed surface.

experiments were performed using three electrode systems [17], where the coating acted as the working electrode (WE), the platinum wire acted as the counterelectrode, and the silver/silver chloride (Ag/AgCl) acted as the reference electrode. The area of the WE was 0.78 cm^2 and was fixed for all the samples.

EIS experiments were carried out by changing the frequency of a 10 mV sinusoidal voltage from 100 kHz to 0.01 Hz. The potentiodynamic experiments were performed from -0.4 V to $+0.8 \text{ V}$ versus Ag/AgCl at 1 mV/s scan rate. The potentiostat used in this study was a VersaSTAT (Princeton Applied Research, Oak Ridge, TN, USA), and data analysis was carried out using the Metrohm Autolab Nova 1.10 software.

The 304 SS plate was abraded with an emery paper from $60 \mu\text{m}$ up to $300 \mu\text{m}$ to remove the native oxides from the surface prior to starting electrochemical experiments. All electrochemical experiments were conducted in triplicate at room temperature ($27 \pm 1^\circ\text{C}$) to generate reproducible data.

2.3. Characterization of Coating. The morphology of the deposited coatings and 304 SS plate was determined by an SEM (Philips XL 30) operated at 15 kV. Prior to taking the images of the samples, these were coated with platinum to increase their conductivity and avoid a charging effect.

XRD (Philips X'Pert-MPD) studies of the coatings and 304 SS plate were performed using Cu-K α radiation ($\lambda = 1.54059 \text{ \AA}$) generated at 40 kV and 100 mA. The scanning rate to scan XRD data from 10 to 90° was at $0.5^\circ/\text{min}$.

3. Results and Discussion

3.1. Adhesion Test of Sprayed Coatings. Adhesion measurements were carried out after deposition of coatings onto the concrete surface by arc thermal spraying. This was measured for four samples, and the average was calculated. The average adhesion values of 304 SS- and Ti-sprayed surfaces were 3.39 and 2.72 MPa, respectively. The SS-sprayed coating exhibits higher adhesion values than Ti-sprayed coating. The standard deviation of SS- and Ti-sprayed coating was calculated, and these were 0.40 and 0.24 MPa, respectively. This indicates that SS coating adhered strongly to the concrete surface, whereas Ti-sprayed coating adhered 1.25 times lesser than the 304 SS coating. The higher adhesion values of the SS coating may be attributed to small interfacial separation between the concrete substrate and metallic particles, while that for Ti was large [25].

3.2. Morphology of SS Plate and Sprayed Coating. The morphologies of the 304 SS plate and deposited coatings on the mild steel substrate were characterized by SEM. Figure 2 shows the SEM images of the deposited coatings and 304 SS plate. The SS plate surface exhibited a smooth and very finely scratched line (Figure 2(a)), while the deposited coatings had many cracks and defects over the surfaces (Figures 2(b) and (c)).

The scratched line on the plate surface was caused by abrasion with an emery paper up to $300 \mu\text{m}$ because this grade of the emery paper is hard and makes some fine

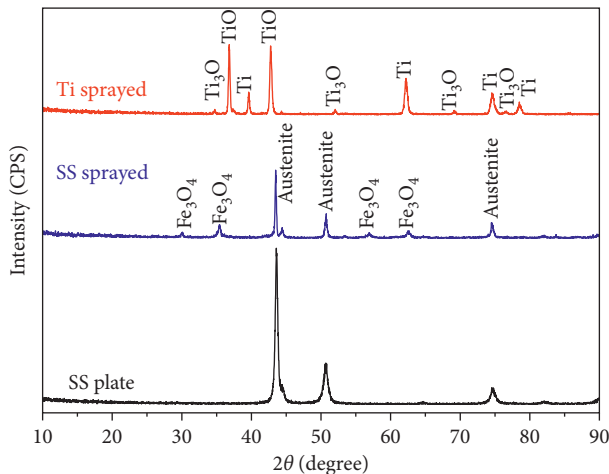


FIGURE 3: XRD of the SS plate and sprayed coatings by the arc thermal spray process ($0.5^\circ/\text{min}$).

defects/lines on the surface. The SS-sprayed surface showed coagulated valleys and uneven deposition, while the Ti-sprayed surface showed uniform, nanosized globular, and fine elongated cracks. The fine cracks on the Ti-sprayed surface might be due to formation of thin and nanoscaled brittle oxides. The morphology of SS-sprayed coating can be attributed due to the sudden cooling of melted metal particles at room temperature ($27 \pm 1^\circ\text{C}$).

The microstructure of the SS-sprayed coating (Figure 2(b)) could allow the deposition of aggressive ions, water, and moisture particles on valleys, which cause localized or crevice corrosion. The Ti-sprayed coating also exhibited fine cracking on the surface but had little influence on the deposition of water molecules. Owing to the smooth microstructure of the Ti coating, water molecules may slide off the surface.

3.3. Phase Identification of SS Plate and Sprayed Coatings by XRD. XRD was performed to determine the phases present in the coatings and plate surfaces. The results are plotted between $2\theta = 10^\circ$ and 90° versus intensity in counts per second (CPS) and shown in Figure 3. The SS plate and sprayed surfaces exhibited the austenite phase of the Fe-Cr-Ni alloy, that is, 304 SS [26, 27]. Besides this phase in the SS-sprayed surface, magnetite (Fe_3O_4) is also observed, and it is due to the partial oxidation of coating during the spraying process.

XRD of Ti-sprayed coating showed Ti [28] and two oxides such as TiO and Ti_3O_5 , which were formed due to higher melting point of it than SS where there are possibilities to oxidize the deposited coating. The another reason to oxidize the Ti is high affinity of it with atmospheric oxygen and thus to form surface oxide films such as TiO or Ti_3O_5 . The formation of these two oxides of Ti in open atmosphere has also been reported by other researchers [29, 30]. However, these oxides are amorphous, brittle, and unstable in in vivo conditions which easily can be removed simply by brushing with soft tissues [31–33].

3.4. Electrochemical Studies of SS Plate and Sprayed Coating in pH 4 Solution

3.4.1. EIS Studies. The samples were immersed in pH 4 solution for different periods of exposure. EIS was carried out to study their corrosion characteristics. These results are shown in Figures 4 and 5. The electrical equivalent circuit (EEC) is shown in the corresponding Nyquist plots. The EEC of the SS plate exposed to the pH 4 solution for 1 h is shown in Figure 4(a). In the Nyquist plot of the SS plate, the sample after 1 h of exposure is differentiated by two depressed semicircle loops such as one at high while another at the lower studied frequency. For more clarity of plots at high frequency, the Nyquist result of samples is shown in Figure S1 (supplementary figure). These results can be explained either by the heterogeneity of the solid surface or by the dispersion of some physical properties. The interface of the surface cannot be considered as an ideal capacitor due to heterogeneity of the surface, and it may involve a constant-phase element (CPE) as a substitute of the ideal capacitor. The first EEC consists of the solution resistance (R_s), polarization resistance (R_p), and CPE1 due to the metal surface and nonideal double-layer capacitance behaviour [34–36]. The R_p and CPE1 are parallel to each other. However, the second EEC contains the charge transfer resistance (R_{ct}) and CPE2. The formation of R_{ct} may be due to formation of the protective passive layer on the SS plate surface in acidic pH solution after 1 h of exposure. These two EECs are connected in series to each other.

The EECs for the SS- and Ti-sprayed coating systems are somewhat different from the SS plate, and they are inserted in Figure 4(a). The different EECs for these coatings may be attributed to the inherent property of the arc thermal spray process, where coatings suffer from surface defects. Due to reaction on the metal surface, R_{ct} participated owing to initiation of the corrosion process in acidic pH solution. The reaction on the metal surface caused by R_{ct} led to the formation of a passive/oxide layer on the metal surface, which increased the resistance and reduced the corrosion reaction. The CPE1 due to a nonideal behaviour of the coating surface and R_p are parallel to each other, while another EEC is connected in series to R_p which contains CPE2 and R_{ct} [15]. The CPE2 and R_{ct} are parallel to each other.

The Nyquist plots reveal the real characteristics of the samples after 1 h of exposure (Figure 4(a)). The samples were exposed to the solution for 1 h to stabilize the potential; thereafter, EIS measurements were performed.

Figure 4(a) shows the two semicircle loops in the Nyquist plots exhibited by coated samples. The SS- and Ti-sprayed coatings show zigzag and scattered plots which might be due to low conductivity of electrolytes, deposition of defective coating, formation of a defective passive film, and the presence of more resistive elements such as Ti in Ti-sprayed coating while Cr and Ni in SS-sprayed samples [37–40]. These results are attributed to the fact that both sprayed samples exhibit capacitive properties due to the presence of defects. However, the Ti coating imposed a resistance greater than the SS coating due to the formation of a passive/oxide film with capacitive behaviour which enabled surface resistance to penetrate the ions of the acidic solution.

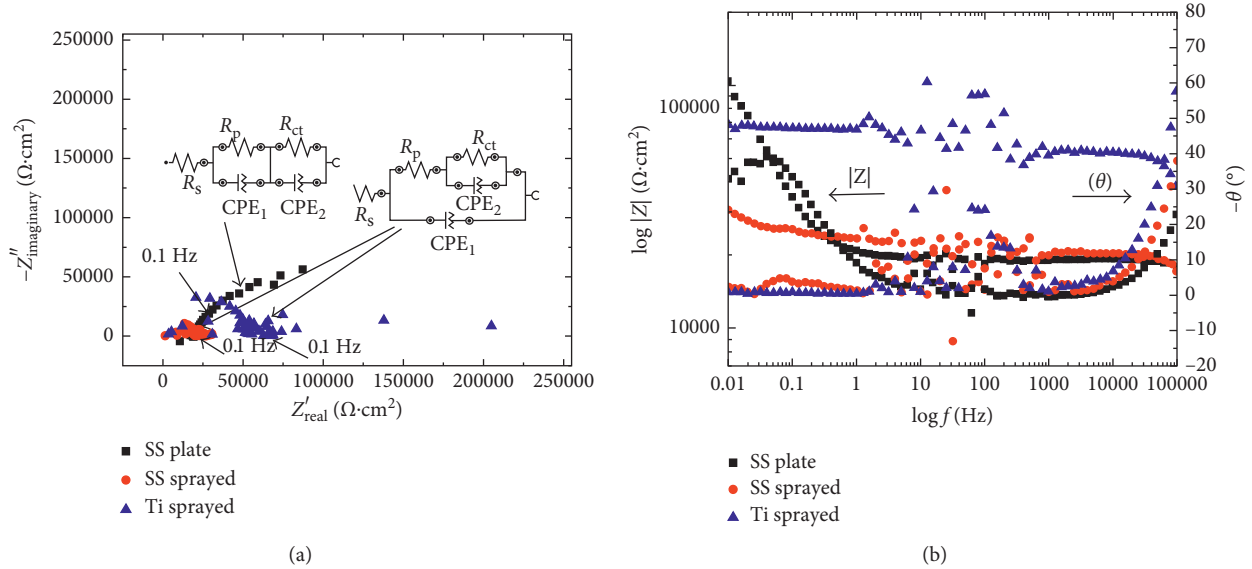


FIGURE 4: Impedance spectra: (a) Nyquist and (b) Bode $|Z|$ and (θ) of the SS plate and sprayed coatings in pH 4 solution after 1 h of exposure (100 kHz to 0.01 Hz).

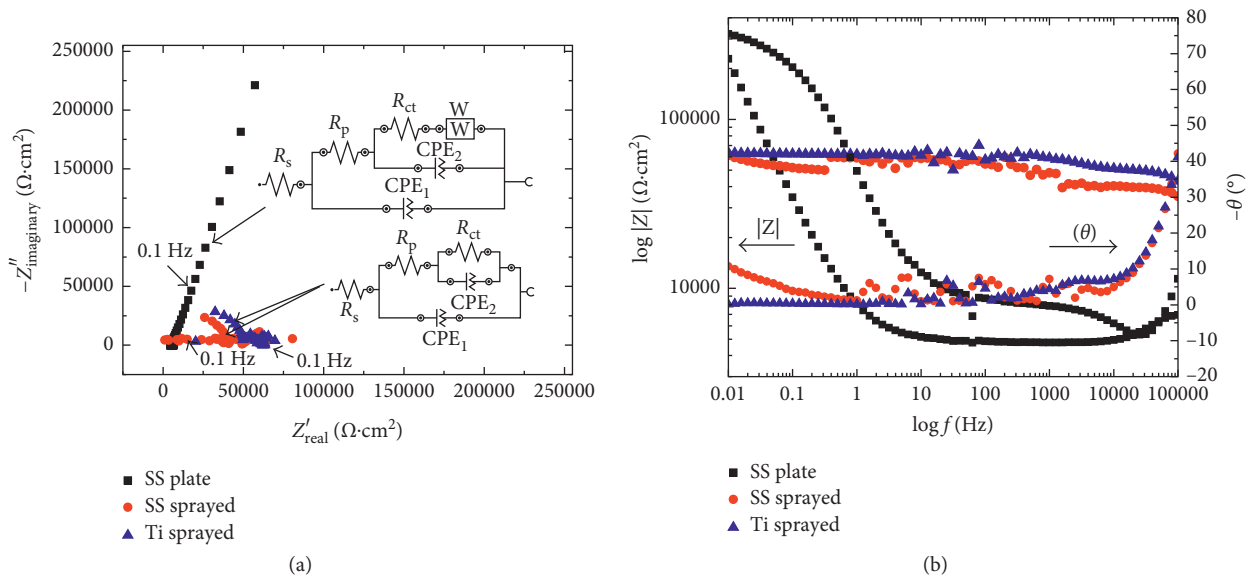


FIGURE 5: Impedance spectra: (a) Nyquist and (b) Bode $|Z|$ and (θ) of the SS plate and sprayed coatings in pH 4 solution after 312 h of exposure (100 kHz to 0.01 Hz).

In the sulfuric acid solution, the Ti surface tends to form defective passive films with high resistance. Similar results have been observed by Baron et al. on TiAlV and TiAlNb alloys in Tyrode’s solution [41].

The dimensions of the semicircle loop of SS plate samples clearly show high capacitive property that enables the surface to resist the penetration of the solution. The capacitive property of the passive film on the SS plate was attributed to the formation of Cr-enriched oxide and NiO in the H_2SO_4 -contaminated water solution [42].

The dimensions of the semicircle loops of SS- and Ti-sprayed coatings were less than those of the SS plate because the sprayed samples were more susceptible to corrosion,

owing to the formation of defects/pores on the coating surface in the solution after 1 h of exposure.

The impedance at low frequency (0.01 Hz) and the phase $\theta (^{\circ})$ of Bode plots were plotted against $\log |Z| (\Omega \cdot \text{cm}^2)$ versus $\log f (\text{Hz})$ and $\theta (^{\circ})$ versus $\log f (\text{Hz})$ in Figure 4(b), respectively. The impedance values of the SS plate sample were greater than those of the SS and Ti coatings. The SS coating exhibited lower impedance values because of the presence of more defects/pores at locations where the chances of penetration by the acidic solution are high, and this initiated the deterioration of the coating.

From the $\log |Z| (\Omega \cdot \text{cm}^2)$ - $\log f (\text{Hz})$ Bode plots (Figure 4(b)), it can be seen that, at high frequency (100 kHz), resistance was

moreover identical to that observed at low frequency, that is, 0.01 Hz, which might be attributed to the low conductivity of acidic pH solution.

In this study, the solution was prepared by adding a few drops of 0.1 M-H₂SO₄ to distilled water. The solution conductivity was very low, which caused the resistance in total impedance. The conductivity of the solution is an important parameter that must be considered in electrochemical studies. However, the Ti coating exhibited higher impedance than the SS coating due to formation of a thick and protective passive oxide film. The low impedance values of the sprayed samples are due to the presence of more defects or less interfacial resistance between the splats of coating than on the SS plate sample.

The surface finish and coating microstructure play an important role to determine the corrosion resistance properties of materials in the solution. The pH 4 solution is very aggressive and causes localized or pitting corrosion of the oxide films formed during exposure [43–45].

The defective parts of coatings can function as an anode, while the remaining acts as a cathode, resulting in the formation of microgalvanic cells on the surface. The presence of microgalvanic cells enhances the corrosion rate of materials; thus, there is a chance of getting low impedance. Such observations are found in SS- and Ti-sprayed coatings. In view of the above, it can be observed that the SS coating exhibited valley-type deposits (Figure 2(b)) where the acidic solution could stagnant/deposit and cause localized and crevice corrosion. During the initial period of exposure, both sprayed coatings had defects that resulted in lower impedance values than the SS plate surface.

The SS plate shows a -40° shift of the phase angle maxima at the lower studied frequency and reveals high resistance to corrosion in the pH 4 solution (Figure 4(b)). On the other hand, Ti and SS coatings exhibited -1° and -2° shifts, respectively, which indicate their susceptibility to corrosion during the initial period of exposure [37]. In the middle frequency range, the samples exhibited scattering which might be due to the capacitive response of the defective passive film that was formed during exposure of the samples to H₂SO₄ solution [38–40].

The shifting of maxima at the higher studied frequency (100 kHz) is due to the deposition of corrosion products on the SS-sprayed sample, whereas on the Ti-coated sample, it is due to formation of the resistive passive film. It can be seen that the Ti coating exhibited approximately -57° shift followed by the SS coating at -38° , while the SS plate had the lowest shift at -23° . These results indicate that the Ti-sprayed surface formed a protective passive film owing to reaction at the coating/solution interface. Thus, the Ti coating exhibited higher resistance to the acidic solution.

As the exposure periods were extended, the increased dimensions of semicircle loops in the Nyquist plots showed increased corrosion resistance [46]. The bigger loops in the Nyquist plots reveal high resistance to corrosion in any environment. Such results can be seen from Figure 5(a) after 312 h of exposure to pH 4 solution. The EEC for the SS plate after 312 h of exposure is inserted in Figure 5(a). The Warburg impedance (W) is caused by diffusion of the

protective passive layer on the SS plate surface in the H₂SO₄-contaminated solution. R_{ct} and W are parallel to the CPE2 [16].

At longer periods of exposure (312 h), many parameters are involved owing to the complex reaction process on the metal/solution interface.

All samples exhibited two loops in the Nyquist plots, one at higher and another at lower frequencies. The loops formed at higher and lower frequencies because of the solution resistance and the reaction at the metal/solution interface, respectively [47–51]. As the exposure period is increased, strengthening of the passive film on the SS plate may occur [52]. However, in case of Ti, there is a possibility of formation of the protective passive film due to transformation of unstable titanium oxides into stable oxides, while on SS-sprayed samples, it is due to deposition of corrosion products on the coating defects in H₂SO₄-contaminated water solution [53]. The two semicircle loops of Ti and SS coatings were successfully distinguished from each other for this exposure period. Therefore, the Ti coating had provided greater protection than the SS coating. These two diffused semicircle loops on sprayed coatings are not clearly seen because of the reduced conductivity of the solution and scattered data.

The dimensions of semicircle loops in the Nyquist plot of the Ti coating were bigger, indicating that the anodic surface area of the coating was decreased by the formation of the protective oxide film rather than SS coating. The SS plate had higher resistance to the H₂SO₄-contaminated solution owing to the formation of the protective passive film [42].

The SS plate surface exhibited the protective passive film that is resistant to corrosion because the values of both Z'_{real} and $-Z''_{imaginary}$ axes are increased (Figure 5(a)). From the initial to the prolonged exposure, the SS plate showed higher resistance to corrosion which can be attributed to the formation of compact and uniform passive layers [42].

On the other hand, the SS and Ti coatings showed less resistance to corrosion than the SS plate because of the formation of surface defects/cracks, which enhanced the corrosion rate due to penetration of aggressive solution. It can be seen from Figure 5(a) that the SS and Ti coatings exhibit diffused semicircle loops separated by two small loops.

The bigger loop shifted toward $Z''_{imaginary}$ because of the formation of the capacitive passive film/corrosion products. The lower frequency loop shifted toward Z'_{real} of the Nyquist plots (Figure 5(a)) because of the increased resistance to corrosion.

The nature of corrosion products/passive films plays a major role in controlling the corrosion of the sprayed samples at prolonged exposure [53]. In case of the SS plate and Ti coating, the passive film controls the corrosion of the samples. There is no role played by chemistry; rather, morphology controls the corrosion of samples.

The impedance values measured at lowest frequency (0.01 Hz) in Figure 5(b) were found to be the highest than those of 1 h of exposure to acidic pH solution for all samples. The impedance values of both sprayed coatings exhibited almost identical characteristics, but those of the Ti coatings were higher. This result is attributed to the fact that the Ti coating is more resistant to corrosion in the H₂SO₄ solution

TABLE 1: Electrochemical parameters of the SS plate, SS-sprayed coating, and Ti-sprayed coating extracted after fitting of EIS data to suitable EECs with different exposure periods in pH 4 solution.

Time (h)	1			312		
Sample ID	SS plate	SS sprayed	Ti sprayed	SS plate	SS sprayed	Ti sprayed
R_s ($k\Omega\cdot\text{cm}^2$)	6.77	5.20	8.64	5.02	5.37	8.45
R_p ($k\Omega\cdot\text{cm}^2$)	166.00	16.02	48.19	22.82	20.15	21.07
CPE ₁						
Q_1 (1×10^{-6}) ($\Omega^{-1}\cdot\text{cm}^{-2}\cdot\text{s}^n$)	2.7	62.0	7.3	29.6	41.6	37.2
n_1	0.99	0.99	0.99	0.95	0.92	0.93
$C_{\text{eff}1}$ ($\mu\text{F}\cdot\text{cm}^{-2}$)	2.68	62.0	7.22	29.0	41.0	36.5
R_{ct} ($k\Omega\cdot\text{cm}^2$)	11.87	9.15	10.97	350.02	11.56	46.33
CPE ₂						
Q_2 (1×10^{-6}) ($\Omega^{-1}\cdot\text{cm}^{-2}\cdot\text{s}^n$)	91.6	252.3	105.8	20.9	156.1	38.5
n_2	0.75	0.44	0.54	0.91	0.46	0.60
$C_{\text{eff}2}$ ($\mu\text{F}\cdot\text{cm}^{-2}$)	94.19	731.72	120.11	25.44	312.13	56.62
W (1×10^{-6}) ($\Omega\cdot\text{cm}^2\cdot\text{s}^{-0.5}$)	—	—	—	4.2	—	—

at pH 4 after 312 h of exposure [45, 54–56]. The Ti and SS coatings exhibited higher resistance at the highest studied frequency due to formation of passive films and deposition of corrosion products in defects/pores, respectively, and showed higher impedance.

After 312 h of exposure, the corrosion of SS and Ti coatings in acidic solution was controlled by their respective corrosion products and passive film [53]. The impedance value of Ti coating was greater than that of the SS-sprayed coating owing to the more stable and adherent passive oxide film formed on its surface after exposure to the solution. The SS plate had the highest impedance values compared to the sprayed coatings.

The phase shift θ ($^\circ$)- $\log f$ (Hz) Bode plots of samples after 312 h of exposure to solution are shown in Figure 5(b). The scattered data shown in the middle frequency range are attributed due to the defective/porous oxide film caused by the corrosion products of SS and Ti coatings.

The shifting of the phase angle maxima toward -75° for the SS plate was attributed to the formation of the homogeneous passive film on the surface, which revealed the strengthening of the film in the solution. This result indicates that the passive film/corrosion products formed on the plate are surface resisted to the attack of corrosive ions [57].

The impedance data were validated by Kramers–Kronig (K-K) transformation by transforming the real axis into the imaginary axis and vice versa. The K-K transformations are shown in Figure S2 and have been described elsewhere [58–60]. These results confirm the agreement between the experimental data and K-K transformations, which is accordance with the linear system theory.

Brug's formula has been widely used to extract effective capacitance values from CPE parameters for studies on double layers [61]. Brug et al. [62] have established the relationship between CPE parameters and effective capacitance (C_{eff}) associated with the CPE which can therefore be expressed as follows:

$$C_{\text{eff}} = \frac{Q1}{n} R^{(1-n)/n}, \quad (1)$$

where Q is the CPE parameter such as nonideal double-layer capacitance, R is a resistance caused by dissolution of the

metal or alloy at the metal/solution interface in low frequency, and n is the CPE exponent ($-1 < n < 1$). When n is ~ 1 , 0.5 , 0 , and -1 , the CPE is equivalent to a capacitor, the Warburg diffusion, a resistor, and an inductor, respectively.

After fitting of EIS data to a suitable EEC, the electrochemical parameters are shown in Table 1. The R_s is very high for all systems due to low conductivity of the solution. The R_s is gradually decreased with increasing exposure periods due to involvement of more ions after reaction of metals in acidic pH solution [53].

The R_p and R_{ct} values of samples are gradually decreased and increased, respectively, as exposure periods increased. The R_p is emphasizing due to resistance caused by inhomogeneity of the metal surface, and it is decreased due to corrosion. The R_{ct} is increased for SS plate and Ti-sprayed coating due to protective nature of passive film while SS sprayed coating owing to deposition of corrosion products on surface. The corrosion products and passive oxide film increase their thickness as exposure periods were increased, resulting in high R_{ct} than 1 h of exposure [63]. The capacitance of the metal/coating surface and passive film/corrosion products is derived as $C_{\text{eff}1}$ and $C_{\text{eff}2}$, respectively. The $C_{\text{eff}1}$ is dramatically increased as R_p is decreased with exposure periods, which indicates that the metal/coating surface started to corrode, but as the R_{ct} is increased, $C_{\text{eff}2}$ is decreased. The $C_{\text{eff}2}$ result was attributed to that the surface became homogenized due to formation of the passive layer or corrosion products on the metal/coating interface after 312 h of exposure. However, it is found that the C_{eff} is greater for SS coating than the Ti coating and SS plate in all exposure periods. It indicates that the SS coating is more inhomogeneous and defective than other samples. The thickening of the oxide film was attributed to anodic oxidation and formation of the protective passive film/corrosion products that reduced the penetration of aggressive ions [64]. The corrosion product itself caused resistance to corrosion due to uniform and adherent deposition.

After 312 h of exposure, W was observed for the SS plate, possibly resulting from diffusion of the protective passive layer on the surface [65, 66]. As exposure periods are increased, the passive film strength also increased.

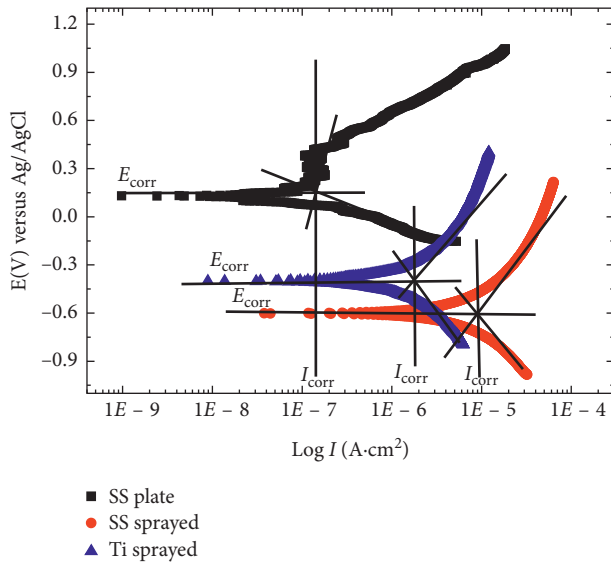


FIGURE 6: Potentiodynamic plots of the SS plate and sprayed coatings in pH 4 solution after 312 h of exposure (1 mV/s).

After 1 h of exposure, R_p is found to be highest for all samples due to a barrier type of protection exhibited by the coatings. The NiO , Fe_2O_3 , FeO , and Cr_2O_3 thin films are formed on the SS plate [42] which give the protection against corrosion. Initially, the metal or coating surface does not start to react with solution resulting in high R_p , but once proper reaction has occurred, the surfaces start to corrode. At the time of corrosion initiation, R_{ct} will involve which causes resistance to penetration of the solution toward the metal surface. Therefore, R_p is decreased and R_{ct} is increased as exposure periods are increased. The film formed on the surfaces was imperfect and rough [67, 68] after 1 h of exposure; thus, the dispersion coefficient (n) is less for CPE2. As the exposure periods were increased, the R_{ct} values increased and CPE decreased for passive layer/corrosion products of the samples. R_{ct} is high for all samples due to deposition of corrosion products on SS-sprayed coating and the protective passive layer on Ti-sprayed coatings and the SS plate after 312 h of exposure.

3.4.2. Potentiodynamic Studies. Potentiodynamic studies were carried out after 312 h of exposure, and results are shown in Figure 6. The SS plate showed pitting and many breakdown potentials during anodic scanning. The breakdown potentials may be caused by oxidation of the metal surface due to impressed current which form a new phase or a metastable passive film, that altered the passive film properties [69]. Therefore, there is a chance that another oxide phase could form on the surface, which might be protective in nature.

The current density of the SS plate is lower than that of Ti and SS coatings during anodic scanning. The interesting observation is found in case of Ti and SS coatings that there is a gradual increase in anodic current density during anodic scanning. It may be due to corrosion or transformation of unstable oxide films of these samples, and whatever corrosion products/passive film formed was deposited on the surface.

The anodic and passive corrosion current of the Ti coating was lower than that of the SS coating, which means that, in this case, the former is more likely to form compact, protective, and adherent passive oxide films [70, 71].

The passive film of Ti-sprayed coating resisted the penetration of corrosive species of the solution; thus, the reducing corrosion rate is observed. During cathodic scanning, all samples exhibited hydrogen evolution reaction which dominated over the oxygen reduction reaction [72].

The electrochemical parameters were extracted after fitting of potentiodynamic plots to the Tafel region using the Stern–Geary equation

$$I_{\text{corr}} = \frac{B}{R_{\text{total}}} \quad (2)$$

The Stern–Geary constant (B) can be calculated by putting the values for corrosion current density (I_{corr}) and total polarization resistance (R_{total}) in (2). The extracted data on the corrosion potential (E_{corr}), I_{corr} , R_{total} , B , and the corrosion rate of samples after 312 h of exposure to pH 4 solution are shown in Table 2.

The E_{corr} of the SS plate and SS and Ti coatings are 0.138, -0.594 , and -0.403 V versus Ag/AgCl, respectively. The SS plate exhibited nobler E_{corr} than the Ti coating followed by the SS coating.

The nobler potential of the SS plate is due to formation of the Cr-enriched oxide film, whereas others exhibited the active potential. The active E_{corr} of SS- and Ti-sprayed coatings compared to the SS plate is attributed to the presence of defects on the coating surface.

Lai et al. observed that when SS was exposed to H_2SO_4 -contaminated water solution, it formed NiO , Fe_2O_3 , FeO , and Cr_2O_3 thin films which were protective in nature and noble [42]. The active potential of SS coating was due to the presence of defective or porous oxide/corrosion films that made the sample more susceptible to corrosion and exhibit the mixed potential [73].

The studied pH solution was acidic and led to the deterioration of the samples. During exposure, the formed corrosion products deposited on the sample surface. The corrosion products blocked the defects/pores of the samples and resisted the penetration of the solution [74, 75].

The iron oxides were more active and therefore exhibited the active potential. The Ti coating exhibited a nobler potential than SS coating because it had only fine and elongated cracks (Figure 2(c)), which stifled the aggressive species of the solution from reaching the base metal. In contrast, the SS coating contains many connected pores and valley morphology where the acidic solution can accumulate and induce crevice corrosion.

These results indicate that the passive film formed on the Ti-sprayed coating after exposure to pH 4 solution is protective, nonporous, compact, and resistant to the penetration of aggressive ions in the solution. The SS coating has porous and nonprotective corrosion products/iron oxides.

The R_{total} values of the SS plate, SS-sprayed coating, and Ti-sprayed coating are 379.860, 33.792, and 68.464 $\text{k}\Omega\cdot\text{cm}^2$, respectively. The higher R_{total} value of Ti coating compared to the SS coating suggests that it can be used as a coating to

TABLE 2: Electrochemical parameters extracted after fitting of potentiodynamic plots to the Tafel region.

Sample ID	Electrochemical parameters				
	E_{corr} (V) versus Ag/AgCl	I_{corr} ($\mu\text{A}\cdot\text{cm}^{-2}$)	R_{total} ($\text{k}\Omega\cdot\text{cm}^2$)	B (V)	Corrosion rate ($\mu\text{m}\cdot\text{y}^{-1}$)
SS plate	0.138	0.382	379.860	0.15	5.132
SS sprayed	-0.594	19.803	33.792	0.67	266.043
Ti sprayed	-0.403	1.913	68.464	0.13	42.703

protect the materials in H_2SO_4 -contaminated water solution, even at low pH. The B values were calculated by using (2), and it was found that the SS plate and Ti-sprayed coating were identical and less active, while SS-sprayed coating showed 0.67 V which is more pronounced to corrosion [76]. The B value of the SS plate and Ti-sprayed coating is under the active control, while the SS-sprayed surface exhibits active dissolution values which influence the corrosion phenomena. The calculated I_{corr} value of SS-sprayed samples reveals the activeness of coating, while the SS plate and Ti-sprayed coating control the corrosion process in acidic solution at longer duration of exposure.

The corrosion rate ($\mu\text{m}\cdot\text{y}^{-1}$) was calculated by the following equation [77]:

$$\text{Corrosion rate } (\mu\text{m}\cdot\text{y}^{-1}) = \frac{3.27 \times I_{\text{corr}} \times \text{EW}}{d}. \quad (3)$$

The corrosion rate in (3) is expressed in micrometres per year ($\mu\text{m}/\text{year}$) and I_{corr} in $\mu\text{A}\cdot\text{cm}^{-2}$. The I_{corr} was obtained by dividing the total surface area of the working electrode under the corrosion current (μA). EW represents the equivalent weight ($\text{g}\cdot\text{mol}^{-1}$), and d is the density ($\text{g}\cdot\text{cm}^{-3}$).

The corrosion rate of the SS coating is $266.043 \mu\text{m}\cdot\text{y}^{-1}$ and is greater than that of the SS plate and Ti coating by 51.84 and 6.23 times, respectively. This result indicates that the SS is not an effective coating material for deposition by the arc thermal spray process in pH 4 solution and long duration of exposure.

The corrosion rate data of the SS coating revealed that it totally dissolved/corroded down to the base substrate. The initial coating thickness was $200 \mu\text{m}$, while the corrosion rate was $266.043 \mu\text{m}\cdot\text{y}^{-1}$. Thus, it may be reported that the Ti coating was effective in protecting the surface than the SS coating. The Ti can be used as a coating material to protect the waste water reservoir and extend its service life.

3.4.3. Characterization of Corrosion Products after Potentiodynamic Studies in pH 4 by Different Techniques. The morphology of corrosion products was examined by SEM, and results are shown in Figure 7. On the SS plate surface, the passive film was adherent, uniform, and regularly deposited, thus preventing the penetration of solution (Figure 7(a)). The edges of the surface show few cracks caused by the destructive potentiodynamic experiment, and the passive film prevented the cracking. After potentiodynamic studies, the SS plate surface did not show any other type of corrosion products/rust.

The SS coating exhibited different sizes of corrosion product morphology with micropore formation (Figure 7(b)). The net-like microstructure of corrosion products is

attributed to the presence of porous iron oxides. Through the net and thread morphologies, the acidic solution easily penetrated the substrate and formed corrosion products.

The morphology of corrosion products formed on the Ti coating was totally different from that on the SS plate and sprayed coating. The passive films formed on the Ti-sprayed surface exhibit microcracks, plate, and globular morphology (Figure 7(c)). The globular particles block the micro- and macrocracks on the top surface. Therefore, enhanced corrosion resistance was observed after 312 h of exposure than on SS-sprayed coating.

Passive oxide films of Ti coating contain plate-like microstructures that were uniformly deposited on the surface. Similar morphologies were not observed in the corrosion products of the SS plate and sprayed coating.

The phases present in the corrosion products of all samples after potentiodynamic studies were studied by XRD. The identification of phases in corrosion products is shown in Figure 8. The SS plate exhibits the presence of tetraaenite (FeNi) and Fe. It is reported that FeNi is unstable and can deteriorate into other forms, if it exposes for long term to low-temperature environments [78].

The presence of lepidocrocite ($\gamma\text{-FeOOH}$) in the corrosion products of SS-sprayed coatings confirmed that this coating was susceptible to corrosion in acidic solution. However, Ti coating exhibits composite oxides along with Ti and TiO . Therefore, the improved corrosion resistance of Ti-sprayed coating is observed by formation of TiO_2 (rutile and anatase), and this observation corroborates with EIS and potentiodynamic results. The passive oxides of Ti such as TiO_2 and Ti_3O_5 have formed. The TiO_2 is thermodynamically more stable than others [79]. Therefore, the Ti-sprayed coating is attributed to improved corrosion resistance properties of coating in H_2SO_4 solution. The transformation of Ti into TiO_2 in the H_2SO_4 environment is well documented elsewhere [80, 81]. TiO_3 and some amount of TiO (Figure 3) may be transformed into TiO_2 and Ti_3O_5 due to a strong oxidizing ability of H_2SO_4 solution. Thus, corrosion products/passive film of Ti-sprayed coating exhibits some peaks of TiO (Figure 8). Therefore, corrosion is observed after 312 h of exposure to H_2SO_4 solution. Once proper transformation of Ti and TiO into the stable form occurred, then the corrosion rate would be completely suppressed.

4. Conclusions

From the above results and discussion, the following can be concluded:

- (1) The EIS and potentiodynamic studies revealed the protective properties of Ti coating due to formation

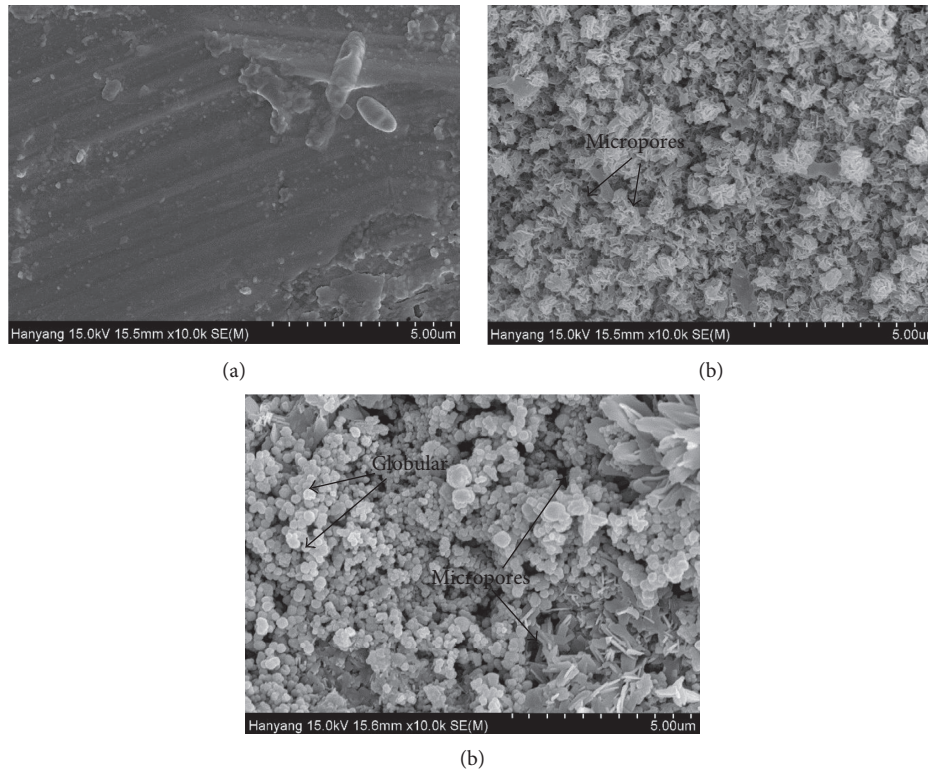


FIGURE 7: SEM images of corrosion products formed on the (a) SS plate, (b) SS-sprayed coating, and (c) Ti-sprayed coating after potentiodynamic studies in pH 4 solution.

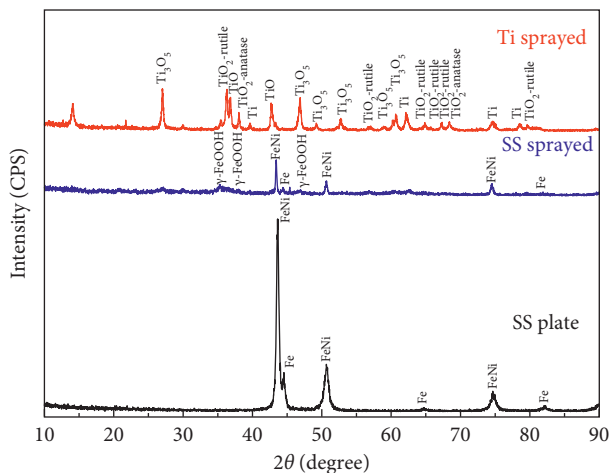


FIGURE 8: XRD of the SS plate and sprayed coatings after potentiodynamic studies in pH 4 solution (0.5°/min).

of the protective oxide film at longer duration of exposure to acidic solution.

- (2) The improved corrosion resistance properties of Ti-sprayed coating than SS-sprayed coating after 312 h of exposure to acidic solution is attributed to transformation of unstable oxides into stable, protective, and adherent TiO_2 (rutile and anatase) which is a thermodynamically stable oxide.
- (3) Examination of the corrosion product morphology by SEM revealed the compact, globular, and crystalline

corrosion products/oxide films on the Ti sample, while the SS sample formed defective and microcrack-bearing corrosion products.

- (4) The SS plate showed uniform, crack-free passive films, with no trace of corrosion products after 312 h of exposure to acidic solution.

Conflicts of Interest

The authors declare no conflicts of interest.

Authors' Contributions

Jitendra Kumar Singh and Jin-ho Park conducted the experiments and wrote the initial draft of the manuscript. Han-Seung Lee designed the experiments. Jitendra Kumar Singh and Han-Seung Lee analyzed the data and wrote the final manuscript. Han-Seung Lee, Mohamed A. Ismail, and Jitendra Kumar Singh reviewed and contributed to the final revised manuscript. All authors contributed to the analysis of the data and read the final paper.

Acknowledgments

This research was supported by the Korea Ministry of Environment (MOE) as Public Technology Program based on Environmental Policy (no. 2015000700002) and Basic Science Research Program through the National Research Foundation of Korea (NRF) funded by the Ministry of Science, ICT and Future Planning (no. 2015R1A5A1037548)

Supplementary Materials

Figure S1: Nyquist plots (at higher frequency ranges) of the SS plate and sprayed coatings in pH 4 solution after 1 h of exposure (100 kHz to 40 kHz). Figure S2: Kramers–Kronig transformation of the EIS data obtained for the SS plate and sprayed coatings in pH 4 solution after (a) 1 h and (b) 312 h (100 kHz to 0.01 Hz). (*Supplementary Materials*)

References

- [1] H. S. Jensen, P. N. L. Lens, J. L. Nielsen et al., “Growth kinetics of hydrogen sulfide oxidizing bacteria in corroded concrete from sewers,” *Journal of Hazardous Materials*, vol. 189, no. 3, pp. 685–691, 2011.
- [2] M. Lupsea, L. Tiruta-Barna, and N. Schiopu, “Leaching of hazardous substances from a composite construction product—An experimental and modelling approach for fibre-cement sheets,” *Journal of Hazardous Materials*, vol. 264, pp. 236–245, 2014.
- [3] Q. Guo, “Increases of lead and chromium in drinking water from using cement-mortar-lined pipes: initial modelling and assessment,” *Journal of Hazardous Materials*, vol. 56, no. 1-2, pp. 181–213, 1997.
- [4] E. Owaki, R. Okamoto, and D. Nagashio, “Deterioration of concrete in an advanced water treatment plant,” in *Concrete under Severe Condition: Environment and Loading*, E. Gjorv, E. Odd, K. Sakai, and N. Banthia, Eds., E & FN Spon, London, UK, 1998.
- [5] R. N. Swamy and S. Tanikawa, “An external surface coating to protect concrete and steel from aggressive environments,” *Materials and Structures*, vol. 26, no. 8, pp. 465–478, 1993.
- [6] D. Crowe and R. Nixon, “Corrosion of stainless steels in waste water applications,” 2016, http://www.hwea.org/wp-content/uploads/2015/07/150204_Corrosion_of_Stainless_Steels_in_Wastewater_Applications.pdf.
- [7] B. B. Bhalerao and S. J. Arceivala, “Application of corrosion control techniques in municipal water and waste water engineering,” 2016, <http://eprints.nmlindia.org/5825/1/129-139.PDF>.
- [8] “Alkalinity profiling in wastewater operations, ops challenge laboratory event 2015,” 2017, http://www.rmwea.org/docs/Alkalinity_Profiling_in_Wastewater_Operations_White_Paper_OPS_2015_ED_1.20.15.pdf.
- [9] V. Kumar, “Protection of steel reinforcement for concrete: a review,” *Corrosion Reviews*, vol. 16, no. 4, pp. 317–358, 1998.
- [10] A. I. Fernández-Abia, J. Barreiro, D. González-Madruga, and L. N. López de Lacalle, “Effect of mechanical pre-treatments in the behavior of nanostructured PVD-coated tools in turning,” *International Journal of Advanced Manufacturing Technology*, vol. 73, no. 5–8, pp. 1119–1132, 2014.
- [11] S. Rodríguez-Barrero, J. Fernández-Larrinoa, I. Azkona, L. N. López de Lacalle, and R. Polvorosa, “Enhanced performance of nanostructured coatings for drilling by droplet elimination,” *Materials and Manufacturing Processes*, vol. 31, no. 5, pp. 593–602, 2016.
- [12] L. Pawlowski, *The Science and Engineering of Thermal Spray Coatings*, John Wiley & Sons Ltd., West Sussex, UK, 2nd edition, 2008.
- [13] G. Jandin, H. Liao, Z. Q. Feng, and C. Coddet, “Correlations between operating conditions, microstructure and mechanical properties of twin wire arc sprayed steel coatings,” *Materials Science and Engineering: A*, vol. 349, no. 1-2, pp. 298–305, 2003.
- [14] H. S. Lee, J. K. Singh, M. A. Ismail, and C. Bhattacharya, “Corrosion resistance properties of aluminum coating applied by arc thermal metal spray in SAE J2334 solution with exposure periods,” *Metals*, vol. 6, no. 3, pp. 1–15, 2016.
- [15] H. S. Lee, J. K. Singh, and J. H. Park, “Pore blocking characteristics of corrosion products formed on aluminum coating produced by arc thermal metal spray process in 3.5 wt.% NaCl solution,” *Construction and Building Materials*, vol. 113, pp. 905–916, 2016.
- [16] H. S. Lee, J. H. Park, J. K. Singh, and M. A. Ismail, “Protection of reinforced concrete structures of waste water treatment reservoirs with stainless steel coating using arc thermal spraying technique in acidified water,” *Materials*, vol. 9, no. 9, pp. 1–20, 2016.
- [17] H. B. Choe, H. S. Lee, and J. H. Shin, “Experimental study on the electrochemical anti corrosion properties of steel structures applying the arc thermal metal spraying method,” *Material*, vol. 7, no. 12, pp. 7722–7736, 2014.
- [18] A. Guenbour, A. Benbachir, and A. Kacemi, “Evaluation of the corrosion performance of zinc-phosphate-painted carbon steel,” *Surface and Coatings Technology*, vol. 113, no. 1-2, pp. 36–43, 1999.
- [19] N. Cinca, C. R. C. Lima, and J. M. Guilemany, “An overview of intermetallics research and application: status of thermal spray coatings,” *Journal of Materials Research and Technology*, vol. 2, no. 1, pp. 75–86, 2013.
- [20] D. F. Bettridge and R. G. Ubank, “Quality control of high-temperature protective coatings,” *Materials Science and Technology*, vol. 2, no. 3, pp. 232–242, 1986.
- [21] H. D. Steffens, Z. Babiak, and M. Wewel, “Recent developments in arc spraying,” *IEEE Transactions on Plasma Science*, vol. 18, pp. 974–975, 1990.
- [22] H. A. M. Muhamad, S. N. Hayati, A. S. Kiyai, and M. S. N. Binti, “Critical process and performance parameter of thermal arc spray coatings,” *International Journal of Materials Engineering Innovation*, vol. 5, no. 1, pp. 12–27, 2014.
- [23] J. R. Davis, *Surface Engineering for Corrosion and Wear Resistance*, ASM International, Geauga County, OH, USA, 2001.
- [24] KS F4716, *Cement Filling Compound for Surface Preparation*, Korean Agency for Technology and Standards (KATS), Seoul, Korea, 2001.
- [25] S. Shrestha and A. J. Sturgeon, “Use of advanced thermal spray processes for corrosion protection in marine environments,” *Surface Engineering*, vol. 20, no. 4, pp. 237–243, 2004.
- [26] L. Wang and J. Sun, “Molybdenum modified AISI 304 stainless steel bipolar plate for proton exchange membrane fuel cell,” *Journal of Renewable and Sustainable Energy*, vol. 5, no. 2, p. 021407, 2013.
- [27] M. Dadfar, M. H. Fathi, F. Karimzadeh, M. R. Dadfar, and A. Saatchi, “Effect of TIG welding on corrosion behavior of 316L stainless steel,” *Materials Letters*, vol. 61, no. 11-12, pp. 2343–2346, 2007.
- [28] J. Liu, F. Chen, Y. Chen, and D. Zhang, “Plasma nitrided titanium as a bipolar plate for proton exchange membrane fuel cell,” *Journal of Power Sources*, vol. 187, no. 2, pp. 500–504, 2009.
- [29] X. Cheng and S. G. Roscoe, “Corrosion behaviour of titanium in the presence of calcium phosphate and serum proteins,” *Biomaterials*, vol. 26, no. 35, pp. 7350–7356, 2005.
- [30] J. Pouilleau, D. Devilliers, F. Garrido, S. Durand-Vidal, and E. Mahe, “Structure and composition of passive titanium oxide film,” *Materials Science and Engineering: B*, vol. 47, no. 3, pp. 235–243, 1997.
- [31] S. Kumar, T. S. N. Narayanan, S. G. Raman, and S. K. Seshadri, “Thermal oxidation of cp-Ti: evaluation of characteristics and corrosion resistance as a function of treatment time,”

- Materials Science and Engineering: C*, vol. 29, no. 6, pp. 1942–1949, 2009.
- [32] J. E. Sundgren, P. Bodo, and I. Lundstrom, “Auger electron microscopic studies of the interface between human tissue and implants of titanium and stainless steel,” *Journal of Colloid and Interface Science*, vol. 110, no. 1, pp. 9–20, 1984.
- [33] C. J. Goodacre, G. Bernal, K. Rungcharassaeng, and J. Y. Kan, “Clinical complications with implant and implant prosthesis,” *Journal of Prosthetic Dentistry*, vol. 90, no. 2, pp. 121–132, 2003.
- [34] S. Gudic, J. Radosevic, and M. Kliskic, “Study of passivation of Al and Al-Sn alloys in borate buffer solution using electrochemical impedance spectroscopy,” *Electrochimica Acta*, vol. 47, no. 18, pp. 3009–3016, 2002.
- [35] F. J. Martin, G. T. Cheek, W. E. O’Grady, and P. M. Natishan, “Impedance studies of the passive film on aluminium,” *Corrosion Science*, vol. 47, no. 12, pp. 3187–3201, 2005.
- [36] Y. J. Liu, Z. Y. Wang, and W. Ke, “Study on influence of native oxide and corrosion products on atmospheric corrosion of pure Al,” *Corrosion Science*, vol. 80, pp. 169–176, 2014.
- [37] V. Maurice, W. P. Yang, and P. Marcus, “XPS and STM study of passive films formed on Fe-22Cr (110) single-crystal surfaces,” *Journal of The Electrochemical Society*, vol. 143, no. 4, pp. 1182–1200, 1996.
- [38] A. Goossens and D. D. Macdonald, “A photoelectrochemical impedance spectroscopic study of passive tungsten,” *Journal of Electroanalytical Chemistry*, vol. 352, no. 1-2, pp. 65–81, 1993.
- [39] D. D. Macdonald, E. Sikora, and G. Engelhardt, “Characterizing electrochemical systems in the frequency domain,” *Electrochimica Acta*, vol. 43, no. 1-2, pp. 87–107, 1998.
- [40] H. Song and D. D. Macdonald, “Photoelectrochemical impedance spectroscopy I. Validation of the transfer function by Kramers-Kronig transformation,” *Journal of The Electrochemical Society*, vol. 138, no. 5, pp. 1408–1410, 1991.
- [41] A. Baron, W. Simka, and W. Chrzanowski, “EIS tests of electrochemical behaviour of Ti6Al4V and Ti6Al7Nb alloys,” *JAMME*, vol. 21, pp. 23–26, 2007.
- [42] W. Y. Lai, W. Z. Zhao, Z. F. Yin, and J. Zhang, “EIS and XPS studies on passive film of AISI 304 stainless steel in dilute sulfuric acid solution,” *Surface and Interface Analysis*, vol. 44, no. 4, pp. 418–425, 2012.
- [43] R. T. Loto, “Pitting corrosion evaluation of austenitic stainless steel type 304 in acid chloride media,” *Journal of Materials and Environmental Science*, vol. 4, pp. 448–459, 2013.
- [44] V. Mitrovic-Scepanovic and R. J. Brigham, “The localized corrosion of stainless steel in high purity sulphate solutions,” *Corrosion Science*, vol. 27, no. 6, pp. 545–553, 1987.
- [45] A. Fattah-alhosseini and S. Vafaeian, “Passivation behavior of a ferritic stainless steel in concentrated alkaline solutions,” *Journal of Materials Research and Technology*, vol. 4, no. 4, pp. 423–428, 2015.
- [46] J. B. Wen, J. L. Ma, and J. G. He, *Al-Base Sacrificial Anode Material for Corrosion Protection*, Chemical Industry Press, Beijing, China, 2012.
- [47] C. Liu, Q. Bi, and A. Matthews, “EIS comparison, performance of PVD TiN and CrN coated mild steel in 0.5 N NaCl aqueous solution,” *Corros. Sci.*, vol. 43, pp. 1953–1961, 2001.
- [48] O. de Rincon, A. Rincon, M. Sanchez et al., “Evaluating Zn, Al and Al-Zn coatings on carbon steel in a special atmosphere,” *Construction and Building Materials*, vol. 23, no. 3, pp. 1465–1471, 2009.
- [49] M. M. Verdian, K. Raeissi, and M. Salehi, “Corrosion performance of HVOF and APS thermally sprayed NiTi intermetallic coatings in 3.5% NaCl solution,” *Corrosion Science*, vol. 52, no. 3, pp. 1052–1059, 2010.
- [50] D. Yang, C. Liu, X. Liu, M. Qi, and G. Lin, “EIS diagnosis on the corrosion behavior of TiN coated NiTi surgical alloy,” *Current Applied Physics*, vol. 5, no. 5, pp. 417–421, 2005.
- [51] Y. C. Xin, J. Jiang, K. F. Huo, G. Y. Tang, X. B. Tian, and P. K. Chu, “Corrosion resistance and cytocompatibility of biodegradable surgical magnesium alloy coated with hydrogenated amorphous silicon,” *Journal of Biomedical Materials Research Part A*, vol. 89, no. 3, pp. 717–726, 2009.
- [52] H. Y. Ha and T. H. Lee, “Determining factors for the protectiveness of the passive film of FeCrN stainless steel formed in sulfuric acid solutions,” *Corrosion Science and Technology*, vol. 12, no. 4, pp. 163–170, 2013.
- [53] J. K. Singh and D. D. N. Singh, “The nature of rusts and corrosion characteristics of low alloy and plain carbon steels in three kinds of concrete pore solution with salinity and different pH,” *Corrosion Science*, vol. 56, pp. 129–142, 2012.
- [54] C. Boissy, C. Alemany-Dumont, and B. Normand, “EIS evaluation of steady-state characteristic of 316L stainless steel passive film grown in acidic solution,” *Electrochemistry Communications*, vol. 26, pp. 10–12, 2013.
- [55] T. Balusamy, M. Jamesh, S. Kumar, and T. S. N. Sankara Narayanan, “Corrosion resistant Ti alloy for sulphuric acid medium: suitability of Ti-Mo alloys,” *Materials and Corrosion*, vol. 63, pp. 803–806, 2012.
- [56] T. P. Cheng, J. T. Lee, and W. T. SAI, “Passivation of titanium in molybdate-containing sulphuric acid solution,” *Electrochimica Acta*, vol. 36, no. 14, pp. 2069–2076, 1991.
- [57] H. Luo, C. Dong, K. Xiao, and X. Li, “The passive behaviour of ferritic stainless steel containing alloyed tin in acidic media,” *RSC Advances*, vol. 6, no. 12, pp. 9940–9449, 2016.
- [58] A. Fattah-alhosseini and S. Vafaeian, “Influence of grain refinement on the electrochemical behavior of AISI, 430 ferritic stainless steel in an alkaline solution,” *Applied Surface Science*, vol. 360, pp. 921–928, 2016.
- [59] A. Fattah-alhosseini, H. Elmkhah, and F. R. Attarzadeh, “On the electrochemical behavior of PVD Ti-coated AISI 304 stainless steel in borate buffer solution,” *Journal of Materials Engineering and Performance*, vol. 26, no. 4, pp. 1792–1800, 2017.
- [60] B. A. Boukamp, “Practical application of the Kramers-Kronig transformation on impedance measurements in solid state electrochemistry,” *Solid State Ionics*, vol. 62, no. 1-2, pp. 131–141, 1993.
- [61] B. Hirschorn, M. E. Orazem, B. Tribollet, V. Vivier, I. Frateur, and M. Musiani, “Determination of effective capacitance and film thickness from constant-phase-element parameters,” *Electrochimica Acta*, vol. 55, no. 21, pp. 6218–6227, 2010.
- [62] G. J. Brug, A. L. G. van den Eeden, M. Sluyters-Rehbach, and J. H. Sluyters, “The analysis of electrode impedances complicated by the presence of a constant phase element,” *Journal of Electroanalytical Chemistry and Interfacial Electrochemistry*, vol. 176, no. 1-2, pp. 275–295, 1984.
- [63] E. O. Mayne and C. L. Page, “Green corrosion inhibitor: theory and practice,” *British Corrosion Journal*, vol. 7, p. 115, 1972.
- [64] M. Nagayama and S. Kawamura, “Anodic oxidation of ferrous ion on passive iron,” *Electrochimica Acta*, vol. 12, no. 8, pp. 1109–1119, 1967.
- [65] Q. Mohsen and S. A. Fadl-Allah, “Improvement in corrosion resistance of commercial pure titanium for the enhancement of its biocompatibility,” *Materials and Corrosion*, vol. 62, no. 4, pp. 310–319, 2011.

- [66] Q. G. Jiang, Q. Miao, W. P. Liang et al., "Corrosion behavior of arc sprayed Al-Zn-Si-RE coatings on mild steel in 3.5 wt.% NaCl solution," *Electrochimica Acta*, vol. 115, pp. 644–656, 2014.
- [67] B. Cox and Y. M. Wong, "Simulating porous oxide films on zirconium alloys," *Journal of Nuclear Materials*, vol. 218, no. 3, pp. 324–334, 1995.
- [68] A. Al-Negheimish, A. Alhozaimy, R. R. Hussain, R. Al-Zaid, J. K. Singh, and D. D. N. Singh, "Role of manganese sulfide inclusions in steel rebar in the formation and breakdown of passive films in concrete pore solutions," *Corrosion*, vol. 70, no. 1, pp. 74–86, 2014.
- [69] W. Lai, W. Zhao, F. Wang, C. Qi, and J. Zhang, "EIS study on passive films of AISI 304 stainless steel in oxygenous sulfuric acid solution," *Surface and Interface Analysis*, vol. 41, no. 6, pp. 531–539, 2009.
- [70] A. Singh, B. P. Singh, M. R. Wani, D. Kumar, J. K. Singh, and V. Singh, "Effect of anodization on corrosion behaviour and biocompatibility of Cp-titanium in simulated body fluid," *Bulletin of Materials Science*, vol. 36, no. 5, pp. 931–937, 2013.
- [71] M. Jamesh, T. S. N. Sankara Narayanan, and P. K. Chu, "Thermal oxidation of titanium: evaluation of corrosion resistance as a function of cooling rate," *Materials Chemistry and Physics*, vol. 138, no. 2-3, pp. 565–572, 2013.
- [72] B. Jegdic, D. M. Drazic, and J. P. Popic, "Corrosion potential of 304 stainless steel in sulfuric acid," *Journal of the Serbian Chemical Society*, vol. 71, no. 5, pp. 543–551, 2006.
- [73] D. Dzhurinskiy, E. Maeva, E. Leshchinsky, and R. G. Maev, "Corrosion protection of light alloys using low pressure cold spray," *Journal of Thermal Spray Technology*, vol. 21, no. 2, pp. 304–313, 2012.
- [74] A. Meroufel and S. Touzain, "EIS characterization of new zinc-rich powder coatings," *Progress in Organic Coatings*, vol. 59, no. 3, pp. 197–205, 2007.
- [75] C. M. Abreu, M. Izquierdo, M. Keddou, X. R. Novoa, and H. Takenouti, "Electrochemical behavior of zinc-rich epoxy paints in 3% NaCl solution," *Electrochimica Acta*, vol. 41, no. 15, pp. 2405–2415, 1996.
- [76] C. Andrade and J. A. Gonzalez, "Quantitative measurements of corrosion rate of reinforcing steels embedded in concrete using polarization resistance measurements," *Materials and Corrosion*, vol. 29, no. 8, pp. 515–519, 1978.
- [77] S. W. Dean, "Electrochemical methods of corrosion testing," in *Electrochemical Techniques for Corrosion*, R. Baboian, Ed., NACE, Houston, TX, USA, 1977.
- [78] Z. Wu, H. Bei, F. Otto, G. M. Pharr, and E. P. George, "Recovery, recrystallization, grain growth and phase stability of a family of FCC-structured multi-component equiatomic solid solution alloys," *Intermetallics*, vol. 46, pp. 131–140, 2014.
- [79] R. Bansal, J. K. Singh, V. Singh, D. D. N. Singh, and P. Das, "Optimization of oxidation temperature for commercially pure titanium to achieve improved corrosion resistance," *Journal of Materials Engineering and Performance*, vol. 26, no. 3, pp. 969–977, 2017.
- [80] Z. J. Liu, X. Zhong, J. Walton, and G. E. Thompson, "Anodic film growth of titanium oxide using the 3-electrode electrochemical technique: effects of oxygen evolution and morphological characterizations," *Journal of The Electrochemical Society*, vol. 163, no. 3, pp. E75–E82, 2016.
- [81] M. A. Selimin, Z. Malik, N. Anjang, M. I. Idris, and H. Z. Abdullah, "Effect of sulphuric acid concentration on anodised titanium for biomedical application," in *Proceedings of the Third International Conference on Advances in Civil, Structural and Mechanical Engineering-CSM*, pp. 46–50, Birmingham, UK, April 2015.

Research Article

Predictive Analysis for the Thermal Diffusion of the Plasma-Assisted Machining of Superalloy Inconel-718 Based on Exponential Smoothing

Chen Shao-Hsien ¹ and Kun-Tan Tsai²

¹The Graduate Institute of Precision Manufacturing, National Chin-Yi University of Technology, Tai-Chung, Taiwan

²Department of Mechanical Engineering, National Chin-Yi University of Technology, Tai-Chung, Taiwan

Correspondence should be addressed to Chen Shao-Hsien; e6036@ncut.edu.tw

Received 6 September 2017; Revised 23 December 2017; Accepted 9 January 2018; Published 3 April 2018

Academic Editor: Shuo Yin

Copyright © 2018 Chen Shao-Hsien and Kun-Tan Tsai. This is an open access article distributed under the Creative Commons Attribution License, which permits unrestricted use, distribution, and reproduction in any medium, provided the original work is properly cited.

Nickel base and titanium base materials have been widely applied to engines in aerospace industry, and these engines are essential components of airplanes. The machining characteristics of aerospace materials may cause machining cutters to be worn down in a short time and thus reduce the accuracy of processing. The plasma-assisted machining adopted in the research is a kind of the complex machining method. In the cases of nickel base and titanium base alloys, the method can heat workpieces in an extremely short duration to soften the materials for the ease of cutting so that the cutting force, cutter wear, and machining cost will all be reduced. The research adopted plasma heating to soften parts of the materials and aimed to explore the heating of nickel base alloy. The temperature variation of the materials was investigated and measured by adjusting the current and feed velocity. Moreover, Inconel-718 superalloy was adopted for the comparison with nickel base alloy for the observation of the influence and change brought by heat, and the method of exponential smoothing was adopted to conduct the prediction and analysis of thermal diffusion for understanding the influence and change brought by electric current on nickel base materials. Finally, given the current from 20 A to 80 A and feed velocity from 1,000 mm/min to 3,000 mm/min, the influence of thermal diffusion was investigated and the related model was built.

1. Introduction

Today, high heat-resistant materials of high strength have been widely applied in aerospace industry and national defense industry. However, the materials with better mechanical properties are harder to be machined in general. It becomes a great challenge for modern industries which require higher surface accuracy of the workpiece, higher machining efficiency, and lower machining cost. One of the common issues is higher machining cost if some specific processes are adopted in production. Based on the concept of complex machining, one of the solutions is the integration of a plasma welding machine and a lathe machine (or a milling machine) [1]. Applying the heat source of plasma-assisted machining to soften materials first will create an extremely short heating duration before cutter reaches the

workpiece. During the extremely short heating duration, the workpiece will absorb heat and soften its materials, leading to phase changes.

In recent years, foreign scholars investigate heat-assisted machining by exploring the machining characteristics with the use of various heat sources (such as laser and plasma). There are many related literatures. Shin [2] and other scholars compared the other technologies, which were traditional machining, laser machining, and plasma-assisted machining, by measuring the residual stress with an X-ray diffraction and analyzing the temperature distribution of heat conduction. Their experiments indicated that both laser-assisted machining and plasma-assisted machining provide great surface accuracy and removal rate for difficult-to-machine materials.

Lamikiz and Celaya [3] conducted a plasma-assisted milling experiment for Inconel-718. The results showed

that the cutting force can be reduced by 25%, the lifetime of the cutter can be extended by about 100%, and the removal rate can be enhanced by 250%. It indicated the importance and the significant difference caused by preheating with an additional heat source.

Anderson et al. [4] investigated the laser-assisted machining for Inconel-718 and then analyzed the machining cost. The results showed that the cutting force can be reduced by 25%, surface roughness can be 2-3 times better, and the life of the cutter can be extended by 200% to 300% if the removal temperature of materials is increased from the room temperature to 360°C.

Leshock et al. [5] developed a plasma heating-assisted system for lathe machines. First, the plasma heating was generated by the surface temperature through the numerical simulation and an infrared radiation thermometer. The results of numerical simulation and experiment were consistent. Then, the simulation analysis showed all operating parameters which influenced the surface temperature. Finally, the operating conditions of plasma-assisted machining were corrected in accordance with the experimental results. Compared to traditional machining, the plasma-assisted machining can reduce the cutting force by 30% and extend the lifetime of the cutter by about 40%.

Hyndman et al. [6] expanded the exponential smoothing application to automatic operation prediction. It has been proven that each exponential smoothing method can provide prediction which is consistent with the results of the state-space model.

Paul [7] indicated that exponential smoothing is one of the essential quantization technologies for prediction. Since the accuracy of prediction depends on the exponential smoothing constant, an appropriate constant is critical for error reduction in prediction. In the research, the optimum value of exponential smoothing was selected based on MSE and MAD, and it will be verified by the trial-and-error method.

The cutting of nickel-based materials is very difficult due to short tool life and severe surface abuse of the machined surface. The key strengthening of superalloys are austenitic base solid solution strengthening, precipitation strengthening, and grain boundary strengthening [8–12]. Nickel-based alloys have low thermal conductivity, machining hardness, and the affinity between the tool and the chip to cause rapid tool wear [13, 14].

2. Theoretical Analysis and Introduction

2.1. Plasma Heating Theory. Plasma heating is the method for workpiece heating and melting by ejecting the superheated and high-speed gas stream electrolyzed through the electric arc discharge under normal atmosphere. Plasma, called the 4th state of matter, is composed of positively charged ions and negatively charged free electrons which are electrolyzed from gas atoms or molecules. Because the overall positive and negative electric charges to equal of the gas, so called plasma.

The extremely high energy density of the plasma-assisted machining tool is caused by the following effects:



FIGURE 1: Plasma heat source movement in the feed direction at the feed velocity.

- (1) Mechanical compression effect: to increase the energy density and temperature of the arc column by the nozzle diameter
- (2) Thermal compression effect: to enhance the current density and temperature again by injecting cooling water into the nozzle to reduce the temperature of the nozzle inner wall
- (3) Magnetic contraction effect: to reduce the cross section area of the arc and to increase the current density for arc stability since the arc current can be deemed as infinite current lines in the same direction, and each current line is attractive to all the others

Based on the effects, the cross section area of the plasma arc will be reduced so that the energy of the plasma arc will be concentrated to increase the density to 105-106 W/cm² and temperature to 10,000–20,000°C. Thus, the plasma gas, ejecting at a speed of 104–107 m/s, will create a huge impact force. When the plasma gas reaches the surface of the workpiece, a lot of heat will be released to heat the workpiece with an extremely high temperature [15].

2.2. Heat Conduction in Plasma-Assisted Machining. Temperature is the key in the machining process. Workpieces will be heated with different temperatures in accordance with the types of heat transfer and the physical properties of the workpiece. The 3 types of heat transfer, heat conduction, heat convection, and heat radiation, can operate alone or simultaneously [7, 16]. Figure 1 shows the plasma heat source movement in the feed direction at the feed velocity, F . The plasma heat source will heat the cutting surface regularly and cause the thermal superposition effect. Assuming that the heat is uniform, the transient state of the machining process is analyzed. The power can be shown as the following expression [17, 18]:

$$Q = 0.24 \times I \times V \times \eta, \quad (1)$$

where I is the current of plasma-assisted machining, V is the voltage of plasma-assisted machining, and η is the thermal efficiency of plasma-assisted machining.

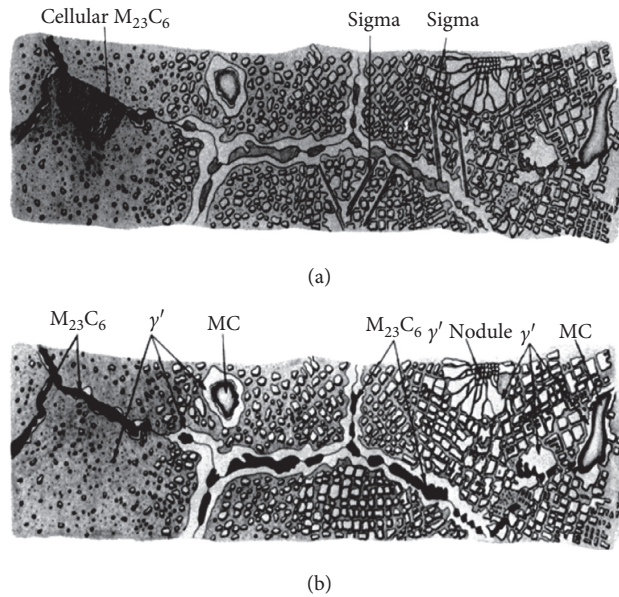


FIGURE 2: Coherency strain generated by precipitates and the base [18].

The feed speed of the high-speed CNC machine tool is in direct proportion to the spindle speed, the number of flutes, and the feed rate per flute. The feed speed in the experiment in the research is shown as the following expression:

$$F = F_t \times Z \times N \text{ mm/min}, \quad (2)$$

where F_t is the feed rate per flute, Z is the number of flutes, and N is the spindle speed.

The relationship between machining speed and heat is shown as the following expression [19]:

$$Q = \frac{V \times I}{S} \times 60. \quad (3)$$

2.3. Material Characteristics of Inconel-718. The strengthening mechanism for nickel base superalloy can be divided into (1) austenitic base solid-solution strengthening; (2) precipitation strengthening for γ' and γ'' ; and (3) grain boundary strengthening [8–12].

- (1) Austenitic base solid-solution strengthening: Inconel-718 alloy contains about 19% of Cr and 3% of Mo. Since the atomic volumes of Cr and Mo are both larger than those of Ni, the substitutional solid solution will be formed when it is solubilized in the base. Thus, the grain lattice of the base will be distorted and the strain will be generated for strengthening.
- (2) Precipitation strengthening for γ' and γ'' : both of γ' and γ'' are regular and coherent precipitates. Generally, their strengthening effect is caused by
 - (a) the reversed phase boundary and defect hardening when the dislocation generates precipitates;
 - (b) coherency strain as shown in Figure 2;
 - (c) the climb or by-passing forced by dislocation to form the dislocation loop of precipitates when the volume of precipitates is large enough;

(d) the size or the volume percent of precipitates.

- (3) Grain boundary strengthening: the effect is generated by the precipitation of carbide to block the grain boundary sliding. A small amount of B (boron) is segregated to the grain boundary to reduce the diffusion. Moreover, the grain size and direction can be controlled to enhance the strengthening effect and the mechanical properties.

2.4. Machining Characteristics of Inconel-718. In the modern cutting history, nickel base superalloy is categorized to a kind of difficult-to-machine materials. The major reasons are listed in the subsequent sections [20, 21].

2.4.1. Large Work Hardening. Since γ' and γ'' phases are both FCC, their mechanical properties are better ductility, and the difference between their lattice constants is about 1%. Through the coherent precipitation strengthening effect of the γ' phase, the strengthening mechanism for nickel base superalloy keeps high mechanical strength, as shown in Figure 3 and Table 1. Since it coheres to the base well under conditions of the precipitation strengthening of γ' and γ'' in high temperature (650°C), the flow stress is still high even through plastic deformation is higher. During the cutting process, there are extremely high strain rate ($\dot{\gamma} \approx 10^5$) and large plastic deformation in the shear zone [17]. A great amount of solid solution, the precipitates of Inconel-718 materials, will block the dislocation movement during the plastic deformation process. However, the coherent precipitation strengthening effect and the amount of solid solution will increase the high-temperature deformation strength of nickel base alloy and easily damage the cutter [22].

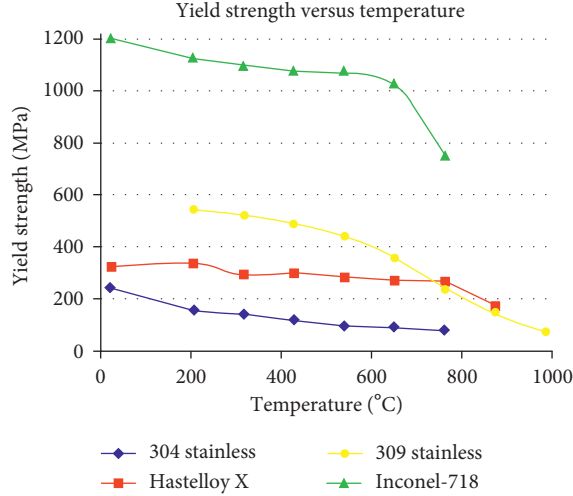


FIGURE 3: Shear strength of Inconel-718 versus temperature [23].

TABLE 1: Inconel-718 different temperature mechanical properties.

Temperature (°C)	Tensile strength (MPa)	Yield strength (MPa)	Elongation (%)
21	1430	1190	21
540	1280	1060	18
650	1230	1020	19
750	950	740	25
870	340	330	88

2.4.2. Low Heat Transfer Rate. The low heat transfer rate of nickel base superalloy is also a major issue related to cutting. In general, most of the heat generated during the cutting process of nickel base superalloy will be transferred to the cutter instead of chips. Moreover, the high yield stress and high tensile strength of nickel base superalloy cause the cutter to withstand the high temperature and high stress. It easily wears the cutter out and may cause tipping [15].

3. Principles of Exponential Smoothing

The exponential smoothing forecasting methods use constants that assign weights to the current demand and previous forecasts to arrive at new forecasts. Their values influence the responsiveness of forecasts to the actual demand and hence influence forecast error. Considerable effort has focused on finding the appropriate values to use. One approach is to use smoothing constants that minimize some function of forecast error [24].

Exponential smoothing adopts the full-time moving average method in time series for applications and predictions. The linear trend of time series can be analyzed and predicted by the first exponential smoothing. Moreover, the second curved trend of time series can be operated by the third exponential smoothing. The principles of the second exponential smoothing are similar to those of the third one. The expressions of the three exponential smoothing are listed as follows [25]:

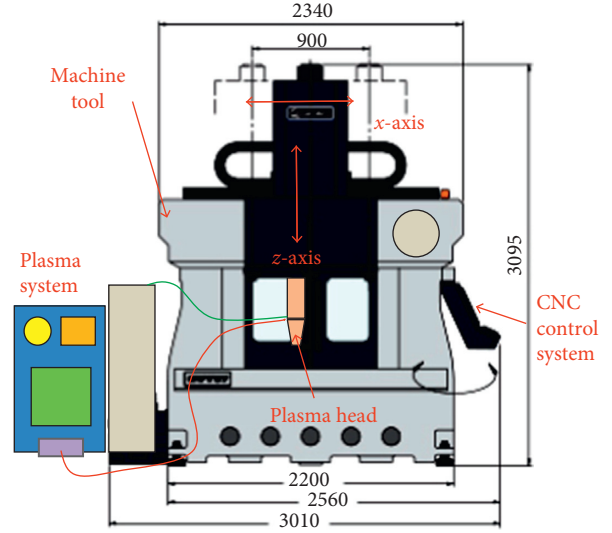


FIGURE 4: Integration of the CNC machine tool and the plasma device.

$$\begin{aligned}
 S_t^{(1)} &= \alpha Y_t + (1 - \alpha) S_{t-1}^{(1)}, \\
 S_t^{(2)} &= \alpha S_t^{(1)} + (1 - \alpha) S_{t-1}^{(2)}, \\
 S_t^{(3)} &= \alpha S_t^{(2)} + (1 - \alpha) S_{t-1}^{(3)},
 \end{aligned} \tag{4}$$

where S_t is the exponential smoothing value of time t , Y_t is the exponential actual value of time t , S_{t-1} is the exponential smoothing value of time $t - 1$, α is the smoothing constant in $[0,1]$, and S_t^3 is the three exponential smoothing value of time t .

The trend prediction in exponential smoothing is the predicted value plus correction value. The prediction model of the three exponential smoothing is listed as follows:

$$\text{Temp}_{\cdot t+T} = a_t + b_t T + c_t T^2, \tag{5}$$

where a_t , b_t , and c_t are the undetermined coefficients of exponential smoothing. Through curve fitting, they can be shown as follows:

$$\begin{aligned}
 a_t &= 3(S_t^{(1)} - S_t^{(2)}) + S_t^{(3)}, \\
 b_t &= \frac{\alpha}{2(1-\alpha)^2} [(6-5\alpha)S_t^{(1)} - 2(5-4\alpha)S_t^{(2)} + (4-3\alpha)S_t^{(3)}], \\
 c_t &= \frac{\alpha}{2(1-\alpha)^2} (S_t^{(1)} - 2S_t^{(2)} + S_t^{(3)}).
 \end{aligned} \tag{6}$$

4. Experimental Device and Method

4.1. Experimental Device. The research adopted a triaxial gantry high-speed machine tool in the experiment as shown in Figure 4. Since the workbench was fixed, the 3 axes, x , y , and z , moved on the crossbeam by travelling 1000 mm, 800 mm, and 700 mm, respectively. The feed velocity was from 1 to 20,000 mm/min, and the maximum revolution of the main

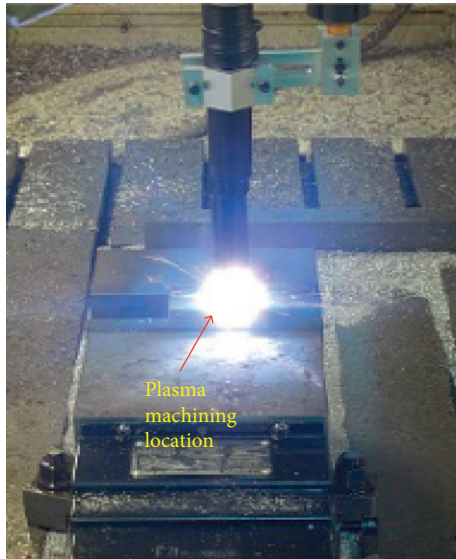


FIGURE 5: Experimental device shooting.

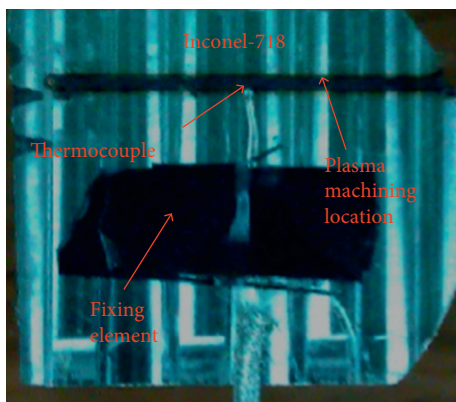


FIGURE 6: Measuring device and the test method.

spindle was 14,000 rpm. The maximum power was 25 KW. In addition, the variable-frequency DC plasma electrode machining head was installed on the main spindle of the CNC machine tool. The pulse current was continuously varying from 5 to 150 A. The input voltage was three-phase AC $220\text{ V} \pm 10\%/60\text{ Hz}$, and the pulse frequency was divided into none, low frequency (0.5~25 Hz), and intermediate frequency (10~100 Hz). Moreover, the current rise time and fall time were 0.1–5 sec and 0.2–10 sec, respectively. The current and voltage to guide the electric arc were 3–30 A and DC 15 V–17 V. Finally, the experiment adopted the K-type thermocouple sensing device to measure the temperature from -200 to 1370°C . The resolution is from -200 to 200°C with the error of 0.1°C , and the sampling rate was 2.5 times per second.

4.2. Experimental Method. The research aimed to explore the temperature distribution of heated nickel base superalloy and to compare the results with those of medium carbon steel. The independent variables were the plasma current I (20, 40, 60, and 80 A) and the feed velocity F (1,000, 2,000, and

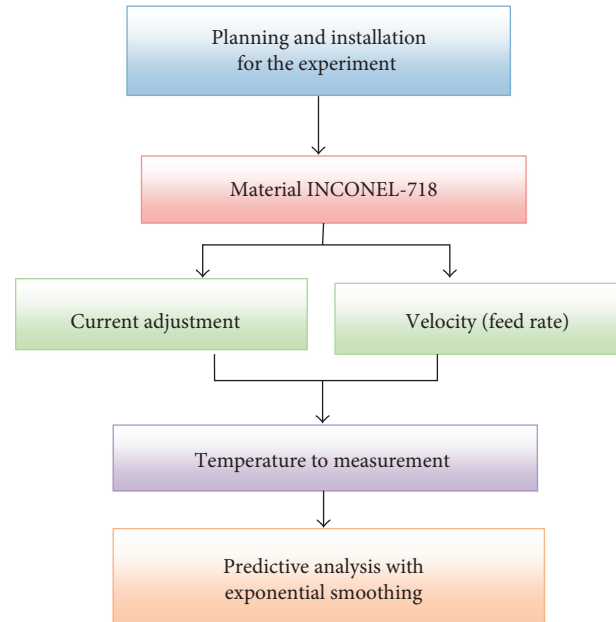


FIGURE 7: Experiment flow chart.

3,000 mm/min). In addition, the thermocouple sense lines were installed on the material surface with 2 mm distance from the center of the weld for not being burned out by the extremely high temperature of the weld electric arc. Figure 5 shows experimental device shooting, Figure 6 shows the measuring method, and Figure 7 shows the experiment flow chart. The main application of this study experiments and predictions, the control factor for the current value and feed rate. Temperature is the target of measurement and prediction. The predicted value is the reference value of the depth of cut.

5. Results and Discussion

5.1. Measurement of Inconel-718 Temperature Distribution. The impacts of current and feed velocity on temperature are discussed in this section. The temperature was measured through the thermocouples installed in the workpiece. Figures 8 and 9 show the relationship between temperature and time under conditions of the feed velocity of 1,000 and 3,000 mm/min, respectively. If the current is larger, the temperature is higher. As the expression (1), when the voltage and current are increased, the heat source power will be increased and then the temperature will be increased rapidly. In addition, if the feed velocity is faster, the temperature will be lower since the faster feed velocity causes less heating duration per unit area.

5.2. Temperature Prediction Based on Exponential Smoothing. In the second section, exponential smoothing was applied to predict the variations of the highest temperatures and actual values. In the experiment, the variation and error were measured under conditions of the fixed feed velocity and variable smoothing constant. Moreover, the experiment adopted the first and three exponential smoothing methods

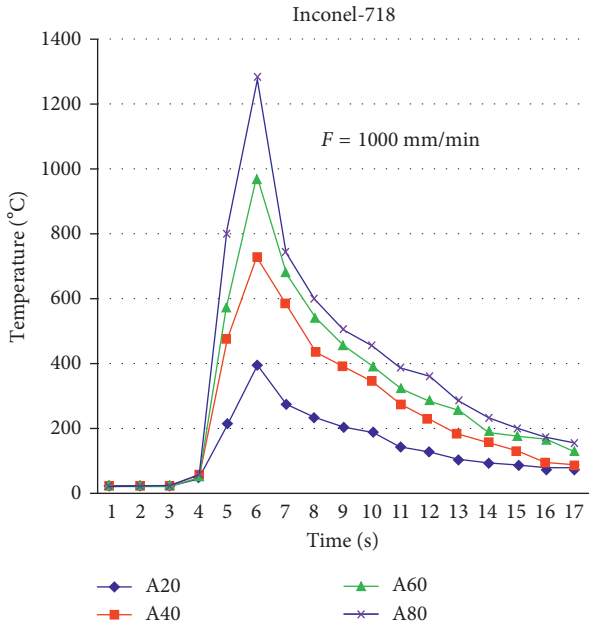


FIGURE 8: Relationship between temperature and time ($F = 1,000$ mm/min).

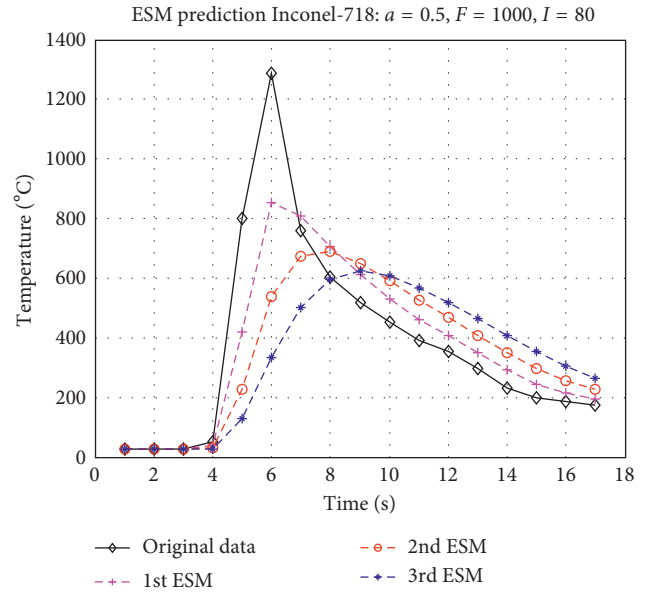


FIGURE 10: Predictive analysis of temperature and time ($F = 1,000$ mm/min and $\alpha = 0.5$).

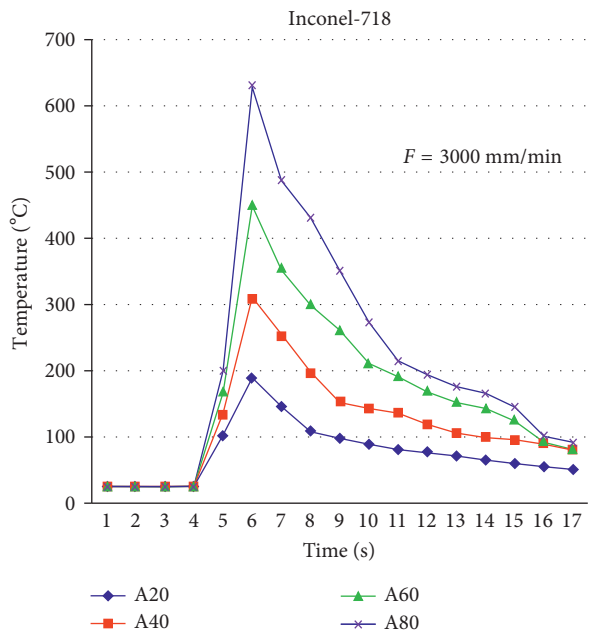


FIGURE 9: Relationship between temperature and time ($F = 3,000$ mm/min).

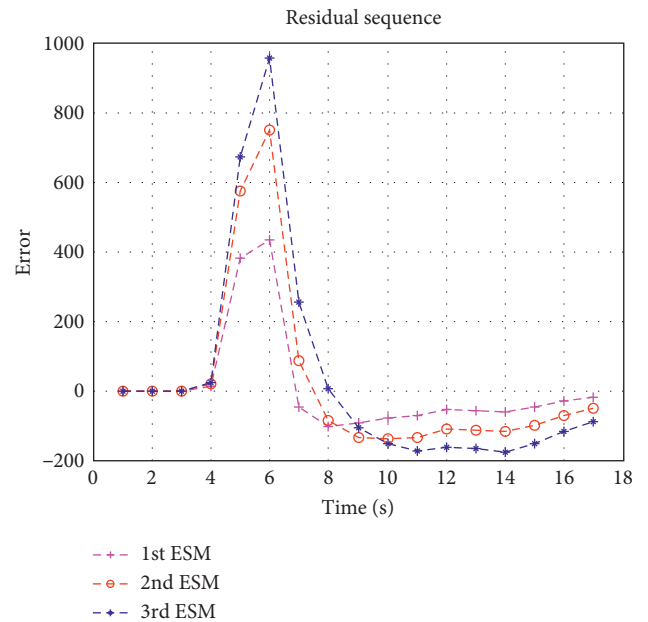


FIGURE 11: Error analysis of temperature and time ($F = 1,000$ mm/min and $\alpha = 0.5$).

for prediction. Input the 80 A current, 1,000 mm/min feed velocity, and smoothing constant for $\alpha = 0.5$, the experimental results are shown in Figure 10. The temperature increased instantly in the period from 5 to 6 seconds. Although the prediction of the first exponential smoothing was more close to the experimental trend, the error was significant as shown in Figure 11.

When applying a larger smoothing constant, such as $\alpha = 0.8$, the prediction of the first exponential smoothing

was more close to the experimental trend than that of the three exponential smoothing as shown in Figure 12. According to the analysis of mean absolute percentage error (MAPE) in Table 2 and as shown in Figure 13, the errors of second and three exponential smoothing methods were both more than those of the single one. Compared with the first exponential smoothing, the trend of the second exponential smoothing was more close to linear equation. Also, the error was larger because of accumulation.

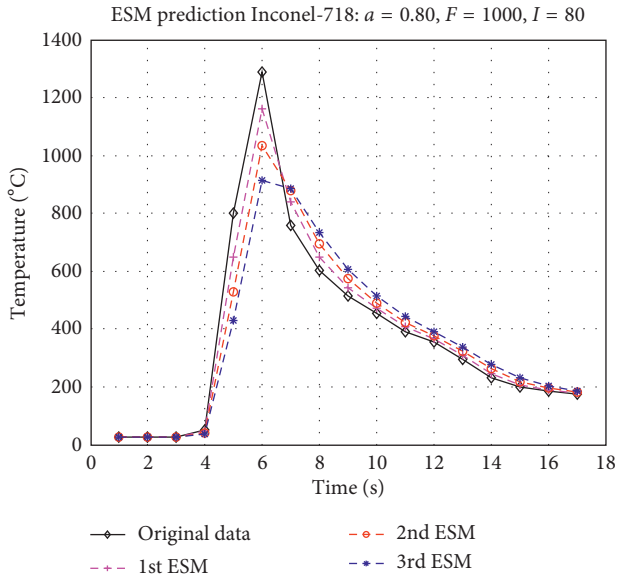


FIGURE 12: Predictive analysis of temperature and time ($F = 1,000$ mm/min and $\alpha = 0.8$).

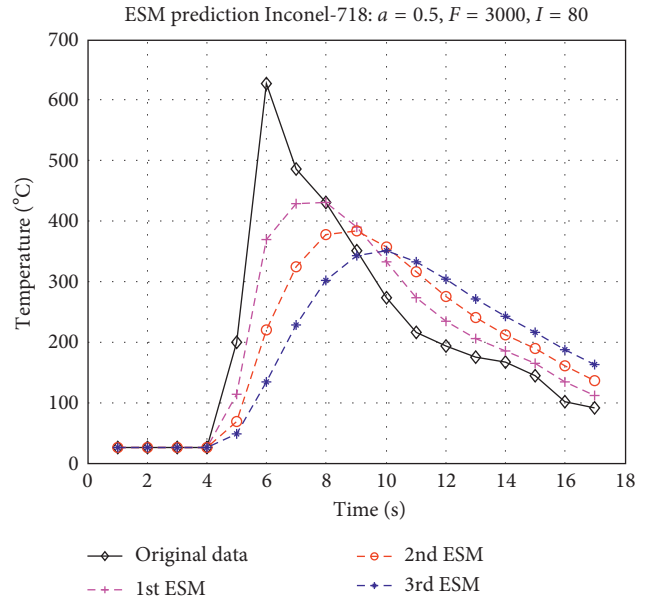


FIGURE 14: Predictive analysis of temperature and time ($F = 3,000$ mm/min and $\alpha = 0.5$).

TABLE 2: Analysis of mean absolute percentage error (MAPE).

	$F = 1000, I = 80$ A		$F = 3000, I = 80$ A	
	$\alpha = 0.5$	$\alpha = 0.8$	$\alpha = 0.5$	$\alpha = 0.8$
1st ESM	1.16	0.17	1.21	0.22
2nd ESM	2.95	0.37	2.63	0.50
3rd ESM	5.25	0.61	4.15	0.82

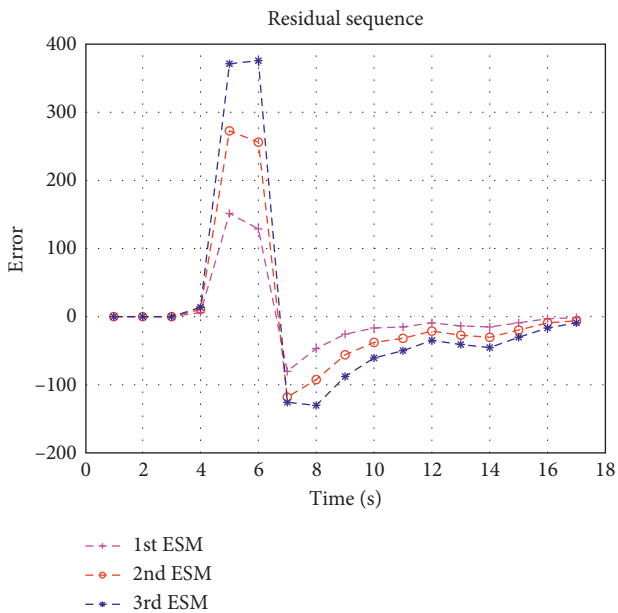


FIGURE 13: Error analysis of temperature and time ($F = 1,000$ mm/min and $\alpha = 0.8$).

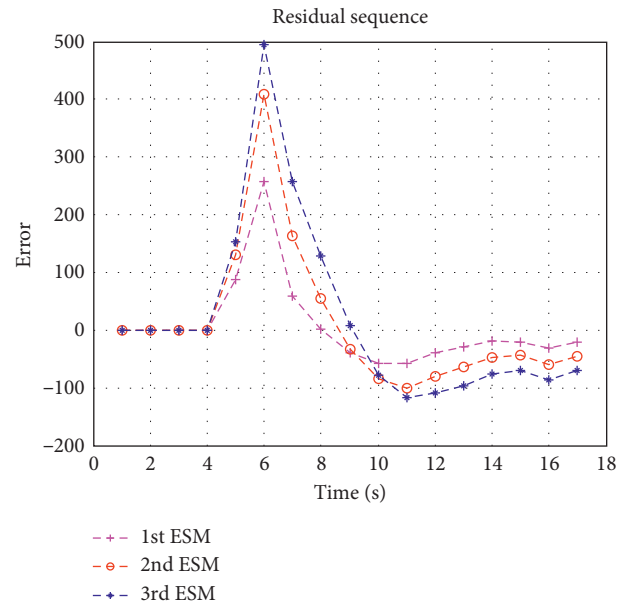


FIGURE 15: Error analysis of temperature and time ($F = 3,000$ mm/min and $\alpha = 0.5$).

When the feed velocity was increased to 3,000 mm/min, the highest temperature became 628°C, which was significantly lower than the temperature of 1,000 mm/min feed

velocity. It was because the heat source was inversely proportional to the velocity and the still duration of the transient state at the point. The smoothing constant $a = 0.5$, and the prediction is shown in Figure 14. Compared to the predictions of the first exponential smoothing, the errors at 3,000 mm/min feed velocity were larger than those at 1,000 mm/min, as shown in Figure 15. On the contrary, the errors of the three exponential smoothing at 1,000 mm/min feed velocity were more than those at 3,000 mm/min. Since the instant temperature variation was larger obviously at

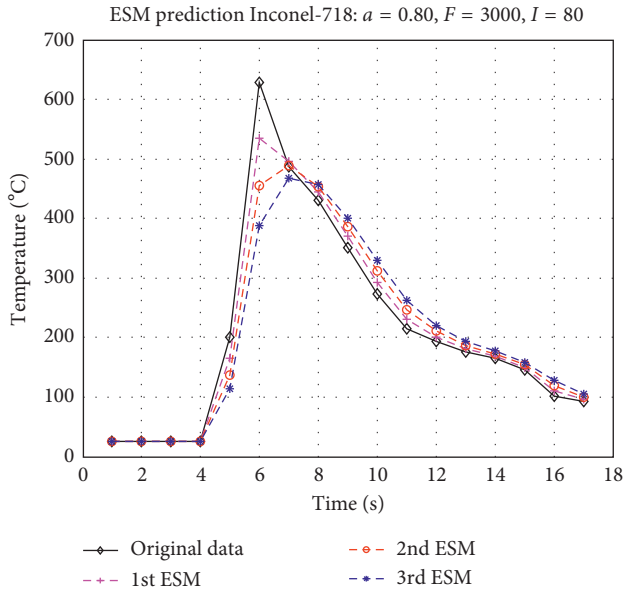


FIGURE 16: Predictive analysis of temperature and time ($F = 3,000$ mm/min and $\alpha = 0.8$).

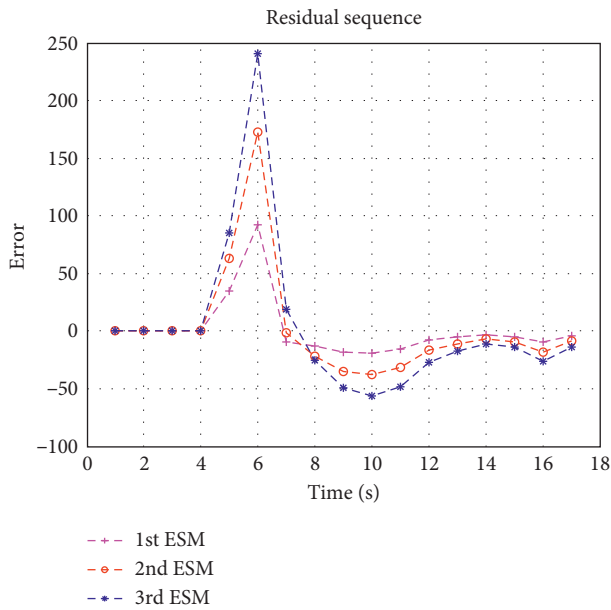


FIGURE 17: Error analysis of temperature and time ($F = 3,000$ mm/min and $\alpha = 0.8$).

TABLE 3: Exponential smoothing prediction model.

Machining	Prediction model
$F = 1000, I = 80$ A, $a = 0.5$	Temp. = $1267 + 584.1T + 536.9T^2$
$F = 1000, I = 80$ A, $a = 0.8$	Temp. = $1293 + 598.8T + 46.1T^2$
$F = 3000, I = 80$ A, $a = 0.5$	Temp. = $585.42 + 311.7T + 32.2T^2$
$F = 3000, I = 80$ A, $a = 0.8$	Temp. = $626.53 + 501.9T + 91.6T^2$

F : feed rate (mm/min); I : electric current (A); Temp.: temperature (°C); T : time (sec).

1,000 mm/min feed velocity, the accumulated errors of the three exponential smoothing became larger. However, at 3,000 mm/min feed rate, the instant temperature variation was less, and then, the accumulated errors of the three exponential smoothing were less than those at 1,000 mm/min.

Applying the larger smoothing constant $a = 0.8$, in prediction, the trend of the single exponential smoothing was more significantly close to the experiment results than that of the three exponential smoothing as in Figure 16. In addition, the errors at $a = 0.8$ smoothing constant were less than those at $a = 0.5$. According to Table 2 and as shown in Figure 17, under conditions of $a = 0.5$ smoothing constant, the mean absolute percentage errors of second and three exponential smoothing methods at 3,000 mm/min feed rate were less than those at 1,000 mm/min.

5.3. Establishment of the Exponential Smoothing Model. Based on the thermal diffusion formula, the thermal conductivity coefficient is directly proportional to the thermal diffusion. Therefore, the low thermal conductivity coefficient of Inconel-718 leads to low thermal diffusion. The exponential smoothing prediction model is built with 2 stages: the rise stage for heating and the fall stage for thermal diffusion. The research aimed at predicting the temperature variation at the highest temperature through the transient state of the heating process. The temperature prediction model of the machining process is proposed and is shown in Table 3. The cutting temperature in superalloy depends on feed-rate and current and can be estimated using a prediction model.

6. Conclusion

Since the material of Inconel-718 easily becomes hard and precipitates the second hardening phase, γ'' , in higher temperature, it is difficult to be cut or machined. If the temperature is higher than the critical points (750–850°C), then the material of Inconel-718 will become easy for cutting. However, the high temperature may soften the cutter and cause impact on the cutting process. In addition, the cutter should not operate at a speed which is too fast. Therefore, the material of Inconel-718 can be softened by plasma heating first to smoothen the cutting process. In the experiment, appropriate current and feed parameters should be adopted for preheating since lower temperature may cause few assistance and higher temperature may damage the cutter in a short period of time.

With the increasing current, the temperature is increased significantly since current is an essential factor to heat plasma. A higher feed velocity also leads to a shorter transient state period at one point. Therefore, for the cutting and machining processes, lower feed velocity and higher current will lead to higher temperature at the cutting temperature point. The errors of the three exponential smoothing at 1,000 mm/min feed velocity were more than those at 3,000 mm/min.

The error of the trend prediction will be less if the smoothing constant α is higher. Moreover, compared to the three exponential smoothing, the trend of the single exponential smoothing is more close to the experimental values. The larger errors of the three exponential smoothing are caused by accumulation, and plasma-assisted machining of nickel-based materials reduces cutting forces and increases tool life. Therefore, the temperature prediction is very important. The exponential smoothing method can correctly predict the temperature. The constant $a=0.8$ is small and the best.

Conflicts of Interest

The authors declare that they have no conflicts of interest.

References

- [1] D.-X. Du, *The Study of Processing Characteristics of Laser Assisted Machining Applied to the SKD-11 Molding Tool Steel Material*, Department of Mechanical Engineering, National Chung Cheng University, Chiayi, Taiwan, 2006.
- [2] Y. C. Shin, L. Shuting, F. E. Pfefferkorn, P. Rebro, J. C. Rozzi, and F. P. Incropera, *Thermally (Laser and Plasma) Assisted Machining: Its Potential and Future*, Abrasives Magazine Inc., Byron center, MI, USA, pp.16–23, 2000.
- [3] A. Lamikiz and A. Celaya, “Plasma assisted milling of heat-resistant super-alloys,” *Journal of Manufacturing Science and Engineering*, vol. 126, p. 274, 2004.
- [4] M. Anderson, R. Patwa, and Y. C. Shin, “Laser-assisted machining of Inconel 718 with an economic analysis,” *International Journal of Machine Tools & Manufacture*, vol. 46, no. 14, pp. 1879–1891, 2006.
- [5] C. E. Leshock, J.-N. Kim, and Y. C. Shin, “Plasma enhanced machining of Inconel 718: modeling of workpiece temperature with plasma heating and experimental results,” *International Journal of Machine Tools & Manufacture*, vol. 41, no. 6, pp. 877–897, 2001.
- [6] R. J. Hyndman, A. B. Koehler, R. D. Snyder, and S. Grose, “A state space framework for automatic forecasting using exponential smoothing methods,” *International Journal of Forecasting*, vol. 18, no. 3, pp. 439–454, 2002.
- [7] S. K. Paul, “Determination of exponential smoothing constant to minimize mean square error and mean absolute deviation,” *Global Journal of Research in Engineering*, vol. 11, no. 3, 2011.
- [8] Z. Y. Wang, K. P. Rajurkar, J. Fan, S. Lei, Y. C. Shin, and G. Petrescu, “Hybrid machining of Inconel 718,” *International Journal of Machine Tools & Manufacture*, vol. 43, no. 13, pp. 1391–1396, 2003.
- [9] M. Rahman, W. K. H. Seah, and T. T. Teo, “Machinability of Inconel-718,” *Journal of Material Processing Technology*, vol. 63, pp. 199–204, 1997.
- [10] G. Germain, P. Dal Santo, and J. L. Lebrun, “Comprehension of chip formation in laser assisted machining,” *International Journal of Machine Tools and Manufacture*, vol. 54, no. 3, pp. 230–238, 2011.
- [11] R. Muhammad, “Thermally enhanced ultrasonically assisted machining of Ti alloy,” *CIRP Journal of Manufacturing Science and Technology*, vol. 7, no. 2, pp. 159–167, 2014.
- [12] D. G. Thakur, B. Ramamoorthy, and L. Vijayaraghavan, “Machinability investigation of Inconel 718 in high-speed turning,” *International Journal of Advanced Manufacturing Technology*, vol. 45, no. 5-6, pp. 421–429, 2009.
- [13] M. C. Shaw, *Metal Cutting Principles*, Oxford University Press, Oxford, UK, 1984.
- [14] C. T. Sim, N. S. Stoloff, and W. C. Hangel, *Super-Alloys*, A Wiley- Interscience Publication, 1987.
- [15] X. K. Ming, *Non-Traditional Processing*, Quanhua Publishing House, Nanjing, China, 1978, in Chinese.
- [16] S. Skvarenina and Y. C. Shin, “Laser-assisted machining of compacted graphite iron,” *International Journal of Machine Tools & Manufacture*, vol. 46, no. 1, pp. 7–17, 2006.
- [17] W. Zhongyin, D. Liguang, and X. Faren, “Study of heat conduction mathematic model of plasma hot machining,” *Journal of Guangxi Institute of Technology*, vol. 5, no. 4, pp. 45–50, 1994.
- [18] H.-Y. Bor, *A Study on the Elevated Temperature Brittleness and Fracture Mechanism of Mar-M247 Super-Alloy*, National Chiao Tung University, Hsinchu, Taiwan, 1998.
- [19] Welding Laboratory, *Shenyang Mechanical and Electrical Engineering Institute*, China Science Press, Beijing, China, 1978.
- [20] S.-H. Chen, “Study on application of grey prediction model in super-alloy MAR-247 machining,” *Advances in Materials Science and Engineering*, vol. 2015, Article ID 704143, 10 pages, 2015.
- [21] H. G. Chun, T. Y. Cho, J. H. Yoon, and G. H. Lee, “Improvement of surface properties of Inconel718 by HVOF coating with WC-metal powder and by laser heat treatment of the coating,” *Advances in Materials Science and Engineering*, vol. 2015, Article ID 468120, 7 pages, 2015.
- [22] M. Alauddin, M. A. El Baradie, and M. S. J. Hashmi, “End-milling machinability of Inconel-718,” *Journal of Engineering Manufacture*, vol. 210, no. 1, pp. 11–22, 1996.
- [23] H. V. Ravinder, “Forecasting with exponential smoothing—what’s the right smoothing constant,” *Review of Business Information Systems—Third Quarter*, vol. 17, no. 3, p. 117, 2013.
- [24] S. J. Shaffer, *Hardness Testing at Elevated Temperatures*, Bruker TMT, Cherry Hill, NJ, USA, 2014.
- [25] J. W. Taylor, “Exponential smoothing with a damped multiplicative trend,” *International Journal of Forecasting*, vol. 19, no. 4, pp. 715–725, 2003.

Research Article

Microstructure and Wear Resistance of TIG Remelted NiCrBSi Thick Coatings

Guo-lu Li,¹ Ya-long Li,^{1,2} Tian-shun Dong ,¹ Hai-dou Wang,² Xiao-dong Zheng,^{1,2} and Xiu-kai Zhou¹

¹School of Materials Science and Engineering, Hebei University of Technology, Tianjin 300130, China

²National Key Laboratory for Remanufacturing, Academy of Armored Forces Engineering, Beijing 100072, China

Correspondence should be addressed to Tian-shun Dong; dongtianshun111@163.com

Received 30 November 2017; Accepted 18 February 2018; Published 21 March 2018

Academic Editor: Shuo Yin

Copyright © 2018 Guo-lu Li et al. This is an open access article distributed under the Creative Commons Attribution License, which permits unrestricted use, distribution, and reproduction in any medium, provided the original work is properly cited.

The self-fluxing NiCrBSi coatings with 800 μm thickness were prepared on the surface of AISI1045 steel substrate by plasma spraying. And the remelted coating was obtained using by the tungsten inert gas (TIG) arc process. The microstructure, surface roughness, hardness, phase composition, and wear resistance of the sprayed coating and remelted coating were systematically investigated. The results demonstrate that TIG remelted treatment can significantly eliminate the microscopic defects in thick coating and improve its density. The surface roughness (Ra) of the remelted coating is only 18.9% of the sprayed coating. The hardness of the remelted coating is 26.8% higher than that of the sprayed coating. The main phases in the sprayed coating are changed from $\gamma\text{-Ni}$, Cr_7C_3 , and Cr_2B to $\gamma\text{-Ni}$, Cr_{23}C_6 , CrB , Ni_3B , and Fe_3C . The wear mass loss of the remelted coating is only 17.1% of the sprayed coating. Therefore, a Ni-based thick coating with good wear resistance can be obtained by plasma spraying and remelted technique.

1. Introduction

Because of their high ability to withstand extremes of temperature, excellent wear resistance, and high corrosion properties, Ni-based self-fluxing alloy coating has been widely used in petroleum, chemical, power, defense, and other fields [1–3]. At present, Ni-based self-fluxing alloy coating is mainly prepared by flame spraying and plasma spraying. However, the abovementioned methods are quite prone to produce microdefects within the coating, such as delamination, micropores, cracks, and so on. These microdefects reduce its density and the bonding strength between the coating and the metal substrate, which results in the decrease of the life of coating. In addition, some studies have shown that the thick coating has better wear resistance and fatigue properties than the thin coating within a certain range [4, 5]. However, thick coating is likely to peel from the substrate during the preparation process due to the large internal stress and other factors [6, 7]. Therefore, thick coating is difficult to be applied in production practice.

Some studies have proved that the thin coating can be surface modified and strengthened by remelting to eliminate

the layer structure of coating, reduce the porosity, and improve the interface bonding with the substrate [8], which are beneficial for improving the coating's performance [9] and prolonging the service life of the parts [10–12]. Unfortunately, little attention has been paid to the remelted of thick coatings.

In the present work, the NiCrBSi coating with the thickness of 800 μm was prepared on the AISI1045 substrate by plasma spraying. And the thick remelting coating was produced by tungsten inert gas (TIG) arc process. The microstructure, morphology evolution, the friction, and wear properties of coating before and after remelting were systematically analyzed. The purpose of this research is to produce the thick coating and improve the service life of the coating.

2. Experimental Procedure

The substrate selected is AISI1045 steel with a size of 10 mm \times 10 mm \times 10 mm. The sprayed raw material is a commercial NiCrBSi self-fluxing alloy powder with a particle size of 10 μm –60 μm , and the chemical composition is given in Table 1.

The powder was preheated, and the substrate AISI1045 steel was cleaned and grit-blasting before spraying. The coating with the average thickness of 800 μm was prepared by using the BT-G3 plasma spraying system with compressed air as main and powder feeding gas. The sprayed coating was remelted by the TIG method with YC-300WX welding machine. Process parameters of sand blasting, spraying, and remelting are given in Table 2.

The microstructures and compositions of the coatings were analyzed by Hitachi S4800 field emission scanning electron microscope (SEM) equipped with an energy dispersive X-ray spectrometer (EDS). The phase identification of the samples before and after remelting was conducted by a D/max/2500 PC type X-ray diffractometer with monochromatic Cu K α radiation. The tube voltage and current were 40 kV and 150 mA, respectively, and the scanning speed and range were chosen 3 $^\circ$ /min and 20 $^\circ$ ~90 $^\circ$, respectively. The microhardness was evaluated on a Shimadzu HMV-2000 Vickers hardness tester.

The wear resistance test was carried out on UMT-2 multifunction friction and wear tester. The diameter of the GCr15 ball was 4 mm, and its Rockwell hardness was 61 HRC. In order to ensure the consistence of the experimental conditions, the samples were grinded with SiC sandpaper from #400 to #1000 before the experiment, until the surface roughness (Ra) of the sample was less than 0.8 μm , and then polished. Experimental conditions were as follows: load 30 N; frequency 10 Hz; test duration 20 min; amplitude 4 mm; and room temperature. The surface roughness, the three-dimensional morphology, and the wear mass loss of the coatings after wear testing were measured by the Phase Shift MicroXAM-3D topography instrument.

3. Results and Discussion

3.1. Microstructure. Figure 1 shows the morphology of the sprayed coating. It can be seen that a typical mechanical bonding has formed between the coating and the substrate from Figure 1(a). There are many inclusions, voids, unmelted particles, and microcracks in the coating, and the interface between the coating and the substrate is nonuniform. The flattening degree of particles varies when they hit the substrate continuously during the spraying process due to the heating and acceleration action of flame flow on the powder is different. The coating presents a typical lamellar structure, consisting of flat striped and spherical particles, and a distinct interface or crack forms. As shown in Figure 1(b), the length of the strip particles is 10.1 μm ~45.6 μm ; the thickness is 1.5 μm ~9.8 μm ; and the particle diameter is 5.1 μm ~25.2 μm . The porosity of the coating measured by image processing software Image J2x is 5.6%.

The cross-sectional morphology of the remelted coating is shown in Figure 2(a). After remelting, the lamellar structure of the original coating disappears. The interface between coating and substrate is smooth, and there are no obvious microcracks, voids, and other defects inside the coating. Figure 2(b) shows that the remelted coating has a bright area of 4.5 μm thickness at the bottom of the coating. The porosity of the remelted coating measured with Image J2x software is 0.2%, which indicates that the density has

TABLE 1: Chemical composition of NiCrBSi powder.

Element	Cr	B	Si	Mn	Re	Ni
wt. %	17	2.5	3	2	0.5	Bal.

TABLE 2: Grit-blasting, spraying, and remelting process parameters.

Process	Parameters	Values
Grit blasting	Air pressure (MPa)	0.7
	Blasting distance (mm)	300
	Blasting angle ($^\circ$)	90
Plasma spraying	Voltage (V)	60
	Current (A)	500
	Spraying distance (mm)	150
	Cooling of substrate	Air blow
	Gas flow rate (L/min)	Ar(80) H ₂ (130)
	Coating thickness (mm)	0.80
TIG remelting	Current (A)	90
	Arc length (mm)	2
	Argon flow (L·min ⁻¹)	10
	Scanning speed (mm·min ⁻¹)	150
	Step size (mm)	3

been improved remarkably. At the interface of the coating, the lamellar structure disappears, and the columnar crystal grows with the recrystallization phenomenon, which helps to improve the interface bonding strength.

The EDS analysis is performed by selecting 6 points in the vertical direction of the interface from the substrate to the sprayed coating. Point 1 and point 2 are located in the substrate, and point 3 is located in the interface between the substrate and the coating. Points 4, 5, and 6 are located in the coating. EDS spectrum analysis shows that the main component of point A in Figure 1(b) is atom fraction: 46.99% O, 1.50% Si, 15.75% Cr, and 35.75% Ni, which indicates that point A is oxidized inclusion.

The EDS analysis is performed on 6 points near the interface between the remelted coating and the substrate. The point 1 and point 2 are located in the substrate. The atomic radii of B and C elements are small, and the concentration gradient is large at the interface; hence, they are able to diffuse into the substrate for a long distance. Although the concentration gradient of the Ni element at the interface is also high, its atomic radius is large; hence, its diffusion distance is short in the substrate. Point 3 is located in the bright area, where the contents of Ni and Cr element are higher, and B and C elements are enriched; since the activities of B and C elements are very high, B and C are easy to form compounds with Cr and Ni. Points 4, 5, and 6 are located inside the remelted coating, so the remelted coating contains a small amount of Cr, Si, and B elements which dissolves in γ -Ni solid solution. In addition, the remelted coating also contains more iron, which is due to a small amount of substrate was remelted and went into the remelted coating. Under the action of stirring of the arc force [13], Fe atoms were distributed roughly uniformly in the remelted coating.

In order to understand the interface bonding between the coating or remelted coating and the substrate more

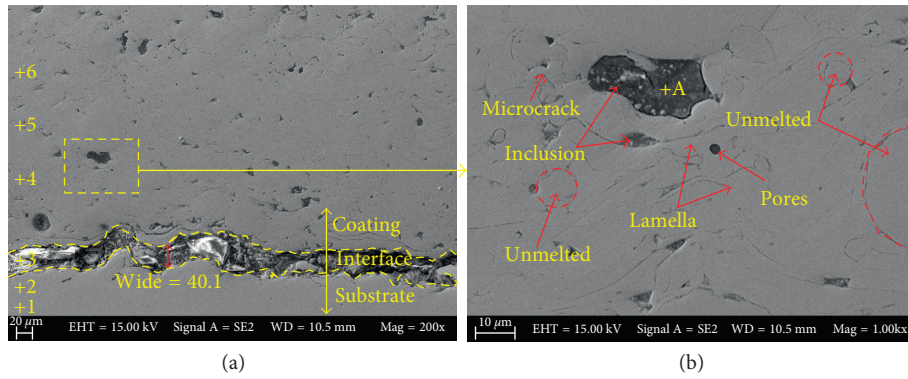


FIGURE 1: SEM morphology of sprayed coating: (a) low magnification and (b) high magnification.

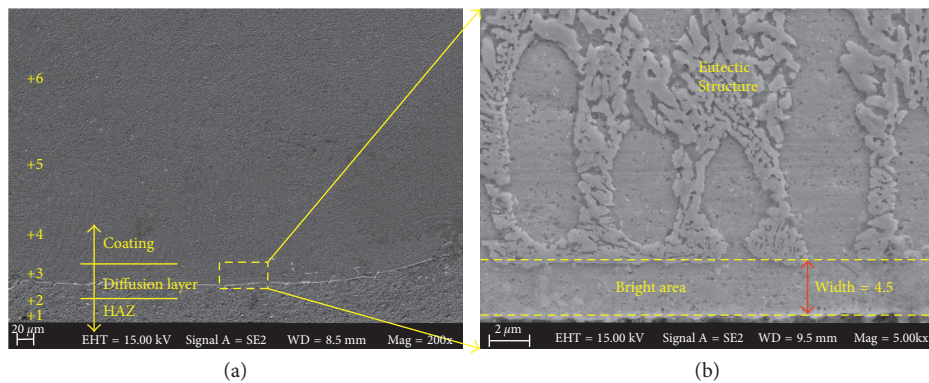


FIGURE 2: SEM morphology of remelted coating cross section: (a) low magnification and (b) high magnification.

clearly, the element distribution of the interface was detected by line scanning, as shown in Figure 3. Compared with the sprayed coating, the elements of Fe, Ni, Cr, B, and Si at the interface of remelted coating have a certain gradient. This indicates that the dissolution and diffusion of elements between the two sides of the interface have occurred which is caused by the concentration and temperature gradients during the remelting process.

The first law of diffusion can be described as follows:

$$J = -D \frac{dc}{dx}, \quad (1)$$

where D is the diffusion coefficient. Besides the temperature and diffusion time, the diffusion of element is also affected by the element diffusion coefficient D and the concentration gradient dc/dx .

The concentration gradients of Fe and Ni at the interface of substrate AISI1045 steel and NiCrBSi coating are very large, which would help to accelerate diffusion, while the C and B elements have a small atomic radius, which is also beneficial for diffusion. The EDS line scanning of interface of the sprayed coating and the substrate is shown in Figure 3(a). It is obviously seen that Fe, Ni, Cr, B, and C elements are steep changes, indicating that there is no diffusion between each other. The coating and the substrate only belongs to mechanical bonding. The EDS line scanning of the interface of the remelted coating and the substrate is shown in Figure 3(b). Obviously, diffusion of Fe, Ni, Cr, B, and C elements occurred

at the interface. The combination of remelted coating and substrate belongs to metallurgical bonding.

The XRD spectra of NiCrBSi powder, sprayed coating, remelted coating bottom, and remelted coating surface are shown in Figure 4. It can be seen that the main phases of the powder are γ -Ni, Cr_7C_3 , Cr_2B , CrB , and Ni_3B ; the main phases of the coating are γ -Ni, Cr_7C_3 , and Cr_2B ; the surface of the remelted coating are γ -Ni, Cr_7C_3 , Cr_{23}C_6 , and CrB ; and the bottom phases of the remelted coating are γ -Ni, Cr_{23}C_6 , CrB , Ni_3B , and Fe_3C . Therefore, the remelted coating has more new strengthening phases, such as Cr_{23}C_6 , CrB , Ni_3B , and Fe_3C .

The sprayed coating and a few substrates are melted to form molten pool under the influence of the arc heat. After the arc is removed, the molten pool solidifies. The growth diagram of the interface microstructure of the remelted coating during the solidification process is shown in Figure 5. The bonding layer between the remelted coating and substrate has grown in form of plane crystal and then grown away from the interface in the form of dendrites. The microstructure of remelted coating is obviously different among the interface layer, the middle of remelted coating, and the top. The remelted coating is combined with the substrate to form a bright area. The middle part is dendrites, and the upper part is smaller dendrites whose microstructure is relatively fine. The microstructures of the central and the top parts are having little difference, and the direction of dendrite growth is in a certain angle with the interface. In

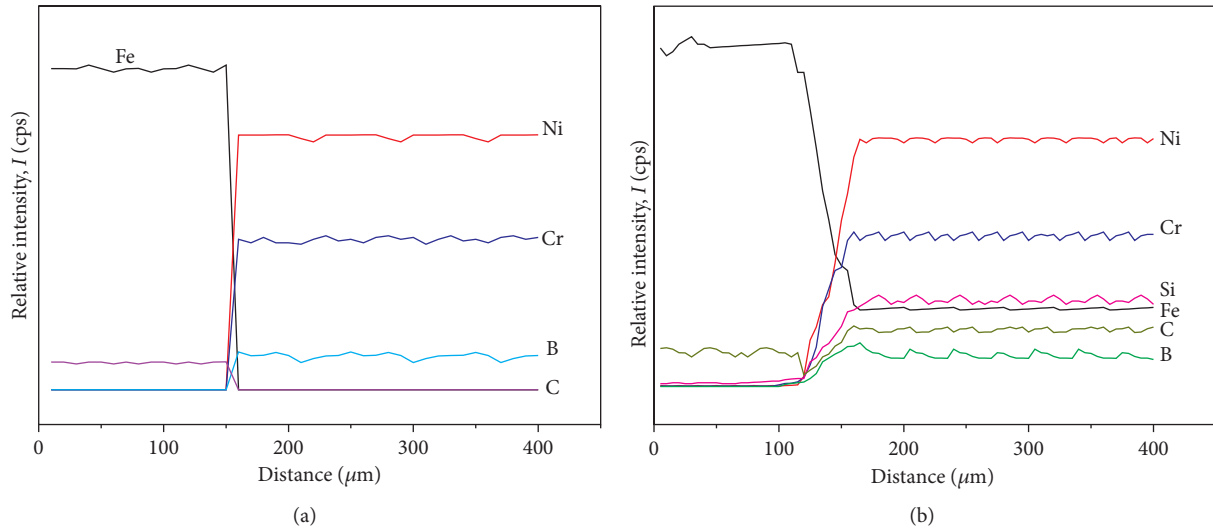


FIGURE 3: Element distributions along thickness of the sprayed and remelted coating: (a) sprayed coating and (b) remelted coating.

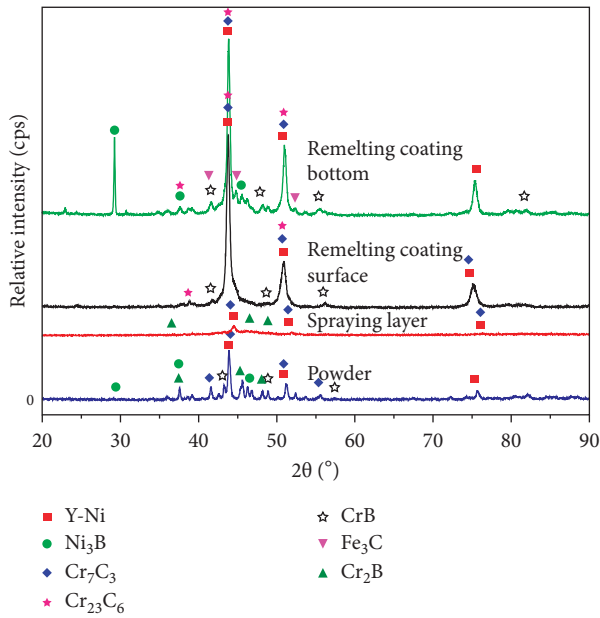


FIGURE 4: XRD patterns of powder, sprayed coating, and remelted coating.

remelted coating, dendrite growth is not only controlled by heat flow direction, but also affected by molten pool disturbance and crystalline anisotropy. Therefore, the growth direction of the dendrite structure shows a certain angle with the normal interface of the solid-liquid interface.

According to the principle of solidification kinetics [14, 15], the crystallization process of the liquid phase is driven by the force of the phase transformation and then overcomes the energy barrier with the help of energy fluctuation, so the crystallization is realized by nucleation and growth. The new phases Cr_{23}C_6 , CrB , Ni_3B , and Fe_3C formed in the remelted coating can be used as nucleus, and the agitation in the remelting process makes the microstructure more refined. The overall microstructure of the

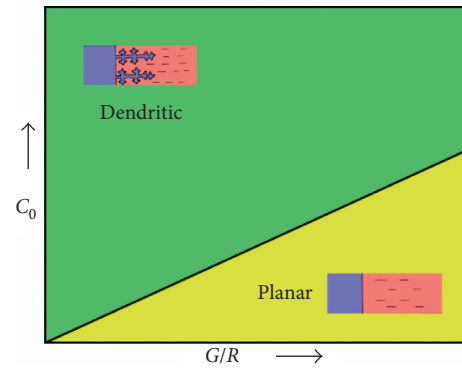


FIGURE 5: Crystal growth patterns of different components undercooled.

remelted coating is shown in Figure 6(a). Figures 6(b)–6(d) are local (B, C, and D) amplification of Figure 6(a), respectively. The main influence factors of the crystalline morphology of the TIG remelted coating are the liquid phase composition in the molten pool and the shape control factor K [14]. The shape control factor is expressed as follows:

$$K = \frac{G}{R}, \quad (2)$$

where G is the temperature gradient of the interface of liquid-solid and R is the interface moving speed. The interface morphology of liquid-solid of the remelted coating mainly depends on the size of the G/R ratio. The solidification velocity R tends to zero at the bottom of the molten pool, and G is very large [14]. Therefore, K has a very large value, where the solidified structure grows at a low velocity plane to form a planar crystal, which is called “bright area,” as shown in Figure 6(b). The width of bright area is $4.5 \mu\text{m}$ (Figure 2(b)). With the increase of the distance from the binding interface, the solidification rate R increases [14]; hence, K decreases, which is beneficial to dendrites formation, as shown in Figures 6(c) and 6(d).

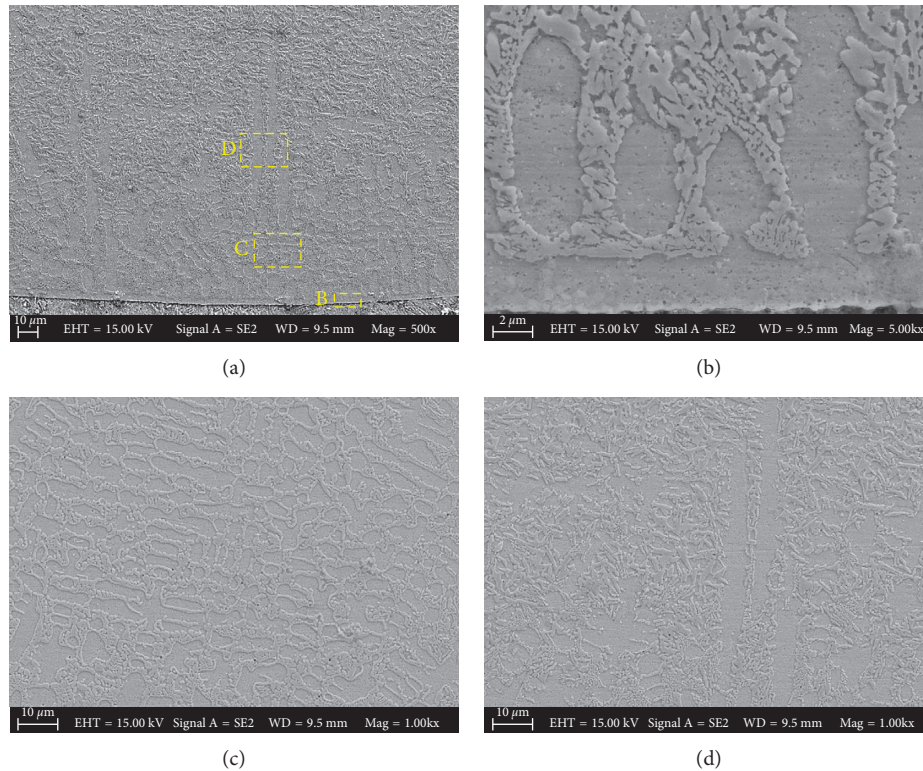


FIGURE 6: Microstructure and morphology of remelted coating: (a) overall structure, (b) planar crystal, and (c, d) dendritic crystal.

In fact, the bright area is planar crystal. As shown in Figure 2(b), the width of bright area is $4.5 \mu\text{m}$, which is often considered as feature of metallurgical bonding. In addition, because of the good corrosion resistance of the bright area, it can be displayed in the form of the bright area. From the element distributions along thickness of the remelted coating in Figure 3 and XRD of the remelted coating in Figure 4, the bright area is γ -Ni, in which a small amount of Fe and Cr elements are dissolved.

The eutectic structures of the remelted coating are shown in Figures 7(a) and 7(b), and EDS results of point E and point F are shown in Figures 7(c) and 7(d). The eutectic structure consists of gray strip γ and black γ' . According to the XRD results presented in Figure 4, it can be determined that the gray strip γ is γ -(Fe, Ni, and Cr), where a small amount of carbon gets into the lattice gap and leads to lattice deformation, and the black γ' are hard phases formed of Cr_{23}C_6 , CrB, Ni_3B , and Fe_3C .

3.2. Surface Roughness. The three-dimensional morphology of the surface of the sprayed coating and the remelted coating is shown in Figures 8(a) and 8(b). The maximum roughness R_z max, minimum roughness R_z min, and average roughness R_a of the sprayed and remelted coating are shown in Table 3. It is obviously seen that R_a of the surface of the remelted coating is only 18.9% of the sprayed coating. In fact, the surface quality of remelted coating obtained by this experiment is better than that of vacuum remelting, and R_a of the TIG remelted coating is 25.2% compared with the vacuum remelted coating [16]. This fully demonstrates that

the TIG remelted coating makes the surface roughness of the sprayed coating significantly reduce.

Previous literatures showed that the size and number of defects in the coating affected the roughness [17, 18]. In this study, there are many defects inside the sprayed coating, such as unmelted particles, voids, inclusions, and so on, which can increase the coating surface roughness. After TIG remelting treatment, the unmelted particles are remelted, most of the pores are eliminated, and the state and distribution of the particles are more homogeneous compared with the sprayed coating. As a result, the surface roughness is greatly decreased.

3.3. Hardness. Figure 9 shows the hardness change curve on the cross section of the sprayed coating and remelted coating. It can be seen that the hardness of the two coatings are all remarkably higher than that of AISI1045 steel substrate, whose hardness is $300 \text{HV}_{0.1}$. The average hardness of the remelted coating ($900 \text{HV}_{0.1}$) is higher than that of sprayed coating ($710 \text{HV}_{0.1}$). The hardness of the remelted coating is about 26.8% higher than that of the sprayed coating. Moreover, the fluctuation of the hardness of coating is greater. The reasons are as follows:

- (1) The internal structure of the sprayed coating is loose, which reduces hardness of the coating. However, the convection and the stirring effect of arc on the molten pool during the remelting process causes gas escaping from the molten pool [19–22]. Meanwhile, due to the deoxidation role of Si and Mn in the

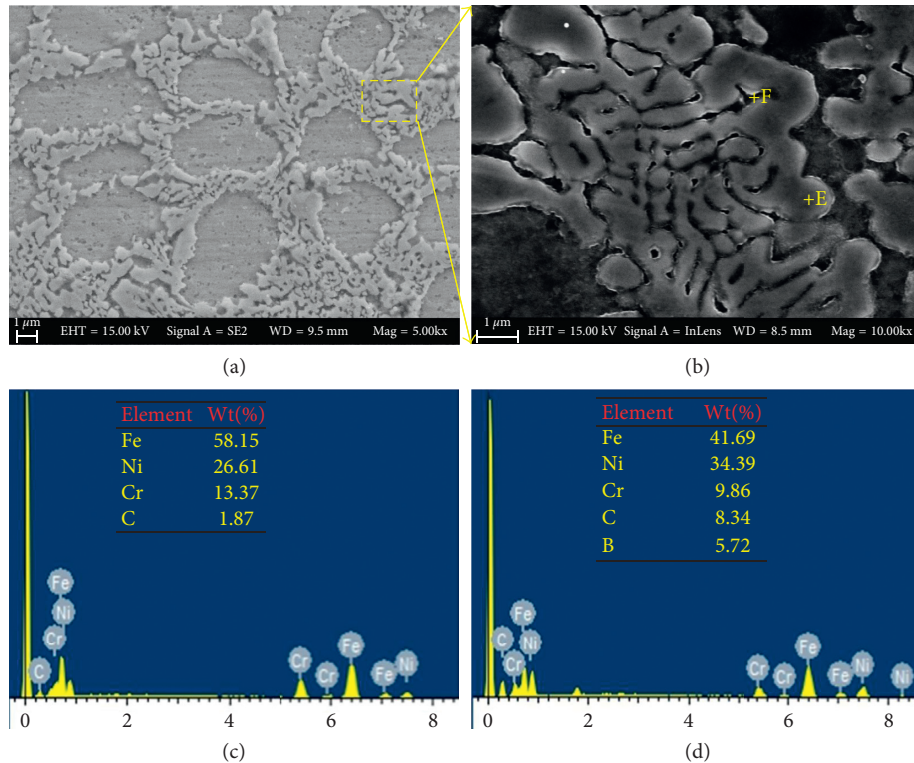


FIGURE 7: Eutectic structure and the energy spectrum and weight percentage of point E and point F.

molten pool, the oxidation inclusions can be removed effectively. Therefore, the microstructure of the remelted coating has become more compact and uniform, and its hardness is increased.

- (2) Although there are some hard phases, such as Cr_7C_3 and Cr_2B , and a part of unmelted or semimelting particles in the sprayed coating, the research by Ohmori et al. shows that the interfacial bonding area of sprayed coating is generally less than 1/3 of the total interface and 2/3 or more is the unbound interface, which are unfavourable for the hardness [23]. However, after the remelting, the microstructure of remelting coating becomes more compact and uniform, a large number of dispersed carbides formed, and the harden phases such as fine skeleton like Ni_3B , CrB , and Cr_{23}C_6 disperse evenly in $\gamma\text{-Ni}$, which makes the hardness of remelted coating increase and uniform.

In addition, it is necessary to point out that there is significant transition zone between the hardness of the remelted coating and the substrate, and there is no obvious transition zone between the sprayed coating and the substrate. This is because Ni and Cr in the coating have diffused into the substrate during the remelting process, leading to the formation of some hard phases such as Cr_{23}C_6 and CrB . At the same time, Ni and Cr can increase the hardenability of substrate. In fact, such transition zone is beneficial for the interface bonding between the remelted coating and the substrate. This phenomenon also confirms the bonding between the coating and the substrate is a typical

mechanical combination, whereas the bonding between the remelted coating and the substrate is a typical metallurgical combination.

3.4. Wear Resistance. Figure 10 shows the friction coefficient curve of the sprayed and remelted coating. 0~100 s is the fluctuating stage, and 100~1200 s is the stable wearing stage. The average coefficient of friction of the sprayed coating is 0.551, while the average coefficient of friction of the remelted coating is 0.392. It is evident that the friction coefficient and the range of fluctuation of sprayed coating are larger than that of remelted coating.

The 3D topography of the wear scar of two coatings is shown in Figures 11(a) and 11(b). At room temperature, the width and depth of wear scar of the sprayed coating are larger than that of the remelted coating. According to Figure 12(a), the widths of the wear scar of the sprayed and remelted coating are 1.132 mm and 0.5132 mm, respectively, and the depths of wear scar are 26.79 mm and 10.03 mm, respectively. The wear mass losses of the sprayed and remelted coating are measured by 3D profilometer, as seen in Figure 12(b). The wear mass losses of the sprayed and remelted coating are 0.2102 mm^3 and 0.0357 mm^3 , respectively, and the latter is only 17.1% of the former. Therefore, the wear property of remelted coating has been significantly improved after remelting.

The SEM morphology of surface wear of the sprayed coating is shown in Figure 13(a). Its local magnification is shown in Figure 13(b). It can be seen that the surface of the sprayed coating shows spalling and delamination. The

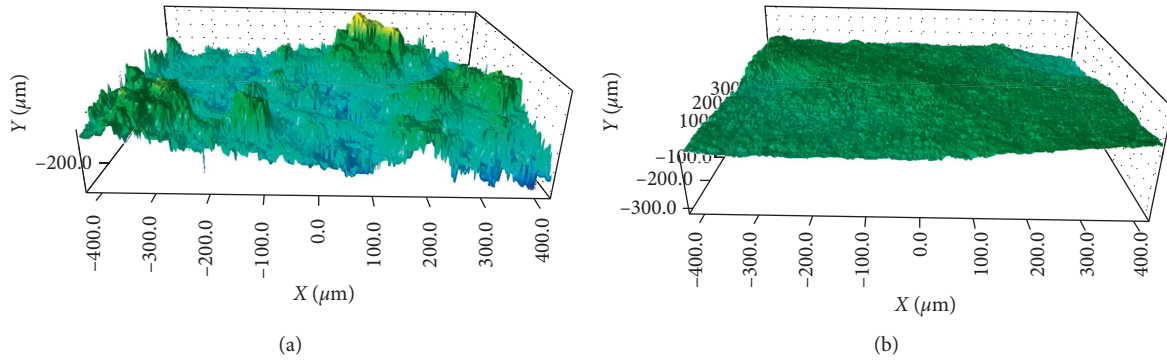


FIGURE 8: 3D morphologies of coatings obtained by a laser scanning microscope: (a) sprayed coating and (b) TIG remelted coating.

TABLE 3: Surface roughness of spraying and remelting coating.

	Rz max (μm)	Rz min (μm)	Ra ave (μm)
Plasma spraying	266.936	202.416	12.651
Vacuum remelted coating [16]	143.841	139.739	9.512
TIG remelted	31.239	28.836	2.403

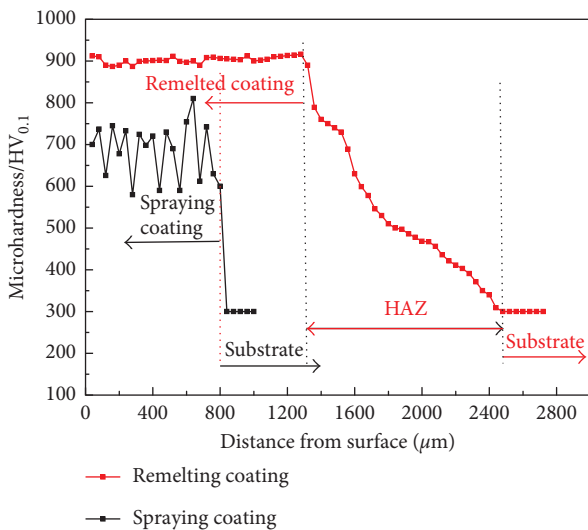


FIGURE 9: Microhardness of sprayed and remelted coating.

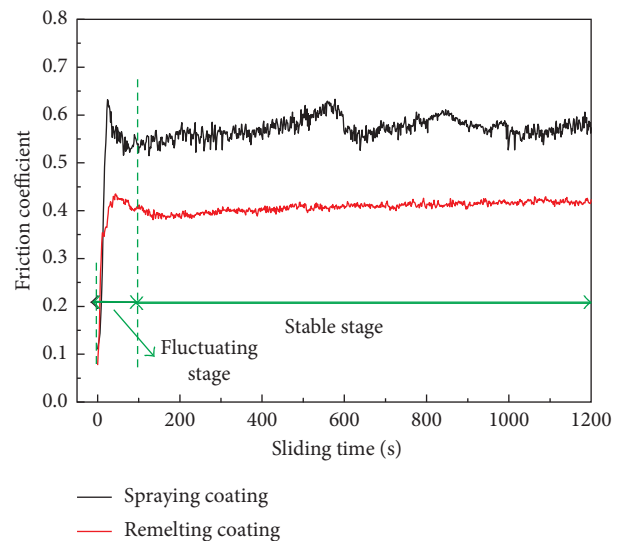


FIGURE 10: The friction coefficient curve of the sprayed and remelted coating.

spalling phenomenon of the coating is serious, and there are many spalling pits, where some microcracks, pores, and unmelted particles of $20\ \mu\text{m}\sim 50\ \mu\text{m}$ can be found. In addition, the spalling pits are filled with lots of strip debris, whose diameters are $1\ \mu\text{m}\sim 2.5\ \mu\text{m}$ (Figure 13(c)), and the oxygen content is high, together with a small amount of Si element (Figure 13(d)). Therefore, the wear mechanism of the coating is mainly lamellar cracking and oxidation wear.

The SEM morphology of surface wear of the remelted coating is shown in Figure 14(a). There are some furrows on the surface of the remelted coating (Figure 14(b)). The furrows are filled with lots of debris, whose shapes are fine granular and its diameter is $0.5\ \mu\text{m}\sim 0.8\ \mu\text{m}$ (Figure 14(c)), and the oxygen content is high (Figure 14(d)). Therefore, the

wear mechanism of remelted coating is mainly micro-abrasive wear and oxidation wear.

The reasons for the improvement of wear resistance of remelted coating are as follows:

- (1) There are many inherent microcracks in the sprayed coating, and they are likely to extend in the wear process under the alternating load, which lead to the spalling eventually (Figure 13(b)). While for the remelted coating, TIG remelted eliminates the inherent defects of the coating and improves the wear resistance of the remelted coating accordingly.
- (2) From the point of view of phase change, according to the theory of Colaco, *R* [24],

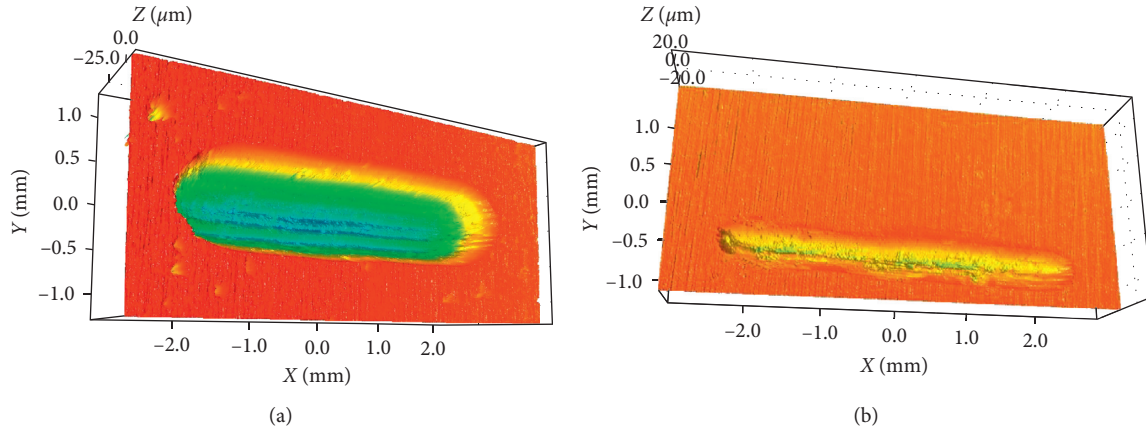


FIGURE 11: Three-dimensional morphology of worn track: (a) sprayed coating and (b) remelted coating.

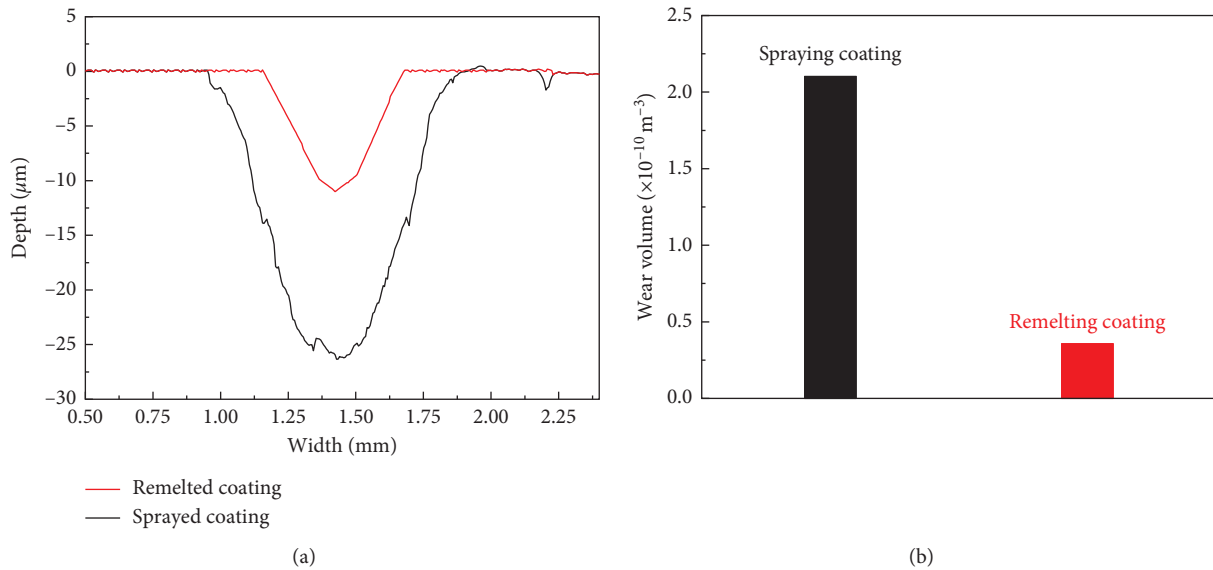


FIGURE 12: (a) Outline of wear scar of sprayed and TIG-remelted coatings and (b) wear mass loss.

$$Q' = K' d^3 \sqrt{\frac{H_0}{x^2} + \frac{\beta}{x}} + \lambda' \left[\frac{32F_N}{\pi \tan^2 \varphi} + \frac{x^2}{H_0 + \beta x} \right]^{1/2}, \quad (3)$$

where Q' is the wear rate, K' is the wear coefficient, d is the particle diameter, H_0 is the hardness of the coating, x is the hard reinforced particle volume fraction, β is constant, λ' is the probability of hard particles pulled out of the wear surface, F_N is the load of abrasive grains, and φ is the angle of tapered abrasive grains. In this work, the main factors affecting the wear resistance of the coating are the particle diameter of hard particles (d), hard reinforced particle volume fraction (x), and the probability of hard particles pulled out of the wear surface (λ').

Compared with the sprayed coating, the remelted coating produces more dispersed fine skeleton-like Cr_{23}C_6 , CrB , and Ni_3B phases which indicates that hard reinforced particle volume fraction (x) is higher and the average diameter of these hard particles (d) are smaller than that of the

spraying coating. In addition, the dispersed fine skeleton-like Cr_{23}C_6 , CrB , and Ni_3B in remelting coating can effectively prevent extend of crack and prevent the remelted coating from spalling. Compared with sprayed coating, the cohesive strength and interfacial bonding strength are obviously improved, leading to the probability of hard particles pulled out of the wear surface (λ') is lower. Hence, the wear rate (Q') of the remelted coating is smaller than that of sprayed coating.

In conclusion, the wear property of remelted coating is remarkably better than that of sprayed coating.

4. Conclusions

- (1) A Ni-based thick coating with good wear resistance can be obtained by plasma spraying and remelting.
- (2) After TIG remelting, the porosity decreases from 5.6% to 0.2%, and the microstructure and the compactness of the coating are improved significantly. The combining state

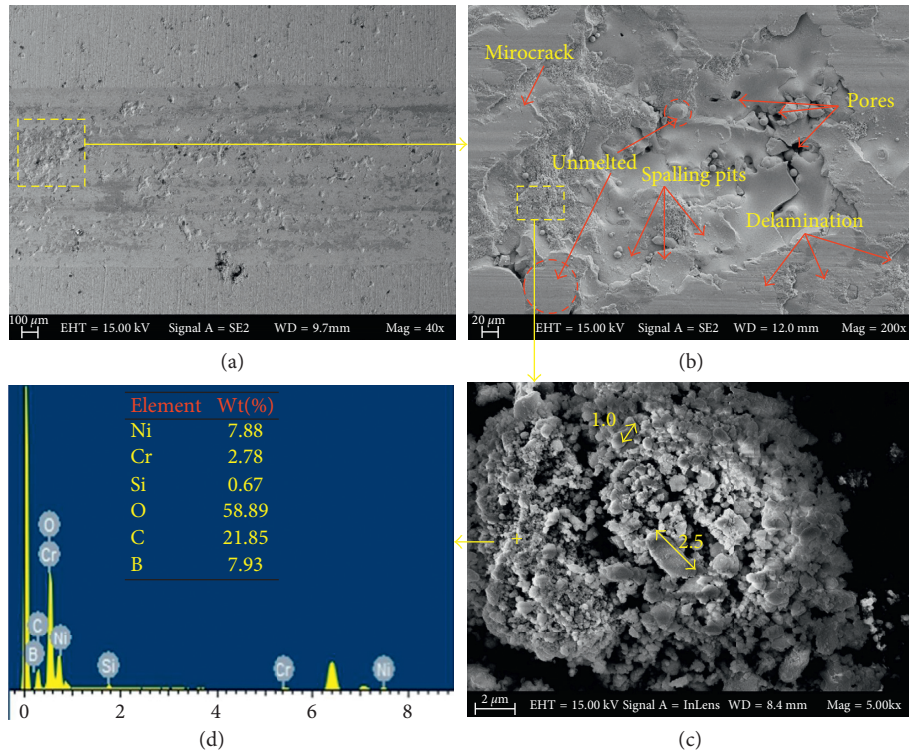


FIGURE 13: The sprayed coating: (a) wear scar, (b) surface wear morphology, (c) debris morphology, and (d) energy spectrum and weight percent of debris.

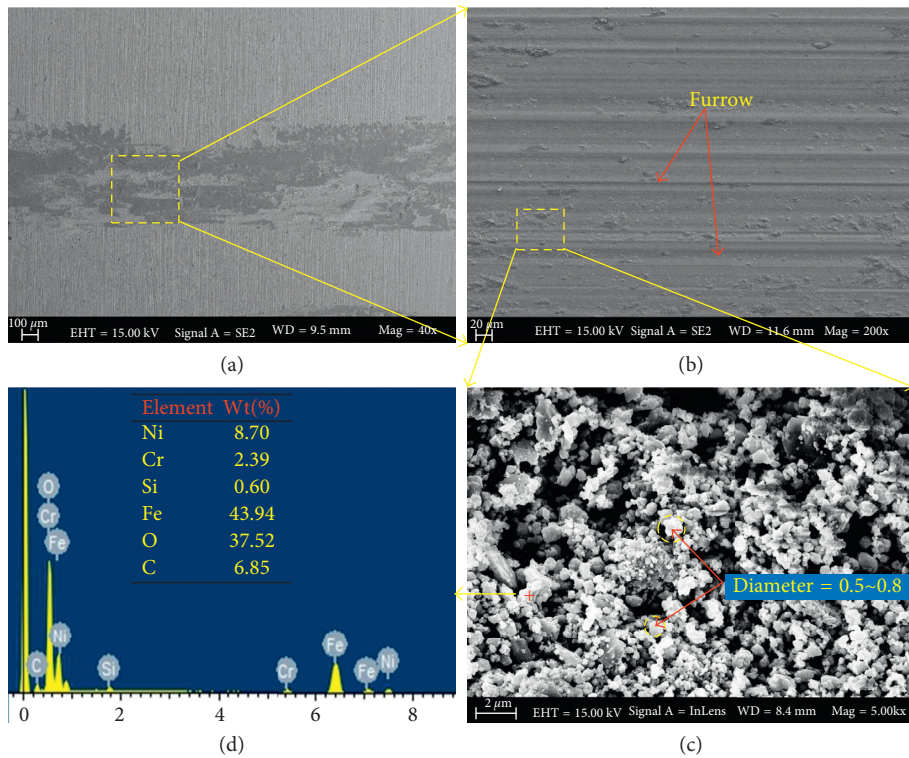


FIGURE 14: The remelted coating: (a) wear scar, (b) surface wear morphology, (c) debris morphology, and (d) energy spectrum and weight percent of debris.

between the coating and the substrate is changed from mechanical bonding to metallurgical bonding.

- (3) After remelting, the main phases in the sprayed coating are changed from γ -Ni, Cr_7C_3 , and Cr_2B to γ -Ni, Cr_{23}C_6 , CrB, Ni_3B , and Fe_3C .
- (4) The average hardness of sprayed coating is $710 \text{ HV}_{0.1}$, and its hardness is not even ($580\text{--}800 \text{ HV}_{0.1}$). After TIG remelting, the average hardness of coating is $900 \text{ HV}_{0.1}$, and its hardness is uniform. The average hardness of remelted coating is increased by 26.8% compared with that of the sprayed coating.
- (5) The wear resistance of remelted coating is superior than that of the sprayed coating, and the wear volume of remelted coating is only 17.1% greater than that of sprayed coating. The wear mechanism of the sprayed coating is lamellar cracking and oxidation wear, while the wear mechanism of the remelted coating is microabrasive wear and oxidation wear.

Conflicts of Interest

The authors declare that they have no conflicts of interest.

Acknowledgments

The work was financially supported by the National Natural Science Foundation of China (NSFC) under Grant nos. 51675158 and 51535011 and the Natural Science Foundation of Heibei Province of China under Grant no. E2016202325.

References

- [1] J. M. Miguel, J. M. Guilemany, and S. Vizcaino, "Tribological study of NiCrBSi coating obtained by different processes," *Tribology International*, vol. 36, no. 3, pp. 181–187, 2003.
- [2] Shabana, M. M. M. Sarcar, K. N. S. Suman, and S. Kamaluddin, "Tribological and corrosion behavior of HVOF sprayed WC-Co, NiCrBSi and Cr_3C_2 -NiCr coatings and analysis using design of experiments," *Materials Today: Proceedings*, vol. 2, no. 4-5, pp. 2654–2665, 2015.
- [3] L. Janka, J. Norpoth, and R. Trache, "Influence of heat treatment on the abrasive wear resistance of a Cr_3C_2 -NiCr coating deposited by an ethene-fuelled HVOF spray process," *Surface and Coatings Technology*, vol. 291, no. 3, pp. 444–451, 2016.
- [4] Z.-Y. Piao, B.-S. Xu, H.-D. Wang, and C.-H. Pu, "Effects of thickness and elastic modulus on stress condition of fatigue-resistant coating under rolling contact," *Journal of Central South University of Technology*, vol. 17, no. 5, pp. 899–905, 2010.
- [5] A. Nakajima, T. Mawatari, and M. Yoshida, "Effects of coating thickness and slip ratio on durability of thermally sprayed WC ceramic coating in rolling/sliding contact," *Wear*, vol. 241, no. 6, pp. 166–173, 2000.
- [6] J. Liu, R. Bolot, S. Costil, and M. P. Planche, "Transient thermal and mechanical analysis of NiCrBSi coatings manufactured by hybrid plasma spray process with in-situ laser remelting," *Surface and Coatings Technology*, vol. 292, no. 8, pp. 132–143, 2016.
- [7] L. Jiangwei, W. Yan, S. Costil, and R. Bolot, "Numerical and experimental analysis of molten pool dimensions and residual stresses of NiCrBSi coating treated by laser post-remelting," *Surface and Coatings Technology*, vol. 318, no. 10, pp. 341–348, 2017.
- [8] S. Zhou, J. Lei, X. Dai, J. Guo, Z. Gu, and H. Pan, "A comparative study of the structure and wear resistance of NiCrBSi/50 wt.% WC composite coatings by laser cladding and laser induction hybrid cladding," *International Journal of Refractory Metals and Hard Materials*, vol. 60, no. 32, pp. 17–27, 2016.
- [9] Š. Houdková, E. Smazalová, M. Vostřák, and J. Schubert, "Properties of NiCrBSi coating, as sprayed and remelted by different technologies," *Surface and Coatings Technology*, vol. 253, no. 34, pp. 14–26, 2014.
- [10] R. González, M. A. García, I. Penuelas et al., "Microstructural study of NiCrBSi coatings obtained by different processes," *Wear*, vol. 263, no. 1–6, pp. 619–624, 2007.
- [11] N. Serres, F. Hlawka, S. Costil, C. Langlade, and F. Machi, "Microstructures of metallic NiCrBSi coatings manufactured via hybrid plasma spray and in situ laser remelting process," *Journal of Thermal Spray Technology*, vol. 20, no. 1-2, pp. 336–343, 2011.
- [12] R. Gonzalez, M. Cadenas, R. Fernandez, J. L. Cortizo, and E. Rodriguez, "Wear behaviour of flame sprayed NiCrBSi coating remelted by flame or by laser," *Wear*, vol. 262, no. 3-4, pp. 301–307, 2007.
- [13] Y. Tao, K. Sindo, and L. Zhen, "Grain refining by ultrasonic stirring of the weld pool," *Acta Materialia*, vol. 106, no. 45, pp. 144–154, 2016.
- [14] G. Yi-min, *Metal Solidification Principle*, Xi'an Jiaotong University Press, Xi'an, China, 2009.
- [15] W. Kurz and D. J. Fisher, *Fundamentals of Solidification*, High Education Press, Beijing, China, 2010.
- [16] Z. Wen, Y. Bai, J. Yang, J. Huang, and L. Zhang, "Effect of vacuum remelting on microstructure and wear resistance of NiCrMoY coatings deposited by supersonic atmospheric plasma spraying," *Surface and Coatings Technology*, vol. 281, no. 1, pp. 62–67, 2015.
- [17] S. Johansson, P. H. Nilsson, R. Ohlsson, and B.-G. Rosén, "Experimental friction evaluation of cylinder liner/piston ring contact," *Wear*, vol. 271, no. 3-4, pp. 625–633, 2011.
- [18] M. Egawa, K. Miura, M. Yokoi, and I. Ishigami, "Effects of substrate bias voltage on projection growth in chromium nitride films deposited by arc ion plating," *Surface and Coatings Technology*, vol. 201, no. 3, pp. 4873–4878, 2007.
- [19] L. Tong, T. Yi, S. Shuang, X. Guo, J. Lia, and D. Wang, "Continuous electron beam melting technology of silicon powder by prefabricating a molten silicon pool," *Vacuum*, vol. 143, no. 5, pp. 336–343, 2017.
- [20] M. Xiangmeng, Q. Guoliang, and Z. Zengda, "Sensitivity of driving forces on molten pool behavior and defect formation in high-speed gas tungsten arc welding," *International Journal of Heat and Mass Transfer*, vol. 107, no. 7, pp. 1119–1128, 2017.
- [21] X. Wang, X. Chen, Q. Sun, H.-S. Di, and L.-N. Sun, "Formation mechanism of d-ferrite and metallurgy reaction in molten pool during press-hardened steel laser welding," *Materials Letters*, vol. 206, no. 9, pp. 143–145, 2017.
- [22] J. Yang, J. Han, H. Yu et al., "Role of molten pool mode on formability, microstructure and mechanical properties of selective laser melted Ti-6Al-4V alloy," *Materials and Design*, vol. 110, no. 15, pp. 558–570, 2016.
- [23] A. Ohmori and C. J. Li, "Quantitative characterization of the structure of plasma sprayed Al_2O_3 coating by using copper electroplating," *Thin Solid Films*, vol. 201, no. 2, pp. 241–252, 1991.
- [24] R. Colaco and R. Vilar, "Abrasive wear of metallic matrix reinforced materials," *Wear*, vol. 255, no. 1–6, pp. 643–650, 2003.

Research Article

The Influence of Anode Inner Contour on Atmospheric DC Plasma Spraying Process

Kui Wen,^{1,2} Min Liu,^{1,2} Kesong Zhou,^{1,2} Xuezhong Liu,^{1,2} Renzhong Huang,² Jie Mao,² Kun Yang,² Xiaofeng Zhang,² Chunming Deng,² and Changguang Deng²

¹*School of Materials Science and Engineering, Central South University, Changsha 410083, China*

²*National Engineering Laboratory for Modern Materials Surface Engineering Technology, The Key Lab of Guangdong for Modern Surface Engineering Technology, Guangdong Institute of New Materials, Guangzhou 510651, China*

Correspondence should be addressed to Min Liu; liumin_gz@163.net and Kesong Zhou; kszhou2004@163.com

Received 5 July 2017; Accepted 7 September 2017; Published 31 October 2017

Academic Editor: Shuo Yin

Copyright © 2017 Kui Wen et al. This is an open access article distributed under the Creative Commons Attribution License, which permits unrestricted use, distribution, and reproduction in any medium, provided the original work is properly cited.

In thermal plasma spraying process, anode nozzle is one of the most important components of plasma torch. Its inner contour controls the characteristics of plasma arc/jet, determining the motion and heating behaviors of the in-flight particles and hence influencing the coating quality. In this study, the effects of anode inner contour, standard cylindrical nozzle, and cone-shaped Laval nozzle with conical shape diverging exit (CSL nozzle) on the arc voltage, net power, thermal efficiency, plasma jet characteristics, in-flight particle behaviors, and coating properties have been systematically investigated under atmospheric plasma spraying conditions. The results show that the cylindrical nozzle has a higher arc voltage, net power, and thermal efficiency, as well as the higher plasma temperature and velocity at the torch exit, while the CSL nozzle has a higher measured temperature of plasma jet. The variation trends of the plasma jet characteristics for the two nozzles are comparable under various spraying parameters. The in-flight particle with smaller velocity of CSL nozzle has a higher measured temperature and melting fraction. As a result, the coating density and adhesive strength of CSL nozzle are lower than those of cylindrical nozzle, but the deposition efficiency is greatly improved.

1. Introduction

Thermal plasma spraying has been widely used to prepare high quality coatings, such as wear-, corrosion-, and oxidation-resistant coatings [1, 2] and thermal- and environmental-barrier coatings [3, 4]. Although a large number of experimental and modeling results concerning the plasma spraying process have been published [5–7], the complicated interactions of the plasma with electromagnetic, thermal, and acoustics phenomena are still not fully understood [8]. In plasma spraying, the anode nozzle is one of the key components of the plasma torch. Slight geometrical structure modification will result in a strong change in the length and stability of the plasma arc, the characteristics of plasma jet, and the thermal efficiency of plasma torch. The effects of anode nozzle on the plasma spraying process can be summarized in the following two aspects. First, the anode outer contour controls the formation and the intensity of

turbulence that affects the cold ambient air entrained into the plasma jet [9, 10]. Secondly, the anode inner contour determines the behavior of plasma arc inside the torch and the distributions of plasma jet temperature and velocity. Both factors will ultimately influence the coating quality, such as porosity and adhesive strength. In addition, compared with the anode outer contour, the inner contour plays a more important role in the plasma spraying process.

With regard to the vacuum plasma spraying (VPS), Cao et al. [11] reported that the plasma temperature gradient of Laval nozzle, consisting of a convergent part, a cylindrical channel, and a bell-shaped divergent exit (CCD-bell nozzle), was smaller than that of standard cylindrical nozzle (cylindrical nozzle), and it can improve the deposition efficiency and density of coatings. Rahmane et al. [12] proved that the length of the bell-shaped part also had a significant effect on the plasma jet characteristics. As the pressure decreased, the plasma jet of the longer CCD-bell nozzle reached the

supersonic state, while that of the shorter one was still in the subsonic state. Certainly, only when the working parameters were set properly, the Laval nozzle could accelerate the plasma jet to supersonic and improve the plasma spraying process [13].

As for the atmospheric plasma spraying (APS), Henne et al. [9, 14] proved that the CCD-bell nozzles were useful for reducing the entrainment of cold ambient air and extending the axial length hot core of the plasma jet, and also the corresponding coating qualities and deposition efficiency of the Laval nozzle were improved. In addition, Schwenk et al. [15, 16] designed several Convergent-Divergent Laval nozzles with bell-shaped diverging exit (CD-bell nozzle). In contrast to the cylindrical nozzle, these CD-bell nozzles can gain lower arc voltage fluctuations and acoustic levels and higher thermal and deposition efficiency, while there is no significant difference in porosity and adhesive strength.

Obviously, the aforementioned investigations mainly focused on the effects of cylindrical nozzles and bell-shaped Laval nozzles on the APS process. Studies with regard to the Laval nozzle with conical shape diverging exit (CSL nozzle) were seldom reported. In our study, we have found that the deposition efficiency is improved by the CSL nozzle, but the corresponding adhesive strength is reduced. It is different from the results of the bell-shaped Laval nozzles that are reported in the previous work. The difference in those results indicated that the intrinsic relationship between the anode nozzle and the coating had not been fully revealed.

In this paper, in order to clarify the effects of anode inner contour of cylindrical nozzle and CSL nozzle on plasma spraying process under APS conditions, the plasma jet characteristics, in-flight particle motion and heating behaviors, and coating properties were systematically investigated.

2. Experimental Details

2.1. Plasma Torch. At present, most commercial plasma torches applied in APS use anodes with cylindrical channel, and some also use anodes with Laval-like diverging exits. Therefore, all the following experiments were performed by the F6 atmospheric plasma spraying facility (GTV GmbH, Luckenbach, Germany), which was equipped with two different inner contour anode nozzles. Figure 1(a) shows a cylindrical nozzle with an exit diameter of 6.0 mm and a cylindrical channel length of 20.0 mm. The schematic of a CSL nozzle is shown in Figure 1(b), the corresponding throat and nozzle exit diameters are 7.0 mm and 12.5 mm, and the axial length of the divergent part is 26.0 mm. In addition, it is worth mentioning that the total length of the CSL nozzle is 2.0 mm longer than that of the cylindrical nozzle.

2.2. Diagnostic Equipment. The enthalpy probe system (Tekna Plasma Systems Inc., Canada) and DPV-eVOLUTION system (Tecnar Automation Ltd., Canada) were used to measure the characteristics of plasma jet and in-flight particles, respectively. The plasma temperature was obtained by calculating the energy balance of the circulating cooling water in the enthalpy probe, while the Bernoulli

equation was used to calculate the local velocity for low Mach number gas flow. The external and internal diameters of the enthalpy probe are 4.76 mm and 1.32 mm, and the corresponding area of orifice is 1.368 mm². The shortest measurement distance to the nozzle exit was set at 60 mm to avoid thermal overload of the probe tip. In-flight particle velocity, temperature, and diameter were measured by an optical sensing device DPV-eVOLUTION system. The surface temperature of the particle was measured by a high precision two-color pyrometer based on Planck's radiation law, which assumes the in-flight particles are gray body emitters with the same emissivity at both color bands. The velocity (V) was calculated by multiplying the real distance (S) of the slits on the photomask by the magnification factor (K) of the lens and then dividing the "time of flight" (t) between the two peaks of the particle signal; namely, $V = S \times K / t$. It is worth mentioning that the powder particles were radially injected into the plasma jet. More detailed theoretical information on the two measurement systems can be found in [17–20].

Figure 2 depicts the relative position of plasma torch and enthalpy probe system, while the DPV-eVOLUTION is located at the same position as the enthalpy probe system. Plasma torch was mounted on the six degrees of freedom robot to ensure the axis of the plasma torch coinciding with the axis of the enthalpy probe tip. The axial test positions (z -direction) of the plasma jet can be adjusted by liner movement of the plasma torch along the axis, while the radial test positions (x -direction) were controlled by the displacement controller.

2.3. Preparation of Al₂O₃ Coatings. A bulk AISI 1045 steel sheet with a dimension of $\Phi 25.4 \times 6.0$ mm was employed as the substrate. Since aluminum oxide coatings have a wide range of industrial applications, a commercial fused Al₂O₃ powder (5–22 μ m, HC Stark GmbH, Germany) was selected as feedstock in the experiments, as shown in Figure 3. Argon was chosen as the carrier gas (5 slpm, standard liter per minute), the inner diameter of the feedstock injector is 1.5 mm, and the corresponding powder feed rate is 16.25 g/min. Other detailed spraying parameters are shown in Table 1. Note that a NiAl layer is deposited on the substrate as bonding coating prior to the deposition of Al₂O₃. Microstructures of the Al₂O₃ coatings were characterized by scanning electron microscopy (Nova NanoSEM 430, FEI, Netherlands). The adhesive strength was performed through tensile adhesion test on a universal mechanical test machine (GOPPOINT Testing Equipment Co., Ltd., China) based on the ASTM C633-01 standard [21]. Three specimens for each spraying distance (90, 110, and 130 mm) were tested to obtain the mean adhesive strength and relative deposition efficiency (RDE). The latter is defined as the average increment of coating weight per spraying cycle, namely, the weight of Al₂O₃ coating divided by the total number of spraying cycles.

2.4. Spraying Parameters. In the actual industrial production, the adjustable spraying parameters are mainly working current, plasma gas composition, and flow rate. Therefore, it can

TABLE 1: Spraying parameters for online measurement and Al_2O_3 coatings deposition.

Case	Current (A)	Ar (slpm)	H_2 (slpm)	Spraying distance (mm)
I	650	40	10	60–150
II	450, 550, 650	40	10	90
III	550	40, 50, 60, 70, 80	10	90
IV	550	60, 62, 64, 66, 68	10, 8, 6, 4, 2	90
V	650	40	10	70, 90, 110
VI	650	40	10	90, 110, 130

Note. (1) Case III, the flow rate of H_2 maintains 10 slpm; (2) Case IV, the total flow rate of mixture gas is 70 slpm.

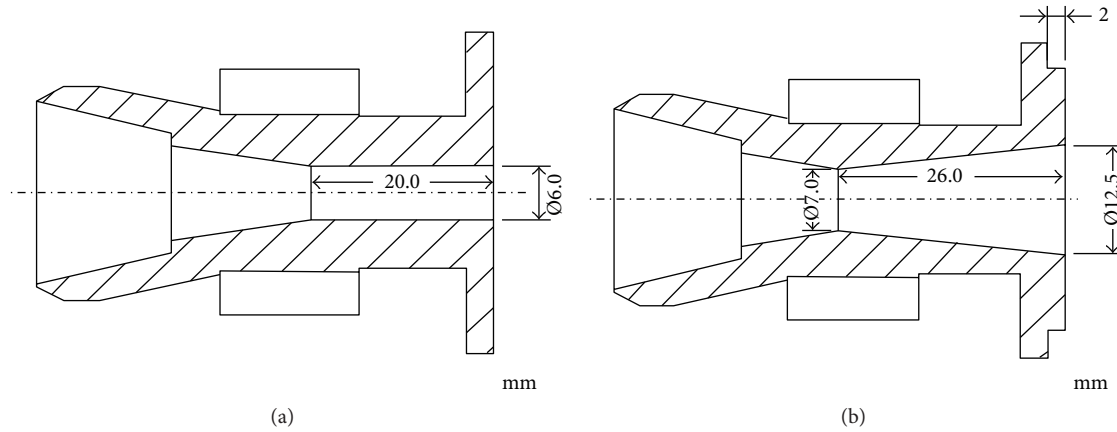


FIGURE 1: Schematic diagrams of anode nozzle inner contour: (a) cylindrical nozzle and (b) CD-conical nozzle.

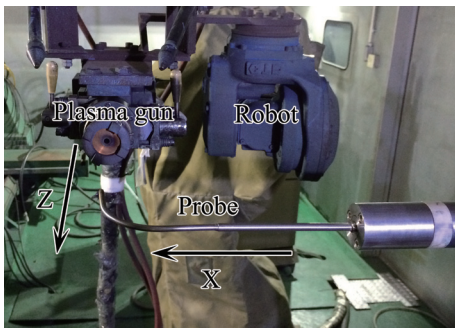


FIGURE 2: The relative position of the enthalpy probe and plasma gun.

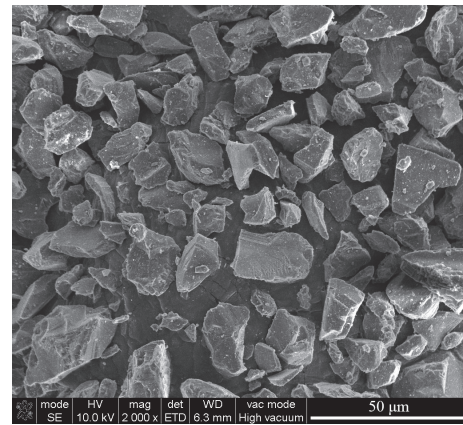


FIGURE 3: The morphology of fused Al_2O_3 powders.

better understand the spraying process of the two nozzles under different conditions by changing these parameters, which can provide experimental basis for the production process. The spraying parameters used in diagnostic measurement and coating fabrication are given in Table 1. Case I was used to measure the axial and radial distribution of plasma temperature and velocity. Case II, Case III, and Case IV were applied to investigate the influence of working current, argon flow rate, and hydrogen content on the plasma jet characteristics. Case V allowed measuring the in-flight particle temperature and velocity. Case VI was used to deposit the Al_2O_3 coatings.

3. Results and Discussion

3.1. Characteristics of Plasma Jet. Table 2 shows the voltage of the two nozzles under different working currents, as well as the corresponding net power and thermal efficiency. Here, only the case of 650 A is chosen to analyze the effect of the anode structure on the plasma jet characteristics, while the effect of the working current will be discussed in detail in the following parts. It can be seen from the table that, although both cylindrical and CSL nozzles operated with the same spraying parameters, the cylindrical nozzle has a slightly

TABLE 2: Different working currents correspond to the arc voltage, net power, and thermal efficiency (Ar/H₂: 40/10 slpm).

Current (A)	Voltage (V)		Net power (kW)		Thermal efficiency (%)	
	Cylindrical	Laval	Cylindrical	Laval	Cylindrical	Laval
450	75.4	75.3	18.9	17.6	55.7	52.0
550	74.8	73.3	22.9	20.9	55.7	51.9
650	74.3	72.0	26.0	23.9	53.8	51.0

Note. The voltage is the average value and is obtained by reading from the console window of spraying equipment.

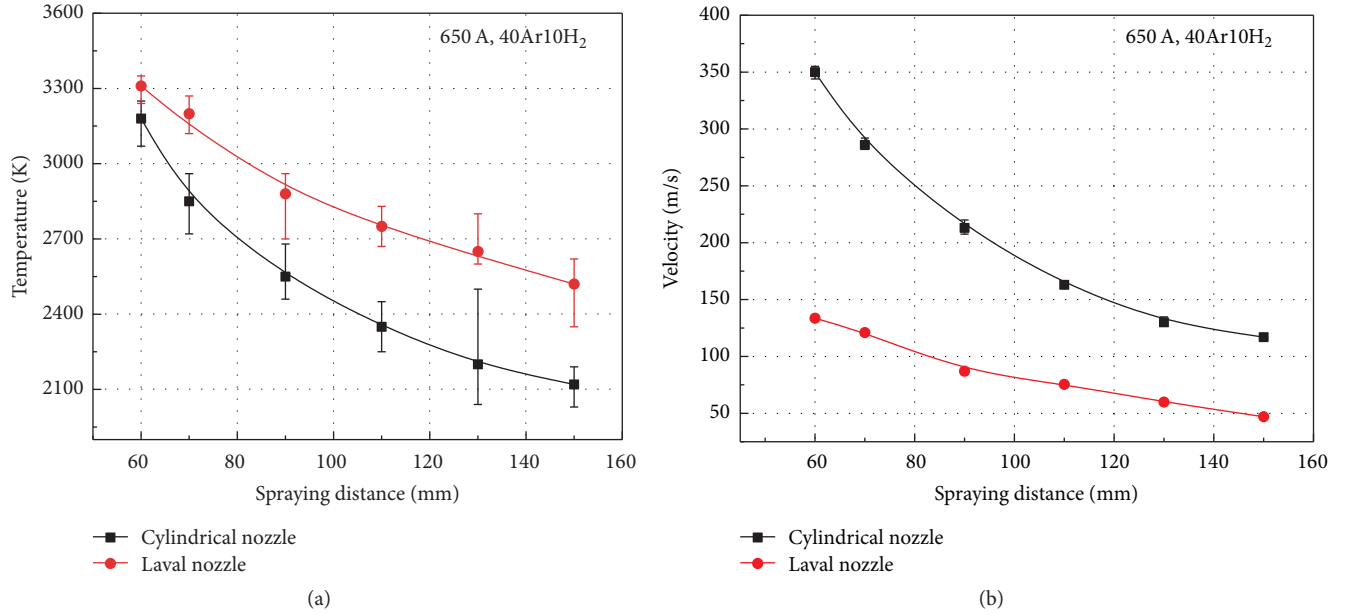


FIGURE 4: Axial profiles of measured plasma jet temperature (a) and velocity (b).

higher net power. Figure 4 presents the measured plasma temperature and velocity as functions of spraying distance. The plasma temperature of the CSL nozzle is about several hundreds of Kelvin higher than that of the cylindrical nozzle at the same measurement position. But the plasma velocity of the former is smaller within the whole measurement range, and the velocity difference became increasingly large towards the nozzle exit. Moreover, the plasma jet of CSL nozzle has a slower decrease in plasma temperature and velocity.

For the sake of convenience, we first analyze the reason for the difference in plasma velocity. Unlike the VPS, Laval nozzles typically produce subsonic plasma jets in an atmospheric environment [16, 22], which is consistent with what we observed in experiment. In this case, the plasma velocity at the throat of cylindrical nozzle is larger than that of CSL nozzle, because the velocity is inversely proportional to the throat cross-section area. Moreover, the velocity of the CSL nozzle in the divergent channel can be briefly illustrated by the relationship between the cross-section area and the velocity of the isentropic fluid flow, which is given as follows:

$$(\text{Ma}^2 - 1) \cdot \frac{du}{u} = \frac{dA}{A}, \quad (1)$$

where Ma is the Mach number and u , du , dA , and A are the gas velocity, increment of velocity, cross-section area,

and increment of the cross-section area, respectively. The Ma of subsonic flow is less than 1.0; thereby the items in the parentheses are negative. Obviously, if dA is greater than zero, du must be less than zero in order to satisfy the equality condition. This fact means that the plasma flow experienced a deceleration process in the divergent part of the CSL nozzle, resulting in a smaller plasma velocity inside of the CSL nozzle.

The higher net power indicates that the plasma of cylindrical nozzle contains more energy (E) which consists of internal energy ($c_p T$) and kinetic energy ($V^2/2$); namely, $E = c_p T + V^2/2$. While the plasma velocity of cylindrical nozzle is much larger than that of the CSL nozzle, so it is difficult to determine which nozzle produces plasma with a higher temperature. In order to reveal the reason for the difference in temperature, a 3D numerical model was developed to compute the heat transfer and gas dynamics for two nozzles. The predicted plasma temperature distributions at the nozzle exit are shown in Figure 5, it can be seen that the temperature of cylindrical nozzle is higher. However, this is the opposite of the measurement results shown in Figure 4(a). After careful analysis, the contradictory result should be attributed to the decay rate of plasma temperature. As mentioned by Schwenk et al., the CD-bell nozzle can reduce the arc voltage fluctuations [15, 16] which enhanced the instability of the plasma jet and caused more cold air entrainment.

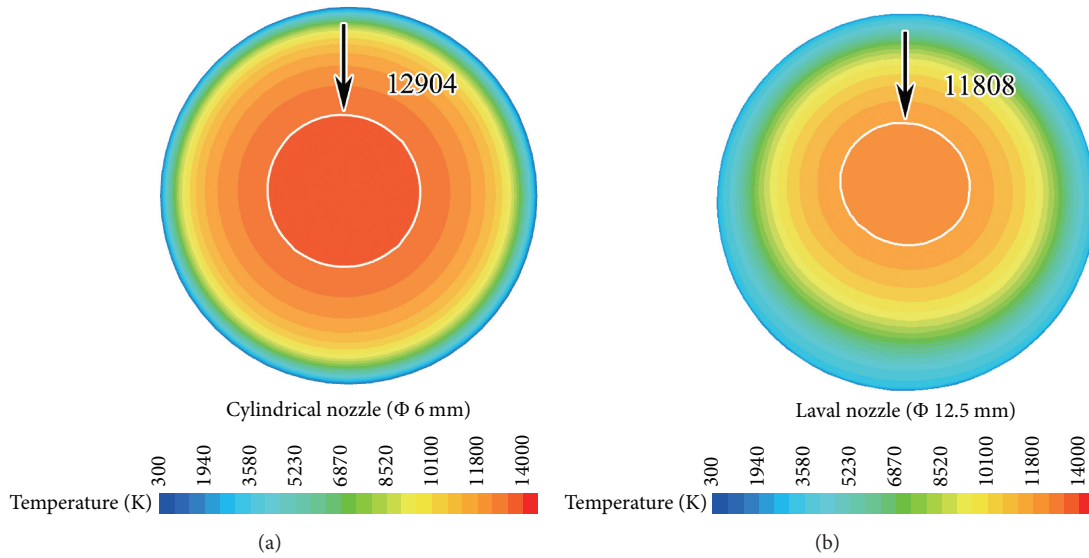


FIGURE 5: Predicted plasma temperature distributions at the exit of cylindrical nozzle (a) and CSL nozzle (b).

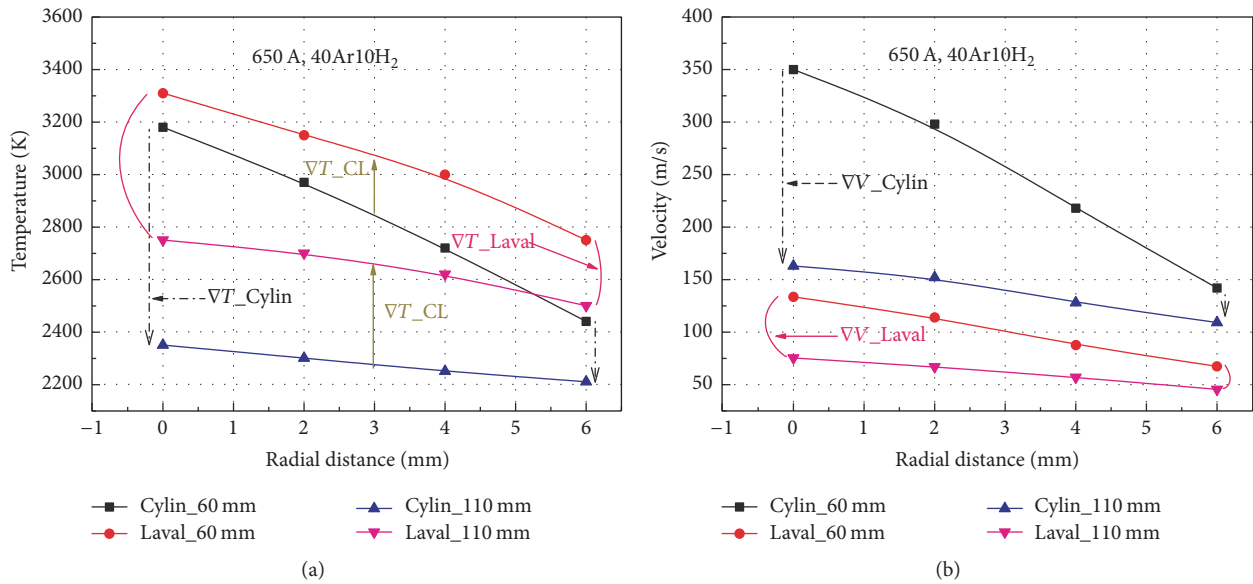


FIGURE 6: Radial profiles of measured plasma jet temperature (a) and velocity (b).

This phenomenon may also occur in the CSL nozzle with weaker arc fluctuations due to the similar inner structure. As a result, even though the plasma jet exits from cylindrical nozzle with a higher temperature, the strong ambient air entrainment caused the plasma temperature and velocity to decrease rapidly [23].

The radial distributions of plasma temperature and velocity of the two nozzles at the spraying distance of 60 mm and 110 mm are shown in Figure 6. It can be seen that the radial temperature and velocity gradients of the cylindrical nozzle jet at the 60 mm are larger than those of the CSL nozzle jet. These discrepancies are mainly caused by the different nozzle outlet radius that determines the size of the plasma jet. The outlet radius of the CSL nozzle is 6.25 mm,

while it is only 3.0 mm for the cylindrical nozzle. This fact means that the former can produce a plasma jet with larger diameter. Therefore, the measurement positions of the cylindrical nozzle probably reached the strong turbulent region of the plasma jet, but that of the CSL nozzle did not. As the spraying distance extended to 110 mm, the interaction between the plasma jet and the cold ambient air became more significant, which reduced the radial temperature and velocity gradients. This phenomenon was more noticeable for cylindrical nozzle. In addition, at the same spraying distance, the radial temperature of the CSL nozzle jet was higher than that of the cylindrical nozzle. For example, in the case of 60 mm spraying distance, the plasma temperature at the radial position of 6.0 mm of the CSL nozzle was about

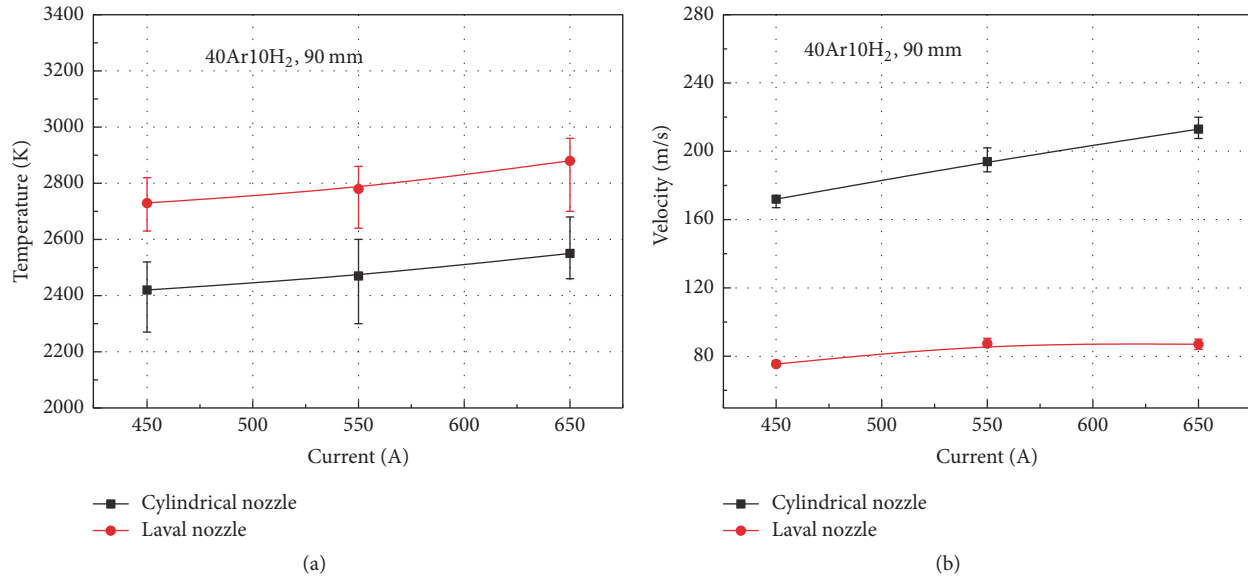


FIGURE 7: The distribution of plasma temperature (a) and velocity (b) at the different working current conditions.

2750.0 K, which was nearly equal to the temperature at the radial distance of 4.0 mm of the cylindrical nozzle.

According to Figure 6, from 60 mm to 110 mm spraying distance, the changing tendencies of the temperature difference and velocity difference of the plasma jet for two nozzles are comparable. For the sake of simplicity, only plasma temperature difference will be considered here to analyze the plasma characteristics. The symbols ∇T_{Cylin} and ∇T_{Laval} represent the plasma temperature difference of cylindrical and CSL nozzle, respectively. Both of them decreased with the increase of radial distance, and the corresponding variation of ∇T_{Cylin} was greater in radial direction. This fact means that the temperature reduction of the CSL nozzle jet was smoother within the entire measurement range, while a larger temperature decrease occurred in the central region of the cylindrical nozzle jet. The symbol ∇T_{CL} denotes the temperature difference between the cylindrical nozzle and CSL nozzle for a given spraying distance. Obviously, the ∇T_{CL} at the distance of 110 mm was larger than that of 60 mm. This fact proves once again that the plasma hot core was lengthened by the CSL nozzle. Based on the discussion of Figures 4–6, it is sensible to conclude that the CSL nozzle was able to obtain a homogeneous plasma jet with larger diameter and longer hot core compared to the cylindrical nozzle.

The influence of the electric power on the characteristics of plasma jet was studied by using different working currents (i.e., 450, 550, and 650 A); the corresponding arc voltage, net power, and thermal efficiency were listed in Table 2. As can be seen from this table, for both cylindrical and CSL nozzles, the increase in current results in increasing the net power but reducing the voltage and thermal efficiency; some previously published literatures have reported similar results [24, 25]. The plasma temperature and velocity dependencies on the current are shown in Figure 7. With the increase of current, the plasma temperature and velocity increase linearly, while there is a lesser velocity increase for CSL nozzle.

In general, the arc voltage in direct current nontransferred plasma torch is approximately linearly dependent on the arc length which is determined by the balance between electromagnetic force and flow drag force [26]. The increase of current implies that a greater Lorentz force acts on the anode arc column and forces the arc to move upwards to reduce the arc voltage. Moreover, the increase in current also leads to more electric power (j^2/σ , where j and σ are the current density and plasma electric conductivity) dissipating into plasma gas in the form of thermal energy, allowing more plasma forming gas to take part in the heating and ionization process. Therefore, besides the gas temperature increase, the expansion effect was also enhanced by the decreased gas density. Consequently, the plasma jet exited from the nozzle with a higher velocity and extended the plasma jet in the axial direction. In addition, the cathode jet formed in front of the cathode also played a positive role in increasing plasma velocity. Equation (2) can be used to describe the relationship between the current and the maximum velocity that the cathode jet may be reached [27]:

$$u_{\max} = \left(\frac{\mu_0 I}{2\pi\rho} \right)^{1/2}, \quad (2)$$

where u_{\max} , μ_0 , I , and ρ are the maximum velocity of cathode jet, permeability of vacuum, working current, and plasma density, respectively. The numerator in (2) increased as the working current increased from 450 A to 650 A, while the denominator was reduced due to the decrease in density. As a result, the increased u_{\max} increases the velocity of the superimposed axial plasma flow.

Table 3 lists the relationship between the argon flow rate and the plasma arc voltage, net power, and thermal efficiency of the two nozzles. For given current, the values of these variables are increased with the argon flow rate. Take the arc voltage of cylindrical nozzle as an example: when the flow

TABLE 3: The relationship between Ar flow rate and arc voltage and net power and thermal efficiency (current: 550 A).

Working gas (slpm)		Voltage (V)		Net power (kW)		Thermal efficiency (%)	
Ar	H ₂	Cylindrical	Laval	Cylindrical	Laval	Cylindrical	Laval
40	10	74.8	73.3	22.9	20.9	55.7	51.9
50	10	78.0	76.0	24.4	22.7	56.9	54.3
60	10	79.9	79.5	25.6	24.8	58.3	56.7
70	10	81.0	82.4	26.4	26.2	59.3	57.9
80	10	82.5	85.2	27.3	28.3	60.2	60.4

Note. H₂ flow rate is 10 slpm.

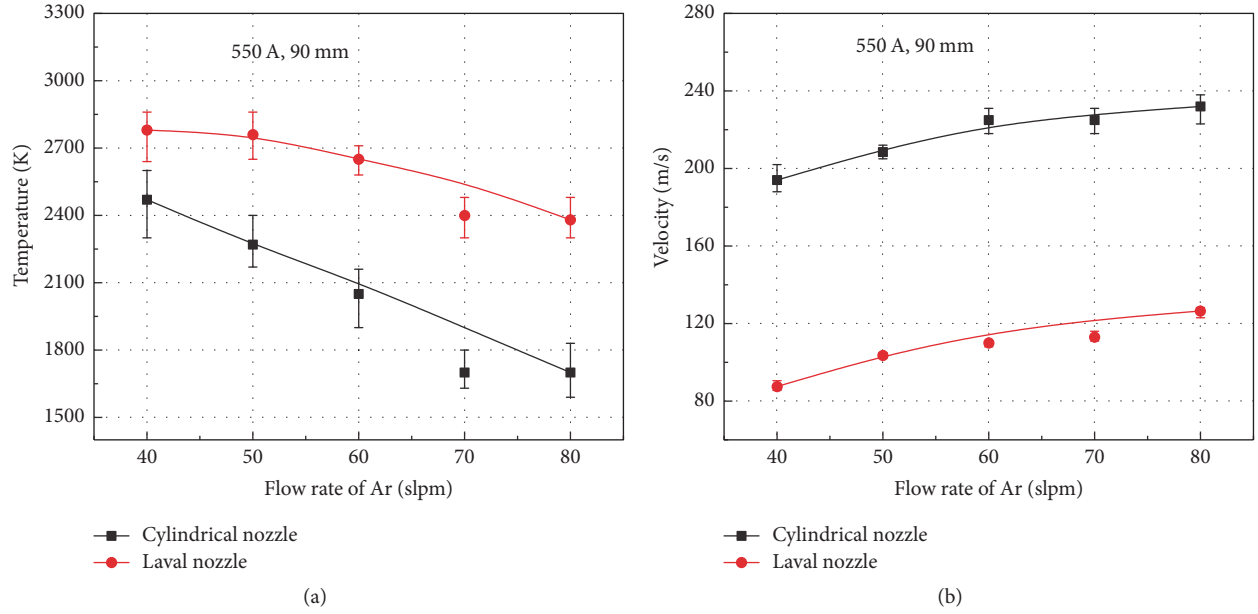


FIGURE 8: The profiles of plasma jet temperature (a) and velocity (b) with different Ar flow rate (flow rate of H₂: 10 slpm).

rate of argon increased from 40 to 80 slpm, the corresponding arc voltage increased from 74.8 to 82.5 V. Because the rise of the total gas flow rate increased the drag force that pushes the plasma arc to move downstream, this fact can also be qualitatively described by the following relation [28]:

$$L_{\text{arc}} \sim \frac{\rho^{5/4} U_{\text{gas}}}{I}, \quad (3)$$

where L_{arc} and U_{gas} are the arc length and the velocity of working gas, respectively. The increase of argon flow rate not only increased the density of mixed gas, but also increased the working gas velocity (U_{gas}). Therefore, when the working current is constant, the arc length was lengthened.

As shown in Figure 8, the plasma velocity increases with the argon flow rate, but the corresponding temperature is reduced. Generally speaking, the increase in net electric power resulting from the increased argon flow rate implies that more energy dissipated into the plasma gas, which tends to increase the plasma temperature. Whereas if the electric power was kept constant, the rise of total gas flow rate resulted in the reduction of the gas temperature [29]. In this study, the decrease of the plasma temperature due to the argon flow rate increase cannot be compensated by the corresponding

electric power increment. Similar to the temperature, there were also two opposite phenomena in plasma velocity. On the one hand, the decrease of temperature caused a higher gas density, which resulted in declining plasma velocity. On the other hand, if the temperature remains constant, the gas velocity has to increase to satisfy the continuity equation with the increase of argon flow rate. As a result, the effect of the second phenomenon was more pronounced under our experimental conditions, and the plasma velocity was increased.

In order to investigate the influence of hydrogen content on the characteristics of plasma jet, the total gas flow rate was kept at 70 slpm. The values of plasma arc voltage, net power, and thermal efficiency for different hydrogen content were listed in Table 4. The increase of hydrogen content results in an increase in arc voltage, net power, and thermal efficiency. Moreover, the hydrogen content had a greater influence on these variables of the CSL nozzle than that of the cylindrical nozzle. Figure 9 shows the profiles of plasma jet temperature and velocity as functions of the hydrogen content. It can be observed that the plasma temperature and velocity of the two nozzles increased with the hydrogen content.

TABLE 4: The relationship between H₂ content and arc voltage and net power and thermal efficiency (current: 550 A).

Working gas (slpm)		Voltage (V)		Net power (kW)		Thermal efficiency (%)	
Ar	H ₂	Cylindrical	Laval	Cylindrical	Laval	Cylindrical	Laval
68	2	67.3	61.6	21.3	18.2	57.5	53.6
66	4	70.9	68.0	22.4	20.5	57.4	54.8
64	6	74.6	72.6	23.9	22.2	58.2	55.7
62	8	77.3	76.1	24.9	23.5	58.5	56.2
60	10	79.9	79.5	25.6	24.8	58.3	56.7

Note. Total gas flow rate is 70 slpm.

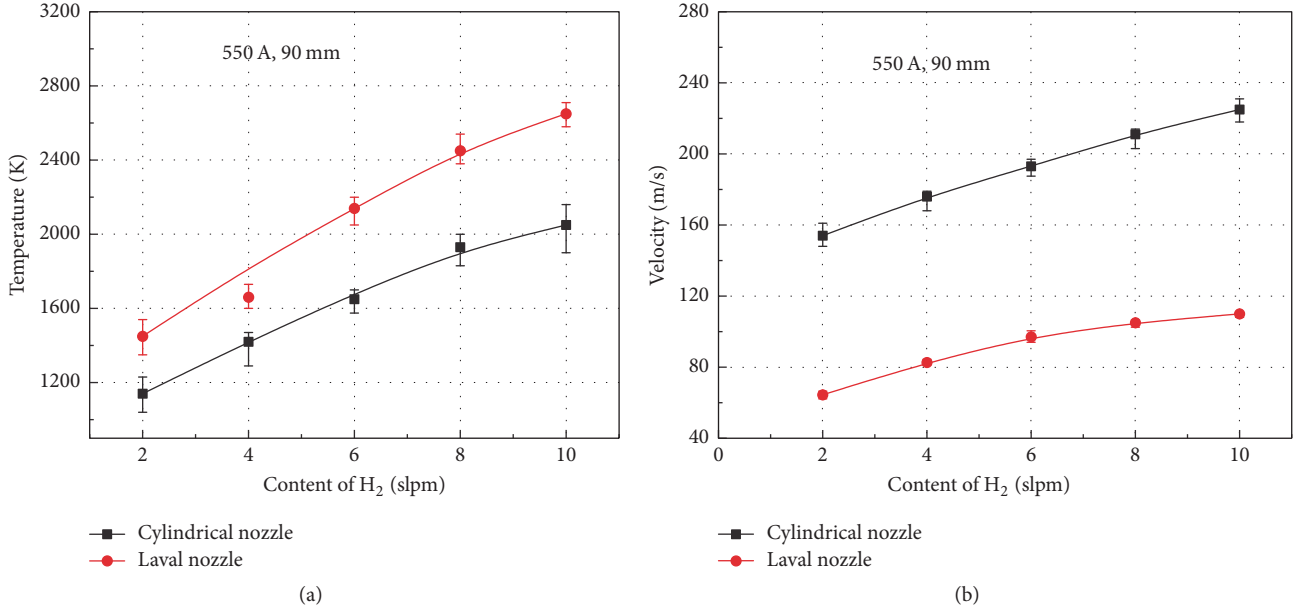


FIGURE 9: The profiles of plasma jet temperature (a) and velocity (b) with different H₂ content (total gas flow rate: 70 slpm).

The hydrogen has a high specific heat and thermal conductivity, both requiring a larger electric field to sustain the plasma arc [30]. Therefore, for a given current, the arc voltage has to increase in order to provide a higher electric field strength. In other words, the increase of hydrogen content required more electric power to maintain the stability of the plasma arc, which led to the increase of the plasma temperature. As discussed in the effect of working current, the increased temperature resulting from the increased electric power leads to decreased gas density, which enhances the expansion effect of the plasma gas. In addition, the increase in hydrogen content reduces the total density of the mixed working gas, because the density of hydrogen is much lower than that of argon. Thus, the ratio in the parentheses of (2) increased with the decrease of gas density and finally increased the maximum velocity of cathode jet.

3.2. In-Flight Particle Behavior. Figure 10(a) presents the measured particle temperature decrease with the increase of the spraying distance. The temperature profile of the CSL nozzle has a greater downward trend and with a larger temperature until 90 mm distance. All measured temperatures are observed in the range of melting (2,323 K) and boiling

(3,253 K) point of the Al₂O₃ powder; it implies that the particle surface was in the molten state. In general, the heat transfer between the plasma jet and in-flight particle can be described by the following equation:

$$q_{\text{conv}} = \frac{\beta_1 \beta_2 \text{Nu}_s \bar{k} (T_\infty - T_w)}{(2r_p)}, \quad (4)$$

where q_{conv} is the specific heat flux at the particle surface and β_1 and β_2 are the two factors used to correct the Knudsen and evaporation effects. Nu_s , \bar{k} , T_∞ , T_w , and r_p are the Nusselt number, average thermal conductivity within the Knudsen layer, plasma temperature, particle surface temperature, and particle radius, respectively. Apparently, the heat transfer occurred as long as there was a temperature difference. By comparing Figures 4(a) and 10(a), the temperature of plasma jet was higher than that of particle at the given spraying distance. According to (4), the temperature of particle should be further increased theoretically. However, the fact is that the particle temperature declined slightly. Actually, there is no contradiction here, because the particle temperature depends primarily on the ambient gas temperature of the flight trajectory. Recalling Section 2.2, the particles were fed

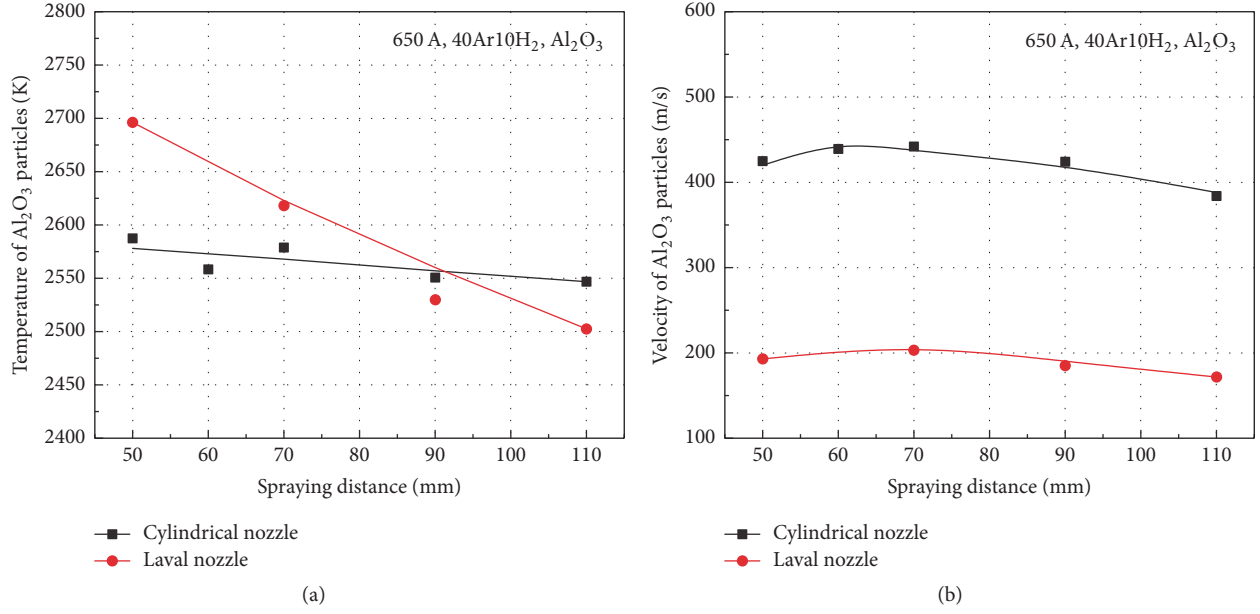


FIGURE 10: The profiles of Al_2O_3 particle surface temperature (a) and velocity (b).

along the radial direction, which means the centerline of in-flight particle jet was deviated from that of plasma jet. That is, the in-flight particle at the measured position has passed through the high temperature region; namely, $T_\infty - T_w > 0$. In addition, although the CSL nozzle has a lower plasma temperature at the nozzle exit, the extended plasma jet core region and the smaller plasma velocity prolong the particles residence time, which allows the injected particles to be better heated. However, the smaller velocity also extended the residence time of the particle in the cold environment, resulting in a larger decrease rate of in-flight particle along the spraying distance. Finally, the particle temperature of CSL nozzle was lower than that of cylindrical nozzle beyond 90 mm.

The dependence of the measured particle velocity on the spraying distance of the two nozzles is shown in Figure 10(b). They show a similar behavior that the particle velocity increases first and then gradually slows down. Moreover, the particle velocity of CSL nozzle is much lower than that of cylindrical nozzle over the whole measured range. Those phenomena can be revealed by the particle motion which is mainly controlled by the fluid drag and thermophoresis forces in the plasma jet. According to Newton's second law, the force balance can be written as [31]

$$\frac{d\vec{u}_p}{dt} = \frac{18\rho C_D}{24r\rho_p} \cdot |\vec{u} - \vec{u}_p| \cdot (\vec{u} - \vec{u}_p) + \vec{F}_t. \quad (5)$$

Here, \vec{u} , \vec{u}_p , and \vec{F}_t are the vectors of plasma velocity, particle velocity, and thermophoresis force, respectively. The symbols ρ_p , C_D , and t are the particle density, drag coefficient, and time. The increase in particle velocity means that the plasma jet has a larger velocity ($\vec{u} - \vec{u}_p > 0$), but unfortunately the plasma properties at 50 mm distance were

not measured, because the high heat loads increase the risk of damaging the enthalpy probe. Combining the features of the plasma velocity in Figure 4(b), it can be deduced that the in-flight particles have a maximum velocity in the range of 50 to 60 mm, and then they show a linear decrease over the whole range beyond 60 mm spraying distance. In addition, a larger plasma velocity of cylindrical nozzle is responsible for its larger particle velocity, because the larger relative velocity ($\vec{u} - \vec{u}_p$) corresponds to a stronger acceleration process.

3.3. Al_2O_3 Coating Properties. The surface morphologies of the Al_2O_3 coatings fabricated using the cylindrical and CSL nozzles are demonstrated in Figure 11, and the spraying distance is 110 mm. It can be observed that the coating prepared by the former has a rough surface consisting of semimolten particles, irregular splats, splashing fingers, and some open voids. However, the coating produced via the latter presents smoother surface with less semimolten particles and few splashing fingers. This fact indirectly reflects that the particles of the CSL nozzle were molten more sufficiently, which was mainly caused by the different characteristics of the plasma jet. As discussed earlier, the measured particle temperature was risen due to the extended plasma jet and the longer particle residence time; in fact, the particle melt fraction was also increased. In addition, the particle temperature of CSL nozzle was still above the melting point even though it has experienced a drastic decrease. All in all, the difference in particle temperature and melting fraction of the two nozzles is attributed to the residence time and small thermal conductivity of the Al_2O_3 powder. The later usually results in a considerable temperature gradient inside the particles, which has been confirmed by previous numerical simulation results [32].

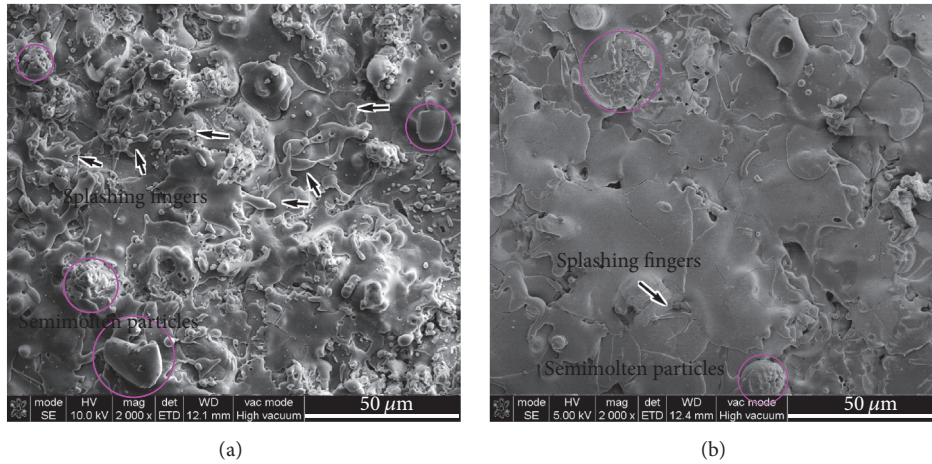


FIGURE 11: Surface micrographs of Al_2O_3 coatings prepared by cylindrical nozzle (a) and CSL nozzle (b) (current: 650 A, Ar/H_2 : 40/10 slpm, spraying distance: 110 mm).

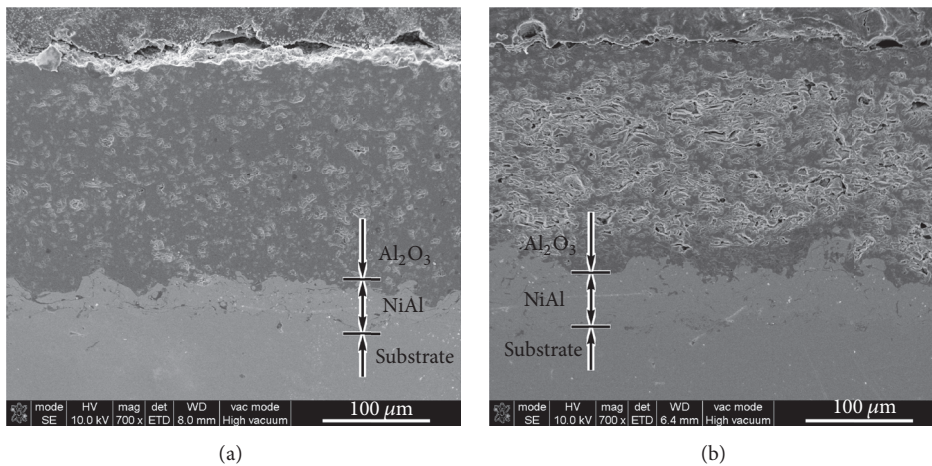


FIGURE 12: Cross-sectional SEM micrographs of Al_2O_3 coatings prepared by cylindrical nozzle (a) and CSL nozzle (b) (current: 650 A, Ar/H_2 : 40/10 slpm, spraying distance: 110 mm).

Figure 12 depicts the cross-sectional micrographs of the Al_2O_3 coatings. A dense coating was obtained by the cylindrical nozzle, whereas the coating produced by the CSL nozzle had a large number of pores, and the contact between the coating splats was not very good. Figure 13 shows the adhesive strength and the RDE of the coatings produced by the two nozzles at different spraying distances. Two phenomena can be observed in Figure 13(a): one is that the adhesive strength decreased with the increase of the spraying distance, and the other one is that the adhesive strength of the coating produced via the cylindrical nozzle was almost twice higher than via CSL nozzle. Figure 13(b) presents the average incremental weight of the Al_2O_3 coatings per spraying cycle. It is clear that the CSL nozzle has a higher RDE in the preparation of the coating.

By overall considering the particle velocity, melting state, and coating properties, it can be found that the effect of the particle velocity on the coating adhesive strength and porosity was greater than that on the melting state

under the present experimental conditions. Even though the coating prepared by the cylindrical nozzle contained more semimolten particles, the higher velocity means that the in-flight particle impacted on the substrate or as-sprayed coating with a higher kinetic energy, which enhanced the compaction effect of the coating. This improved the contact between the coating lamellas and also facilitated the filling of the pores with molten particles. As discussed in Section 3.1, the plasma jet of the CSL nozzle had a larger diameter and lower velocity. In this case, more particles can stay in the high temperature core region and undergo better effective heating, which resulted in more molten particles deposited on the substrate or as-sprayed coating, thereby increasing the RDE.

The results of the coating properties in this study are somewhat different from those reported in previous investigations, which presented that the coating properties of cylindrical and bell-shaped Laval nozzles were in the same range except the deposition efficiency. This fact suggests that the coating properties are strongly related to the structure

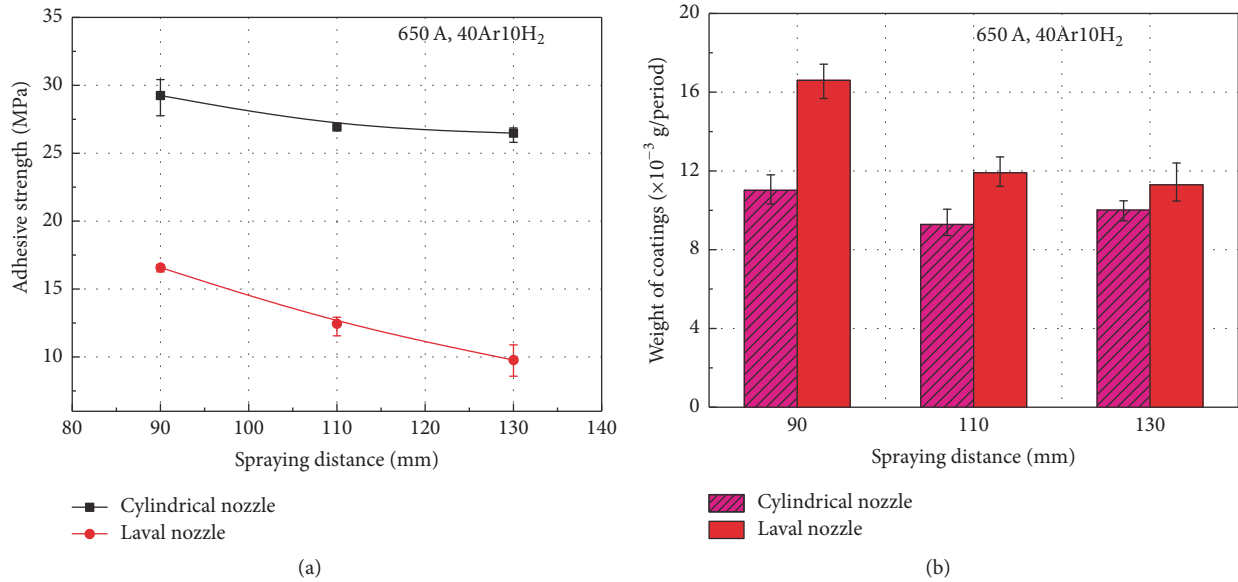


FIGURE 13: Adhesive strength (a) and average increment of coating weight per cycle (b) for different spraying distance.

of anode nozzles and the other factors such as the spraying parameters and substrate properties.

4. Conclusions

Thermal plasma spraying is normally regarded as a mature technology, but the detailed effect of the anode nozzle contour on the spraying process is still not fully understood. In this work, both for cylindrical and CSL nozzles, the plasma jet characteristics, in-flight particle behaviors, and coating properties have been systematically studied by experimental method, and the intrinsic relationship between them has been also revealed. The essential results obtained are as follows:

- (1) For given current and plasma forming gas, the cylindrical nozzle exhibits higher arc voltage, net power, and thermal efficiency and has a higher temperature and velocity distributions at the nozzle exit. However, the plasma jet of the CSL nozzle is characterized by a higher temperature and smaller velocity with a slower downward trend in the whole measured range, which is attributed to the less entrainment of ambient cold air.
- (2) Both for cylindrical and Laval nozzles, the values of arc voltage, net power, thermal efficiency, plasma temperature, and velocity are increased with the working current, Ar flow rate, and H₂ content, whereas the increase in current and argon flow rate leads to a decrease of the thermal efficiency and plasma temperature, respectively.
- (3) The smaller particle velocity of CSL nozzle prolongs the residence time in the high temperature region, which leads to a higher particle temperature and a larger melting fraction, but it also increases the particle residence time in the cold environment and results in a larger cooling rate. Moreover, there should

be a maximum particle velocity in the range of 50–60 mm distance.

- (4) In contrast to the cylindrical nozzle, the smaller particle velocity of the CSL nozzle leads to lower coating density and adhesive strength. Nevertheless, the RDE is higher because the homogeneous plasma jet has a larger diameter, which allows more particles to experience better heating.

Conflicts of Interest

The authors declare that they have no conflicts of interest.

Acknowledgments

This work was financially supported by the Guangdong Natural Science Foundation (2016A030312015), Guangdong Technical Research Program (201313050800031, 201413050502008, 2014B070706026, and 2013B061800053), and Guangdong Academy of Sciences (2017GDASCX-0843, 2016GDASPT-0206, and 2016GDASPT-0317).

References

- [1] P. Fauchais, "Understanding plasma spraying," *Journal of Physics D: Applied Physics*, vol. 37, no. 9, pp. R86–R108, 2004.
- [2] R. C. Tucker, Ed., *ASM Handbook, Volume 5A: Thermal Spray Technology*, ASM International, 2013.
- [3] F. Chang, K. Zhou, X. Tong, L. Xu, X. Zhang, and M. Liu, "Microstructure and thermal shock resistance of the peg-nail structured TBCs treated by selective laser modification," *Applied Surface Science*, vol. 317, pp. 598–606, 2014.
- [4] X. F. Zhang, K.-S. Zhou, X. Wei, B.-Y. Chen, J.-B. Song, and M. Liu, "In situ synthesis of α -alumina layer at top yttrium-stabilized zirconia thermal barrier coatings for oxygen barrier," *Ceramics International*, vol. 40, no. 8, pp. 12703–12708, 2014.

- [5] G. Mariaux and A. Vardelle, "3-D time-dependent modelling of the plasma spray process. Part I: Flow modelling," *International Journal of Thermal Sciences*, vol. 44, no. 4, pp. 357–366, 2005.
- [6] E. Nogues, M. Vardelle, P. Fauchais, and P. Granger, "Arc voltage fluctuations: Comparison between two plasma torch types," *Surface and Coatings Technology*, vol. 202, no. 18, pp. 4387–4393, 2008.
- [7] M. Alaya, C. Chazelas, and A. Vardelle, "Parametric Study of Plasma Torch Operation Using a MHD Model Coupling the Arc and Electrodes," *Journal of Thermal Spray Technology*, vol. 25, no. 1-2, pp. 36–43, 2016.
- [8] A. Vardelle, C. Moreau, N. J. Themelis, and C. Chazelas, "A Perspective on Plasma Spray Technology," *Plasma Chemistry and Plasma Processing*, vol. 35, no. 3, pp. 491–509, 2015.
- [9] R. Henne, E. Bouyer, V. Borck, and G. Schiller, "Influence of anode nozzle and external torch contour on the quality of the atmospheric DC plasma spray process, Thermal spray 2001: New surface for a new millennium," in *Proceedings of the Thermal spray: New surface for a new millennium (ITSC)*, C. C. Berndt, K. A. Khor, and E. Lugscheider, Eds., pp. 471–478, ASM International, 2001.
- [10] Y. Gao and L. T. An, "Characteristic of the arc length and voltage in a DC Bi-Anode plasma torch, Thermal spray connects: Explore its surfacing," in *Proceedings of the Thermal spray connects: Explore its surfacing potential (ITSC)*, E. Lugscheider, Ed., ASM International, Basel, Switzerland, 2005.
- [11] M. Cao, F. Gitzhofer, D. V. Gravelle, R. Henne, and M. I. Boulos, "A torch nozzle design to improve plasma spraying techniques," *Plasma Sources Science and Technology*, vol. 6, no. 1, pp. 39–45, 1997.
- [12] M. Rahmane, G. Soucy, M. I. Boulos, and R. Henne, "Fluid Dynamic Study of Direct Current Plasma Jets for Plasma Spraying Applications," *Journal of Thermal Spray Technology*, vol. 7, no. 3, pp. 349–356, 1998.
- [13] R. Bolot, D. Klein, and C. Coddet, "Influence of the nozzle design on the structure of a plasma jet under vacuum conditions," in *Proceedings of the International thermal spray conference*, E. Lugscheider, Ed., pp. 938–943, Essen, Germany, 2002.
- [14] R. H. Henne, V. Borck, D. Siebold et al., "Converging-Diverging nozzles for improved atmospheric plasma spraying," in *Proceedings of the 3rd European Congress on Thermal Plasma Processed*, pp. 247–266, 1995.
- [15] A. Schwenk, G. Nutsch, and H. Gruner, "Modified nozzle for the atmospheric plasma spraying," in *Proceedings of the Thermal Spray 2003 Advancing the Science and Applying the Technology*, R. M. Basil and M. Christian, Eds., pp. 573–579, ASM International, 2003.
- [16] A. Schwenk, H. Gruner, S. Zimmermann, K. Landes, and G. Nutsch, "Improved nozzle design of de-laval-type nozzles for the atmospheric plasma spraying," in *Proceedings of the Thermal spray solution, advances in technology and application (ITSC)*, DVS, Osaka, Japan, 2004.
- [17] G. Mauer, A. Guignard, R. Vaßen, and D. Stöver, "Process diagnostics in suspension plasma spraying," *Surface and Coatings Technology*, vol. 205, no. 4, pp. 961–966, 2010.
- [18] G. Mauer, R. Vaen, and D. Stöver, "Plasma and particle temperature measurements in thermal spray: Approaches and applications," *Journal of Thermal Spray Technology*, vol. 20, no. 3, pp. 391–406, 2011.
- [19] S. Yin, M. Meyer, W. Li, H. Liao, and R. Lupoi, "Gas Flow, Particle Acceleration, and Heat Transfer in Cold Spray: A review," *Journal of Thermal Spray Technology*, vol. 25, no. 5, pp. 874–896, 2016.
- [20] M. Rahmane, G. Soucy, and M. I. Boulos, "Analysis of the enthalpy probe technique for thermal plasma diagnostics," *Review of Scientific Instruments*, vol. 66, no. 6, pp. 3424–3431, 1995.
- [21] ASTM, "Standard test method for adhesion or cohesion strength of thermal spray coatings," 2001.
- [22] R. Henne, T. Kavka, J. Arnold, and G. Schiller, "Improvement of DC thermal plasma spraying by reducing the cold gas entrainment, Thermal spray connects: Explore its surfacing," in *Proceedings of the Thermal Spray Connects: Explore Its Surfacing Potential (ITSC)*, E. Lugscheider, Ed., Basel, Switzerland, 2005.
- [23] J. R. Fincke, W. D. Swank, and D. C. Haggard, "Entrainment and demixing in subsonic argon/helium thermal plasma jets," *Journal of Thermal Spray Technology*, vol. 2, no. 4, pp. 345–350, 1993.
- [24] Z. Guo, S. Yin, H. Liao, and S. Gu, "Three-dimensional simulation of an argon-hydrogen DC non-transferred arc plasma torch," *International Journal of Heat and Mass Transfer*, vol. 80, pp. 644–652, 2015.
- [25] B. Selvan, K. Ramachandran, K. P. Sreekumar, T. K. Thiagarajan, and P. V. Ananthapadmanabhan, "Numerical and experimental studies on DC plasma spray torch," *Vacuum*, vol. 84, no. 4, pp. 444–452, 2009.
- [26] J. P. Trelles, *Finite element modeling of flow instabilities in arc plasma torches [Doctoral, thesis]*, University of Minnesota, 2007.
- [27] S. Paik, P. C. Huang, J. Heberlein, and E. Pfender, "Determination of the arc-root position in a DC plasma torch," *Plasma Chemistry and Plasma Processing*, vol. 13, no. 3, pp. 379–397, 1993.
- [28] E. R. Eckert, E. Pfender, and S. A. Wutzke, "Symptomatic behavior of an electric arc with a superimposed flow," *AIAA Journal*, vol. 6, no. 8, pp. 1474–1482, 1968.
- [29] A. Capetti and E. Pfender, "Probe measurements in argon plasma jets operated in ambient argon," *Plasma Chemistry and Plasma Processing*, vol. 9, no. 2, pp. 329–341, 1989.
- [30] P. Fauchais, J. V. R. Heberlein, and M. I. Boulos, *Thermal Spray Fundamentals. from Powder to Part*, Springer, 2014.
- [31] H. P. Li and X. Chen, "Three-Dimensional Modeling of the Turbulent Plasma Jet Impinging upon a Flat Plate and with Transverse Particle and Carrier-Gas Injection," *Plasma Chemistry and Plasma Processing*, vol. 22, no. 1, pp. 27–58, 2002.
- [32] X. Chen and E. Pfender, "Unsteady heating and radiation effects of small particles in a thermal plasma," *Plasma Chemistry and Plasma Processing*, vol. 2, no. 3, pp. 293–316, 1982.

Research Article

Thermal Effect on Structural Interaction between Energy Pile and Its Host Soil

Qingwen Li,^{1,2} Lu Chen,¹ and Lan Qiao¹

¹Department of Civil Engineering, University of Science and Technology Beijing, Beijing 100083, China

²State Key Laboratory of Building Safety and Built Environment, China Academy of Building Research, Beijing 100013, China

Correspondence should be addressed to Qingwen Li; qingwenli@ustb.edu.cn

Received 6 April 2017; Revised 23 June 2017; Accepted 4 July 2017; Published 15 August 2017

Academic Editor: Shuo Yin

Copyright © 2017 Qingwen Li et al. This is an open access article distributed under the Creative Commons Attribution License, which permits unrestricted use, distribution, and reproduction in any medium, provided the original work is properly cited.

Energy pile is one of the promising areas in the burgeoning green power technology; it is gradually gaining attention and will have wide applications in the future. Because of its specific structure, the energy pile has the functions of both a structural element and a heat exchanger. However, most researchers have been paying attention to only the heat transfer process and its efficiency. Very few studies have been done on the structural interaction between the energy pile and its host soil. As the behavior of the host soil is complicated and uncertain, thermal stresses appear with inhomogeneous distribution along the pile, and the peak value and distribution of stress will be affected by the thermal and physical properties and thermal conductivities of the structure and the host soil. In view of the above, it is important to determine thermal-mechanical coupled behavior under these conditions. In this study, a comprehensive method using theoretical derivations and numerical simulation was adopted to analyze the structural interaction between the energy pile and its host soil. The results of this study could provide technical guidance for the construction of energy piles.

1. Introduction

In the 1980s, geotechnical engineers in Austria and Switzerland began to use the building foundation as a heat exchanger for the ground-source heat pump (GSHP). The GSHP is a device that can better utilize the energy stored in the soil to transfer the stored heat energy to the structure using pipes laid underground and realize energy balance during both winter and summer. In summer, the host soil acts as a heat sink by transferring the heat from the buildings into the host soil. In winter, the host soil acts as a heat source and transports the heat from the host soil to the buildings. Energy pile is one of the promising areas in the burgeoning green power technology; it is gradually gaining attention and will have wide applications in the future. By taking advantage of the good thermal conductivity of concrete in the energy pile and the large heat exchange area between the pile and the host soil, the performance of the heat exchanger could be improved. Moreover, the energy pile can save the cost of drilling holes and preserve the underground space resources. Compared to the conventional GSHP that has been in use

in the past 20 years, the energy pile system (bored pile, precast concrete pile, and underground diaphragm wall) has witnessed rapid development globally, especially in Canada, Japan, and some European countries.

Because of its specific structure, the energy pile has the functions of both a structural element and a heat exchanger. It must withstand not only forces such as the frictional force and tip resistance, and the stresses as in the case of normal piles, but also the thermal stresses caused by the temperature changes during heat transfer. However, most researchers have been paying attention only to the heat transfer process and efficiency. In connection with heat transfer in an energy pile, Gao et al. (2008) studied the thermal performance and ground temperature of vertical pile-foundation heat exchangers and aimed at providing guidelines for improving the design of large-scale ground-coupled heat pumps in a district heating and cooling system [1]; Moon and Choi (2015) studied the heating performance characteristics of a GSHP system with energy piles and energy slabs [2]; Faizal et al. (2016) analyzed the heat transfer enhancement mechanism of geothermal energy piles [3]; Caulk et al. (2016) reported

the parameterization of a calibrated geothermal energy pile model [4]; Ghasemi-Fare and Basu (2016) presented a predictive assessment of heat exchange performance of geothermal piles [5]. Regarding studies on laying of piles, Cui et al. (2011) analyzed the heat transfer performance of pile geothermal heat exchangers with spiral coils [6]; Go et al. (2014) designed an energy pile with a spiral coil by considering the effective thermal resistance of the borehole and the effects of groundwater advection [7]; Xiang et al. (2015) developed a new practical numerical model for the energy pile with spiral coils [8]; Fadejev and Kurnitski (2015) used a whole building simulation software to simulate the geothermal energy piles and borehole design with heat pump [9]; Park et al. (2015) studied the coil-type ground heat exchanger by considering the relative constructability and thermal performance of a cast-in-place concrete energy pile [10]; Park et al. (2016) calculated the influence of coil pitch on the thermal performance of coil-type cast-in-place energy piles [11]; Yang et al. (2016) conducted laboratory investigations to analyze the thermal performance of an energy pile with spiral coil ground heat exchanger [12]. Several scholars had conducted research on the heat exchange efficiency of energy piles. Bozis et al. (2011) evaluated the effects of design parameters on the efficiency of heat transfer in energy piles [13]; Park et al. (2015) estimated the constructability and heat exchange efficiency of large diameter cast-in-place energy piles with various configurations of heat exchange pipes [14]; Yoon et al. (2015) reported the thermal efficiency and cost analysis of different types of ground heat exchangers in energy piles [15]; Cecinato and Loveridge (2015) analyzed the factors influencing the thermal efficiency of energy piles [16]; Astrain et al. (2016) performed a comparative study of different heat exchanger systems in a thermoelectric refrigerator and their influence on efficiency [17]; Akrouch et al. (2016) conducted experimental, analytical, and numerical studies on the thermal efficiency of energy piles in unsaturated soils [18]. On energy piles, there are some more research papers which provide technical guidelines for the construction of heat exchanger [19–21].

Numerical simulation is an important prediction method in engineering because of its high accuracy and low cost and the rapid development of computer techniques. Hence, many scholars use analytical tools such as finite element analysis software and finite difference software to solve problems on energy piles. Bezyan et al. (2015) built a 3D model to simulate the heat transfer in geothermal pile-foundation heat exchangers with a spiral pipe configuration [22]; Pu et al. (2015) developed a new practical numerical model for the energy pile with vertical U-tube heat exchangers [23]. Further, several scholars had conducted research on energy piles using numerical simulation methods [24–26]. Most of the above research work covers theoretical analysis, laying of piles, heat exchange efficiency, field test, and numerical simulation of energy piles. However, studies on the structural interaction between the energy pile and its host soil are scarce. As the behavior of the host soil is complicated and uncertain, thermal stresses appear with inhomogeneous distribution along the pile, and the peak value and distribution of stress would be influenced by the thermal and physical properties

and thermal conductivities of the structure and the host soil. In view of the above, it is important to determine the thermal-mechanical coupled behavior under these conditions. In this study, a comprehensive method using theoretical derivations and numerical simulation was adopted to analyze the structural response between the energy pile and its host soil. The results of this study can provide technical guidance for the construction of energy piles engineering.

2. Theoretical Analysis

As the foundation of the structure, the energy pile should be able to withstand forces such as the frictional force and tip resistance and the stresses as in the case of normal piles. The lateral friction force of the energy pile can be calculated by the β method.

$$q_l = \sigma_v ktg\beta, \quad (1)$$

where $\beta = ktg\phi$, k is the soil pressure coefficient, ϕ is internal friction angle, and σ_v is the vertical effective stress.

The tip resistance force can be obtained using the rigid-plastic body theory; the tip resistance force is given by

$$q_t = CN_c + \frac{1}{2}\gamma_1 BN_r + \gamma h N_q, \quad (2)$$

where N_c is the effect factor of cohesion, N_r is the loading factor for the weight of the soil, N_q is the overload factor, B is the diameter of the tip of the pile, h is the depth of the buried soil, γ_1 is the specific gravity of the soil, and γ is the average specific gravity of the soil.

The thermal stress due to temperature variations resulting from heat transfer should be considered. According to Fourier's law, the equation for heat conduction could be expressed as

$$\frac{\partial T}{\partial t} = \frac{1}{C_p \rho} \left(k_x \frac{\partial^2 T}{\partial x^2} + k_y \frac{\partial^2 T}{\partial y^2} \right), \quad (3)$$

where T is the temperature, C_p is the specific heat, and ρ is the density; k_x and k_y are the thermal conductivities in the x - and y -directions, respectively.

For deformable materials, the stress increment caused by a change in temperature is given by

$$\Delta\sigma_{ij} = -\delta_{ij} K \alpha^T \Delta T, \quad (4)$$

where $\Delta\sigma_{ij}$ is the stress increment, δ_{ij} is the Kronecker delta; when $i = j$, its value is 1, and when $i \neq j$, its value is 0; K is the bulk modulus, α^T is the coefficient of thermal expansion, and ΔT is the temperature increment.

According to the generalized Hooke's law,

$$\sigma_{ij} = 2G\varepsilon_{ij} + 3\lambda\varepsilon_{kk}\delta_{ij}, \quad (5)$$

where σ_{ij} is the stress, ε_{ij} is the total strain, ε_{kk} is the normal strain, $\lambda = E\nu/(1 + \nu)(1 - 2\nu)$, and $G = E/2(1 + \nu)$.

Lewis and Schrefler (1987) proposed the effective stress σ_{ij} [27] caused by change in temperature as follows.

$$\sigma_{ij} = 2G \left(\varepsilon_{ij} + \delta_{ij} \frac{\nu}{1 - 2\nu} \varepsilon_{kk} \right) - K \alpha^T \Delta T \delta_{ij}. \quad (6)$$

TABLE 1: Parameters of different layers of soil.

Layers	Density (kg/m ³)	Bulk (Pa)	Parameters		
			Shear (Pa)	Cohesion (Pa)	Friction angle (°)
Silty clay 1	1630	6.349×10^6	3.101×10^6	14.3	23.2
Silty-fine sand	1750	6.818×10^6	3.516×10^6	0	25.4
Silty clay 2	1740	6.944×10^6	3.968×10^6	17.6	20.6
Silty clay 3	1720	7.639×10^6	4.365×10^6	13.7	24.4
Floury soil	1750	8.472×10^6	5.984×10^6	11.4	26.3
Fine sand 1	1860	20.556×10^6	6.175×10^6	0	17.8
Fine sand 2	1820	20.556×10^6	6.175×10^6	0	17.8
Silty clay 4	1780	25.510×10^6	9.398×10^6	26.5	27.1

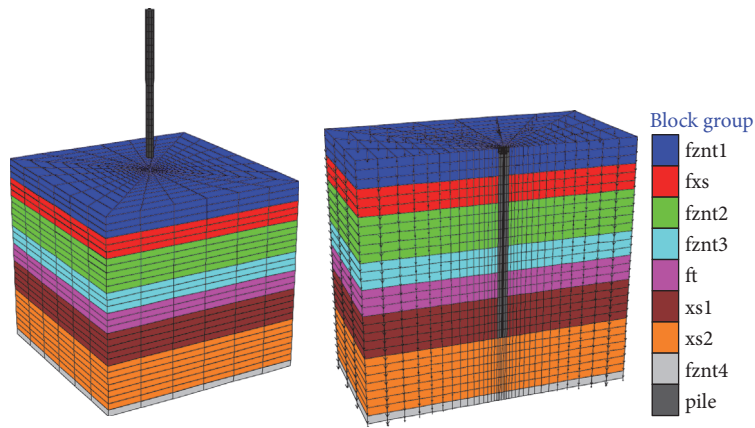


FIGURE 1: Simulation model of energy pile.

3. Numerical Simulation of Normal Pile

3.1. Simulation Model and Parameters. To predict the structural response between the energy pile and its host soil, a 3D model was built in finite difference software FLAC3D, as shown in Figure 1.

In the model, the physical element was used to build the pile and host soil, and the “*interface*” command was adopted to simulate the contact surfaces between the pile and the host soil. The length of the pile is 11 m along the Z-direction. The pile has a radius of 0.3 m. The host soil zone has a length of 16 m, X (−8 m, 8 m), a width of 16 m, Y (−8 m, 8 m), and a height of 15 m, Z (−15 m, 0 m); it was divided into eight layers of soil with different thicknesses. The pile was represented as an isotropic elastic model with the parameters of C30 concrete, having an elasticity modulus of 30 GPa and Poisson’s ratio of 0.2. The parameters of the soil layers are presented in Table 1.

3.2. Simulation of Pile. To obtain accurate results of simulation, 12 monitoring points (0 m, 1 m, 2 m, 3 m, 4 m, 5 m, 6 m, 7 m, 8 m, 9 m, 10 m, and 11 m) were set to monitor the lateral friction stress, axial stress, and tip resistance stress under different loads (55 kN, 110 kN, 165 kN, 220 kN, 275 kN, 330 kN, 385 kN, 440 kN, 495 kN, 550 kN, 690 kN, 825 kN, 960 kN, 1100 kN, and 1375 kN). A typical contour of the lateral

stresses under a load of 385 kN, obtained from simulation results, is shown in Figure 2.

Based on the results obtained under different loads, the graphs for lateral stress versus depth are plotted as shown in Figure 3.

From Figure 3, it can be seen that the lateral friction stresses change at the interface of different layers, which indicates that the lateral friction stresses are affected by the soil properties; they tend to increase toward the end of the pile and have the largest value at the end of the pile. For different loads, the curves follow the same trend; the larger the loads, the larger the lateral friction force.

A typical contour of the axial stress under a load of 385 kN is shown in Figure 4, based on the results of numerical analysis. The variation in axial stress along the depth under different loads is shown in Figure 5.

With increase in depth, the axial stresses decrease; the rate of decrease is gradual at the top of the pile, but the rate increases as the depth increases. Moreover, under different covered loading, a larger load causes a higher axial stress.

3.3. Analysis of Mechanical Characteristics of the Pile. The tip resistance stress and lateral friction stress are the important parameters in the analysis of mechanical characteristics of the pile. From the predicted results of simulation, the variation in total stress and the percentages of tip resistance and lateral

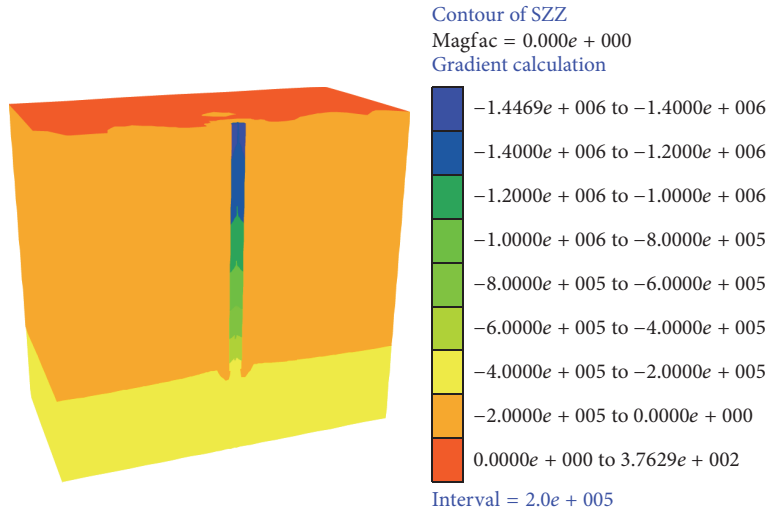


FIGURE 2: Typical contour of lateral stress under a load of 385 kN.

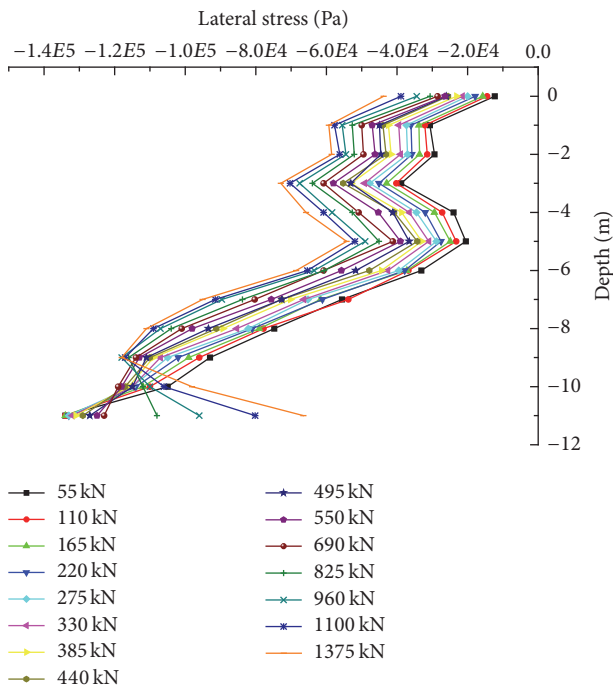


FIGURE 3: Variation in lateral stress along the depth of the pile.

friction stresses were calculated; these are shown in Figures 6 and 7, respectively.

From these figures, it can be seen that both the tip resistance stress and lateral friction stress vary with different loads. A larger load leads to a larger proportion of tip resistance stress and a lower proportion of lateral friction stress. Under smaller loading levels (less than 495 kN), the loads are mainly taken up by the lateral friction stress; most of the load is resisted in the host soil by the lateral friction effect, and the tip resistance stresses play a small role. With the increase in covered loads, the lateral stress increases. After the covered load exceeds 690 kN, the increase in load is

taken up by the tip resistance stress; the major load-bearing role is gradually taken by the tip resistance stress, and the proportion of tip resistance stress increases.

3.4. Pile Stability Analysis. The load-displacement curve is a direct representation of the stability of the pile. From the simulation results, the load-displacement curve for the pile is plotted, as shown in Figure 8.

According to the technical code for building pile foundation, for buildings with height less than 100 m, the allowable displacement is 350 mm; for buildings with heights in the range of 100–200 m, the allowable value of settling is 250 mm; and for buildings with heights greater than 200 m, the allowable value of settling is 150 mm. Thus, to ensure absolute safety, 150 mm was chosen in this study as the allowable value of settling. As shown in Figure 8, there is a significant increase in tip displacement with increase in covered loading. At loads greater than 825 kN, the displacement of the pile increases sharply. When the covered loading increases to 1100 kN, the settling value exceeds 180 mm, which would affect the safety of the structures. Hence, in real engineering structures, if the load is greater than 875 kN, the length or the quantity of piles should be revised to improve the bearing capacity.

4. Numerical Simulation of Energy Pile under Thermal Effect

4.1. Superficial Soil Temperature and Working Temperature. In Beijing area, the ground surface temperature is approximately -5°C in winter, and it reaches 28.5°C in summer. The temperature of the host soil would become stable with increase in depth. The variations in superficial soil temperature with depth in winter and summer are shown in Figure 9.

According to the stipulations in “Technical Code for Ground-Source Heat Pump System, 2009, China [28],” in summer, the working temperature at the water outlet of the heat exchanger pipe should not exceed 33°C , and the working temperature at the water inlet of the heat exchanger

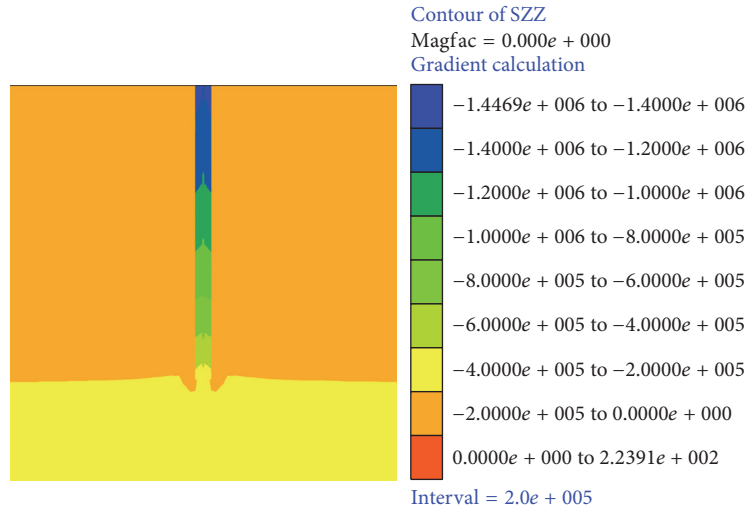


FIGURE 4: Typical contour of axial stress under a load of 385 kN.

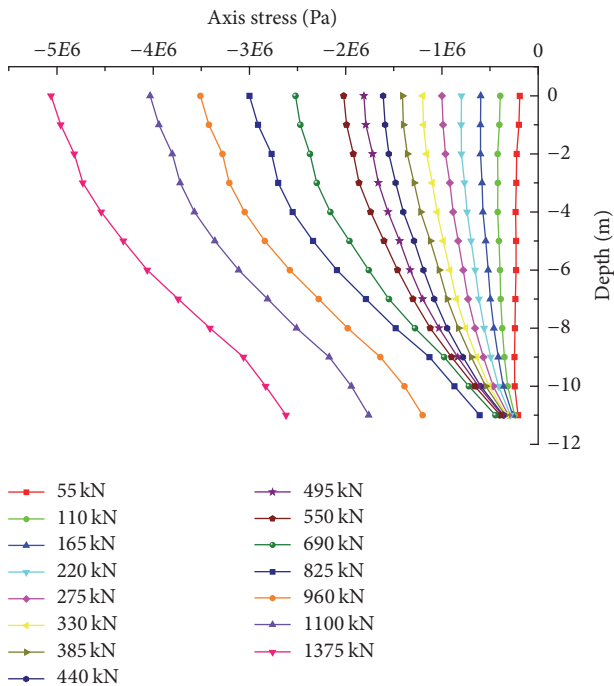


FIGURE 5: Variation in axial stress along the depth of the pile.

pipe should be more than 4°C. In this numerical simulation, to estimate the worst-case scenario for the stability of the energy pile, the two extreme temperatures (33°C and 4°C) were assumed as the working temperatures in summer and in winter, respectively.

4.2. Simulation Parameters and Boundary Conditions. Recent studies on energy piles show that spiral coil with the largest heat exchange surface of the fluid pipe is the optimal type of heat exchanger for a cast-in-place energy pile. From the results of thermal efficiency analysis, it is found that the spiral coil type has the best heating and cooling performance, with

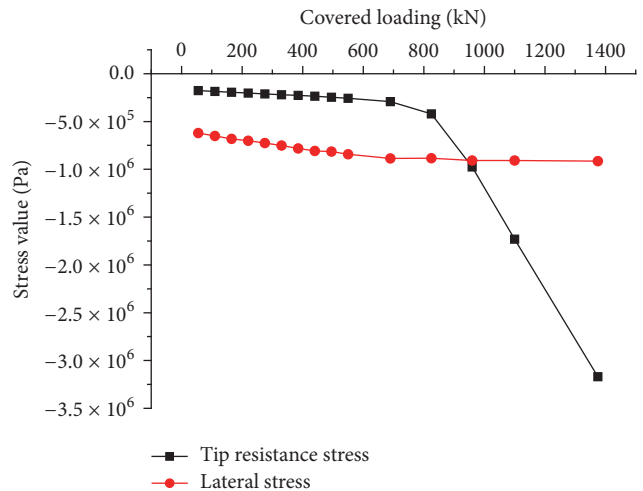


FIGURE 6: Total stress under different loads.

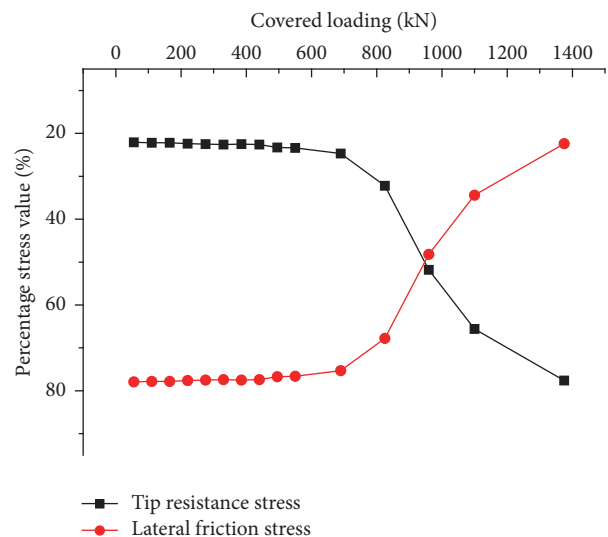


FIGURE 7: Share of stresses under different loads.

TABLE 2: Thermal parameters of different layers of host soil and concrete.

	Thermal expansivity (1/K)	Thermal conductivity coefficient, X-direction (W/m/K)	Thermal conductivity coefficient, Y-direction (W/m/K)
Silty clay 1	$1.8e^{-5}$	1.36	1.28
Silty clay 2	$1.8e^{-5}$	1.36	1.28
Floury soil	$1.5e^{-5}$	1.14	1.06
Fine sand 2	$2.1e^{-5}$	0.98	1.02
Silty-fine sand	$2.3e^{-5}$	1.19	1.13
Silty clay 3	$1.8e^{-5}$	1.36	1.28
Fine sand 1	$2.1e^{-5}$	0.98	1.02
Silty clay 4	$2.2e^{-5}$	1.46	1.45
Concrete	$1.2e^{-5}$	1.28	1.28

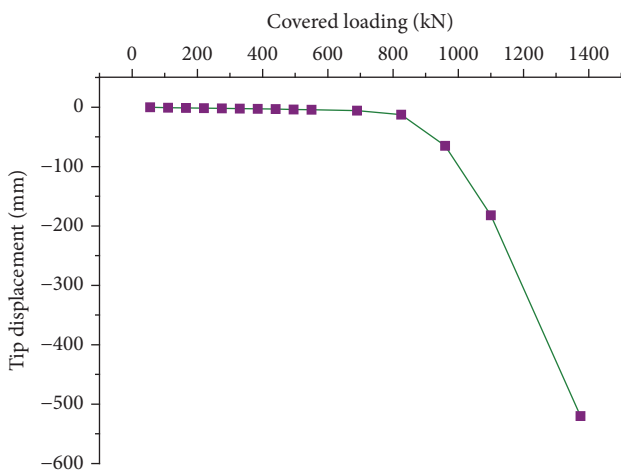


FIGURE 8: Load-displacement curve under different covered loading.

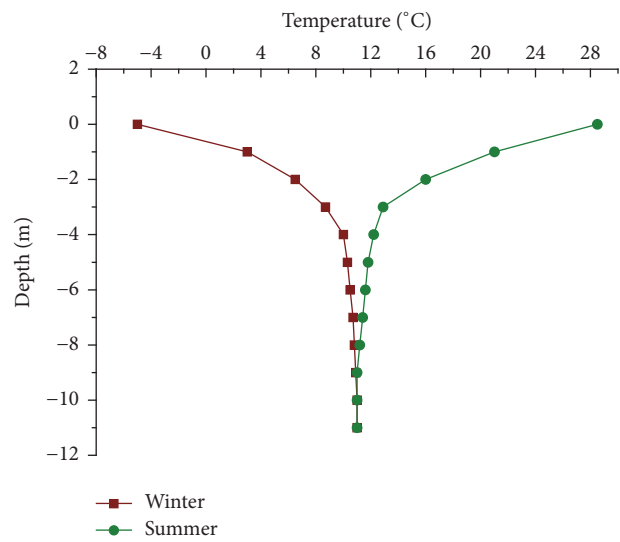


FIGURE 9: Variation in temperature with depth.

thermal efficiency nearly 150% of that of the double-U type [29]. A typical spiral coil heat exchanger cast-in-place energy pile and its detailed dimensions are shown in Figure 10. Based on the above results, in this simulation, a heat exchanger with spiral coil was selected; to simplify the modeling process and apply appropriate temperature boundary conditions, the spiral coil heat exchanger system can be equivalent to the form of a cylinder with 0.5 m external diameter which was selected. A working temperature of 33°C was assigned to the equivalent pipe in summer, and a working temperature of 4°C was assigned to the equivalent pipe in winter. The boundary conditions for temperature in the different layers of the soil, shown in Figure 9, were applied for the simulation.

In the simulation, nonhomogeneous thermal conductivities of the soil were applied by considering the effect of different levels of compaction, uneven layers, and other soil properties. The thermal parameters of the specimens obtained by cutting rings from different positions were tested using a DRE-III heat conductivity coefficient tester. The measuring probe and the testing instrument are shown in Figure 11.

The test results of the thermal parameters of different layers of the host soil and concrete are presented in Table 2.

4.3. Analysis of Simulation Results. In FLAC3D software, the pore pressure command was used to analyze the heat diffusion in the energy pile. From the simulation results, the typical thermal diffusion contour was obtained; this is shown in Figure 12.

During the simulation, the monitoring points were set at intervals of 1 m for reading the output. From the simulation results, the curves for the predicted temperature and its variation on the energy pile surface in winter and summer were obtained; the curves corresponding to winter and summer are shown in Figures 13(a) and 13(b), respectively.

Based on the simulation results, the thermal stresses were estimated. Further, the percentage share of the lateral friction stress and tip resistance stress under different covered loading in winter and summer was estimated; the corresponding values in the case of a normal pile were also estimated. These results are shown in Figure 14.

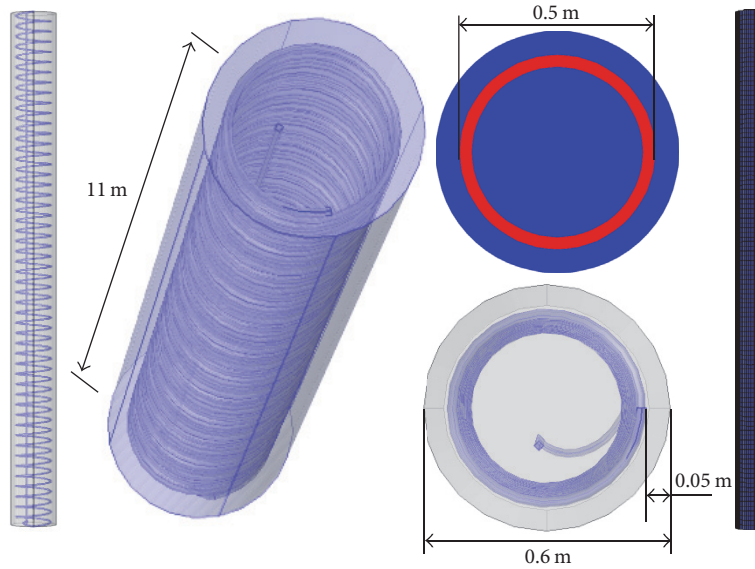


FIGURE 10: Conceptual model and simulation model of energy pile.



FIGURE 11: DRE-III heat conductivity coefficient tester and measuring probe.

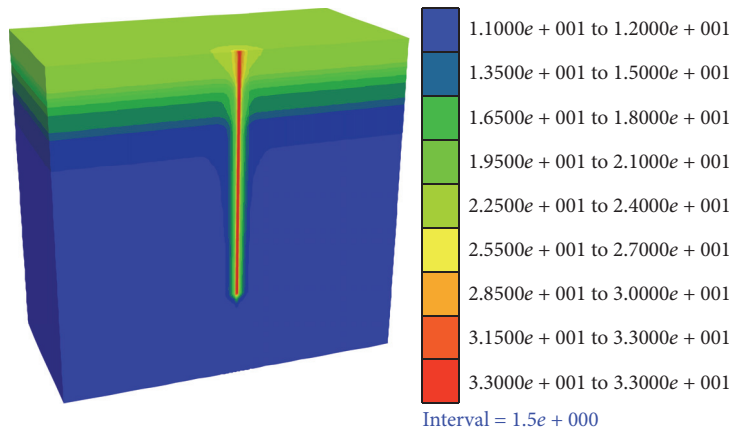


FIGURE 12: Thermal diffusion contour of energy pile in summer.

As shown in Figure 14, the lateral friction stress increases with load in summer; this provides some advantage in maintaining the stability of the energy pile. However, in winter, because of the effect of low temperature, the proportion of lateral friction stress in the total stress decreases with load; this will have an adverse effect in maintaining the stability of the energy pile.

5. Discussion and Conclusion

In this paper, using finite difference simulation, a series of predicted results on the structural interaction between the energy pile and its host soil are presented.

(1) The lateral friction stress changes at the interface of different layers, which indicates that the lateral friction force is affected by the soil properties; it tends to increase toward

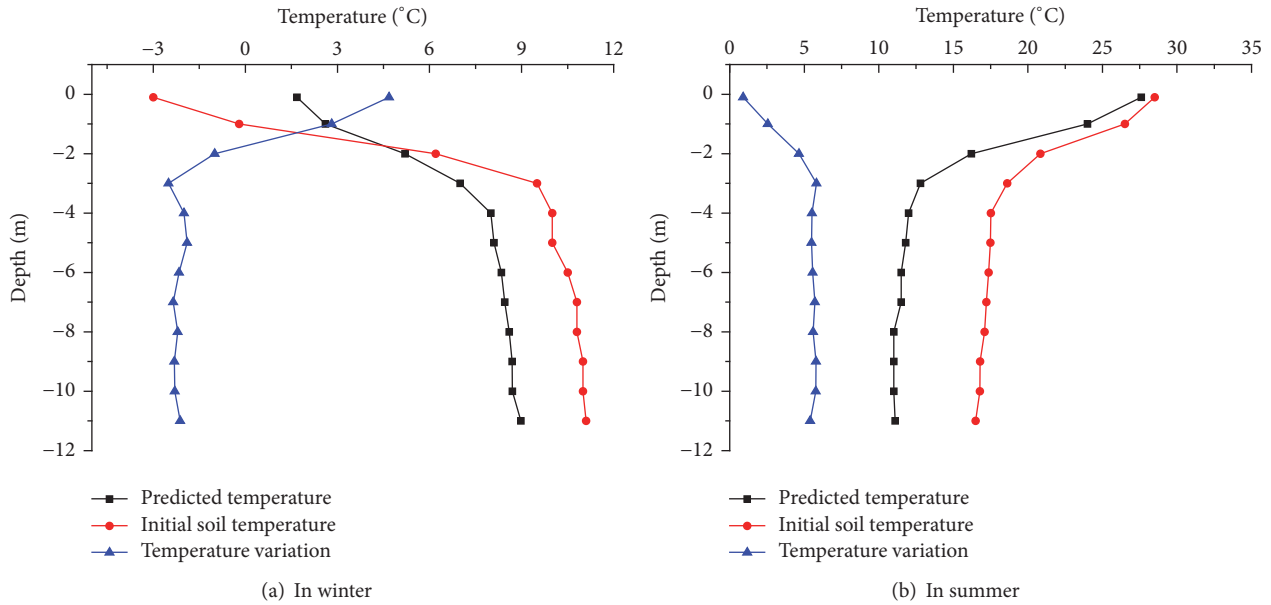


FIGURE 13: Predicted temperature and its variation on energy pile surface.

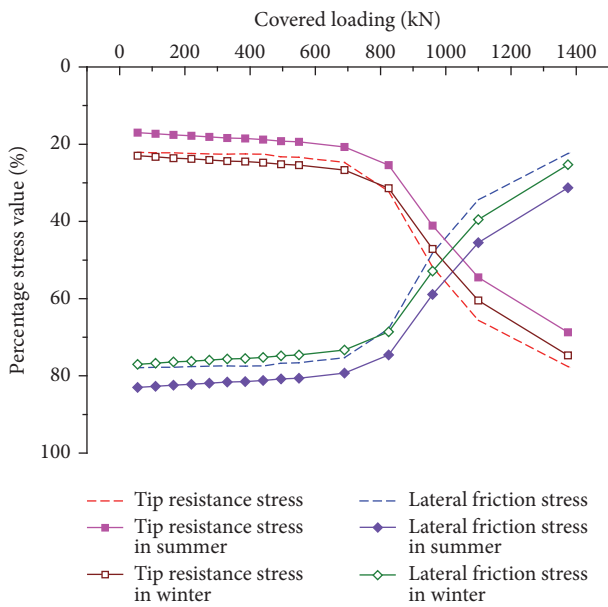


FIGURE 14: Percentage stress value under different covered loading in winter and summer.

the end of the pile and has the largest value at the end of the pile. For different loads, the curves follow the same trend; the larger the covered loading, the larger the lateral friction stress.

(2) Both the tip resistance stress and lateral friction stress are different under different covered loading. A larger load leads to a larger proportion of tip resistance stress and a lower proportion of lateral friction stress. Under smaller loading levels, the load is mainly taken up by the lateral friction stress; a large proportion of the load is resisted in the host soil by the lateral friction effect, and the tip resistance stress plays a

small role. With the increase in covered loading, the lateral stress increases. After the covered loading exceeds 690 kN, the increase in load is taken up by the tip resistance stress; the major load-bearing role is gradually taken by the tip resistance stress, and the proportion of tip resistance stress increases.

(3) There is a significant increase in tip displacement with increase in covered loading. At loads greater than 825 kN, the displacement of the pile increases sharply. When the covered loading increases to 1100 kN, the settling value exceeds 180 mm, which would affect the safety of the structure. Hence, in real engineering structures, if the covered loading is greater than 875 kN, the length or the quantity of the pile should be revised to improve bearing capacity.

(4) In summer, the lateral friction stress increases with load; this provides some advantage in maintaining the stability of the energy pile. However, in winter, because of the effect of low temperature, the proportion of lateral friction stress in the total stress decreases with load; this will have an adverse effect in maintaining the stability of the energy pile. Hence, it is necessary to provide more supporting capacity to ensure the stability of the energy pile.

Conflicts of Interest

The authors declare that they have no conflicts of interest.

Acknowledgments

This work was supported by the Opening Funds of State Key Laboratory of Building Safety and Built Environment (no. BSBE2015-06) and Joint Research Program between University of Science and Technology Beijing and National Taipei University of Technology (no. TW201703).

References

- [1] J. Gao, X. Zhang, J. Liu, K. S. Li, and J. Yang, "Thermal performance and ground temperature of vertical pile-foundation heat exchangers: a case study," *Applied Thermal Engineering*, vol. 28, no. 17-18, pp. 2295–2304, 2008.
- [2] C.-E. Moon and J. M. Choi, "Heating performance characteristics of the ground source heat pump system with energy-piles and energy-slabs," *Energy*, vol. 81, pp. 27–32, 2015.
- [3] M. Faizal, A. Bouazza, and R. M. Singh, "Heat transfer enhancement of geothermal energy piles," *Renewable and Sustainable Energy Reviews*, vol. 57, pp. 16–33, 2016.
- [4] R. Caulk, E. Ghazanfari, and J. S. McCartney, "Parameterization of a calibrated geothermal energy pile model," *Geomechanics for Energy and the Environment*, vol. 5, pp. 1–15, 2016.
- [5] O. Ghasemi-Fare and P. Basu, "Predictive assessment of heat exchange performance of geothermal piles," *Renewable Energy*, vol. 86, pp. 1178–1196, 2016.
- [6] P. Cui, X. Li, Y. Man, and Z. Fang, "Heat transfer analysis of pile geothermal heat exchangers with spiral coils," *Applied Energy*, vol. 88, no. 11, pp. 4113–4119, 2011.
- [7] G.-H. Go, S.-R. Lee, S. Yoon, and H.-B. Kang, "Design of spiral coil PHC energy pile considering effective borehole thermal resistance and groundwater advection effects," *Applied Energy*, vol. 125, pp. 165–178, 2014.
- [8] Y. Xiang, H. Su, W. Gou et al., "A new practical numerical model for the energy pile with spiral coils," *International Journal of Heat and Mass Transfer*, vol. 91, pp. 777–784, 2015.
- [9] J. Fadejev and J. Kurnitski, "Geothermal energy piles and boreholes design with heat pump in a whole building simulation software," *Energy and Buildings*, vol. 106, pp. 23–34, 2015.
- [10] S. Park, D. Lee, H.-J. Choi, K. Jung, and H. Choi, "Relative constructability and thermal performance of cast-in-place concrete energy pile: Coil-type GHEX (ground heat exchanger)," *Energy*, vol. 81, pp. 56–66, 2015.
- [11] S. Park, S. Lee, D. Lee, S. S. Lee, and H. Choi, "Influence of coil pitch on thermal performance of coil-type cast-in-place energy piles," *Energy and Buildings*, vol. 129, pp. 344–356, 2016.
- [12] W. Yang, P. Lu, and Y. Chen, "Laboratory investigations of the thermal performance of an energy pile with spiral coil ground heat exchanger," *Energy and Buildings*, vol. 128, pp. 491–502, 2016.
- [13] D. Bozis, K. Papakostas, and N. Kyriakis, "On the evaluation of design parameters effects on the heat transfer efficiency of energy piles," *Energy and Buildings*, vol. 43, no. 4, pp. 1020–1029, 2011.
- [14] S. Park, C. Sung, K. Jung, B. Sohn, A. Chauchois, and H. Choi, "Constructability and heat exchange efficiency of large diameter cast-in-place energy piles with various configurations of heat exchange pipe," *Applied Thermal Engineering*, vol. 90, pp. 1061–1071, 2015.
- [15] S. Yoon, S.-R. Lee, J. Xue, K. Zosseder, G.-H. Go, and H. Park, "Evaluation of the thermal efficiency and a cost analysis of different types of ground heat exchangers in energy piles," *Energy Conversion and Management*, vol. 105, pp. 393–402, 2015.
- [16] F. Cecinato and F. A. Loveridge, "Influences on the thermal efficiency of energy piles," *Energy*, vol. 82, pp. 1021–1033, 2015.
- [17] D. Astrain, P. Aranguren, A. Martínez, A. Rodríguez, and M. G. Pérez, "A comparative study of different heat exchange systems in a thermoelectric refrigerator and their influence on the efficiency," *Applied Thermal Engineering*, vol. 103, pp. 1289–1298, 2016.
- [18] G. A. Akrouh, M. Sánchez, and J.-L. Briaud, "An experimental, analytical and numerical study on the thermal efficiency of energy piles in unsaturated soils," *Computers and Geotechnics*, vol. 71, pp. 207–220, 2016.
- [19] Y. Hamada, H. Saitoh, M. Nakamura, H. Kubota, and K. Ochifuji, "Field performance of an energy pile system for space heating," *Energy and Buildings*, vol. 39, no. 5, pp. 517–524, 2007.
- [20] O. Ghasemi-Fare and P. Basu, "A practical heat transfer model for geothermal piles," *Energy and Buildings*, vol. 66, pp. 470–479, 2013.
- [21] H. Park, S.-R. Lee, S. Yoon, and J.-C. Choi, "Evaluation of thermal response and performance of PHC energy pile: field experiments and numerical simulation," *Applied Energy*, vol. 103, pp. 12–24, 2013.
- [22] B. Bezyan, S. Porkhial, and A. A. Mehrizi, "3-D simulation of heat transfer rate in geothermal pile-foundation heat exchangers with spiral pipe configuration," *Applied Thermal Engineering*, vol. 87, pp. 655–668, 2015.
- [23] L. Pu, D. Qi, K. Li, H. Tan, and Y. Li, "Simulation study on the thermal performance of vertical U-tube heat exchangers for ground source heat pump system," *Applied Thermal Engineering*, vol. 79, pp. 202–213, 2015.
- [24] A. A. Mehrizi, S. Porkhial, B. Bezyan, and H. Lotfizadeh, "Energy pile foundation simulation for different configurations of ground source heat exchanger," *International Communications in Heat and Mass Transfer*, vol. 70, pp. 105–114, 2016.
- [25] S. Chen, J. Mao, and X. Han, "Heat transfer analysis of a vertical ground heat exchanger using numerical simulation and multiple regression model," *Energy and Buildings*, vol. 129, pp. 81–91, 2016.
- [26] Z. Han, X. Ju, X. Ma, Y. Zhang, and M. Lin, "Simulation of the performance of a hybrid ground-coupled heat pump system on the basis of wet bulb temperature control," *Applied Thermal Engineering*, vol. 108, pp. 980–988, 2016.
- [27] R. W. Lewis and B. A. Schrefler, *The Finite Element Method in Deformation and Consolidation of Porous Media*, Wiley, New York, NY, USA, 1987.
- [28] PRC, "M.o.H.a.U.-R.D.o.t., Technical code for ground-source heat pump system," China building industry press, 2009.
- [29] J. Luo, H. Zhao, S. Gui, W. Xiang, J. Rohn, and P. Blum, "Thermo-economic analysis of four different types of ground heat exchangers in energy piles," *Applied Thermal Engineering*, vol. 108, pp. 11–19, 2016.